The rheology of pore and crystal bearing magmas

Thesis submitted in accordance with the requirements of the University of Liverpool for the degree of Doctor of Philosophy by

Rebecca Coats

March 2019

I hope you are blessed with a heart like a wildflower.

Strong enough to rise again after being trampled upon,

tough enough to weather the worst of the summer storms,

and able to grow and flourish even in the most broken places.

- Hearts Like Wildflowers, Hearts Like Yours | Nikita Gill

Contents

List of figures and tables

Chapter 1:

Chapter 2:

Chapter 3:

Chapter 4:

Chapter 5:

Chapter 6:

With iambic drum

arrived mother of autumn

accreting a weather beneath a walled arete,

-Untitled | Republic of Verse

Abstract

Magmas are viscoelastic multi-phase materials, comprising of a complex mixture of melt, vesicles (or pores) and crystals. Their rheology describes the way in which they deform - flow or fail - in response to local stresses. As magmas rise through the conduit, they are subjected to transient pressure (stress) and temperature conditions which cause their composition, componentry, and ultimately their rheology, to evolve. The dynamic nature of magmas means constraining their evolving rheology is an arduous task, and consequently failure forecasting models have disparities from observations. Knowledge gaps arise from a lack of understanding of magma behaviour as it undergoes (seismogenic) rupture, transitioning from the viscous to the brittle field. To effectively forecast volcanic hazards and thus improve risk mitigation strategies, a magma's rheological dynamism needs to be well constrained for use in magma transport and volcanic eruption models.

With the aim of improving our knowledge of magma rheology, this doctoral dissertation details experimental studies carried out on natural volcanic products and synthetic silicate analogues. The natural materials, collected from Mt. Unzen lava dome, were highly crystalline ($\varphi_x \approx 0.75$) and variably porous ($0.09 \leq \varphi_p \leq 0.35$). Uniaxial compressive experiments carried out at room and high (900 °C) temperature showed that sample strength decreased with porosity and increased with sample temperature and applied strain rate. At high temperature, as strain rate was increased, samples displayed non-Newtonian, shear thinning behaviours. As strain rate was increased further, the samples displayed an increasingly brittle response, which was then superseded by macroscopic failure. The critical Deborah numbers, which describe the onset of non-Newtonian behaviour, De_{n-N}, and failure, De_{fail}, were found to decrease with porosity.

Variably crystalline ($0.0 \leq \varphi_x \leq 0.5$), negligibly porous ($\varphi_p \leq 0.03$), synthetic samples were created to constrain the effects of crystals on magma rheology. The rheological response of these samples to deformation was examined both *ex situ* and *in situ*, using synchrotron-based computed X-ray micro-tomography (sXCT).

Ex situ testing was used to further constrain the critical Deborah number at the onset of non-Newtonian behaviour for variably crystalline materials. The findings revealed that the empirically derived critical packing fraction, φ_*, was a better fit to the data than the mathematically derived maximum packing fraction, φ_m. By combining this result with the constraint obtained for natural samples, the Deborah number at the onset of non-Newtonian behaviour for multi-phase magmas was cast as $De_{n-N} = -1.7 \times 10^{-4}\varphi_p + 10^{-3}(1 - \frac{\varphi_x}{\varphi_*})$, where at or above a porosity of 0.27, $De_{n-N} = De_{fail}$. *Ex situ* experiments also revealed that crystal fracture and resulting dilatancy may be leading causes of non-Newtonian.

In situ testing provided evidence for the microstructural evolution of shearing magma, indicating that dilation of multiphase magma resulted from small tears that nucleated at melt-crystal boundaries and increased in size and number with increasing strain, strain rate and crystallinity. 3-D quantification of the porosity evolution through time found that sample porosity increased from its initial fraction, φ_{pi},

as a function of crystal fraction, strain, ε, and strain rate, $\dot{\varepsilon}$, following $\varphi_p = \{[0.36log(\dot{\varepsilon}) + 2.99]\varphi_x\}\,\varepsilon + \varphi_{pi}$.

The holistic approach taken in this study provides robust constraints on the evolution of magma across the viscous-brittle transition, necessary to model magma transport, magmatic fragmentation and the source mechanisms of seismicity in volcanic conduits. The observed dilation concomitant with deformation of shear-thinning multiphase magma implies that shear may prompt physicochemical changes such as filter pressing and volatile exsolution which may aid in mobilising the magma. The dilation of magma also exacerbates pore connectivity and thus permeable outgassing, which regulate the potential explosivity of eruptions. In closing, this experimental study gives a fresh insight into the dynamic nature of magmas. Conclusions drawn are likely to play a central role in the modelling and forecasting of volcanic eruptions.

Acknowledgements

It is with no exaggeration that I write that the following pages required more sweat, blood and tears than I thought was humanly possible. It is only through the generous kindness, patience and encouragement from the following list that their completion was achieved. So, in no particular order, I would like to address those that brought me to where I am today.

To my loving family, you are the most supportive family I could have asked for. You all believed in me so much, so you threw me a surprise Dr Becky Mexican party before I even started my PhD. Since I was young you have taught me that the outcomes of my endeavours don't matter as long as I've tried my best, and although I sometimes need reminded that it is OK to fail, I have always lived by that philosophy. Without your financial and emotional support, I wouldn't have been where I am today. Thank you.

To my dearest Samuel, without you I wouldn't be sitting here typing this. Thank you for making England feel like my home (which is something I never thought I would say!) by welcoming me into your wonderful family. Thank you for believing in me even when I thought there was nothing to believe in, thank you for being by my side even when I wasn't easy to be beside and mostly thank you for loving me when I thought I was impossible to love. You have made me the happiest person I can ever hope to be, and I never want to go through life without you by my side.

To my wee man Boo. Thank you for making me have a life outside uni. You're the reason I stayed in Liverpool by making the hard times bearable. You kept me in a routine and through looking after you I was able to look after myself. You can have all the treats.

To Anthony, you French beauty, I'm not going to lie, the first time I met you I wasn't sure. I was like who is this guy I have to sleep in a tiny two-man tent at the top of a Mexican volcano with that doesn't understand my accent and questions my navigation skills? But *very* quickly I got to know you and love you. Without your French determinism and love of beer I would have been stuck because none of the equipment would work in the lab, I would have had no one decent to argue with, and would have been so bored (and sober) I probably would have got back on the next train to Glasgow Central. Now I can't imagine what my PhD would have been like without you, probably still unfinished and without compliance... MERCI!

To Jackie, we all know that the rest of this dissertation wouldn't have been the best thing anyone has read without you. For one thing, it would have been covered in s's where s's shouldn't be. However, aside from the fact that you probably proofread this more times than me, I would be lost without you. Your fierce attitude has rubbed off on me and I have now learned the tricks of surviving in the male dominated world of science- complete with conference acrylics. I couldn't have asked for a better supervisor, role model, councillor, scientific advisor and friend. I hope we drink prosecco in many hot tubs to come.

To Yan, when I first came to Liverpool for my interview, I thought I had already made up my mind that I was going to do a PhD at UCL. But when I met you your enthusiasm for experimental

volcanology and for understanding the fundamentals of magma behaviour changed my mind. Its not every interview that your prospective boss buys you a pint and a burger and asks if you want to head to Mexico in three weeks' time, while at the same time showing you a video of something called 'Un poisson magique'. I couldn't have made a better choice. You have created a group of truly brilliant scientists that look at the way rocks and magmas behave just that bit differently to everyone else. You see the true beauty in the world around you and its inspiring. Thanks to you I am an albatross.

To the rest of team EViL, Thanks for being an amazing lab team. You may have never ordered any blue roll when we needed it and always used my mugs for Nespresso, but you were the funniest group of people imaginable. My highlight probably includes dancing to 'Gagman Style' after too many hot tub watermelon coolers in California.

To the Liverpool PhD team. Júlia, Joe[2], Caroline, Simon, Suraya, Elliot, Louise, Mila, Stephan, Sergio, James, John, Mike and so, so many more. Thanks for being the happiest happy hour bunch. Fridays won't be just as happy without you. And to my SCABs, my cheeks won't glitter the same way without you all.

To Fabian, firstly thanks for the poem, intertwined with poems from others, that compliments each chapter of this dissertation. Secondly, thanks for pushing the boundaries of my scientific intellect and helping me understand the basic principles of sintering. Finally, thanks for partying hard with me, so hard in fact that I have a mild head injury from dancing with you at a jazz bar in New Orleans.

To Jamie, thanks for going above and beyond to help me improve my work. Thanks for instilling in me the belief of scientific freedom and most of all having the guts to do something about it. Freedom has always been in our blood and I salute you for bringing it home.

I'm writing these acknowledgements after I completed my viva as I wanted to take the time to thank everyone who helped me get there. So, I wanted to thank my examiners Janine and Mike first of all for listening to me talk for 6 hours, not an easy feat, but also for giving me an important life lesson to never undersell myself. A valid lesson for anywhere in life, not just academic research.

This is a non-exhaustive list and I could go on but lets be honest- no one ever really reads these! So, if you are reading this dissertation- thanks. I apologise for any mistakes now and remind you that (for many reasons) I am leaving the world academia and so don't try and email me. Best to get me on Twitter via @BeckyCoats.

Over the crab-boxers

possessed and repossessed

of their misted water, all drumlin in ripples,

-Untitled | Republic of Verse

Chapter 1: Introduction

1.1. Preface

The purpose of this doctoral dissertation is to further our understanding of the flow behaviour of crystal-bearing magmas, referred to as their *rheology*. The rheological properties of magmas determine a range of physicochemical processes and their dynamics from early melt segregation to transport, storage and eruption. During volcanic eruptions, the rheology of magma influences how it erupts at the surface (Fink and Griffiths, 1998) and therefore the hazards posed by the eruption (e.g. Cassidy et al., 2018). The rheology of magma is dependent on the physical and chemical properties of magma (Dingwell, 2006). As magma ascends, its rheology evolves upon nucleation and growth of crystals (Cashman and Blundy, 2000; Blundy and Cashman, 2001) and bubbles (Gonnermann and Manga, 2007). Its adopted rheology influences the development of strain localisation (Lavallée et al., 2013), rupture (Lavallée et al., 2013), friction along conduit edges (Melnik and Sparks, 2005; Lavallée et al., 2015a), and the development of permeable pathways (Kendrick et al., 2013b) near the conduit walls. The majority of magmas are viscoelastic suspensions of bubbles and crystals in a Newtonian silicate melt phase (Dingwell and Webb, 1989). The viscosity of a magma is controlled by its chemical composition (including volatile content) and its resultant structural configuration, as well as its temperature and confining pressure (e.g. Giordano et al., 2008). The volume fraction, size and shape of crystals and bubbles in the suspension also play a major role in the rheological behaviour of magmas (e.g. Llewellin and Manga, 2005; Caricchi et al., 2007; Mueller et al., 2010; Mader et al., 2013). Importantly, the heterogeneous nature of magmatic suspensions, which display a range of transient properties during diverse magmatic and volcanic properties, makes magmas rheologically complex materials which responds to stresses in ways we have not yet fully quantified.

This introduction acts as a prelude of what is to come in the following chapters and its objective is to give the reader a sufficient background into the fundamentals of magma rheology and why, for volcanic hazard assessment, it is necessary to constrain its properties.

Throughout this dissertation, equations have been formatted so that **tensors** are written in **bold**. Other variables are written in plain text.

1.2. Rheology of viscoelastic materials

The term rheology was conceived by Eugene C. Bingham and Markus Reiner in the 1920s and comes from the Greek words ‘rhéō’, meaning ‘to flow’, and ‘-logica’ meaning ‘the study of’ (Reiner, 1964). The science combines both solid and fluid mechanics and concerns the study of the flow of materials which exhibit a combination of elastic, plastic and viscous behaviour. Examples include soils (e.g. Kutílek, 1972), polymers (e.g. Krieger and Dougherty, 1959), food (e.g. Dickie and Kokini, 1983), bodily fluids (e.g. Mandal et al., 2007), and, evidently, magmas (e.g. McBirney and Murase, 1984).

1.2.1. Maxwell's model of viscoelasticity

A Newtonian *fluid* is one in which a linear relationship exists between the applied stress tensor, $\boldsymbol{\sigma}$, and the strain rate tensor, $\dot{\boldsymbol{\varepsilon}}$, where the slope of the relationship is a scalar constant equal to the fluid's viscosity, μ, so that

$$\boldsymbol{\sigma} = \mu\dot{\boldsymbol{\varepsilon}}. \tag{1.1}$$

If the fluid is isotropic - i.e., its mechanical properties are equal in all directions - the tensors are symmetrical and can effectively be described as one-dimensional scalars, and thus

$$\sigma = \mu\dot{\varepsilon}. \tag{1.2}$$

Similarly, a Hookean *solid* is one where a linear relationship exists between the stress tensor and the strain tensor, $\boldsymbol{\varepsilon}$, where the slope of the relationship is the elasticity tensor of the solid, $\boldsymbol{e}$.

$$\boldsymbol{\sigma} = -\boldsymbol{e}\boldsymbol{\varepsilon}. \tag{1.3}$$

Many substances exhibit properties of both a liquid and a solid, and are known as *viscoelastic* materials (Barnes et al., 1989; Dingwell, 1995; Phan-Thien and Mai-Duy, 2017). The elastic portion can be modelled as a linear equivalent of Hooke's Law:

$$\sigma = E\varepsilon, \tag{1.4}$$

where E is the elastic modulus, whereas the viscous part can be modelled as an isotropic Newtonian fluid (Eqn. 1.2). Simplified, a viscoelastic medium can be modelled as a Maxwell material (Maxwell, 1867), via

$$\sigma + \frac{\mu}{E}\dot{\sigma} = \mu\dot{\varepsilon}, \tag{1.5}$$

where $\dot{\sigma}$ is the rate of stress. According to the model, if the material is put under constant stress the strain comprises two components: 1) an instantaneous elastic component which would relax to its original form if stress were removed and 2), a viscous component whereby if constant stress is applied strain increases over time and is not reversible. Moreover, if a viscoelastic material is under constant strain the stress will relax according to the relaxation time, τ, where

$$\tau = \frac{\mu}{E}. \tag{1.6}$$

For isotropic materials, the elastic modulus can be constrained as two independent moduli, the bulk modulus, K_∞, and the shear modulus, G_∞, at infinite frequencies (Dingwell and Webb, 1989). Thus, a viscoelastic material has a shear component of relaxation where μ_s is the shear viscosity and τ_s is the shear relaxation time, giving

$$\tau_s = \frac{\mu_s}{G_\infty}, \tag{1.7}$$

and a bulk component of relaxation where μ_b is the bulk viscosity and τ_b is the bulk relaxation time, such that

$$\tau_b = \frac{\mu_b}{K_\infty}. \tag{1.8}$$

For an incompressible fluid the bulk viscosity term can be neglected, and for silicate bodies, the bulk and shear moduli are similar in magnitude and are relatively independent of temperature and chemical composition (Dingwell and Webb, 1989). Thus, it is common to refer to silicate melts' shear relaxation rate in order to describe its rheology.

1.2.2. The glass transition

In viscoelastic fluids there is a region in temperature-time space where the material exists in a partially relaxed state (Dingwell and Webb, 1989). This is known as the glass transition interval. The region separates the fully relaxed behaviour of a liquid from the unrelaxed behaviour of a glass. When a material is perturbed from its equilibrium position (e.g. due to a variation in temperature or stress), it may cross the glass transition. If temperature is decreased then the relaxation time is increased, and the transition may be crossed from liquid to glassy state over the observation timescale. If the perturbation is slower than the structural relaxation timescale then the material will have a liquid response over the observation timescale. The response of a material to any given perturbation generates a unique relaxation timescale. In a cooling system, the last temperature at which relaxation may be achieved is known as a fictive temperature (Webb et al., 1992). Likewise, at any temperature, if the rate of perturbation (e.g. strain rate) exceeds the relaxation time then the melt will behave as a solid glass.

In the laboratory, the glass transition interval can be described using the onset or peak of change in physicochemical properties, such as the heat capacity or thermal expansivity, as a glass is heated during differential scanning calorimetry or dilatometry, respectively (Webb and Knoche, 1996). Being time-dependent, the glass transition temperature, T_g, represents its thermal history. In recent years, thermal analyses (i.e., differential scanning calorimetry or dilatometry) have commonly been used to determine T_g by subjecting glass samples to rapid heating rates of 10 °C.min^{-1} (e.g. Wadsworth et al., 2014). Under such conditions, studies have found that the peak of changes in heat capacity or thermal expansivity corresponds to temperature at which the liquid has a viscosity of ca. 10^{12} Pas, providing a simple way to charaterise the rheological state (liquid vs glassy) of viscoelastic bodies (e.g. Webb and Knoche, 1996).

1.2.3. The Deborah and Weissenberg numbers

The rheology of magma can be assessed by evaluating the controlling parameters. Most non-Newtonian fluids have a characteristic relaxation time scale, τ, and are deformed at either a characteristic strain rate, $\dot{\varepsilon}$, frequency, f, or observation time, t_{obs}. Two dimensionless numbers describe the materials behaviour, depending on its stain history.

The Deborah number:

$$\mathrm{De} = \tau f \text{ or } \frac{\tau}{t_{obs}} \tag{1.9}$$

Where if the observation time scale is large ($i.e.\,\mathrm{De} < 1$), the material will behave as a fluid, while if the observation time is small ($\mathrm{i.e.\,De} > 1$), the material will respond as a glass (Phan-Thien and Mai-Duy, 2017).

Or the Weissenberg number,

$$\mathrm{Wi} = \tau\dot{\varepsilon} \tag{1.10}$$

The Weissenberg number defines the ratio of elastic to viscous forces, therefore non-Newtonian behaviour is expected for large Wi (Phan-Thien and Mai-Duy, 2017).

It is a common occurrence for the definitions of the Deborah and Weissenberg numbers to be confused in the literature if terms are not well defined (Poole, 2012).

1.2.4. Non-Newtonian behaviour

The response exhibited by most viscoelastic materials can be modelled by the generalised Herschel-Bulkley relation (1926).

$$\sigma = \sigma_0 + K\dot{\varepsilon}^n, \tag{1.11}$$

where σ_0 is the yield-stress, K is the constant flow consistency and n is the power-law exponent (or flow index). When a non-Newtonian viscoelastic material exhibits a yield-stress, that is a level of stress that a material must overcome to flow, it is known as a *Bingham plastic* (Fig. 1.1a). Whereby it behaves as a rigid body, then once the yield-stress is reached it acts as a viscous fluid. When $n = 1$ then its plastic viscosity is constant and is equivalent to the slope of the line, or the flow consistency. If $n \neq 1$ then the material's plastic viscosity is no longer constant, and it is known as a *Bingham pseudoplastic*. When $n < 1$ the material is *shear-thinning* (Fig. 1.1b) and its viscosity decreases with strain rate. When $n > 1$, the opposite is true, and the material is *shear-thickening* (Fig. 1.1c) and its viscosity increases with strain rate (Mader et al., 2013).

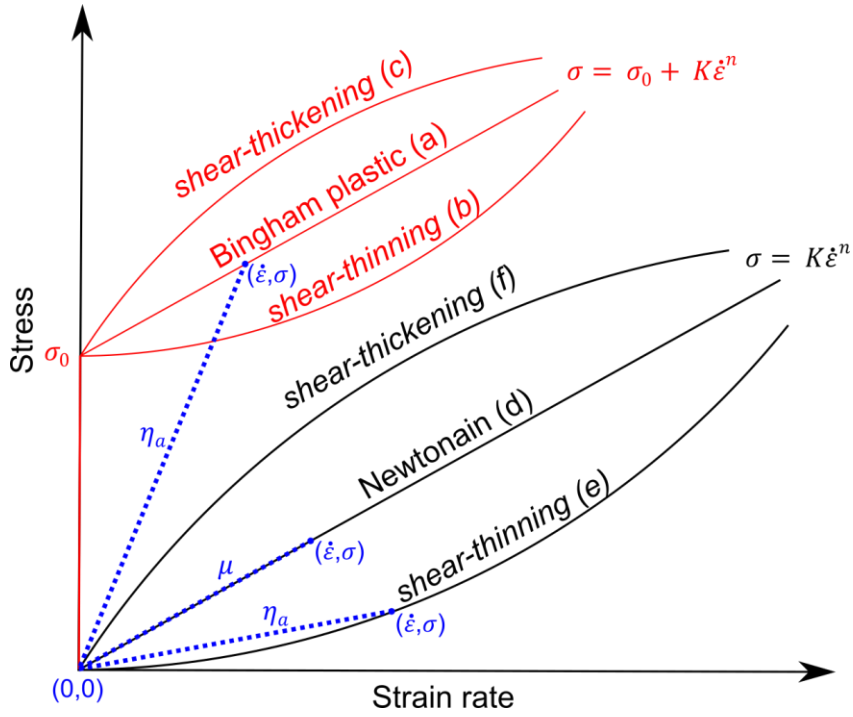

Figure 1.1. Flow curves for (a) a *Bingham plastic* material with (b) *shear-thinning* behaviour and (c) *shear-thickening* behaviour, all of which (in red) can be described by the Herschel-Bulkley (1926) equation. When no yield stress, σ_0, is present, the flow curves represent (d) a Newtonian fluid when $n = 1$, (e) a non-Newtonian shear-thinning fluid when $n < 1$ and (f) a non-Newtonian shear-thickening fluid when $n > 1$. All of which can be described by the power-law reduction of the Herschel-Bulkley (1926) equation (in black). The apparent viscosity, η_a, of the material at any point in stress-strain space $(\dot{\varepsilon}, \sigma)$ is the slope of the line between the origin and that point (in blue). For a Newtonian fluid, $\eta_a = \mu$.

For a material with no yield stress, $\sigma_0 = 0$, the material can be described by the simplified *power-law fluid* relationship,

$$\sigma = K\dot{\varepsilon}^n. \tag{1.12}$$

When $n = 1$, the flow is Newtonian, and its viscosity is equal to the flow consistency; that is, $\mu = K$ (Fig. 1.1d). When $n \neq 1$ then the material's viscosity is no longer constant with strain rate and it is known as a *non-Newtonian fluid*. Therefore, when $n < 1$ the material is a *shear-thinning* fluid (Fig. 1.1e), where its viscosity decreases with strain rate. When $n > 1$, the opposite is true, and the material is *shear-thickening* fluid (Fig. 1.1f) and its viscosity increases with strain rate (Mader et al., 2013).

The apparent viscosity, η_a, is the viscosity of the material at any point in stress-strain rate space $(\dot{\varepsilon}, \sigma)$. It is equal to the slope from the origin $(0,0)$ to that point (Fig. 1.1). For a Newtonian fluid $\eta_a = \mu$ at any point, but for a non-Newtonian fluid the apparent viscosity is variable with stress and strain rate. For a Bingham plastic it is useful to note that the apparent viscosity does not equal its plastic viscosity and is still equivalent to the slope from the origin to any point in in stress-strain rate space

(Mader et al., 2013). Although the existence of a 'true' yield stress is debated and it is generally thought of as the stress at which a flow transitions from an elastic body to a viscous fluid (Heymann et al., 2002).

For many fluids, the reason for non-Newtonian rheology is thought to arise from the arrangement of particles (e.g. molecules) within the fluid and the forces between those particles (e.g. Fig. 1.2; Brown and Jaeger, 2011; Cheng et al., 2011).

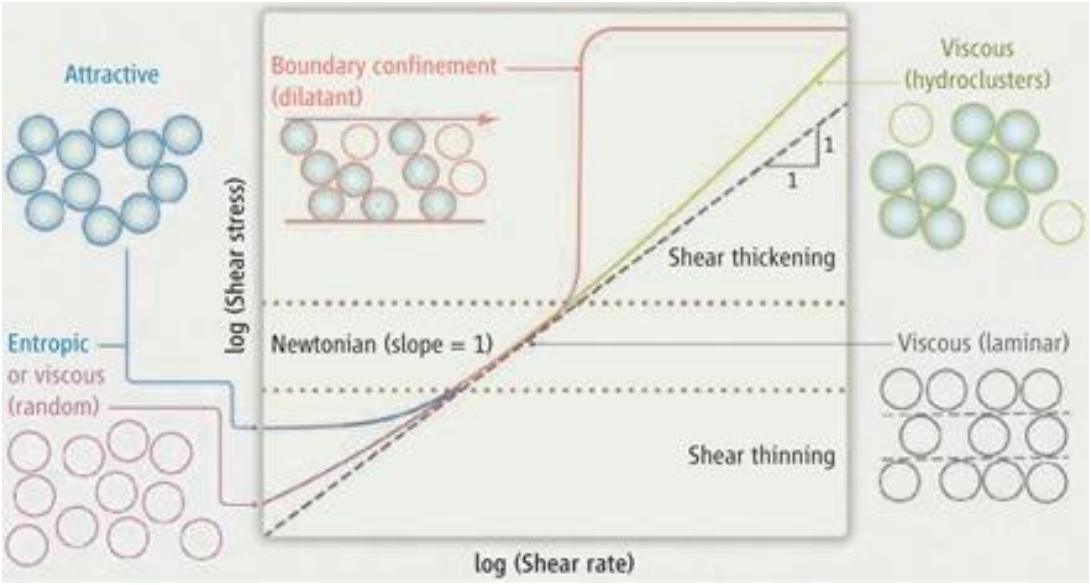

Figure 1.2. Annotation of a log-log plot of shear stress versus shear rate for particle-bearing melts. The different contributions to stresses and their related particle arrangements are shown for shear-thinning, Newtonian, and shear-thickening regimes. When the rate of shear stress increase is lower than the rate of shear rate increase, then the flow is shear thinning. Here, particles are orientated randomly (purple line) and as they become more ordered the flow tends towards the Newtonian regime. The shear thinning effect is exaggerated if there are entropic attractive forces between particles (blue line). When shear stress and shear rate have a 1:1 relationship the flow is Newtonian (dashed line) and the particle response is laminar. However, when the rate of shear stress increase is higher than the rate of shear rate increase, then the flow is shear thickening. Here, particles are clustered (green line) and if a boundary confinement is put in place then this effect is exaggerated (orange line) (from Brown and Jaeger, 2011).

1.2.5. Time-dependent behaviour

In some non-Newtonian fluids, viscosity can be time-dependent (Mewis and Wagner, 2009). A material can be thixotropic, whereby, when held at a constant deformation (strain) rate, its viscosity decreases over time or strain (Fig. 1.3a). Inversely, a material can also be anti-thixotropic (previously referred to as rheopectic), where its viscosity increases over time or strain (Fig. 1.3b). The reason for time-dependent non-Newtonian behaviours is due to time-sensitive changes in the structure of the fluids. This has been related to the time-dependent alignment of particles in thixotropic materials and the time-dependent recovery of structure in anti-thixotropic fluids (Mewis and Wagner, 2009).

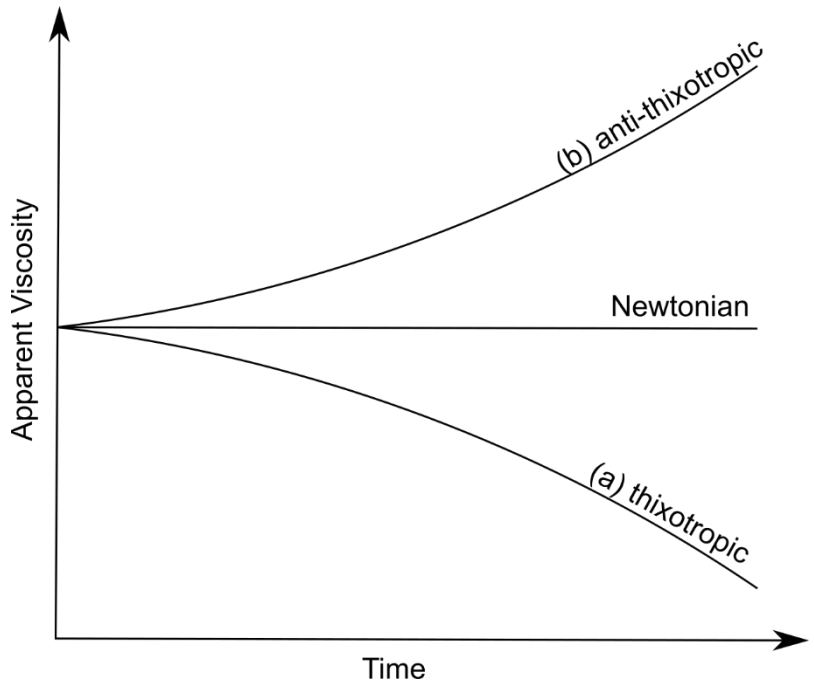

Figure 1.3. Time (strain)-dependent reversible behaviours of viscoelastic fluids. When viscosity decreases with time the material is (a) thixotropic. When viscosity increases with time the material is (b) anti-thixotropic.

1.3. Magma rheology

The rheological behaviour of magmas is complex and controlled by its chemical composition (including volatile content), its molecular configuration, its constituents (crystals and bubbles), and the temperature and pressure of the system (Dingwell, 2006). Moreover, the rate of magma deformation has a firm control on the state of the melt phase (as discussed in previous sections; Dingwell, 1996) as well as on the resultant apparent viscosity of the suspension (Caricchi et al., 2007; Costa et al., 2009).

1.3.1. Impact of melt chemistry

The chemical structure of silicate melts consists of a disordered arrangement of silicon-oxide tetrahedra $(SiO_4)^{4-}$. The silica anions share oxygen with other silicate tetrahedra, where the shared oxygen is known as a bridging oxygen (BO). In cases where the oxygen is only bound to one tetrahedra, commonly due to the presence of other cations balancing the remaining forces, we refer to this oxygen as a non-bridging oxygen (NBO). The continuous structural rearrangement of silicate melts is known as the structural relaxation and is what gives rise to the viscous response of magmas. The degree of polymerisation - i.e., the ratio of non-bringing oxygens to silicate tetrahedra (NBO/T) - determines the intrinsic properties of the melt which control its viscosity, glass transition interval and, ultimately, its rheological behaviour (Giordano and Dingwell, 2003).

In most magmas, volatiles are dissolved in the melt phase. Small fluctuations in the volatile content of a melt, particularly of water and fluorine, can disrupt bridging oxygens. This carries important

consequences on the viscosity and glass transition of the melt, and therefore its response to deformation (Giordano et al., 2004b, 2004a).

Since the early efforts of Shaw (1963) who has constrained the temperature dependence of silicate melt viscosity to be Arrhenian (i.e., so that the viscosity is proportional with the inverse of temperature), technological advances have allowed us to measure the viscosity of silicate melts at sub-solidus conditions, which has demonstrated that the viscosity of silicate melts is non-Arrhenian (Dingwell, 1995). 25 years later, the non-Arrhenian model captures the viscosity of a broad chemical range of natural silicate melts (Giordano et al., 2008), with applicability to a range of magmatic (e.g. Passmore et al., 2012), volcanic (e.g. Castro and Dingwell, 2009), tectonic (e.g. pseudotachylyte; Ujiie et al., 2009; Lavallée et al., 2015a) and anthropogenic (e.g. fly ash; Carpio et al., 2018) processes.

1.3.2. Bubble-bearing magmas

In a melt, bubbles nucleate when volatile concentrations exceed the solubility at a given pressure and temperature conditions (Zhang, 1999); in nature, this may be forced by crystallisation (Martel et al., 1999), decompression (Zhang, 1999), and thermal input (Ghiorso and Sack, 1995; Lavallée et al., 2015b). Bubbles may deform or not depending on the stress field and viscosity of the phases in the suspension. Their equilibrium deformation can be described by the dimensionless capillary number,

$$Ca = \frac{\mu R \dot{\varepsilon}}{\Gamma} \tag{1.13}$$

where μ is the viscosity of the surrounding Newtonian melt, R is the radius of the idealised spherical bubble, $\dot{\varepsilon}$ is the strain rate and Γ is the surface tension (Rust and Manga, 2002). Depending on the capillary number of the bubble, the viscosity of bubble bearing magmas is variable. When restoring tension forces dominate, $Ca \ll 1$, the bubbles remain nearly spherical and act as a barrier to flow and thus have the effect of increasing the viscosity of the suspension. When deformation forces dominate, $Ca \gg 1$, bubbles can be considered inviscid and can become elongated, acting as free slip surfaces for the surrounding melt reducing the apparent viscosity of the suspension (Rust and Manga, 2002).

1.3.3. Crystal-bearing magmas

The crystallisation of silicate melts may result from decompression and/ or cooling (Cashman and Blundy, 2000; Blundy and Cashman, 2001). The nucleation and growth of crystals alters the chemistry and volatile content of the melt, thereby affecting its viscosity (Giordano and Dingwell, 2003). Crystallisation also generates latent heat (e.g. Blundy et al., 2006), which increases the temperature of the suspension and leads to a viscosity reduction (Giordano and Dingwell, 2003).

A suspended crystal phase increases the viscosity of a magma as crystals act as barriers to fluid flow (Einstein, 1911; Roscoe, 1952). In dilute to semi-dilute suspensions, i.e. $\varphi_x \leq 0.25$ (see Mader et al., 2013 and references therein), crystals are thought to accommodate strain through rigid body rotation (Mueller et al., 2010), where the effects on the viscosity from rotation depends on the crystal's orientation with respect to the flow direction. For example, if a crystal's major axis is perpendicular to

the flow direction then the crystal will rotate on its major axis and its contribution to the suspension viscosity will be constant; if the opposite is true the crystal will rotate end-over-end having a variable effect on the viscosity (Mader et al., 2013). However, for most natural magmas, crystal contents are more concentrated, and interaction takes place. In highly concentrated suspensions, strain can further be accommodated by crystal plasticity and fracture (Kendrick et al., 2017).

The physical presence of crystals in a melt phase increases the viscosity of the melt (Lejeune and Richet, 1995; Caricchi et al., 2007). Crystal presence further engenders a non-Newtonian rheology, where the non-Newtonian response observed is predominantly shear thinning (e.g. Caricchi et al., 2007; Lavallée et al., 2007; Cordonnier et al., 2009; Kendrick et al., 2013b; Coats et al., 2018).

1.3.4. The volcanic dilemma: flow or blow?

Magmas can erupt in a variety of styles, including effusive and explosive activity, and occasionally, a simultaneous combination of both. The transition between these two can be considered in simplistic terms as being marked by the glass transition of the melt phase, as explosive activity requires the fragmentation of magma. As with any viscoelastic fluid, a magma can cross its glass transition when a perturbation occurs in temperature-time space (Fig. 1.4). This transition is marked by the critical Deborah number, which for silicate melts is found as 10^{-3} for the onset of non-Newtonian behaviour and 10^{-2} for the onset of brittle behaviour (Webb and Dingwell, 1990b).

Variations in eruption (strain) rate, in chemical composition, and magma temperature can shift the glass transition of the melt during magma ascent. Moreover, the presence of bubbles or crystals modify the distribution of stress in suspensions, shifting the critical Deborah numbers to lower values (Wadsworth et al., 2017b). Therefore, as the stress conditions as well as the physicochemical composition of magma evolves during ascent, the glass transition can be crossed multiple times, which may lead to rupture and healing (Tuffen et al., 2003). If enough potential energy remains following rupture (e.g. from the gas phase), it may be converted into kinetic energy, which would expulse magma fragments, generating an explosive event (Dingwell et al., 1996; Dingwell, 2006).

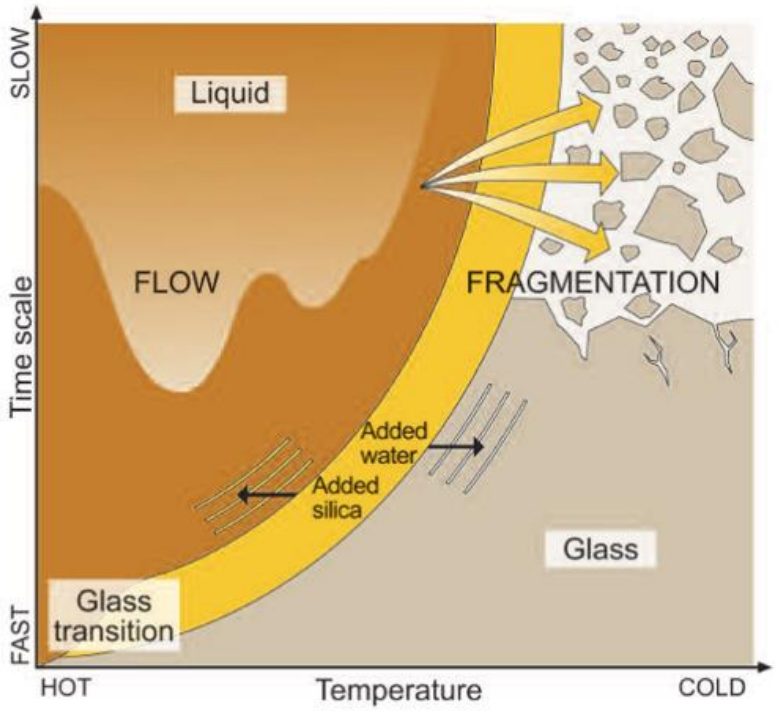

Figure 1.4. The volcanic dilemma: flow or blow? The glass transition separates a relaxed liquid state from an unrelaxed glassy state, shown here in reciprocal time-temperature space. When a relaxed magma crosses its glass transition it fragments, which may result in an explosive. The glass transition of a magma is controlled by its chemical composition (importantly, the concentration of silica and water), its temperature, and the timescale of observation (inversely proportional to the strain rate) (Figure from Dingwell, 2006).

1.3.5. The importance of understanding magma rheology

Magmas are complex multiphase fluids that are subjected to variations in pressure, temperature, chemistry and deformation rate during transportation. As they are erupted, their behaviour can vary vastly in response to these variations and from the evolution of their componentry. By taking approaches to understand the response of magmas to deformation, and attributing these to geophysical signals of unrest, we may increase our ability to forecast, and eventually predict, the development of eruptions in order to mitigate risk associated with their occurrences.

1.4. Laboratory testing in volcanology

By simplifying natural volcanic systems with laboratory-scaled models, volcanologists are able to quantify behaviours that were once only, at best, observable in location (Kavanagh et al., 2018). The aim of laboratory experiments is to identify the controls on processes by systematically varying parameters independently (Kavanagh et al., 2018). Experiments in volcanology involve the dynamic testing of analogue materials (e.g. Fink and Griffiths, 1998) or natural materials under a range of relevant chemical, temperature, pressure, stress and strain conditions (e.g. Hess et al., 2007).

Magmas are complex multiphase mixtures with varying quantities of crystals and pores. Crystals can have a wide range of sizes (including polydispersity), shapes, textures, chemistries and

crystallographic structure (e.g. Mader et al., 2013), which display varying responses to deformation (e.g. plastic vs brittle; (Kendrick et al., 2017). Similarly, pores can have different morphologies, ranging from vesicles to cracks, all which possess various shapes, sizes and tortuosity (e.g. Moitra et al., 2013; Colombier et al., 2017). The constituents can have a dynamic effect on the strength and rheology of a magma (e.g. Manga et al., 1998; Rust and Manga, 2002; Llewellin and Manga, 2005; Heap et al., 2014b, 2014c; Vasseur et al., 2015). To determine the outcome a parameter holds on the response of a system, simplified experiments may be performed. To accomplish this goal, (physically and/or chemically simpler) analogue materials are often used in place of natural materials. It is therefore advantageous to seek an analogue material which at volcanic temperatures and pressures, possesses similar viscoelastic properties to a magma, while having the ability to be doctored to suit experiment requirements. To such purposes, simple materials (without complex elements such as iron), such as borosilicate glass or lime silicate glass, are commonly employed. For instance, these materials have previously been used to study the process of sintering of volcanic ash (Vasseur et al., 2013; Wadsworth et al., 2014, 2016, 2017a; Gardner et al., 2018) and the rheological response of magmatic suspensions (e.g. Lejeune and Richet, 1995; Lejeune et al., 1999; Caricchi et al., 2007; Cordonnier et al., 2012a; Pistone et al., 2012, 2016).

By operating experiments at controlled conditions, we can employ imaging techniques, giving fresh insights into the behaviour of materials. For example, synchrotron based computed X-ray micro-tomography can produce high-resolution, three-dimensional reconstructions of experiments through time (e.g. Madonna et al., 2013; Polacci et al., 2018). This allows experimentalists to look at the internal structures of their samples as the experiment is being performed and integrate their results with other measurements.

An important challenge with laboratory experiments and numerical modelling is optimising scaling to natural processes. When geometric length scales are reduced in order to achieve a given experiment in the laboratory, time and mass must also be scaled (Merle, 2015). To overcome this issue, experimentalists often use dimensional analysis which involves the relation of measurable properties of a material, via their base quantities and units of measurement, to obtain dimensionless numbers (e.g. Stickel and Powell, 2005).

Laboratory experiments are often combined with numerical modelling (e.g. Truby et al., 2015). Numerical modelling employs numbers and equations to describe physical processes given initial and boundary conditions, referred to as the deterministic approach. Alternatively, it also describes the procedure of assessing the probability of a process occurring given only boundary conditions, referred to as the stochastic approach. In numerical modelling, the quality of the output depends significantly on the quality of the input (Kavanagh et al., 2018) - a constraint which may be resolved using laboratory testing under controlled conditions.

In this doctoral dissertation I aim to utilise dynamic laboratory testing on both natural and synthetic magmas to constrain their rheology. Experiments performed on natural samples aim to quantify the impact of porosity on the strength of magma, important to constrain the development of rupture and fragmentation. By selecting specimens collected *in-situ* that have similar chemistries and

crystallinities, but which vary in porosity, I was able to isolate the influence of porosity and demonstrate its link to magma rheology (see Chapter 2). No natural samples exist that have identical chemistry and porosity values but vary methodically in crystal fraction (where crystal size, polydispersity, shape and roughness are also identical); it was therefore necessary to synthesise analogue materials that adhered to these conditions (Chapter 3) to further examine the role of crystallinity on the rheology of magmas (Chapters 4 and 5).

1.5. Structure

Following the Introduction, Chapter 2 will address the flow and failure of natural lava specimens from Mt Unzen lava dome in Japan. Samples of highly crystalline (~ 0.75) and variably porous (0.09-0.35) rocks were tested as 'volcanic rocks' at room temperature, and as 'lavas' at high temperature (~ 900 °C). Results from the study gave a valuable insight into the behaviour of natural dome lavas.

To better parameterise the competing influence of variables on magma rheology, specimens with well constrained chemistry and thermal history, and with a controlled volume of crystals and pores were needed. Chapter 3 details the methods taken to achieve such samples, which were synthesised in-house via newly developed protocols to coveted specifications. Chapter 4 continues with rheological investigations on the synthesised samples; experimental testing using these bespoke specimens facilitated a unique insight into the role crystals play in controlling the viscosity and failure of glassy materials, analogous to magmatic suspensions.

For a comprehensive knowledge of the behaviour of these crystalline analogues, synchrotron-based computed X-ray micro-tomography during dynamic *in-situ* testing was carried out in order to fully constrain the response of the synthetic samples to strain. The employed cutting-edge technology allowed for a 4-dimensional (space and time) rheological study of the crystal-bearing analogue magmas. Both qualitative and quantitative analysis of the samples using visualisation and analysis software provide a novel insight into the behaviour of crystalline magmas during deformation.

The combination of works in Chapter 2 through to Chapter 5 is a significant effort into understanding the response of magmas to forces at shallow depths inside the volcanic conduit. If combined with past, present and future pursuits in the field of volcanology, the present experimental contribution may advance our understanding sufficiently to permit the development of model which may improve our ability to forecast volcanic activity, thereby contributing to mitigation of risk from different volcanic hazards.

1.6. Manuscript status and contribution of co-authors

The status of the manuscripts at the time of doctoral dissertation submission which are associated with Chapters 2 and 5 are outlined below. This includes a description of contributions made from co-authors of the manuscripts.

Chapter 2: Coats, R., Kendrick, J. E., Wallace, P. A., Miwa, T., Hornby, A. J., Ashworth, J. D., Matsushima, T. and Lavallée, Y., 2018: Failure criteria for porous dome rocks and lavas: a study of Mt. Unzen, Japan, Solid Earth, 9, 1299-1328.

Status: Published 8/11/2018

DOI: 10.5194/se-9-1299-2018

Author contributions:

YL and JEK designed the experiments. RC, AJH, TMi, JEK, PAW and JDA carried out the mechanical experiments and physical measurements. PAW collected microprobe data and conducted softening point determination. RC wrote the processing codes, analysed the data and prepared the paper with contributions from all co-authors. RC, JEK, PAW, TMi, AJH, JDA, TMa and YL contributed to the collection and selection of samples and preparation of the paper.

Chapter 5: Coats, R., Lavallée, Y., Kendrick, J. E., Dobson, K., Cai, B., von Aulock, F. W., Wallace, P.A., Le Gall, Atwood, R., Courtois, L., Madi, K., N., Lee, P.: Illuminating dilation by strain localisation in magmas using 4D synchrotron tomography, Geology

Status: Submitted

Author contributions:

JEK, KD, BC, PL and YL designed the experiments. RC and JEK synthesised the samples, RC, JEK, BC, RA, FWvA, PW, NLeG, PL and YL carried out the experiments. BC and RA processed the data. RC analysed the data and prepared the paper with contributions from all co-authors. RC, JEK, KD, BC, RA, FWvA, PW, NLeG, PL and YL contributed to the preparation of the paper.

Over the loch goers,

stoppered at the bottleneck

to the bracken warmth and heather tussock pillow,

-Untitled | Republic of Verse

Chapter 2: Failure criteria for porous dome rocks and lavas: a study of Mt. Unzen, Japan

Abstract

The strength and macroscopic deformation mode (brittle vs ductile) of rocks is generally related to the porosity and pressure conditions, with occasional considerations of strain rate. At high temperature, molten rocks abide to Maxwell's viscoelasticity and their deformation mode is generally defined by strain rate or reciprocally, by comparing the relaxation timescale of the material (for a given condition) to the observation timescale - a dimensionless ratio known as the Deborah (De) number. Volcanic materials are extremely heterogeneous, with variable concentrations of crystals, glass/ melt and vesicles (of different sizes), and a complete description of the conditions leading to flow or rupture as a function of temperature, stress and strain rate (or timescale of observation) eludes us. Here, the conditions which lead to the macroscopic failure of variably vesicular (0.09-0.35), crystal-rich (~ 75 vol. %), pristine and altered, dome rocks (at ambient temperature) and lavas (at 900 °C) from Mt. Unzen Volcano, Japan were examined. It was found that the strength of the dacitic dome rocks decreases with porosity and is commonly dependent on strain rate; when comparing pristine and altered rocks, it was found that the precipitation of secondary mineral phases in the original pore space caused minor strengthening. The strength of the lavas (at 900 °C) also decreases with porosity. Importantly, the results demonstrate that these dome rocks are weaker at ambient temperatures than when heated and deformed at 900 °C (for a given strain rate resulting in brittle behaviour). Thermal stressing (by heating and cooling a rock up to 900 °C at a rate of 4 °C min^{-1}, before testing its strength at ambient temperature) was found not to affect the strength of rocks.

In the magmatic state (900 °C), the rheology of the dome lavas is strongly strain rate dependent. Under low experimental strain rate conditions ($\leq 10^{-4}$ s^{-1}) ductile deformation dominated (i.e., the material sustained substantial, pervasive deformation) and displayed a non-Newtonian, shear thinning behaviour. In this regime, the apparent viscosities of the dome lavas were found to be essentially equivalent, independent of vesicularity, likely due to the lack of pore pressurisation and efficient pore collapse during shear. At high experimental strain rates ($\geq 10^{-4}$ s^{-1}) the lavas displayed an increasingly brittle response (i.e., deformation resulted in failure along localised faults); an increase in strength and a decrease in strain-to-failure as a function of strain rate was observed. To constrain the conditions leading to failure of the lavas, the critical Deborah number at failure (De_c) of these lavas was analysed and compared to that of pure melt (De_{melt}=10^{-3}-10^{-2}; Webb & Dingwell, 1990). It was found that the presence of crystals decreases De_c to between 6.6×10^{-4}-1×10^{-4}. The vesicularity (φ), which dictates the strength of lavas, further controls De_c following a linear trend. The implications of these findings for the case of magma ascent and lava dome structural stability are discussed.

The following is a translation of the abstract in Japanese with the intention of making the work accessible to a range of audiences.

多孔質な岩石及び溶岩の破壊基準：雲仙火山溶岩ドームでの研究

マグマ(溶岩)と岩石のレオロジーと強度は，応力の蓄積と散逸を支配し，噴火様式や山体の構造的安定性に影響を与える．火山噴出物は極端に不均質であり，様々な量・サイズの結晶，ガラス(メルト),気泡を含む．そのため，温度・応力・歪速度の関数として，その流れや亀裂形成を引き起こす状態を完全に記載することは難しい．ここで我々は，雲仙火山において溶岩ドームを形成し様々な発泡度(9-35%)を有する高結晶度(〜75%)な岩石(常温)と溶岩(900度)について，その破壊を引き起こす状態を検討した．その結果，我々は岩石の強度は空隙率とともに減少し，歪速度に依存しないことを発見した： 新鮮な岩石と変質したものでは，後者でわずかに強度が大きい．また，溶岩(900°C)の強度も空隙率とともに減少する．この結果は重要なことに，脆性的振る舞いを起こす歪速度において，常温における岩石の強度は，それを900°Cまで加熱し変形させたときの強度よりも弱いことを示している．このとき，熱応力は岩石の強度に影響を与えない.

高温条件(900°C)では，溶岩のレオロジーは歪速度に強く依存する．低歪速度下($<10^{-4}$ s^{-1})では，溶岩は塑性的に振る舞い(物質が広範な固体変形を持続させる)，非ニュートン流体としてずり粘減の振る舞いを示した．このレジームでは，溶岩の見かけ粘性は，おそらく剪断時の効率的な空隙崩壊のため，発泡度に依存しない．高歪速度下($>10^{-4}$ s^{-1})では，溶岩は益々の脆性的な応答(局所的な断層に沿った破壊による変形)を示す; 歪速度の関数として，強度の増加と破壊へ至るときの歪の減少が観察された．溶岩の破壊を引き起こす状態を制約するため，これら溶岩における破壊時の臨界デボラ数(De_c，緩和時間と実験観察時間の比)を解析し，メルトにおけるそれ(De_{melt}, $=10^{-3}$-10^{-2}; Webb & Dingwell, 1990)と比較した．我々は結晶の存在がDecを6.6×10^{-4}-1×10^{-4}まで減少させることを発見した．またさらに，溶岩の強度に影響する発泡度(φ)もDe_cを線形傾向のようにコントロールする．我々はこれらの発見が与える，マグマ上昇と溶岩ドームの構造的安定性への示唆を議論する.

2.1. Introduction

2.1.1. Lava dome eruptions

Magma ascends to the Earth's surface and erupts through a wide spectrum of eruptive style (e.g. Siebert et al., 2015), which contributes to the construction of different volcanic edifices (e.g. de Silva and Lindsay, 2015). Amongst this activity, lava domes form when viscous magma accumulates and creates mounds of rocks and lava above the vent (Sparks, 1997; Fink and Anderson, 2000). These dome-building events make up approximately 6 % of volcanic eruptions worldwide (Calder et al. 2015) and their characteristics are governed by the rheology of the erupted magmas (Gonnermann and Manga, 2007; Lavallée et al., 2007). The emplacement of lava domes may be endogenous or exogenous, whether growing through inflation from within, or through the piling up of discrete extrusive bodies (Hale and Wadge, 2008). In some extreme cases the latter can manifest as lava spines that extrude in a near-solid state (Angelo Heilprin, 1903; Stasiuk and Jaupart, 1997; Young et al., 1998; Tanguy, 2004; Scott et al., 2008; Vallance et al., 2008; Kendrick et al., 2012; Cashman and Sparks, 2013). Dome eruptions can produce a range of primary hazards, from ash fall to large-scale pyroclastic density currents, generated by gravitational collapse (e.g. Sparks and Young, 2002). They also have the potential to generate secondary hazards such as lahars (e.g. Nevado del Ruiz, Colombia; Pierson et al. 1990); edifice failure induced by magma intrusions (Voight and Elsworth, 1997; Reid et al., 2010), and lava dome collapse, as the mass cools or redistributes (e.g. Elsworth and Voight, 1996). In seismically active areas, strong tectonic earthquakes can both initiate activity and promote structural instability (e.g. Mayu-yama, Japan; Siebert et al. 1987), even in long-dormant systems (e.g. Merapi, Indonesia; Surono et al. 2012). The eruption, emplacement and stability of lava domes reflects the mechanical properties of their constituent materials; thus, it is essential that the evaluation of monitoring data and development of improved hazard forecasting tools at lava dome volcanoes be based on a description of the mechanical and rheological properties of the materials.

2.1.2. Lava dome rheology

The rheology of silicate melts has been explored extensively (e.g. Dingwell and Webb, 1989, 1990; Webb and Dingwell, 1990b; Webb and Knoche, 1996; Fluegel, 2007; Giordano et al., 2008; Cordonnier et al., 2012b). Dingwell and Webb (1989) demonstrated that silicate liquids are viscoelastic bodies, that abide to the glass transition- a temperature-time space that defines their structural relaxation according to the theory of viscoelasticity of Maxwell (1867). Maxwell's work established that the structural relaxation time-scale τ equals the ratio between the melt viscosity μ (in Pa.s) and its elastic modulus at infinite frequency G_∞ (in Pa) according to:

$$\tau = \mu / G_\infty \tag{2.1}$$

Dingwell and Webb (1989) compiled information for different silicate liquids and showed that G_∞ is essentially invariant and approximately $10^{10\pm0.5}$ Pa in the temperature range of interest for magmatic systems. Thus, the relaxation time-scale of silicate melts can simply be related to their viscosity at a given temperature. Extensive experimental efforts in the community have resulted in the creation of a

complete, non-Arrhenian model for silicate melt viscosity, as a function of composition and temperature (e.g. Giordano et al., 2008). The concept of viscoelasticity and relaxation timescale can therefore be applied to a range of volcanic processes.

Viscoelasticity dictates the behaviour of a magma. A rheological description of viscoelastic materials may be cast via the non-dimensional Deborah number, *De* (e.g. Reiner 1964), which is defined by a ratio between Maxwell's relaxation time-scale, τ (Eqn. 2.1) and the time-scale of observation, t_{obs}:

$$De = \frac{\tau}{t_{obs}} \quad (2.2)$$

This relationship states that under observation timescales longer than the relaxation timescale (for a given melt viscosity), a melt may flow like a liquid; but at short observation timescales, a melt may behave as a solid (like a glass). In such a kinetic framework, increasing the temperature reduces the viscosity and therefore the time required for structural relaxation. As the relaxation time-scale is inversely proportional to the structural relaxation rate, it can thus be said that the structural relaxation rate defines the transition between the liquid and solid states (commonly referred to as the glass transition, T_g). Dingwell and Webb (1990) demonstrated that at $De < 10^{-3}$, a silicate melt can be described as a Newtonian fluid. However, when silicate melts are deformed at higher rates where the observation time-scale is short, $10^{-3} < De < 10^{-2}$, the melt structure accumulates damage upon deformation which results in an apparent non-Newtonian behaviour. At $De > 10^{-2}$, silicate melts undergo the glass transition and ruptures (Dingwell and Webb, 1990; Wadsworth et al., 2017b); this is known as the critical Deborah number, De_c - a criteria met in several eruptive scenarios, including fragmentation and explosive eruptions (e.g. Dingwell, 1996).

During transport and eruption, magmas crystallise and volatiles are exsolved (e.g. Cashman, 1992; Martel and Schmidt, 2003), resulting in magmatic suspensions, undergoing significant rheological changes (e.g. Lejeune and Richet, 1995; Barmin et al., 2002). In particular, dome-building eruptions have been observed to produce variably vesicular (generally $\lesssim 0.40$) and crystalline (e.g. 0-100 vol.%) lavas (Castro et al., 2005; Mueller et al., 2005, 2011a; Lavallée et al., 2007; Pallister et al., 2008; Cordonnier et al., 2009; Calder et al., 2015; Heap et al., 2016a). The addition of crystals to a melt increases the effective viscosity (Lejeune and Richet, 1995). At moderate crystal fraction (below ~ 25 vol.%) this can be approximated by the Einstein-Roscoe equation (Einstein, 1911; Roscoe, 1952), and variations thereof (see Mader et al., 2013 and references therein). When particle concentrations reach a critical fraction that promotes interaction (typically ≤ 0.25, depending on crystal morphology (Mader et al., 2013)), the suspension becomes non-Newtonian (Deubelbeiss et al., 2011). Experiments on dome lavas at high temperature have shown that the apparent viscosity of these suspensions decreases with strain rate (Lavallée et al., 2007; Avard and Whittington, 2012) - a shear thinning effect influenced by crystal alignment and interaction (Vona et al., 2011); crystal plasticity (Kendrick et al. 2017), and fracture processes (Lavallée et al., 2008; Kendrick et al., 2013b). The addition of a separate gas phase to a magma adds further rheological complexity (Lejeune et al., 1999), serving to increase or decrease viscosity depending upon the volume fraction of bubbles, pore pressure, the initial viscosity of the melt, the amount of deformation they are subjected to (e.g. Manga

et al., 1998; Llewellin and Manga, 2005), and pore connectivity, which may promote outgassing and pore compaction (e.g. Ashwell and Kendrick et al., 2015). Bubbles will affect the viscosity of the suspension depending on their capillary number, *Ca*, a dimensionless ratio of the deforming viscous stress over the restoring stress from surface tension. A more spherical bubble will generally have a low *Ca*, as restoring stresses dominate, and will behave as a barrier which fluid flow will have to deviate around resulting in an increased viscosity of the suspension. On the other hand, an elongate bubble generally has a high *Ca*, as deforming stresses dominate, and may act as free slip surface causing a decrease in the suspension viscosity (e.g. Manga et al., 1998; Mader et al., 2013). Three-phase models, although less explored than two-phase flows, have been modelled by Truby et al. (2015) by combining two sets of two-phase equations. Despite the aforementioned rheological studies focused on the viscosity of magmatic suspensions, the conditions leading to failure of such magmatic suspensions have received less attention. Following the work of Lavallée et al. (2007), Gottsmann et al. (2009) showed that the presence of crystals may reduce the strain rate required to rupture magma (if one was to consider the melt relaxation rate) to conditions where $De < 10^{-2}$ and Lavallée et al. (2008) and Gottsmann et al. (2009) showed that brittle processes may be active at conditions two orders of magnitude lower than such a purely brittle limit. Cordonnier et al. (2012a) explored the effect of crystallinity on magma rupture, showing that De indeed decreases with crystallinity. However, here we note that when determining the Deborah number for their experimental findings, the relaxation time-scale was calculated using the apparent viscosity of the suspension rather than the viscosity of the interstitial melt, which is the basis for the applicability of viscoelasticity in this scenario (this will be discussed further in section 2.5.2). Important questions remain as to the contribution of vesicles on the rupture of magmas, as the strength of geomaterials in the brittle field is generally described in terms of porosity (e.g. Paterson and Wong, 2005, and references in section 2.1.3).

2.1.3. Lava dome mechanics

Various numerical models have been developed to evaluate the structural stability of lava domes and, with sufficient knowledge of a volcanic edifice and the properties of the materials it holds, collapse events can be modelled effectively (e.g. Elsworth and Voight, 1996). Although elegant and complex, these simulations tend to make non-trivial assumptions regarding vent geometry, dome morphology, and material properties (e.g. Ball et al., 2015). Volcanic domes are composed of materials with a vast spectrum of heterogeneities and degree of coherence (Mueller et al., 2011b; Lavallée et al., 2012, 2018) and although assigning fixed values for the material properties of dome rocks may be computationally beneficial, accounting for the wide range of physical and mechanical properties of dome materials remain a great source of uncertainty. Mechanical testing can be carried out to resolve the behaviour of rocks (see Paterson and Wong, 2005 and references therein) and this has resulted in a recent surge in laboratory testing to advance the understanding of the tensile strength, compressive strength, frictional coefficient and flow behaviour of these heterogeneous dome rocks and magmas as a function of temperature and stresses or strain rates (Smith et al., 2007, 2011; Lavallée et al., 2007;

Hess et al., 2008; Kendrick et al., 2012, 2013b, 2013a; Kolzenburg et al., 2012; Heap et al., 2014b; Hornby et al., 2015; Lamb et al., 2017; Lamur et al., 2017)

The uniaxial compressive strength of volcanic rocks has been found to inversely correlate with porosity (Al-Harthi et al., 1999; Kendrick et al., 2013b; Heap et al., 2014b, 2014c, 2016b; Schaefer et al., 2015), and to positively correlate with strain rate (Schaefer et al., 2015). In volcanic rocks, porosity is made up of vesicles and micro-fractures, which contribute to the mechanical behaviour and strength of the rock (Sammis and Ashby, 1986; Ashby and Sammis, 1990; Heap et al., 2014b; Bubeck et al., 2017; Colombier et al., 2017; Griffiths et al., 2017). Two models have gained traction to explain the strength of rocks. The pore-emanating crack model of Sammis and Ashby (1986), describes the case of a pore-only system where cracks nucleate from the pores and propagate in the direction parallel to the principal stress, when the applied stress overcomes the fracture toughness of a rock. As the applied stress increases, the micro-fractures propagate and coalesce, leading to macroscopic failure. An analytical estimation of this model was derived by Zhu et al., (2010) to estimate the uniaxial compressive stress (σ) of a sample, with a pore radius (r), as a function of its porosity (φ) and the fracture toughness (K_{IC}):

$$\sigma = \frac{1.325}{\varphi^{0.414}} \frac{K_{IC}}{\sqrt{\pi r}} \tag{2.3}$$

In contrast, the sliding wing-crack model of Ashby and Sammis (1990) considers only pre-existing micro-fractures inclined from the principal stress direction. The model describes that first, the frictional resistance of the crack must be overcome before wing-cracks can form, then the fracture toughness must be overcome for them to propagate and interact. The analytical approximation for this model was developed by Baud et al., (2014):

$$\sigma = \frac{1.346}{\sqrt{1+\mu_f{}^2-\mu_f}} \frac{K_{IC}}{\sqrt{\pi c}} D_0^{-0.256} \tag{2.4}$$

where μ_f is the friction coefficient of the crack, c is the half-length of a pre-existing crack, and D_0 is an initial damage parameter (which takes into consideration the number of cracks per unit area and their angle with respect to the principal stress).

Heap et al., (2014b) experimentally demonstrated that neither model fully satisfied the mechanical data obtained for volcanic rocks and suggested that a microstructural model that combines the two mechanisms must be developed to permit the design of simulations considering the mechanical behaviour of microstructurally complex volcanic materials.

The problem of lava dome stability does not simply require knowledge of hot lavas or cold rocks; it further requires understanding of the effects of temperature (e.g. Harris et al., 2002); chemical alteration (e.g. Lopez & Williams 1993; Ball et al. 2015); pore pressure (Farquharson et al., 2016), thermal stressing (Heap et al., 2009, 2010, 2014b; Kendrick et al., 2013a; Schaefer et al., 2015) and mechanical stressing at different rates such as during seismic shaking (Cole et al., 1998; e.g. Voight, 2000; Calder et al., 2002) or magmatic intrusions (Walter et al., 2005) on the mechanical properties of the materials, many aspects of which have been tested in the context of edifices. The cooling of

crystalline lava bodies results in the generation of fractures (Fink and Anderson, 2000; Takarada et al., 2013; Eggertsson et al., 2018) - leaving a highly fractured, blocky mass, the mechanical impact of which is difficult to quantify (Voight, 2000; Voight and Elsworth, 2000). Furthermore, thermal stressing cycles that could result from proximity of hot magma in a conduit, lava dome or edifice following a new eruptive episode, have been found to only weakly modify the strength of commonly micro-fractured volcanic rocks (Heap et al. 2009; Kendrick et al. 2013; Schaefer et al. 2015,), unless they contain thermally liable minerals (Heap et al., 2012, 2013a, 2013b). Recent experiments on porous basalt by Eggertsson et al. (2018) have shown that rocks that are essentially void of micro-cracks (likely due to slow cooling), are however susceptible to fracture damage by thermal stressing (i.e., forming cooling joints); in contrast, micro-fractured rocks, may not necessarily accumulate more damage during cooling, yet upon contraction, pre-existing fracture may widen to give way to the ingression of hydrothermal fluids (e.g. Lamur et al., 2018), further contributing to the stress balance and mechanical response.

2.1.4. Mt. Unzen lava dome

The Unzendake volcanic complex is situated on the Shimabara peninsula in South-Western Japan (Fig. 2.1a). The volcanic complex began to grow 0.5 Ma and now covers 20 km (E-W) by 25 km (N-S) (Takarada et al., 2013). Unzendake exhibits an intricate eruptive history of lava domes, flows and pyroclastic deposits (Nakada and Fujii, 1993) of predominantly dacitic composition (Nakada and Motomura, 1999).

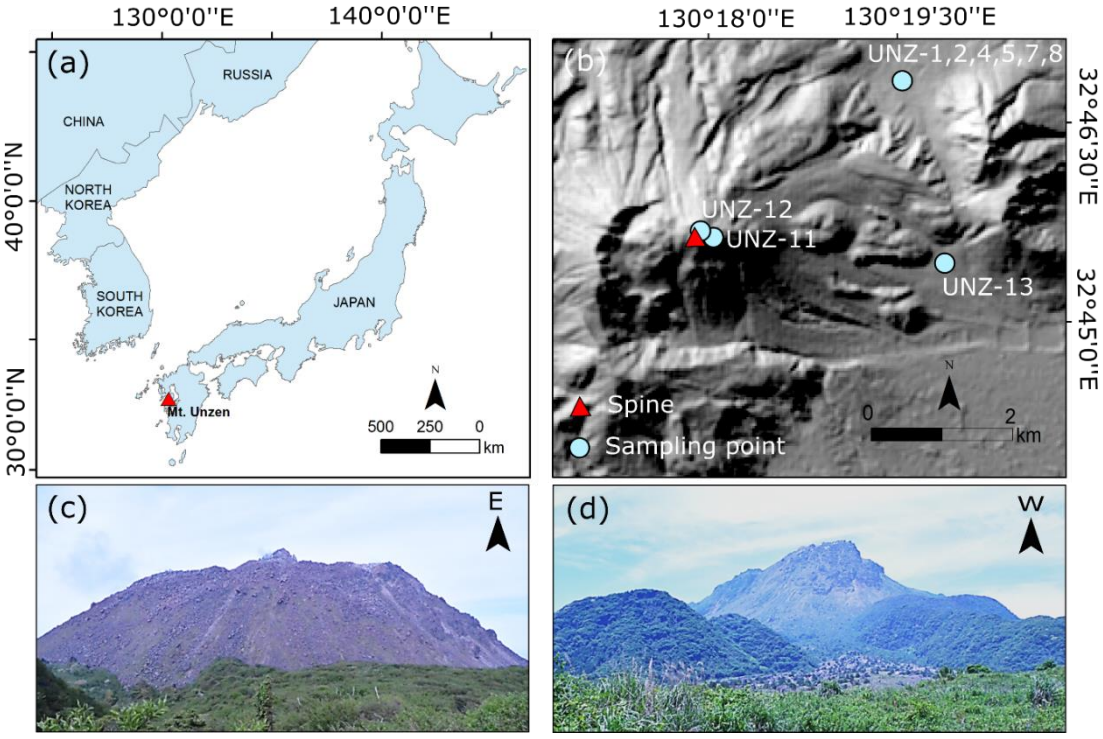

Figure 2.1. (a) Location of Mt. Unzen in South Western Japan; (b) Sample collection locations and location of the erupted spine, the summit of Mt. Unzen at 1500 m above sea level (NASA/METI/AIST/Japan Spacesystems, 2001); view of Mt. Unzen lava dome looking East ~ 0.62 km from the spine (c) and West ~ 3.87 km from the spine (d) in 2016.

On 17 November 1990, after 198 years of quiescence, a phreatic eruption occurred at Mt. Unzen, which was accompanied by multiple earthquake swarms (Matsushima and Takagi, 2000). This was followed shortly afterwards by a phreatomagmatic eruption along with intense edifice swelling, and on 20 May 1991, the extrusion of a lava spine initiated the growth of the Heisei-Shinzan dome complex (Nakada and Fujii, 1993; Takarada et al., 2013). This introduced a 45-month long period of lava dome activity with growth being primarily exogenous in periods of high extrusion rate, and endogenous in times of low effusion rate (Nakada et al., 1995b, 1999a). The final stage of growth was marked by the extrusion of a spine between October 1994 and February 1995 (which can be seen this present day; Fig. 2.1b-c), characterised by pulsatory ascent and seismicity (Umakoshi et al., 2008; Lamb et al., 2015), along fault zones defined by compactional shear (Wallace et al., 2019) and mineral reactions, crystal plasticity and comminution (Wallace et al., 2019). The end of the eruption was followed by cooling of the lava dome and thermal contraction that caused multiple joints (Takarada et al., 2013). Fumarole activity has continued to the present day, with temperatures decreasing from 300 °C in mid-2007 to 90 °C in 2011 (Takarada et al., 2013).

In total, 13 lava lobes were formed, and, at its maximum size, the lava dome was 1.2 km (E-W) by 0.8 km (N-S) wide. In particular lobe 11, which dominated the Eastern side of the complex (Nakada et al., 1995a, 1999b) has long been unstable, which has led to partial collapses that generated several pyroclastic density currents (PDCs; Nakada et al., 1999a; Sakuma et al., 2008). The flows were estimated to have travelled at 200 km hr^{-1}, up to 5.5 km down the Oshigadani Valley (Yamamoto et al., 1993; Takarada et al., 2013). All in all, pyroclastic flows buried and/or burned approximately 800 buildings, with debris flows destroying a further ~ 1,700, and in the summer of 1991 the number of evacuated persons exceeded 11,000 (Nakada et al., 1999a). The Committee of Survey and Countermeasure on Lava Dome Collapse at Mt. Unzen advises that the risk of collapse of lobe 11 is high, an exclusion zone remains active to the E of the summit and access to the lava dome is strictly limited. Data from electro-optical distance measuring instruments suggest that lobe 11 has advanced 1 m in 14 years (measurements from 1997-2011), and recent observations from ground-based synthetic aperture radar show the development of a shear fracture (Kohashi et al., 2012). Therefore, the complete or partial collapse of the lobe and the generation of block-and-ash flows are likely hazards, particularly after large regional earthquakes. The current uncertainty regarding the structural stability of the dome at Mt. Unzen, particularly after seismic activity, has led to recent field campaigns and mechanical studies of the dome material (e.g. Cordonnier et al., 2009; Hornby et al., 2015). The destabilisation of lava domes due to tectonic activity is essentially a superficial process, meaning the stress balance may be considered as a uniaxial problem, and tested as such (e.g. Quane and Russell, 2005).

2.2. Materials and methods

2.2.1. Sample selection

Mt. Unzen lava dome is made up of porphyritic dacite (~ 63 wt.% SiO_2) lava blocks which typically have large (> 3 mm) and abundant (> 25 vol.%) plagioclase phenocrysts, along with lesser amounts of

amphibole (~ 5 vol.%), biotite (~ 2 vol.%) and quartz (~ 2 vol.%) phenocrysts and microphenocrysts set in a partially crystalline (~ 50 vol.%) groundmass of plagioclase, pyroxene, quartz pargasite, and Fe-Ti oxides in a rhyolitic interstitial glass (Nakada & Motomura 1999; Wallace et al. 2019). However, as the dome was formed through both, exogenous and endogenous growth, the petrological history of the eruptive products varies widely and as such the microstructure of the blocks forming the dome varies considerably. Furthermore, lasting heat sources and ongoing fumarolic activity have led to local thermal and hydrothermal alteration of the dome (Almberg et al., 2008). This heterogeneity calls for a variable sample suite to represent the dome material, and to constrain the processes of deformation and cooling that occurred throughout lava dome formation, that influences its current structural stability.

In this study, 9 samples were selected with different properties. Samples UNZ-1, 2, 4, 5, 7, and 8 were collected from easily accessible, June 1993 block-and-ash flow deposits in the Minami-Senbongi area, north-east of the spine; UNZ-13 was collected from the May-August 1991 deposits in the restricted area of the Mizunashi River, east of the spine (see Fig. 2.1b). These rocks were collected as they represent the freshest (unaltered) materials that originate from dome collapse events during eruption, prior to any chemical alteration (e.g. Cordonnier et al., 2008). Sample UNZ-11 was collected on lobe 11 of the dome, selected as it showed signs of hydrothermal alteration (crusted, white and friable). UNZ-12 was collected on the dome, just east of the lava spine, and was chosen specifically for its reddish colour which suggested thermal alteration and oxidation. Each sample block was then cored to make multiple 20 mm diameter cylindrical cores, cut, and then ground parallel to 40 mm in length (Fig. 2.S1) to maintain a 2:1 aspect ratio.

2.2.2. Sample characterisation and preparation

2.2.2.1. Geochemistry

The bulk geochemical compositions of selected samples were determined in a PANalytical Axios Advanced X-Ray Fluorescence Spectrometer (XRF) at the University of Leicester (using fused glass beads prepared from ignited powders). Sample to flux ratio was kept at 1:5, 80 % Li metaborate: 20 % Li tetraborate flux. Results are quoted as component oxide weight percent and re-calculated to include LOI (loss-on-ignition).

The geochemical composition of the interstitial glass in sample block UNZ-4 was determined using a Cameca SX-5 Field Emission Electron Probe Microanalyser (EPMA) at the University of Oxford. A variety of standards were used to calibrate the spectrometers, including Wollastonite for Ca, and Albite for Al, Na and Si. Secondary reference standards, of which the exact chemistry was known, were utilised for better precision and accuracy. These were Labradorite and kn18 glass (comendite obsidian, Kenya), used as the chemistries were similar to those of the Mt. Unzen glass sample. Analyses used an accelerating voltage of 15 KeV, a beam current of 6 nA and a defocussed spot size of 10 μm. The data were checked for major element oxides' totals.

2.2.2.2. Porosity

The porosity and character of the pores (i.e., whether connected or isolated) was assessed using an AccuPyc 1340 helium pycnometer from Micromeritics. Firstly, height (h; in m), radius (r; in m) and mass (m; in kg) were recorded for each cylindrical core sample, providing a constraint on sample density (ρ_s; in kg.m^{-3}):

$$\rho_s = {}^{m}/_{\pi r^2 h}. \quad (2.5)$$

Secondly, the solid density of the rocks (ρ_0) was constrained by measuring the mass and volume of a powdered lump from each rock in a pycnometer; from these measurements, the total porosity of each rock could be estimated via:

$$\varphi_T = 1 - ({}^{\rho_s}/_{\rho_0}). \quad (2.6)$$

To constrain the fraction of isolated pores in the rocks, the skeletal volume ($V_{skeletal}$; in m^3) of each core was measured in the pycnometer. The porosity connected to the outside of the sample (henceforth termed connected porosity), φ_O, could then be calculated via:

$$\varphi_O = 1 - \left({}^{V_{skeletal}}/_{\pi r^2 h}\right), \quad (2.7)$$

and isolated porosity, φ_i, via:

$$\varphi_i = \varphi_T - \varphi_O. \quad (2.8)$$

The porosity determination was used to omit outliers from any sample block to ensure that the rocks of a given porosity were tested and compared to one another.

2.2.2.3 Microstructures

Thin sections of UNZ- 4,11,12 and 13 were prepared with a fluorescent dyed epoxy; selected as they cover a vast range of sample diversity; including both the lower and upper bounds of porosity, and collection site. Images were acquired using a DM2500P Leica microscope in plane-polarised light. To further constrain the microstructures of each sample block, backscattered electron (BSE) images were taken of each sample using a Philips XL30 tungsten filament scanning electron microscope (SEM), equipped with an energy-dispersive X-ray spectrometer (EDS), and a Hitachi TM3000 SEM at the University of Liverpool. Stubs of the samples were set in epoxy, polished and carbon coated, before being imaged in the Philips XL30 at a working distance of 13±0.1 mm using a 20 kV beam voltage, a 60-90 μA beam current and a spot size of 5. Thin sections of the samples were imaged with the Hitachi TM3000 using a 15 kV beam and 10 mm working distance.

2.2.2.4 Thermal Analysis

To constrain the conditions at which to carry out the high temperature uniaxial tests, we evaluated the softening point of the Mt. Unzen dome rock using a Netzsch 402 F1 Hyperion thermomechanical analysis (TMA) at the University of Liverpool. Under a 20 mL min^{-1} argon flow, a 6.37 mm tall, 5.87 mm wide, cylindrical sample of UNZ-8 was placed under a constant load of 3 N and heated at 10 ˚C min^{-1} to 1100 ˚C. The softening point of the material was found as the temperature at which the

applied load counteracts sample expansion by inducing viscous flow (and sample shortening) during heating. This was detected at 824.6 °C, 80.6 minutes into the measurement (Fig. 2.S5). An experimental temperature of 900 °C was selected as, being well above the softening point, this is high enough to allow for flow to occur on the timescales under investigation. This chosen temperature is close to the magmatic temperature (850-870 °C) constrained to have followed mixing (Venezky and Rutherford, 1999) and above the glass transition of Unzen spine material (790 °C) measured by differential scanning calorimetry at a rate of 10 °C min^{-1} (Wallace et al. 2019), though the temperature profile within the conduit and dome during emplacement is poorly constrained.

2.2.2.5 Thermal stressing

Selected cores of pristine material were thermally stressed in a Carbolite box furnace to examine the effects of experimentally induced heating-cooling cycles on the residual strength of rock cores. Cores were subjected to heating at 4 °C min^{-1} followed by 1-hr dwell at 900±3 °C (sample temperature) and cooling at 4 °C min^{-1}. The density and porosity of each sample were measured before and after thermal stressing, and the products were further subjected to uniaxial compressive strength tests.

2.2.3. Uniaxial compression experiments

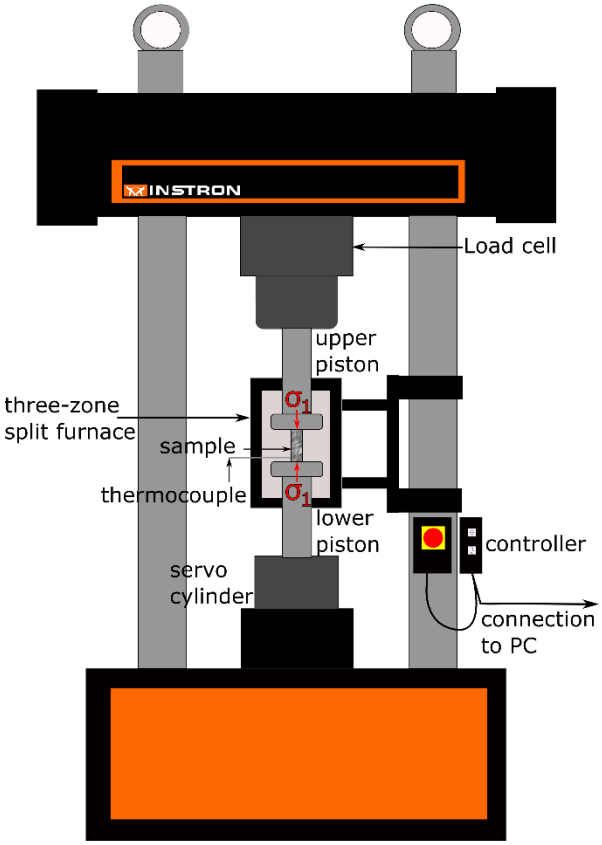

Figure 2.2. Schematic of the uniaxial compressive strength testing set-up in the Experimental Volcanology and Geothermal Research Laboratory at the University of Liverpool. A 100 kN Instron 8862 uniaxial press with a three-zone, split cylinder furnace was used to perform experiments at varying strain rates and temperatures.

Uniaxial compressive strength tests were carried out using a 50 kN 5969 Instron benchtop press and a 100 kN Instron 8862 uniaxial press with a three-zone, split cylinder furnace using the parallel plate method in the Experimental Volcanology and Geothermal Research Laboratory at the University of Liverpool (Fig. 2.2). Experiments were carried out both at ambient temperature (~20 °C) and at high temperature (900 °C, using a heating rate of 4 °C min^{-1}). Tests were conducted at constant strain rates of 10^{-1}, 10^{-3} or 10^{-5} s^{-1} (see Table 2.1 for the range of experimental conditions). The apparatus monitored the applied load and piston extension at 10-1000 Hz (depending on set experiment rate) and the Bluehill® 3 software was used to compute data and calculate strain (ε) and compressive stress from the input sample dimensions. [Note: all mechanical data have been corrected for the compliance of the setup at the relevant experimental temperature, quantified via Instron procedures that monitor length changes due to loading of the pistons in contact with one another]. The end of each experiment was defined by either (1) in the case of viscous flow, when there was a constant stress recorded for a significant amount of time (>1 hour), or (2) in the case of brittle behaviour, a stress drop exceeding 20 % of the monitored peak stress achieved, highlighting that failure had occurred. Repeat experiments were performed on samples with a similar porosity (i.e., within 0.01 of the other sample tested) at various conditions to verify findings.

2.2.3.1. High temperature experiments

Prepared cores were placed upright in between the pistons of the press; the furnace was closed around the sample which was heated at 4 °C min^{-1} to 900±3 °C (sample temperature); a K-type thermocouple was left in contact with the sample at all times and the temperatures of the top, middle and bottom zones of the furnace were monitored throughout the experiment. Following thermal equilibration for 1 hour at target temperature, the piston was then brought into contact with the sample at low load (< 30 N), and the temperature of the sample was read from the thermocouple. A stepped strain-rate experiment (at 10^{-6} then 10^{-5}, 10^{-4} and 10^{-3} s^{-1}) was first carried out to constrain the viscous-brittle transition of the material and inform subsequent testing at unique strain rates. Tests at unique strain rates were then carried out at 10^{-3}, 10^{-4}, 10^{-5} s^{-1}, after which, the samples were cooled to ambient temperature at 4 °C min^{-1} [note: From here, samples deformed at high temperature will be defined as lavas, and those tested at room temperature as rocks].

2.2.3.2. Ambient temperature experiments

Ambient temperature experiments were carried out on all collected sample blocks. Prepared cores were placed upright between the pistons where they underwent compressive tests at various strain rates until failure. The thermally stressed samples were tested at a strain rate of 10^{-3} s^{-1}, whereas the remaining pristine specimens were axially loaded at strain rates of 10^{-1}, 10^{-3}, or 10^{-5} s^{-1} until failure (see Table 2.1).

2.2.3.3. Treatment of data

The strain at failure for these samples was selected using a semi-automated MATLAB script which identified the strain value at peak stress. The static Young's Modulus was computed for each experiment that exhibited a brittle response (e.g. after Heap et al. 2014a) by calculating the slope of

the linear portion of the stress-strain curve via an automated script written in MATLAB and available at https://doi.org/10.5281/zenodo.1287237. To ensure that only the linear portion was selected, points within 10 % of the maximum slope were considered to define the Young's modulus for that sample (Fig. 2.S6), minimising the potential contribution of mechanical data obtained during crack closure (during initial loading) and during strain hardening (beyond the onset of dilation).

For samples that demonstrated a viscous response, the apparent viscosity (η_a; in Pa.s) was calculated using the equation of Gent (1960) developed for the parallel-plate viscometric method, given the absence of slip along the sample/piston interfaces:

$$\eta_a = \frac{2\pi F h^4}{3V\dot{\varepsilon}(V+2\pi h^3)} \tag{2.9}$$

where F (N) is the applied force on the sample; h (m) is the height of the sample; V (m^3) is the initial volume of the sample, assumed constant, and $\dot{\varepsilon}$ (s^{-1}) is the applied strain rate.

Table 2.1. Sample properties, measurement data, experimental conditions, mechanical response and resulting properties of each sample. Y: yes; N: no; n/a: not applicable.

Sample	Total porosity	Connected porosity	Strain rate (s^{-1})	Temperature (°C)	Peak force (N)	Peak Stress (MPa)	Strain to failure	Thermally treated	Altered	Viscosity (Pa.s)	De number	Young's modulus (GPa)
UNZ-1-2	0.21	0.19	1.E-05	20	6789	21.38	0.0049	N	N	N/A	N/A	7.45
UNZ-4-13	0.09	0.07	1.E-05	20	7180	22.71	0.0043	N	N	N/A	N/A	7.40
UNZ-5-1	0.20	0.18	1.E-05	20	11779	37.09	0.0070	N	N	N/A	N/A	10.58
UNZ-5-5	0.20	0.19	1.E-05	20	9022	28.49	0.0061	N	N	N/A	N/A	7.84
UNZ-7-1	0.29	0.28	1.E-05	20	4750	15.10	0.0071	N	N	N/A	N/A	3.85
UNZ-7-10	0.31	0.30	1.E-05	20	4600	14.63	0.0066	N	N	N/A	N/A	3.63
UNZ-7-12	0.32	0.31	1.E-05	20	2895	9.20	0.0046	N	N	N/A	N/A	2.86
UNZ-7-6	0.28	0.28	1.E-05	20	4889	15.41	0.0060	N	N	N/A	N/A	4.27
UNZ-8-1	0.17	0.17	1.E-05	20	6000	19.15	0.0048	N	N	N/A	N/A	6.93
UNZ-8-10	0.15	0.15	1.E-05	20	12570	39.62	0.0052	N	N	N/A	N/A	12.84
UNZ-8-12	0.17	0.14	1.E-05	20	10600	33.44	0.0043	N	N	N/A	N/A	10.67
UNZ-8-6	0.17	0.17	1.E-05	20	8540	26.90	0.0049	N	N	N/A	N/A	9.65
UNZ-4-25	0.16	0.14	1.E-05	20	3497	11.07	0.0048	N	N	N/A	N/A	3.48
UNZ-4-26	0.16	0.11	1.E-05	20	10981	34.64	0.0080	N	N	N/A	N/A	6.79

UNZ-1-0	0.21	0.19	1.E-05	20	6320	19.92	0.0043	N	N	N/A	N/A	7.16
UNZ-2-4	0.12	0.10	1.E-05	20	13361	41.98	0.0061	N	N	N/A	N/A	12.19
UNZ-2-5	0.12	0.10	1.E-05	20	11957	37.68	0.0079	N	N	N/A	N/A	11.50
UNZ-12-4	0.10	0.09	1.E-05	20	15549	48.95	0.0074	N	Y	N/A	N/A	11.18
UNZ-11-2	0.30	0.28	1.E-05	20	6592	20.71	0.0056	N	Y	N/A	N/A	6.21
UNZ-11-3	0.28	0.27	1.E-05	20	4950	15.60	0.0053	N	Y	N/A	N/A	4.88
UNZ-8-21	0.15	0.12	1.E-05	20	11073	34.90	0.0033	N	N	N/A	N/A	14.77
UNZ-1-4	0.21	0.18	1.E-03	20	7681	24.42	0.0050	N	N	N/A	N/A	7.06
UNZ-1-6	0.21	0.18	1.E-03	20	7639	24.08	0.0050	N	N	N/A	N/A	7.19
UNZ-5-2	0.20	0.18	1.E-03	20	14081	44.47	0.0079	N	N	N/A	N/A	10.04
UNZ-5-3	0.20	0.19	1.E-03	20	14065	44.33	0.0065	N	N	N/A	N/A	10.11
UNZ-7-11	0.33	0.33	1.E-03	20	3150	9.98	0.0052	N	N	N/A	N/A	3.05
UNZ-7-2	0.30	0.29	1.E-03	20	5250	16.70	0.0089	N	N	N/A	N/A	4.05
UNZ-7-7	0.30	0.29	1.E-03	20	4750	15.01	0.0074	N	N	N/A	N/A	3.97
UNZ-8-11	0.19	0.17	1.E-03	20	11300	35.53	0.0059	N	N	N/A	N/A	11.32
UNZ-8-3	0.18	0.15	1.E-03	20	9640	30.39	0.0064	N	N	N/A	N/A	10.63
UNZ-8-7	0.17	0.14	1.E-03	20	11350	35.73	0.0043	N	N	N/A	N/A	14.08

UNZ-4-24	0.11	0.09	1.E-03	20	12841	40.47	0.0088	N	N	N/A	N/A	7.30
UNZ-2-1	0.13	0.11	1.E-03	20	15241	47.94	0.0053	N	N	N/A	N/A	15.22
UNZ-2-6	0.13	0.11	1.E-03	20	11115	35.13	0.0070	N	N	N/A	N/A	13.04
UNZ-13-1	0.29	0.27	1.E-03	20	10341	32.52	0.0038	N	N	N/A	N/A	12.70
UNZ-13-2	0.30	0.29	1.E-03	20	6544	20.58	0.0036	N	N	N/A	N/A	9.25
UNZ-12-1	0.09	0.09	1.E-03	20	22126	69.32	0.0089	N	Y	N/A	N/A	14.71
UNZ-12-3	0.09	0.10	1.E-03	20	24227	75.97	0.0092	N	Y	N/A	N/A	16.33
UNZ-11-4	0.30	0.30	1.E-03	20	7066	22.25	0.0059	N	Y	N/A	N/A	5.90
UNZ-11-6	0.30	0.30	1.E-03	20	5507	17.32	0.0065	N	Y	N/A	N/A	4.65
UNZ-1-14	0.20	0.18	1.E-03	20	7681	19.25	0.0028	N	N	N/A	N/A	9.34
UNZ-1-11	0.19	0.16	1.E-03	20	10257	32.36	0.0062	Y	N	N/A	N/A	8.69
UNZ-1-12	0.21	0.18	1.E-03	20	6334	19.92	0.0055	Y	N	N/A	N/A	5.26
UNZ-4-18	0.10	0.09	1.E-03	20	20556	65.17	0.0093	Y	N	N/A	N/A	13.11
UNZ-4-19	0.12	0.10	1.E-03	20	19939	63.22	0.0083	Y	N	N/A	N/A	12.40
UNZ-5-11	0.21	0.21	1.E-03	20	11240	35.42	0.0089	Y	N	N/A	N/A	7.39
UNZ-5-12	0.21	0.21	1.E-03	20	8515	26.89	0.0086	Y	N	N/A	N/A	5.64
UNZ-7-17	0.29	0.29	1.E-03	20	5412	17.16	0.0080	Y	N	N/A	N/A	3.87

UNZ-7-18	0.32	0.32	1.E-03	20	3515	11.10	0.0101	Y	N	N/A	N/A	2.14
UNZ-8-18	0.18	0.16	1.E-03	20	13266	41.81	0.0078	Y	N	N/A	N/A	10.10
UNZ-8-19	0.17	0.15	1.E-03	20	14175	44.63	0.0066	Y	N	N/A	N/A	11.19
UNZ-1-1	0.20	0.17	1.E-01	20	9970	31.33	0.0044	N	N	N/A	N/A	9.83
UNZ-1-3	0.20	0.18	1.E-01	20	8936	28.11	0.0058	N	N	N/A	N/A	8.66
UNZ-4-20	0.10	0.09	1.E-01	20	16342	51.55	0.0095	N	N	N/A	N/A	8.51
UNZ-4-22	0.14	0.09	1.E-01	20	13050	41.33	0.0096	N	N	N/A	N/A	8.20
UNZ-4-4	0.11	0.09	1.E-01	20	13580	42.84	0.0077	N	N	N/A	N/A	9.18
UNZ-4-5	0.10	0.08	1.E-01	20	15160	47.67	0.0069	N	N	N/A	N/A	11.05
UNZ-4-8	0.11	0.09	1.E-01	20	14200	44.69	0.0066	N	N	N/A	N/A	11.20
UNZ-4-9	0.10	0.09	1.E-01	20	12580	39.67	0.0070	N	N	N/A	N/A	9.24
UNZ-7-19	0.31	0.36	1.E-01	20	4492	14.16	0.0092	N	N	N/A	N/A	2.32
UNZ-7-20	0.33	0.32	1.E-01	20	4442	14.03	0.0107	N	N	N/A	N/A	1.82
UNZ-7-4	0.30	0.29	1.E-01	20	3546	11.18	0.0073	N	N	N/A	N/A	2.49
UNZ-7-5	0.32	0.31	1.E-01	20	3300	10.43	0.0077	N	N	N/A	N/A	2.27
UNZ-7-8	0.31	0.31	1.E-01	20	3858	12.15	0.0077	N	N	N/A	N/A	2.38
UNZ-7-9	0.27	0.26	1.E-01	20	5802	18.29	0.0074	N	N	N/A	N/A	3.85

UNZ-8-4	0.15	0.12	1.E-01	20	11600	36.56	0.0058	N	N	N/A	N/A	11.12
UNZ-8-5	0.19	0.16	1.E-01	20	11540	36.42	0.0053	N	N	N/A	N/A	11.71
UNZ-8-8	0.16	0.13	1.E-01	20	9125	28.79	0.0053	N	N	N/A	N/A	9.39
UNZ-8-9	0.15	0.12	1.E-01	20	12910	40.71	0.0056	N	N	N/A	N/A	12.47
UNZ-2-2	0.13	0.10	1.E-01	20	23562	74.18	0.0055	N	N	N/A	N/A	22.79
UNZ-2-3	0.12	0.10	1.E-01	20	22309	70.24	0.0069	N	N	N/A	N/A	19.83
UNZ-12-2	0.10	0.10	1.E-01	20	29086	91.30	0.0083	N	Y	N/A	N/A	15.15
UNZ-12-5	0.10	0.10	1.E-01	20	27638	86.58	0.0101	N	Y	N/A	N/A	11.36
UNZ-11-1	0.30	0.29	1.E-01	20	8840	27.80	0.0077	N	Y	N/A	N/A	6.35
UNZ-11-5	0.30	0.29	1.E-01	20	7780	24.47	0.0065	N	Y	N/A	N/A	6.25
UNZ-5-15	0.21	0.17	1.E-01	20	13805	43.81	0.0081	N	N	N/A	N/A	11.58
UNZ-1-10	0.20	0.18	1.E-05	900	643	2.02	N/A	N	N	1.40E+11	5.17E-07	N/A
UNZ-1-9	0.20	0.17	1.E-05	900	975	3.08	N/A	N	N	8.98E+10	1.20E-06	N/A
UNZ-4-16	0.12	0.11	1.E-05	900	2041	6.41	N/A	N	N	2.87E+11	5.22E-06	N/A
UNZ-4-17	0.12	0.11	1.E-05	900	2077	6.56	N/A	N	N	2.86E+11	5.46E-06	N/A
UNZ-5-10	0.22	0.20	1.E-05	900	1294	4.06	N/A	N	N	1.77E+11	2.09E-06	N/A
UNZ-5-9	0.22	0.20	1.E-05	900	1277	4.02	N/A	N	N	1.71E+11	2.05E-06	N/A

UNZ-7-15	0.29	0.28	1.E-05	900	1540	4.87	N/A	N	N	2.06E+11	3.01E-06	N/A
UNZ-7-16	0.28	0.27	1.E-05	900	1475	4.80	N/A	N	N	2.01E+11	2.93E-06	N/A
UNZ-8-16	0.18	0.16	1.E-05	900	652	2.30	N/A	N	N	9.09E+10	6.70E-07	N/A
UNZ-8-17	0.18	0.16	1.E-05	900	829	2.72	N/A	N	N	1.09E+11	9.40E-07	N/A
UNZ-4-27	0.10	0.09	1.E-04	900	4696	24.28	N/A	N	N	4.55E+10	7.48E-05	N/A
UNZ-7-21	0.27	0.26	1.E-04	900	7117	22.52	0.0851	N	N	8.38E+10	6.43E-05	N/A
UNZ-4-28	0.10	0.08	1.E-04	900	11337	35.73	0.0529	N	N	1.20E+11	1.62E-04	N/A
UNZ-7-22	0.27	0.26	1.E-04	900	8010	25.27	0.0285	N	N	8.62E+10	8.10E-05	N/A
UNZ-8-21	0.17	0.15	1.E-04	900	7012	22.05	N/A	N	N	7.19E+10	6.17E-05	N/A
UNZ-8-22	0.17	0.14	1.E-04	900	7843	24.60	N/A	N	N	3.83E+10	7.68E-05	N/A
UNZ-5-16	0.21	0.19	1.E-04	900	7625	24.08	N/A	N	N	7.17E+10	7.36E-05	N/A
UNZ-1-14	0.20	0.18	1.E-04	900	5278	16.78	N/A	N	N	3.60E+10	3.57E-05	N/A
UNZ-1-7	0.21	0.19	1.E-03	900	11044	34.70	0.0168	N	N	N/A	1.53E-04	3.65
UNZ-1-8	0.22	0.19	1.E-03	900	10637	33.23	0.0258	N	N	N/A	1.40E-04	2.93
UNZ-4-14	0.12	0.10	1.E-03	900	24575	77.60	0.0189	N	N	N/A	7.64E-04	6.32
UNZ-4-15	0.12	0.11	1.E-03	900	21048	66.40	0.0172	N	N	N/A	5.59E-04	5.75
UNZ-5-7	0.21	0.19	1.E-03	900	16503	52.06	0.0155	N	N	N/A	3.44E-04	4.76

UNZ-5-8	0.21	0.09	1.E-03	900	16566	52.21	0.0171	N	N	N/A	3.46E-04	4.53
UNZ-7-13	0.31	0.31	1.E-03	900	7583	23.90	0.0129	N	N	N/A	7.24E-05	2.67
UNZ-7-14	0.31	0.30	1.E-03	900	7187	22.70	0.0090	N	N	N/A	6.54E-05	3.30
UNZ-8-13	0.16	0.13	1.E-03	900	16384	51.63	0.0299	N	N	N/A	3.38E-04	4.19
UNZ-8-14	0.16	0.13	1.E-03	900	16571	52.07	0.0305	N	N	N/A	3.44E-04	4.43
UNZ-8-15	0.17	0.14	1.E-03	900	14382	45.19	0.0310	N	N	N/A	2.59E-04	3.68
UNZ-1-x	0.22	0.21	1.E-06	900	127	0.34	N/A	N	N	1.20E+11	3.47E-07	N/A
UNZ-1-x	0.22	0.21	1.E-05	900	610	1.94	N/A	N	N	7.00E+10	N/A	N/A
UNZ-1-x	0.22	0.21	1.E-04	900	3682	11.72	N/A	N	N	3.85E+10	N/A	N/A
UNZ-1-x	0.22	0.21	1.E-03	900	8383	26.68	0.9180	N	N	N/A	N/A	N/A

2.3. Results

2.3.1. Sample characterisation

2.3.1.1. Mineralogy and geochemistry

Normalised geochemical analysis for bulk and glass geochemistry, obtained by XRF and EPMA respectively, are displayed in Table 2.2. Optical examination of the samples reveals that they consist of 20-50 vol.% phenocrysts and microphenocrysts of plagioclase (> 25 vol.%), amphibole (~ 5 vol.%), biotite (~ 2 vol.%) and quartz (~ 2 vol.%) (Fig. 2.3), where plagioclase and amphibole are the largest of the phenocrysts, and are generally greater than 3 mm. These phenocrysts and microphenocrysts are set in a partially crystalline (~ 50 vol.%) groundmass containing microlites of plagioclase, pyroxene, quartz, pargasite, and Fe-Ti oxides in a peraluminous rhyolitic interstitial glass (as described in Cordonnier et al. 2009). Cristobalite is occasionally observed as pore infills (also recorded by Nakada and Motomura, 1999). The bulk chemistries of samples UNZ-11 and UNZ-12 (deemed visually altered) have slightly more (1.1-1.4 wt.%) SiO_2 and slightly less (0.55-0.63 wt.%) CaO than UNZ-4, whilst K_2O and Na_2O concentrations are almost identical.

Table 2.2. Normalised chemical composition of bulk rocks obtained by XRF analysis and interstitial glass obtained by EPMA. UNZ-4 was selected as it is representative of fresh lavas tested in this study; in contrast, UNZ-11 and UNZ-12 were deemed to display a certain degree of alteration. Original totals were 99.97, 100.39, 100.09, and 99.95 for UNZ-4, UNZ-12, UNZ-11, UNZ-4 glass, respectively, before normalisation for direct comparison. The standard deviation of the UNZ-4 glass was taken from two measurements.

	XRF			Microprobe	
	UNZ-4	UNZ-11	UNZ-12	UNZ-4 glass	standard deviation
SiO_2	64.07	65.2	65.48	79.20	0.20
TiO_2	0.67	0.66	0.61	0.40	0.01
Al_2O_3	16.34	15.98	16.39	11.13	0.02
Fe_2O_3	4.84	4.67	4.35	-	-
FeO	-	-	-	0.92	0.01
MnO	0.10	0.10	0.09	0.01	0.01
MgO	2.57	2.37	2.02	0.07	0.02
CaO	5.18	4.55	4.63	0.56	0.02
Na_2O	3.61	3.56	3.69	2.83	0.09
K_2O	2.31	2.55	2.46	4.87	0.07
P_2O_5	0.17	0.12	0.15	-	-
LOI	0.14	0.23	0.14	-	-
Total	100	100	100	100	0

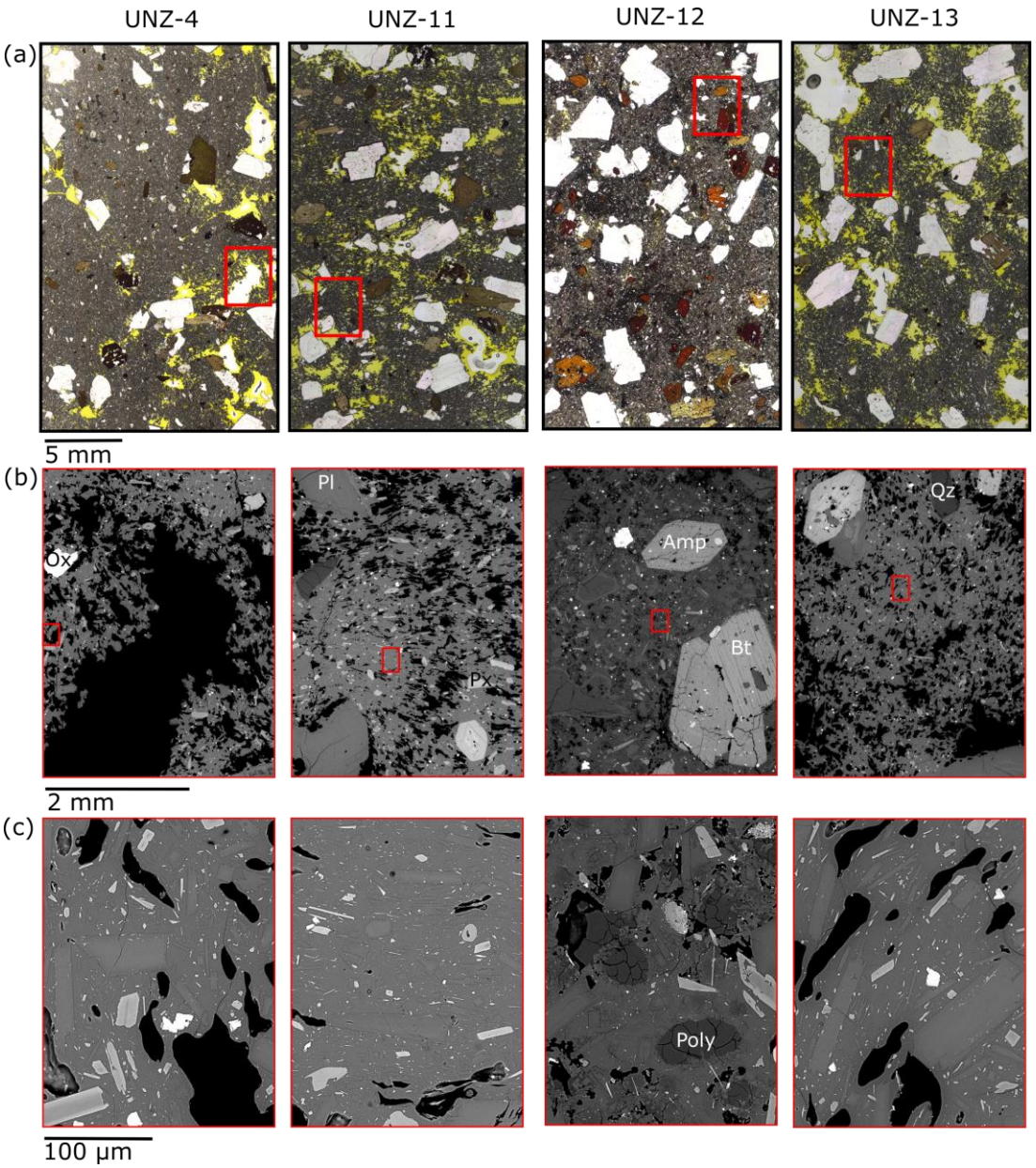

Figure 2.3. Plane-polarised light (a) and backscattered electron images (b,c) of undeformed samples UNZ-4,-11, -12 and -13. (b) is a zoom into the red box in (a), and (c) is a zoom in of the red box in (b), displaying the groundmass textures. Amp: Amphibole, Bt: Biotite, Ox: Oxides, Pl: Plagioclase, Px: Pyroxene, Qz, Quartz, Poly: Silica polymorph. Images are orientated so that the later applied principal stress, σ_1, is in the vertical direction. [Note the scale that is below each set of images.]

2.3.1.2 Rock porosities

The total porosities of the samples determined by helium pycnometry measurements range from 0.10-0.32 (Table 2.3); a scatter which has previously been studied in an investigation of rock frictional properties (Hornby et al., 2015) and which is consistent with field measurements of Mt. Unzen 1991-1995 eruptive products (Kueppers et al., 2005). The pores of the denser products, notably UNZ-4 and UNZ-12, are fully connected, whereas the higher porosity blocks contain a portion (0.01-0.02) of isolated pores. The small standard deviation for the connected, isolated and thus total porosity of the rocks ensures the comparability of mechanical data obtained on samples with similar porosities during repeats.

Table 2.3. Average total connected and isolated porosities for each sample block used. A larger number of cores were measured to calculate the average porosities than those used in strength tests. Note the values are presented to two decimal places but were calculated with four decimal places.

Sample block name	Average total porosity	Standard deviation	Average connected porosity	Standard deviation	Average isolated porosity	Standard deviation	No. samples
UNZ-1	0.21	0.011	0.18	0.012	0.02	0.002	17
UNZ-2	0.13	0.016	0.11	0.018	0.02	0.003	7
UNZ-4	0.12	0.016	0.12	0.021	0.00	0.016	30
UNZ-5	0.21	0.006	0.19	0.009	0.02	0.006	18
UNZ-7	0.30	0.024	0.29	0.025	0.01	0.002	23
UNZ-8	0.16	0.016	0.14	0.016	0.02	0.003	24
UNZ-11	0.30	0.009	0.29	0.011	0.01	0.004	8
UNZ-12	0.10	0.025	0.09	0.026	0.00	0.002	7
UNZ-13	0.32	0.005	0.30	0.004	0.01	0.004	6

2.3.1.3 Microstructures

Microstructural examination can be used to assess any pre-existing anisotropy or fabrics in the lavas. Photomicrographs along with SEM images, of a selected group of samples (UNZ-4,-11,-12,-13) can be seen in Figure 2.3. These samples are shown due to their contrasting nature, covering the span of textures studied here: UNZ-11 and UNZ-12 are visually altered samples; UNZ-13 has a different pore anisotropy than UNZ-11, and UNZ-4 is a typical product of the block-and-ash flow and is representative of the remaining samples tested. The images in Figure 2.3 show the original materials, orientated so that the direction of principal stress, σ_1, applied to the cores prepared of each rock would be in the vertical direction.

It is evident from Figure 2.3 that the pores in the Mt. Unzen dome rock samples are preferentially elongate. In some cases, the elongation has a visually preferred orientation (e.g. UNZ-11,-13), while

in others it is unsystematic (e.g. UNZ-4,-12). In UNZ-11 vesicles, and microlites, appear to bottleneck around phenocrysts in a horizontal direction (i.e., perpendicular to σ_1 imposed in the experiments), whereas in UNZ-13 their alignment is vertical (i.e., parallel to σ_1), indicating a sense of shear in those directions. UNZ-4,-11, and -13 have significant number of larger pores (>1 mm) when compared to UNZ-12, and across the shown sample set, these larger pores appear as pressure shadows around the phenocrysts (e.g. see McKenzie and Holness, 2000). Fractures are only clearly visible in UNZ-4, this is most likely due to higher abundance and larger fracture widths in this sample, allowing them to be visible in both thin section and BSE images. The fractures appear to connect pores via the tip of their major axis.

The groundmass of UNZ-12 contains a scaly-textured silica polymorph that appears to have filled vesicles. Common silica polymorphs seen at Mt. Unzen, and other domes across the world (e.g. Mt. St. Helens; Voight et al. 1981), are cristobalite precipitates, formed from hydrothermal activity (Nakada and Motomura, 1999; Voight et al., 1981, 2009). This silica deposit has filled a considerable amount (~ 50 vol.%) of the vesicles in UNZ-12, reducing its porosity (Fig. 2.3c). Although the polymorph is a sign of alteration, in the highest magnification BSE image, some glass appears to have remained vitreous between silica polymorph areas. In UNZ-11, neither the phenocrysts nor the groundmass show evidence of alteration (Fig. 2.3b,c).

In UNZ-12 the phenocrysts are visually more abundant (> 20 vol.%) than in the other specimens (Fig. 2.3). Nakada and Motomura (1999a) observed that groundmass crystallinity increased from (33 to 50 vol.%) with decreasing effusion rate, as was the case towards the end of the eruption (Nakada et al., 1995b), consistent with ~ 55 vol.% groundmass crystallinity in the 1994-95 spine . These observations are also consistent with the crystal fractions measured in UNZ-12, collected from the near-vent area.

2.3.1.4 The influence of thermal stressing

The skeletal volume, mass and dimensions of each core were measured before and after thermal stressing in order to assess changes in porosity that may accompany microstructural adjustment in the process. Results showed that over the 12 cores subjected to thermal stressing, the change in connected porosity was less than 0.001, which is within the resolution of the method. Thus, it may be said that thermal stressing did not markedly create pores or connect isolated vesicles. It did however cause a slight decrease in the values of Young's Modulus.

2.3.2. Uniaxial compressive experiments

2.3.2.1. Mechanical response of Mt. Unzen dome rocks

Uniaxial compressive strength tests were conducted on 66 cores at ambient temperature. For those samples which had a brittle response to uniaxial compression, the failure process can be segregated into 4 stages (Hoek and Bieniawski, 1965; e.g. Brace et al., 1966; Scholz, 1968; Heap et al., 2014b).

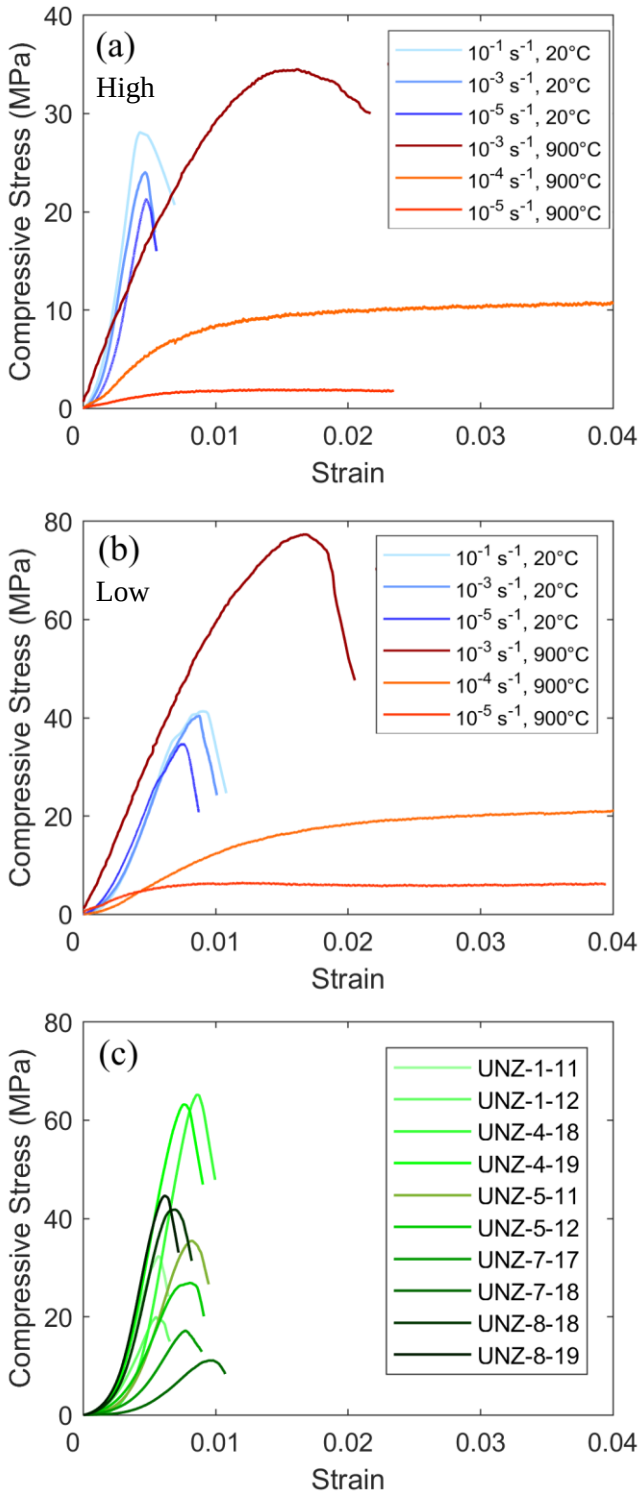

Figure 2.4. Examples of compressive stress-strain curves for (a) high porosity, UNZ-1 (0.21); (b) low porosity, UNZ-4 (0.12) at a range of rates and temperatures and (c) thermally stressed samples, all performed at a strain rate of 10^{-3} s^{-1}. Mechanical data for high temperature experiments are shown in shades of red, low temperature experiments in shades of blue and thermally stressed experiments in shades of green. At high temperature, faster strain rates cause the sample to break whereas at slower strain rates the sample flows. Brittle high temperature experiments fail at considerably higher peak stresses than those performed at ambient temperatures. In the brittle regime, samples deformed at faster rates failed at higher stresses. [Note: there is a difference in Y-scale between (a) and (b) & (c)]

An initial build-up of stress has been attributed to the closure of micro-cracks perpendicular to σ_1, this is the initial convex segment on the stress-strain curve (e.g. Fig. 2.4a,b). The second, linear increase in stress and strain has been attributed to dominantly elastic (recoverable) deformation. Strain hardening, marks the onset of micro-fracturing that imparts permanent, non-recoverable damage, causing deviation from the linear elastic regime during loading (seen as the concave section of the stress-strain curve; Fig. 2.4a,b). Finally, a peak in stress is reached, followed by an abrupt stress drop, this is associated with through-going fracture propagation and coalescence before macroscopic failure is reached. This behaviour is seen in the stress-strain curves (Fig. 2.4a,b, Fig. 2.S3, 2.S4) of all samples deformed in the brittle regime, be it at ambient temperature (for all strain rates) or at high temperatures (for faster strain rates; see section 2.3.2.2).

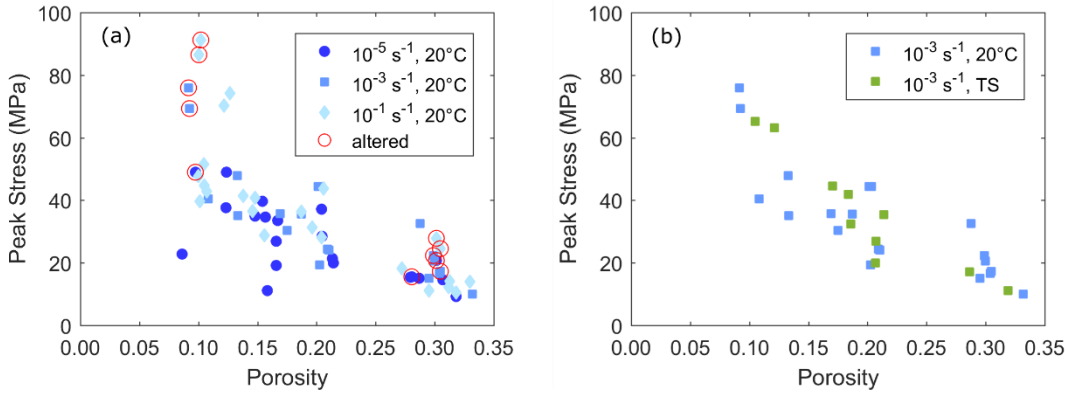

Figure 2.5. (a) The strength (peak stress) of samples tested at ambient temperatures at varying strain rates, highlighting the apparent strengthening of materials deformed at faster rate. Red rings circle the samples that are visibly altered. (b) A comparison of samples that were thermally stressed and those that were not, both tested at ambient temperatures and strain rates of 10^{-3} s^{-1}, demonstrating that there is no change in strength as a function of porosity due to thermal stressing.

The strength of the rocks was observed to decrease with porosity (Fig. 2.5a). The range of strength of dense rocks is higher than porous rocks. We observe that rock strength increases with applied strain rates at all porosities, although this effect is more pronounced for dense rocks. The data suggest that the rocks deemed altered (UNZ-11, UNZ-12) are not weaker, but indeed stronger than pristine rocks with equivalent porosities (see circled data points in Fig. 2.5a).

The overlap between the datasets obtained for thermally stressed and as-collected samples suggests that thermal stressing did not impart significant damage or mineralogical changes (if any) to modify the strength of these rocks (Fig. 2.5). Yet, a closer look at the mechanical data suggests that the initial convex increase in stress with strain is more pronounced for the thermally stressed samples than for their pristine equivalent (Fig. 2.4c), indicating that the thermally stressed samples have more cracks to close than their untreated equivalents. It is therefore likely that thermal stressing has caused the creation or opening of micro-fractures, dislocating the rocks slightly in the process, but not enough to cause a notable increase in porosity or decrease in strength.

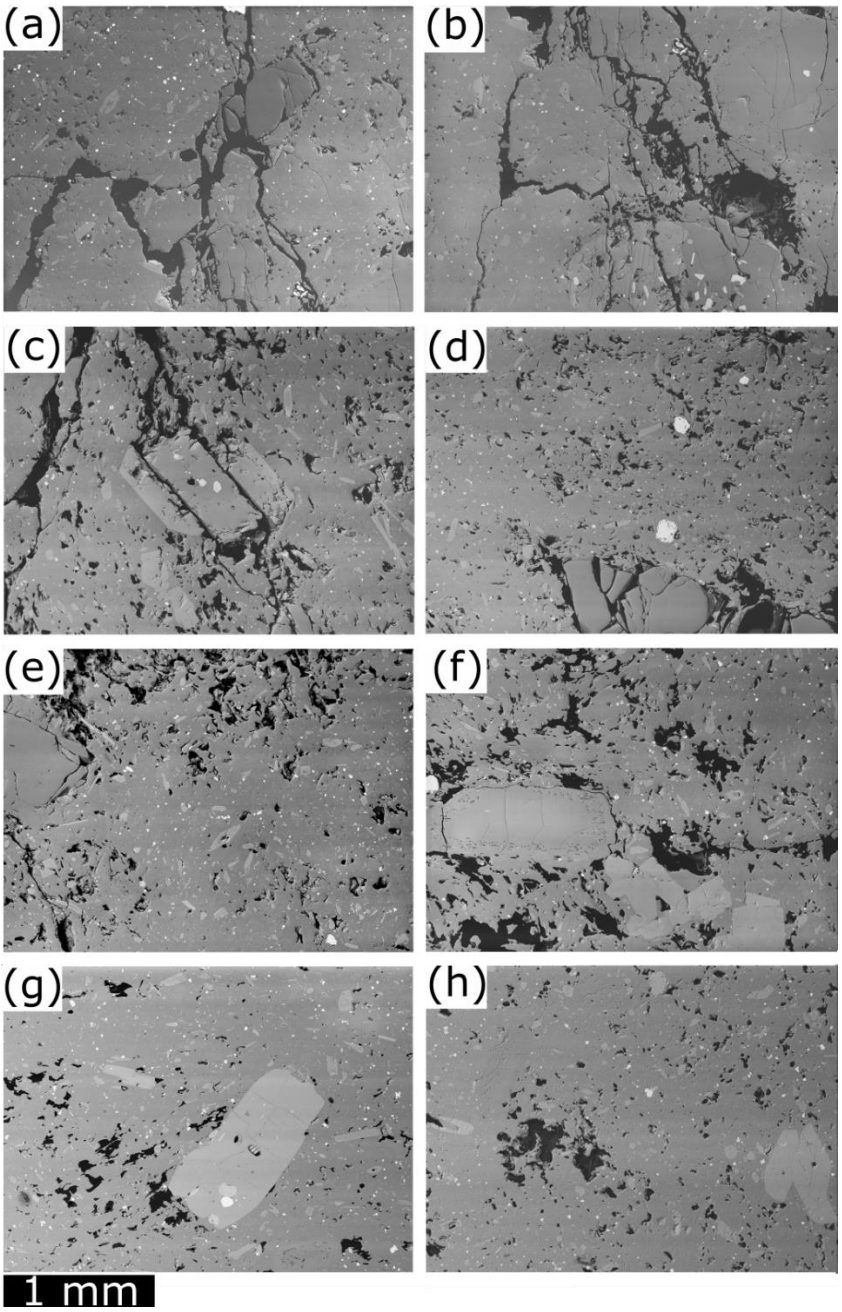

Figure 2.6. Backscattered electron images of polished stubs for samples after strain (a to f) and before strain (g and h). Panels a) and b) show sample UNZ-4-14 after experiencing brittle deformation at a strain rate of 10^{-3} s^{-1}; macroscopic cracks (> 100 µm in width) propagate through both the groundmass and phenocrysts. Panel c) shows sample UNZ-8-14 after experiencing brittle-dominated transitional behaviour at a strain rate of 10^{-3} s^{-1}; pervasive macroscopic fractures (> 100 µm in width) connect porosity and displace phenocrysts along their planes of weakness. Panels d) and e) are representative images of UNZ-8-21 which underwent viscous-dominated transitional behaviour when strained at 10^{-4} s^{-1}; small (< 200 µm in width) microfractures can be seen in the ground-mass glass, phenocrysts are pervasively fractured but show no sign of displacement. Panel f) is an image of sample UNZ-8-16 after experiencing viscous deformation at a strain rate of 10^{-5} s^{-1}; pores are aligned parallel to the direction of shear around phenocrysts with minor fractures < 100 µm in width. Panels g) and h) show UNZ-4 and UNZ-8, respectively, prior to deformation; with few, hairline fractures visible in the phenocrysts and little to no fractures in the smaller crystals or the groundmass glass.

2.3.2.2 Rheological response of Mt. Unzen dome lavas

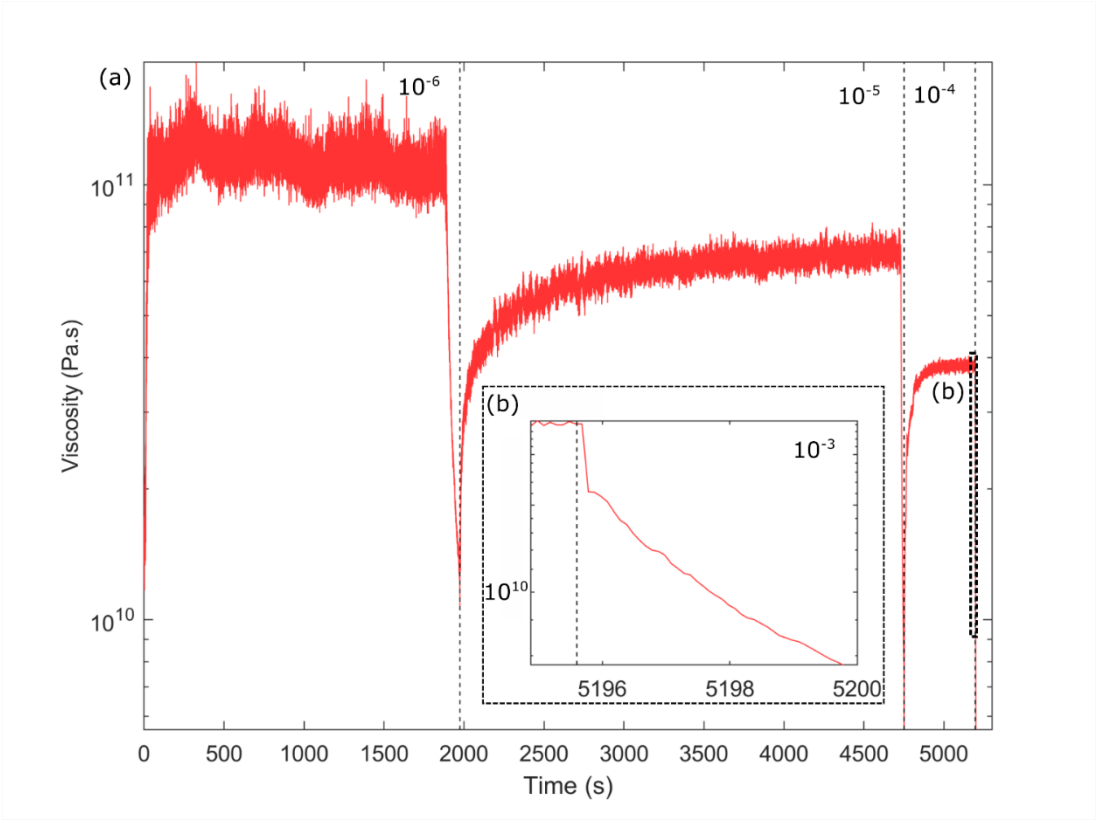

Figure 2.7. Apparent viscosity evolution of UNZ-1 (porosity: 0.22) at 900 ˚C during a stepped strain-rate experiment (10^{-6} s^{-1}, 10^{-5} s^{-1}, 10^{-4} s^{-1}, 10^{-3} s^{-1}); each step is separated by dashed lines. The insert zooms in on the apparent viscosity decrease that accompanies sample failure at 10^{-3} s^{-1}. The decrease in viscosity at each increasing strain rate increment highlights the shear thinning behaviour of these lavas.

The mechanical data of lavas show a wider range of behaviour than those obtained on rocks at ambient temperature (Fig. 2.4a,b). At slower strain rates of 10^{-4} and 10^{-5} s^{-1}, samples may provide a viscous response. Initially, the stress-strain curves exhibit only a mildly convex stress build-up, but then deformation is dominated by a stress relaxation phase which results in a levelling of the stress to a steady value as strain amasses (orange and red lines, Fig. 2.4a,b). This represents the viscous flow of the suspension and, as such, its apparent viscosity can be calculated from the mechanical data. At faster strain rates > 10^{-3} s^{-1}, samples may respond brittlely. In this regime, as at ambient (room) temperature, stress accumulation may eventually lead to failure and a significant stress drop (e.g. maroon line Fig. 2.4b). The behaviour that links the viscous and brittle response is termed transitional. If the plateau in the stress-strain curves is marked with minor stress drops, this signals a transitional response to deformation that is dominantly viscous. Where there is a major drop in the stress-strain curve that takes place over an extended period of strain, we termed this response brittle-dominated transitional (maroon line Fig. 2.4a). This interpretation of mechanical data can also be confirmed by analysing the microstructure of deformed samples (Fig. 2.6). Samples with pervasive macro-fractures that propagate through both groundmass and, to a lesser extent, the phenocrysts have likely undergone fully brittle deformation. Likewise, samples with a response classified as brittle-dominated

transitional also have pervasive macro-fractures, however the phenocrysts are only slightly displaced along their cleavage planes, rather than shattered. Samples that have had a viscous-dominated transitional response to strain display microfractures in both the groundmass and phenocrysts, and those that have had a viscous response show little to no micro-fracturing. A viscous response may also lead to elongation of porosity parallel to the sense of shear.

The evolution of apparent viscosity is strain-rate dependent as shown by the stepped strain rate experiment (Fig. 2.7). An increase in the strain rate resulted in an order of magnitude decrease in viscosity- a thixotropy of similar magnitude as that described for highly crystalline magmas in Lavallée et al. (2007). In this experiment, deformation at low strain rates of 10^{-6} s^{-1}, 10^{-5} s^{-1} and 10^{-4} s^{-1}, is marked by a non-linear increase in apparent viscosity (upon stress relaxation) and plateauing to a constant value for each strain-rate step; this value decreased with increase of the applied strain rate (Fig. 2.7). Deformation was pervasive (i.e., ductile), which, being above T_g, suggests that it may have dominantly occurred via a viscous response. At 10^{-3} s^{-1}, however, the apparent viscosity plummeted as the sample underwent failure along a localised fault, evidencing a transition into the brittle regime (Fig. 2.7b).

At strain rates of 10^{-3} s^{-1} the sample suite tested reached peak stresses of ~ 20-80 MPa (Fig. 2.8a) and strength decreased inversely with porosity. Here the samples responded with a brittle and brittle-dominated transitional response to strain. The mechanical responses of samples tested at high temperature were more repeatable than those carried out at ambient temperature: the strength of samples (within a family with ~ 0.01 porosity range) was within ~ 2 % of each other at low porosities (< 0.20) and within ~ 5 % of each other at high porosities (> 0.20), whereas at ambient temperatures a variation of ~ 60 % is observed in the lower porosity regime (Table 2.1).

When a strain rate of 10^{-4} s^{-1} was applied some of the samples reached peak stresses between ~ 10 and 35 MPa (Fig. 2.7b), before relaxing the stress through substantial strain. Here, the lavas display a viscous and viscous-dominated transitional response to strain. In some samples, an initially viscous response transitioned to fracturing after a certain amount of strain, leading to macroscopic failure. Samples that did not fracture continued to flow viscously with increasing strain, with a component of strain hardening, similar to that seen by Kendrick et al. (2013b). Samples that were subjected to a strain rate of 10^{-5} s^{-1} had a fully viscous response over the strain rates tested (Fig. 2.8c). Remarkably, the peak stresses of samples tested at 10^{-4} and 10^{-5} s^{-1} were seemingly independent of porosity (Fig. 2.8d).

The apparent viscosities calculated from the responses at 10^{-5} and 10^{-4} s^{-1} show an initial increase (due to relaxation in the first 0.7 % strain) and levelling to within a narrow range (see Fig. 2.9a,b). For a given strain rate, we note a small range of apparent viscosities, but importantly, no systematic change in viscosity as a function of sample porosity (within the range tested; Fig. 2.9c).

These results indicate that the transition in deformation mode from macroscopically ductile to brittle behaviour is straddled by our experiments in the range 10^{-5} to 10^{-3} s^{-1}.

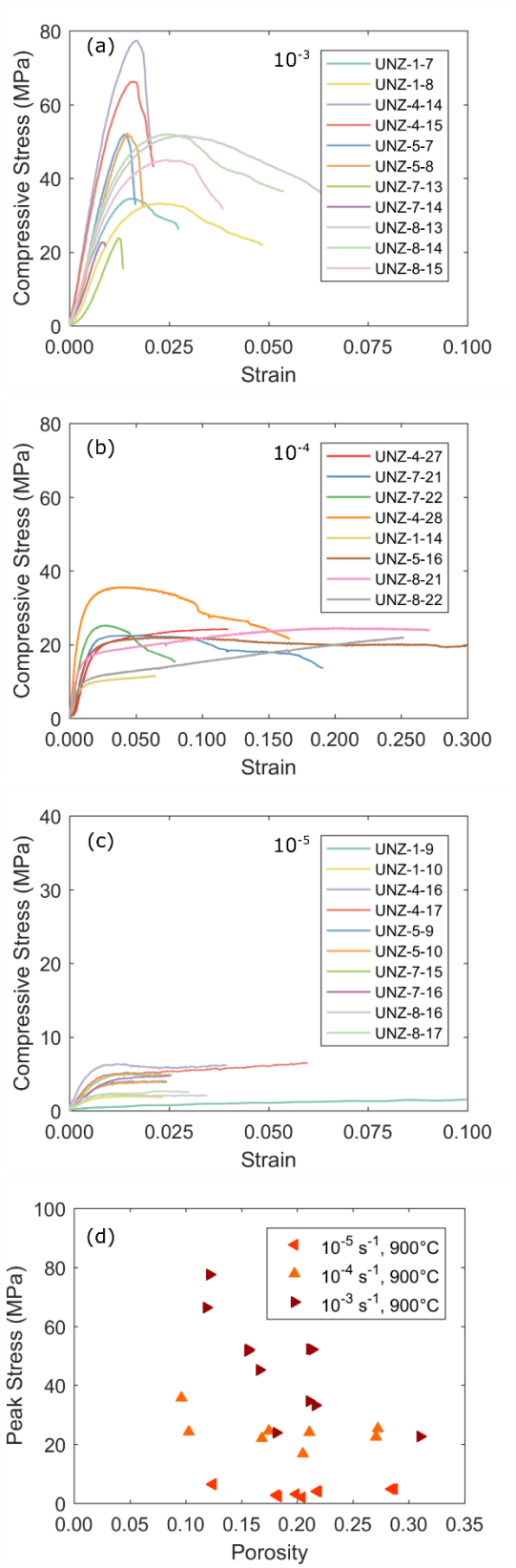

Figure 2.8. High temperature uniaxial experiment results, including stress-strain curves for samples tested at a strain rates of (a) 10^{-3} s^{-1}, (b) 10^{-4} s^{-1}, and (c) 10^{-5} s^{-1}, demonstrating the shift from viscous flow at low rate to increasingly brittle deformation at faster rate. (d) The peak stresses achieved during each experiment carried out at 900 ˚C further highlights this observation and shows the porosity-dependence of strength in the brittle regime.

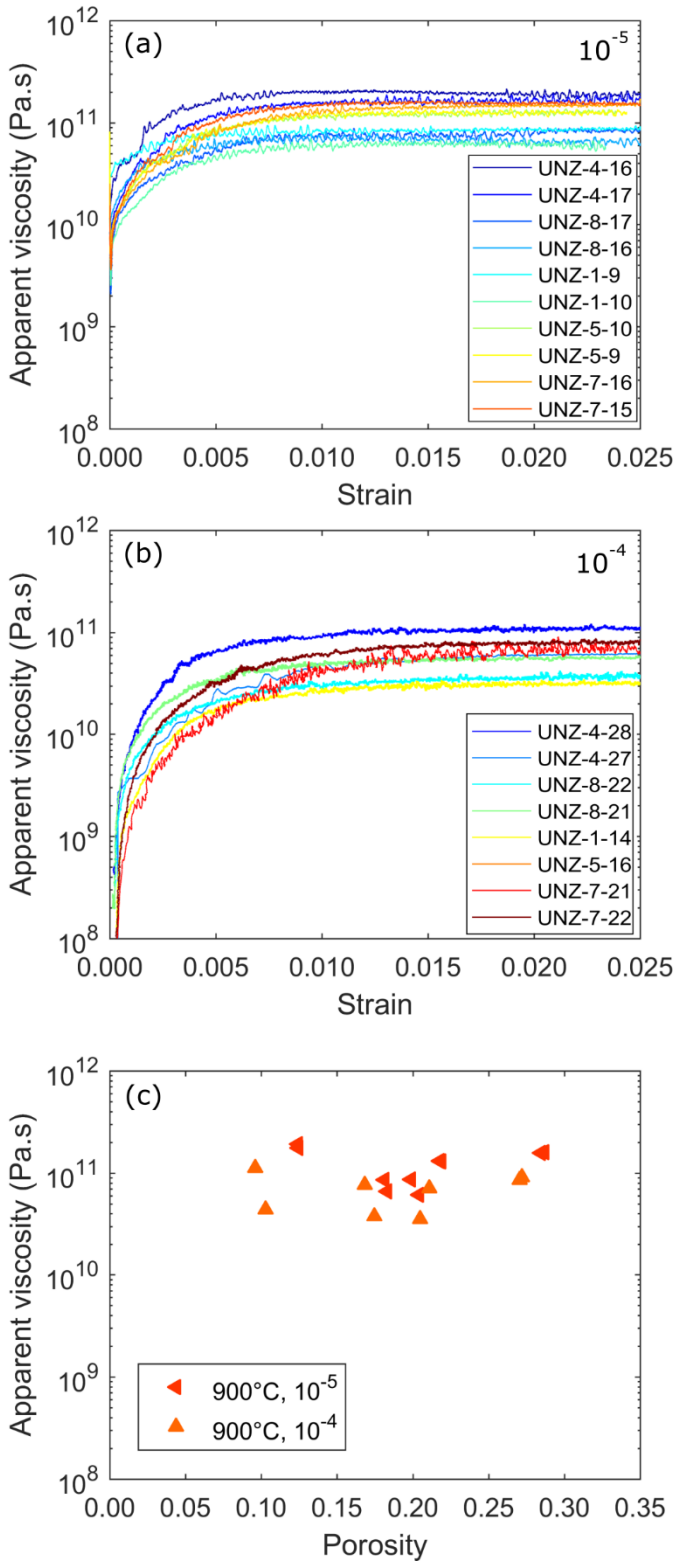

Figure 2.9. Apparent viscosities of porous lavas at 900 ˚C for strain rates of (a) 10^{-5} s^{-1} and (b) 10^{-4} s^{-1}; colours warm from blue to red with increasing sample porosity. (c) Compilation of apparent viscosities as a function of porosity for samples tested at strain rates of 10^{-4} s^{-1} and 10^{-5} s^{-1}. Viscosities decrease between strain rates of 10^{-5} to 10^{-4} s^{-1}, an example of shear thinning in the Unzen samples. Porosity has no control on the apparent viscosities of the samples tested here.

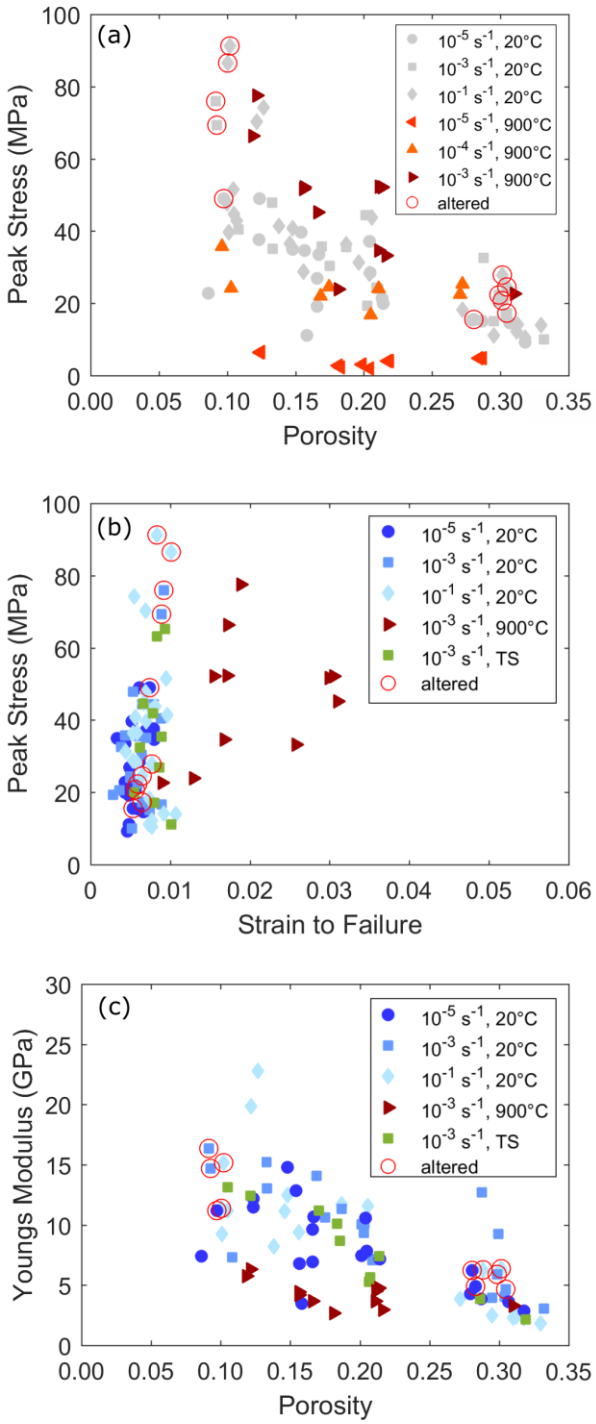

Figure 2.10. Strength and Young's Moduli of Unzen rocks and lavas at different conditions. Shades of blue represent tests carried out at ambient temperatures, shades of red indicate those performed at 900 °C, and green depicts thermally stressed samples which were tested in ambient conditions. The red rings circle the samples which were deemed visibly altered at collection. (a) Peak stress with porosity for all completed experiments. Low temperature tests, as seen in Figure 2.5 (a), are faded to grey. (b) Peak stress with strain at the point of sample failure (i.e. the stain at peak stress) for all experiments with a brittle response. (c) Young's modulus as a function of porosity for all samples that had a brittle response calculated using the slope of the linear portion of the stress-strain curve (see Fig. 2.S6).

2.4. Interpretation of dome rock mechanics

2.4.1. Mechanical responses of rocks and lavas in the brittle and brittle-dominated transitional regime

The experimental findings presented here suggest that the mechanical response of lavas and rocks is similar, but important differences remain. Experiments carried out on rocks at ambient temperature (all strain rates), and on some lavas at strain rates of 10^{-3} s^{-1}, resulted in brittle behaviour. However, there are significant differences in the mechanical response between the two (Fig. 2.4). (1) We noted a shorter convex portion at the onset of the stress-strain curve of tests at high temperature (Fig. 2.S3), which we attribute to a narrowing of pre-existing cracks at high temperature (due to thermal expansion of the materials with heating; e.g. Fig. 2.S5), resulting in a smaller extent of crack closure during initial loading; (2) most high temperature samples have a shallower linear portion of stress-strain build-up, which we hypothesise may reflect a contribution of viscous deformation upon loading, leading to a brittle-dominated transitional classification; and (3) we observed a less angular concave down portion of the stress-strain curve, which we attribute to more pervasive deformation (as seen by longer strain to failure; Fig. 2.10) and micro-fracturing leading to failure. The exception to these findings is in the highest porosity sample, UNZ-7, where there appears to be no significant change in shape between high and ambient temperature experiments (see Fig. 2.S3, 2.S4). This sample was classified in the fully brittle regime. It remains that at higher temperature, lavas are stronger (by 10-40 MPa; Figs 2.4-2.9) than their rock equivalents at ambient temperature. Before delving in their differences (section 2.4.1.4), we will first interpret the results on the strength (section 2.4.1.2) and Young's Modulus (section 2.4.1.3) of porous rocks at ambient temperature.

2.4.1.2 The effect of porosity on material strength

From the results of the uniaxial compressive experiments it is evident that porosity is a major control on the strength of dome materials. Previous studies on volcanic rocks (Al-Harthi et al., 1999; Heap et al., 2014b, 2014c, 2016b; Schaefer et al., 2015) have found a similar correlation in which, to a first order, strength is inversely proportional to the porosity of the rock.

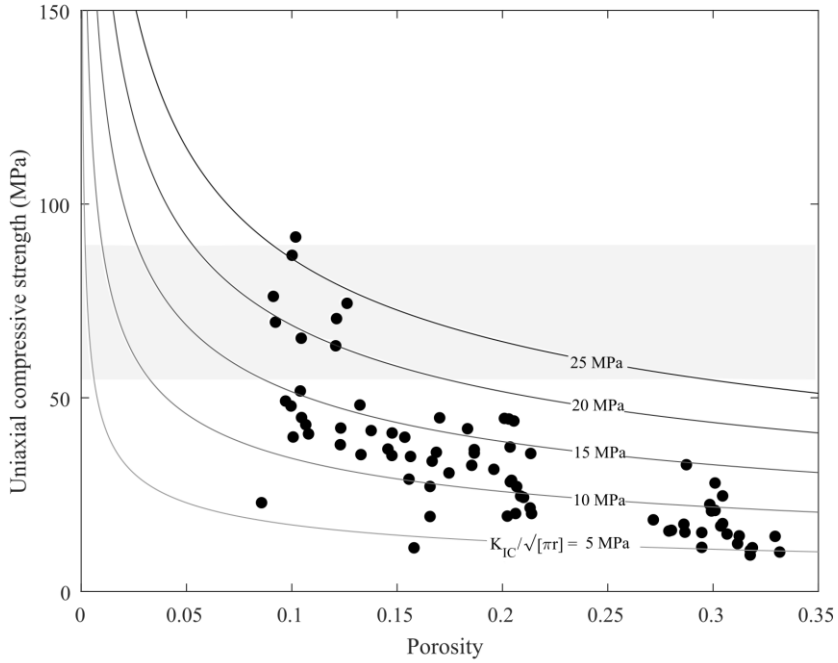

Figure 2.11. Plot of uniaxial compressive stress against porosity showing the ambient temperature mechanical data (black dots), along-side contours of various values of $\frac{K_{IC}}{\sqrt{\pi r}}$ (5-25 MPa) from the pore-emanating crack model (Eqn. 2.2). The range of UCS given by the wing-crack model is also plotted as a shaded region. The mechanical data are cross-cut by the contours, suggesting a change in the dominant porous structure. At porosities > 0.25 the UCS given by the pore-emanating crack model with $\frac{K_{IC}}{\sqrt{\pi r}}$= 5-10 MPa seems to fit the data well. For porosities ranging from 0.12-0.2 the UCS given by the pore-emanating crack model with $\frac{K_{IC}}{\sqrt{\pi r}}$ = 10-15 MPa encloses the data. The UCS for the densest rocks in the study (~0.08-0.12) would suggest yet a higher $\frac{K_{IC}}{\sqrt{\pi r}}$ of 20-25 MPa. For porosities < 0.1 the UCS given by the wing-crack model is similar to the mechanical data (σ = 54.2-89.7 MPa).

Here, the strength of samples with higher porosities display less scatter than those with lower porosities (Fig. 2.10a). Microstructural examination of the samples (Fig. 2.3) reveals the porosity of the porous specimens to be dominated by vesicles, whereas the porosity of the denser samples is dominated by microfractures, which may define a change in the microstructural control on the strength and failure of low and high porosity samples. In these lower porosity specimens, the non-systematic orientation of microfractures could be responsible for the large scatter in strength. The uniaxial compressive strength was calculated for the samples for both the pore-emanating crack model of Sammis & Ashby (1986) (Eqn. 2.3) and the sliding wing crack model of Ashby & Sammis (1990) (Eqn. 2.4). For the former, the uniaxial compressive strength was calculated with varying values of $\frac{K_{IC}}{\sqrt{\pi r}}$ from 5 MPa to 25 MPa (Fig. 2.11). For the latter, approximate values for μ, $\frac{K_{IC}}{\sqrt{\pi c}}$ and D_0 were taken from Paterson and Wong (2005) as 0.51, 20-30 MPa and 0.3-0.44, respectively. This gave a range of estimated strength between 54 and 90 MPa (Fig. 2.11). At higher porosities, > 0.25, the pore-emanating crack model with $\frac{K_{IC}}{\sqrt{\pi r}}$ = 5-10 MPa seems to fit the data well, whereas for most rocks

with porosities of 0.12-0.2 $\frac{K_{IC}}{\sqrt{\pi r}}$ = 10-15 MPa is a better fit. This could be explained by a decrease in the pore radius at these porosities, leading to higher values of $\frac{K_{IC}}{\sqrt{\pi r}}$, though, as the samples are heterogeneous and pore radius variability is high we cannot observe this (Figure 2.3). For the densest rocks in the study (~ 0.08-0.12), the UCS data would suggest yet a higher $\frac{K_{IC}}{\sqrt{\pi r}}$ of 20-25 MPa. The pore-emanating crack model could explain this switch in behaviour if there was a fundamental change in pore radius. However, the switch could also be explained by a transition in failure mechanism from pore-emanating cracks to wing cracks, meaning the wing-crack model would be more applicable. Alternatively, it may be a complex combination of the two. Although the solutions to the sliding wing-crack model are non-unique, as there are few experimentally constrained parameters, when combined with information gained from the pore structures (Fig. 2.3), the results of the modelling presented (Fig. 2.11) give us an insight into the dominant micromechanical failure mode of our samples. It is likely that the complex pore structures of these lavas, generated by a combination of vesiculation, deformation and cooling-driven contraction require an as-yet undefined combination of the two models. The weighting towards one or the other, however indicates that for the higher porosity specimens the behaviour of failure could be described using the pore-emanating crack model of Sammis & Ashby (1986), whereas in the lower porosity samples deformed in uniaxial compression, the main failure mechanism is explained by the sliding wing-crack model of Ashby & Sammis (1990).

This transition in the preference of fracture nucleation site from pore to crack is likely to be gradual and dependent on the pore network architecture of a suite of samples; in these Mt. Unzen samples it is found at a porosity of ~ 0.2. Other studies have also alluded to such a transition when studying permeability, finding a transition from crack-dominated to pore-connectivity-dominated regime of fluid flow at values of ~ 0.14 (Farquharson et al., 2015), 0.155 (Heap et al., 2015b), 0.105-0.31 (Kushnir et al., 2016), ~ 0.15 (Eggertsson et al., 2018), and 0.11-0.18 (Lamur et al., 2017).

Samples UNZ-11 (porosity: 0.30) and UNZ-13 (porosity: 0.32) both have elongated vesicles. The cores were cut so that the vesicles were either perpendicular or parallel to the applied principal stress, σ_1, for UNZ-11 and UNZ-13, respectively (Fig. 2.3). The porosities of the two rocks are comparable, and there is no great difference in strength, indicating that pore orientation may not have a significant influence on strength within dome rocks. Although we do note that UNZ-11 undergoes a higher strain to failure (Fig. 2.10b) and thus lower Young's Modulus (Fig. 2.10c) than UNZ-13, indicating that it is less stiff. Sample UNZ-2 (porosity: 0.13) however, does have a remarkably larger uniaxial compressive strength (~ 20 MPa) and Young's Modulus (~ 5-10 GPa) than samples of similar porosity. This may be due to the high number of spherical isolated pores (Table 2.3, Fig. 2.S2) which act as rigid bodies. However, it cannot be explicitly stated that pore anisotropy did not play a role in this and thus it is possible that the orientation of a pore may have a dominant effect on the strength and stiffness of the dome rock (Bubeck et al., 2017; Griffiths et al., 2017) Thus, future studies on rock strength may benefit from an in-depth study of rock strength as a function of pore fraction, orientation and connectivity.

2.4.1.3 Static Young's Modulus

At ambient temperatures, the static Young's modulus decreases from > 15 GPa to < 5 GPa with increasing porosity (Fig. 2.10c). This is an indication that samples with lower porosities were stiffer than those with higher porosities. However, there were outliers to the data trend, UNZ-13 and UNZ-2 (with average porosities of 0.32 and 0.13, respectively) are stiffer and have higher (> 5 GPa) Young's Moduli than other rocks with similar porosities (see Table 2.1); in UNZ-13, this may be explained by the preferred orientation of pores parallel to the principal stress (Figure 2.3a) (cf, Griffiths et al., 2017). The naturally altered samples, tested at similar conditions, exhibited Young's Moduli trends like those of comparable fresh rocks (Fig. 2.10c).

Lavas deformed at 900 °C at a strain rate of 10^{-3} s^{-1} have systematically lower (~ 5-10 GPa) Young's Moduli. It is this malleability that allows the lava to be deformed to higher strains before macroscopic failure (Fig. 2.10b), an observation recognised in Schaefer et al., (2015) in tests on basaltic lavas.

In addition, thermally stressed samples have slightly lower (~ 0.5-1.5 GPa) Young's Moduli than their unstressed equivalents, as previously noted in dacites from Mt. St. Helens (Kendrick et al., 2013a) and andesites from Colima volcano (Heap et al., 2014b). The slight decrease in static Young's modulus with thermal stresses highlights a potential change in porosity distribution that was not recognised by other means (e.g. total porosity, strength).

2.4.1.4 The effect of temperature on sample strength

Remarkably, when in the brittle regime at high temperature, samples exhibited strengths ~ 10-40 MPa greater than at ambient temperature. This may be attributed to the way the samples respond to stress at higher temperatures. First, upon heating a rock, it expands, which may partially close pre-existing micro-fractures, thus modifying the resultant elastic response of the material (see section 2.4.1.1). Moreover, at 900 °C the presence of interstitial melt in a sample allows for considerably more strain than if it were deformed at ambient temperature (when in a solid, glassy state). The initial strain upon loading would be accommodated by both an instantaneous and a delayed elastic response (e.g. Dingwell and Webb, 1989) and perhaps minor micro-crack closure (e.g. Heap et al., 2014b), before the onset of viscous (e.g. Lavallée et al., 2007) and crystal plastic (e.g. Kendrick et al. 2017) deformation that results in permanent strain (and barrelling of the sample). Thus, at higher temperatures, more strain is accommodated upon loading than at ambient temperature (Fig. 2.7a), leading to higher strain to failure (Fig. 2.10b) and lower Young's Moduli than their rock counterparts (Fig. 2.10c). The Young's Moduli for lavas undergoing failure at high temperature are rate-dependent, perhaps as they may undergo further stress dissipation by viscous relaxation in the melt.

A similar increase in strength with temperature was also noted in basaltic rocks from Pacaya volcano (Schaefer et al., 2015). There, the authors attributed the increase in strength of the glass-poor rock to the closure of micro-cracks (likely formed upon cooling after their eruption) due to thermal expansion, a process that equally occurs in Mt. Unzen dome rocks. Rocks may also become weaker from thermal stressing, this can be due to crack initiation (Heap et al., 2016a), or alteration, via processes such as decarbonation and dehydroxylation (Heap et al., 2012, 2013a, 2013b). A recent

study by Eggertsson et al., (2018), found that samples that hosted microfractures (like Mt. Unzen dome rock) were not affected by thermal stressing, while those that showed a trivial fraction of pre-existing micro-fractures were more readily fractured through thermal stressing and as a result became more permeable.

2.5. Rheology of dome lavas

2.5.1. Viscosity of dome lavas

The style of an eruption - effusive vs explosive - depends on the rheological response of magma (Dingwell, 1996). The urge to understand the alarmingly variable nature of volcanoes, and recent advances in experimental capabilities and computational modelling, have encouraged the community to focus efforts on the development of two and three-phase models of magma rheology (e.g. Lejeune and Richet, 1995; Caricchi et al., 2007; Lavallée et al., 2007; Costa et al., 2009; Mueller et al., 2011b; Truby et al., 2015). Truby et al., (2015) combined two, two-phase flow models (considering melt and crystals, and melt and gas bubbles) to elaborate a three-phase model of magmatic suspensions, further tested against a set of controlled analogue laboratory data. Their model shows that while the addition of crystals increases the viscosity of a suspension, leading to a shear thinning rheology, the addition of gas bubbles (which can deform during shear) has variable consequences. Depending upon the initial crystal volume and maximum packing fraction of those crystals, the addition of gas bubbles may result in a further increase in viscosity or, in other cases, a levelling or a decrease in the apparent viscosity of the suspension. Their model suggests that the addition of bubbles to lavas, above their glass transition, with high normalised crystal fractions, like those seen in volcanic domes, would likely decrease the viscosity of the suspension. However, here, the data show that the presence of vesicles (between 0.09 and 0.33) in dome lavas may not necessarily influence the apparent viscosity (at least not systematically). We advance that this could be due to the high connectivity of the pores present in dome lavas, which allows efficient outgassing, thus the gas cannot act as an isolated phase that can pressurise during shear. Thus, it may be that lavas hosting permeable porous networks may have mostly porosity-independent apparent viscosities (at least across the range examined here), as suggested by Lavallée et al. (2007). Current models relating porosity to viscosity, simply account for the presence of isolated gas bubbles via a capillary number, to calculate the apparent viscosity of a multi-phase suspension (e.g. Rust and Manga, 2002; Llewellin and Manga, 2005; Truby et al., 2015). However, this result highlights important shortcomings to the modelling of shallow magmas, where porous networks tend to develop connectivity, especially in sheared crystal-bearing lavas (e.g. Laumonier et al., 2011; Kushnir et al., 2017). This connectivity controls outgassing, and thus pressure build-up or release, which is responsible for rheological variations in magma and therefore eruption style (effusive vs explosive). Our findings suggest that we need to revise three-phase models to account for gas flow through evolving, deformable bubbles, that may also be connected, in order to constrain the apparent viscosity of magmas in lava domes and other open-system settings.

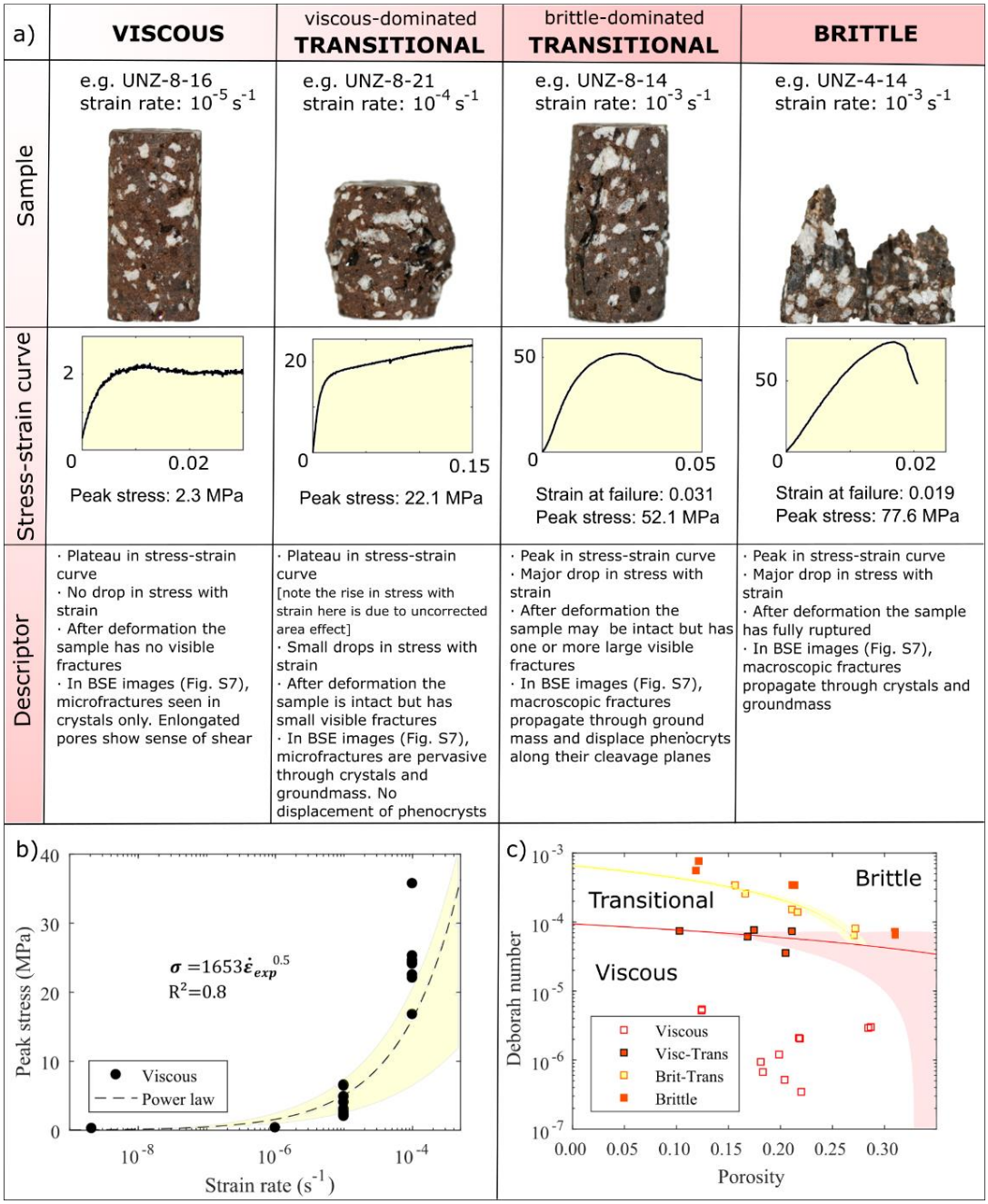

Figure 2.12. (a) A schematic demonstration of sample rheological classification [viscous, viscous-dominated transitional (visc-trans), brittle-dominated transitional (brit-trans) or brittle], depending on the respective shape of the stress-strain curve and the amount of strain experienced (b) Peak stress plotted with strain rate for completed experiments in semi-log space. The power law equation of the line is shown on the figure. Ostwald constants k and b are 1653 and 0.5 respectively. The standard error of estimate is shown on the plot as the yellow window, along with the R^2 value (c) The calculated Deborah number as a function of porosity for each sample tested at high temperature, in semi-log space. The viscous-dominated transitional behaviour is marked by the red line bordered by a red window showing the standard estimate of error. The brittle-dominated transitional behaviour is marked by the yellow line bordered by a yellow window showing the standard estimate of error. The critical Deborah number, De_c, can thus be said to be between $1x10^{-4}$ and $6.6\ x10^{-4}$ for dense (pore-free) crystal-rich dome lavas, deceasing linearly with the addition of pores. We find that the two transitional zones converge at a porosity of approximately 0.27, beyond which no transition zone exists (although this coincides with the limit of the material properties studied). [NOTE: Sample UNZ-4-28 was omitted from this plot as its resulting stress-strain curve was likely due to an experimental artefact caused by chipping of the sample edge]

2.5.2. Failure criterion for porous lavas

During magma ascent, the strain rate, which is proportional to effusion rate (e.g. Goto 1999), plays a key role in determining whether the response of magmas and extruding lavas is that of a solid, or liquid (Webb and Dingwell, 1990b). Here, the macroscopic deformation mode (viscous, viscous-dominated transitional, brittle-dominated transitional or brittle) of lavas was characterised based on their resulting stress-strain curve (section 2.3.2.2; a); these are further supported by micro-structural observations (see Fig. 2.6; Fig. 2.12a). [NOTE: sample UNZ-4-28 was not given a classification as its response to deformation was likely an experimental artefact due to a chipping of the sample edge]. The distinction between these rheological regimes can be made using the Deborah number (Eqn. 2.2). In a recent study on the failure of single phase silicate melts, Wadsworth et al., (2017b) suggest that fractures can propagate above $De \geq 10^{-2}$ when a sample begins to undergo brittle deformation, although these fractures are often blunted by viscous relaxation. When $De \geq 1$ brittle behaviour dominates over viscous deformation and violent rupture of the sample ensues. This dimensionless ratio of the relaxation timescale of the melt (Eqn. 2.1) and the observation timescale can be rewritten as:

$$De = \frac{\mu}{G_\infty t_{obs}} \tag{2.10}$$

where the observation time, $t_{obs,}$ is the inverse of the strain rate of magma deformation, $\dot{\varepsilon}_{obs}$. Thus Eqn. 2.10 can be rewritten as

$$De = \frac{\dot{\varepsilon}_{obs}\,\mu}{G_\infty} \tag{2.11}$$

Magmatic suspensions, like those described in this study, are non-Newtonian materials with a shear thinning response (Caricchi et al., 2007; Lavallée et al., 2007; Cordonnier et al., 2009; Avard and Whittington, 2012; Vona et al., 2013), hence their viscosity is strain rate dependent. It has previously been described that the peak stress, σ, shares a power law relationship with strain rate, $\dot{\varepsilon}_{exp}$, via:

$$\sigma = k\dot{\varepsilon}_{obs}{}^{b} \tag{2.12}$$

where b is the flow behaviour index and k is the flow consistency index (in Pa.s^b), describing the rheology of the fluids (Ostwald, 1925; Lavallée et al., 2007; Jahangiri et al., 2012). For Newtonian bodies b = 1, but for shear thinning suspensions, b decreases below 1 (Caricchi et al., 2007) and reaches a minimum of b = 0.5 for crystal-rich materials (Lavallée et al., 2007; Cordonnier et al., 2009). In the present study the Mt. Unzen dome material tested at 900 °C, by fitting a power law to the peak stress-strain curve we obtained Ostwald constants of k = 1653 and b = 0.5 (Fig. 2.12b). So, we can rewrite Eqn. 2.11, using Eqn. 2.12, to obtain:

$$\mathrm{De} = \frac{\left(\sigma/_{\mathrm{k}}\right)^{1/_{\mathrm{b}}}\mu}{G_\infty}, \tag{2.13}$$

which permits the representation of the Deborah number of material failure as a function of strength (which was shown to be dependent on porosity), for a given temperature (and thus interstitial melt viscosity). For our samples, the interstitial melt viscosity can be estimated at $10^{9.42}$ Pa.s (using its

chemistry and experimental temperature as an input parameter in the GRD viscosity calculator (Giordano et al., 2008)). In Figure 2.12c, we present the data using symbols that illustrate the response of the samples. The onset of transitional behaviour, termed viscous-dominated transitional, is marked by the red line. Similarly, the onset of brittle behaviour, brittle-dominated transitional, is marked by the yellow line. These lines are linear regressions on a semi-log space plot, with their standard error of estimates marked by faded colour windows. Any point that plots between the red and yellow lines would be termed transitional and could demonstrate any type of hybrid behaviour. Above a porosity of 0.27 no transitional zone occurs, and behaviour would be classified as either viscous or brittle. This analysis demonstrates that the critical Deborah number, De_c, which indicates the initiation of rupture, in dome lavas from Mt. Unzen decreases by just over half an order of magnitude over a 0.35 range in porosity; from ~ 7.65×10^{-5} in the densest sample measured to 4.1×10^{-5} in the most porous, following the trend: $De_c=-1.7\times10^{-4}\varphi+9.40\times10^{-5}$ (Fig. 2.12c). Such a magnitude is proportional to the strength decrease of material as a function of porosity (see Fig. 2.10a and Paterson and Wong, 2005 for a discussion), and thus relates the porosity to the ability of high temperature lavas to rupture. By extrapolating the trend and finding the De_c for a hypothetical, pore-free Mt. Unzen sample, we can compare our results to a two-phase (crystals and melt) model for rupture (Wadsworth et al., 2017b). Given that the Mt. Unzen material has a crystal content (microlites and phenocrysts), φ_x, of ~ 0.75, the bulk De_c can be modelled via:

$$\mathrm{De_c} = \mathrm{De_{cx}}\left(1 - \frac{\varphi_x}{\varphi_m}\right), \tag{2.14}$$

where $\mathrm{De_{cx}}$ is the critical Deborah number for a crystal and bubble free melt, 10^{-2}, and φ_m is the maximum packing fraction of the system.

For the Mt. Unzen material φ_m can be assumed to be in the range of ~0.76 - > 0.99, as it is clear from microstructural analysis that our material has not yet reached φ_m (see Fig. 2.3) [maximum packing is defined geometrically as the volume fraction at which there is no space remining for further particles (Mader et al., 2013)]. This gives a modelled De_c in the range of ~1×10^{-4} and 7.6×10^{-4} which is in line with the De_c found by the linear extrapolation of experimental results, 9.4×10^{-5} for the onset of rupture and 6.6×10^{-4} for full rupture (Fig. 2.12c).

Thus both, the addition of crystals (as seen by the fact that De_c of dense dome lavas is reduced by over one order of magnitude compared to that suggested by Dingwell and Webb, (1990)) and vesicles (as shown by the above equation) contributes to an increased brittleness of lava during ascent and eruption at lava domes, and in many other eruptive scenarios.

2.6. Implications for volcanic scenarios

The findings observed here help constrain the impact of rheological evolution on lava domes as they erupt and cool following emplacement. The rheology of magma has a fundamental influence on the style of a volcanic eruption, be it explosive or effusive (Dingwell, 1996; Gonnermann and Manga, 2007). Understanding how magmas respond to changes in petrology, stress and eruptive shearing conditions that occur during ascent in a volcanic conduit may help to enhance models that aim to

predict volcanic activity. The work undertaken here constrains the material behaviour of erupting dome lavas and the relics that remain once the lava cools.

As magma crystallises, its apparent viscosity (generally) increases as the melt evolves, and an increasing fraction of the suspension becomes solid (with slower diffusivity and lower rate of plasticity than the viscous liquid melt), thus the suspension becomes increasingly solid-like. For crystalline magmas, we would expect De_c to be lower than that for silicate liquids (*i.e.*, $De_c < 10^{-2}$; e.g. Gottsmann et al., (2009)). Cordonnier et al., (2012a, 2012b) constrained the failure of silicate liquids with different crystal fractions, and they indeed showed that De_c decreases when crystallinity increases. They suggest that De_c linearly decreases from 10^{-2} to 2×10^{-3} between 0 and 60 vol.% crystals. However, the viscosity used to estimate Maxwell's relaxation rate in the *De* analysis was based on the suspension's apparent viscosity rather than the interstitial melt viscosity. To constrain how the addition of crystals shifts the onset of failure of a material whose rheology is well known it is advantageous to consider the pure melt. Given this, an even larger decrease of De_c would be observed (perhaps down to ~ 9.4×10^{-5} as constrained by failure of our densest lavas). Since the strength of material is known to be strongly influenced by the presence of pores (commonly vesicles in volcanic materials) and micro-fractures (e.g. Paterson and Wong, 2005 for a review of material properties in the brittle field), here we demonstrate that the addition of porosity to magma shifts failure to lower strain rates; thus, under constant ascent conditions, magma may undergo failure simply by vesiculation, without the need for any increase in strain rate.

Upon extrusion, lava cools, contracts and fractures (Lamur et al., 2018). Here we show that the strength of a dome is reduced upon cooling due to contraction and micro-fracturing, leaving a weaker relic structure. This situation may favour the progressive creep of cooling dome structures, as observed in lobe 11 at Mt. Unzen (Kohashi et al., 2012).

Post-emplacement, through time and prolonged exposure to corrosive fluids, dome material may alter (Ball et al., 2015). In this study, the altered rocks tested showed a higher strength than pristine rocks with equivalent porosities. However, previous studies have found that altered volcanic rocks can also be weaker (e.g. Pola et al., 2012). From this distinction we surmise that the structure of the rocks as well as the type of alteration (developing under different conditions in cooling volcanic rocks) may have contrasting effect on the strength of cooled dome lavas. Thus, the data shown here begs for an increased focus on the impact of alteration on volcanic rock strength for improved lava dome structural stability models.

The rate of deformation imposed on dome materials is also an important variable to be considered. In this study, and in others (e.g. Schaefer et al., 2015; Lavallée et al., 2018), volcanic rocks have been shown to withstand higher stresses when deformed at higher strain rates. Previous studies have suggested earthquakes with high ground acceleration have provoked lava dome collapse (Voight, 2000), therefore, it is essential to understand the effect of strain rate on the strength of materials. This is of particular importance for Mt. Unzen as it is located in a very seismically active area. Slow, continuous strain (or recurring stressing cycles) can induce fatigue in a material and promote brittle creep (e.g. Heap and Faulkner, 2008; Heap et al., 2009; Brantut et al., 2013; Kendrick et al., 2013a;

Schaefer et al., 2015) thus weakening the rocks which undergo failure at lower stresses. Thus, over long periods (years) of deformation, such as for lobe 11 at Mt. Unzen, the actual strength of the dome rocks may be lower than those reported here at the lowest strain rate of 10^{-5} s^{-1}). Time-dependent deformation can importantly contribute to catastrophic collapse of volcanic structures (e.g. Mt. St. Helens, Reid et al. 2010). Here we advance that it is crucial for future failure models of volcanic materials to incorporate the effect of strain rate.

Volcanic structures are made of heterogeneous rocks and lavas, with intricate mineralogical assemblages, textures and fabrics, with variable degrees of coherence; thus, their mechanical response may vary widely. Although here we have only tested material from the 1991-1995 eruption of Mt. Unzen, this study has the potential to be applied to other dome-forming volcanoes of similar composition, crystallinity, and porosity. Additionally, the work can also be applied to parts of larger volcanic edifices dominantly constructed by the accumulation of lavas, which may be prone to collapse (Ball et al., 2015). The work presented here can help constrain the behaviour of lavas and rocks involved in lava dome eruptions. We anticipate that the results will form the basis for more advanced numerical simulations of dome eruption and related hazards.

2.7. Conclusion

Uniaxial experiments carried out at ambient and high temperature (900 °C) on a suite of natural lavas from Mt. Unzen have given significant insight into the behaviour of lava domes, both during extrusion and after emplacement. Ambient temperature experiments allowed for the investigation of brittle behaviour, and results from these experiments can be applied to cooling domes (and the relics that they leave in the record) allowing the development of volcanic edifice failure models. Conclusions drawn from experimentation are as follows:

1. In the brittle regime, strength decreases with increasing pore volume both at ambient and high temperatures;
2. Magmas deformed in the brittle regime at high temperature are stronger than rocks of equivalent porosity deformed at ambient temperature;
3. Thermal stressing did not affect the strength of dome rocks within the conditions tested (< 900 ˚C and 4 ˚C min^{-1}), it did however change the morphology of the stress strain curve, indicating the widening of cracks;
4. The presence of alteration may have variable effects, sometimes strengthening volcanic rocks via pore filling;
5. The strength of rocks and lavas (in the brittle field at high temperature) increases with strain rate;
6. The viscosity of dome lavas decreased with strain rate (shear thinning) and did not vary for the range of material crystallinity and porosity studied;
7. Lavas deformed at high temperature and strain rates of > 10^{-4} s^{-1} becomes increasingly brittle, and adopt fully brittle response above 10^{-3} s^{-1}; and
8. The critical Deborah number, De_c of dense dome lavas was found to be ca. 1×10^{-4}. It decreases with porosity according to a linear relationship.

These results reveal that current stability models of cooling lava domes, like that of lobe 11 at Mt. Unzen, require an integration of the complex nature of the materials. The outcome of this study suggests that, as a primary control on rock strength, porosity heterogeneities must be included when modelling failure mechanisms. As secondary controls, it would also be beneficial to include deformation conditions such as temperature and strain rate. Conclusions drawn from high temperature experiments suggest that current three-phase models may not be fully applicable to dome lavas and other crystal-rich lavas. We suggest a new formulation of the Deborah number that applies to porous, crystal-rich lavas and propose that it may help refine the accuracy of models attempting to describe rheological evolution to explain geophysical data monitored during lava dome eruptions.

2.8. Data availability

Supplementary data are available in the Supplement Figs. 2.S1 to 2.S6. The script for the Young's mod- ulus calculation is freely available on GitHub (Coats, 2018). The AST14DEM used in Fig. 1 was retrieved from the online data pool, courtesy of Land Pro- cesses Distributed Active Archive Center (LP DAAC) and the NASA the Japan Ministry of Economy, Trade and Industry (METI), (https://lpdaac.usgs.gov/dataset_discovery/aster/aster_products_table/ast14dem_v003#tools last access: 29 October 2018).

2.9. Supplementary Figures

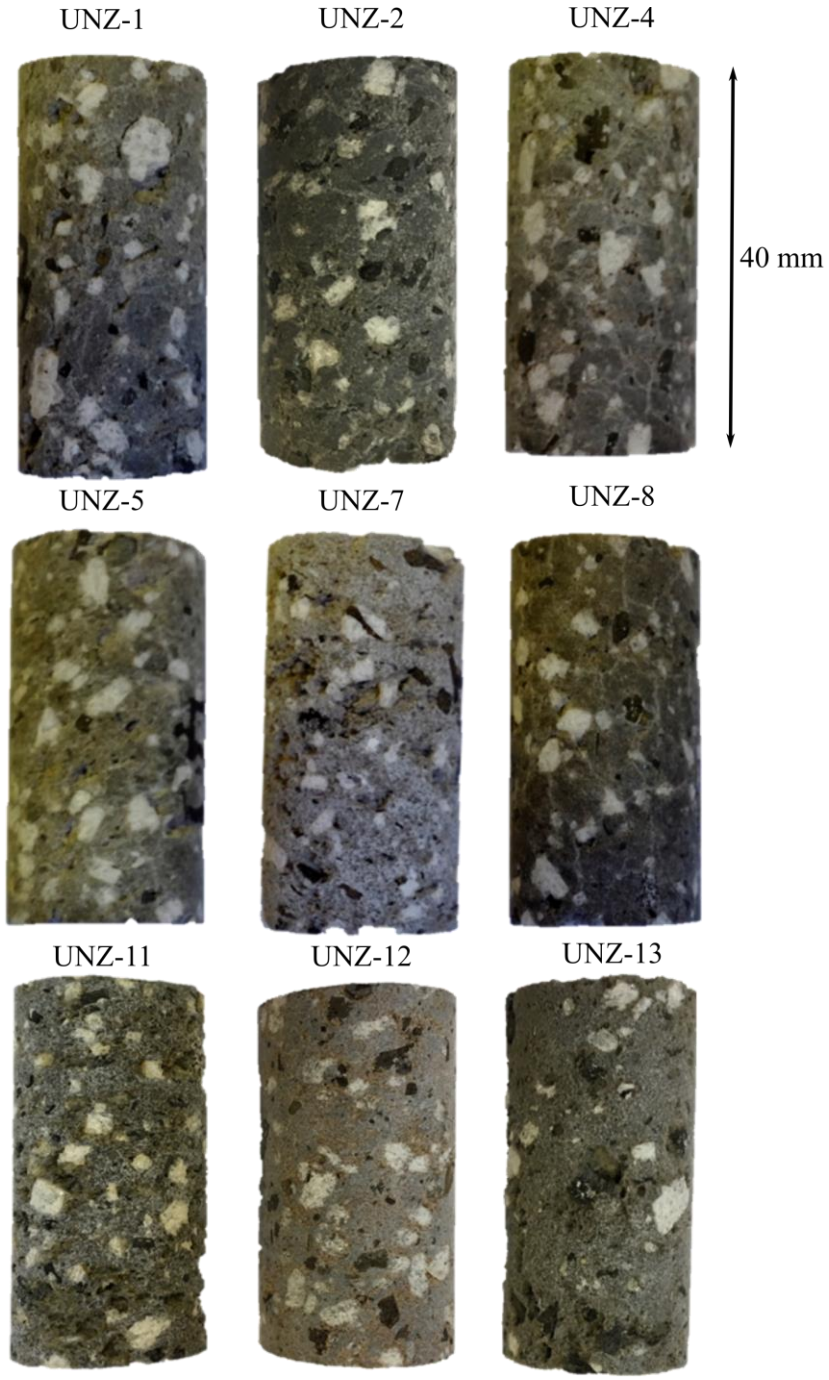

Figure 2.S.1. Images of cores used in the uniaxial compressive stress experiments. The principal stress, σ_1, was applied in the vertical direction. In all cores large phenocrysts of plagioclase and amphibole are recognisable, as well as a network of large pores and cracks. Signs of alteration are visible in certain cores, in UNZ-11 there is a crusty white/yellowish layer around pores and overall it has a friable texture, and in UNZ-12 a reddish hue is visible.

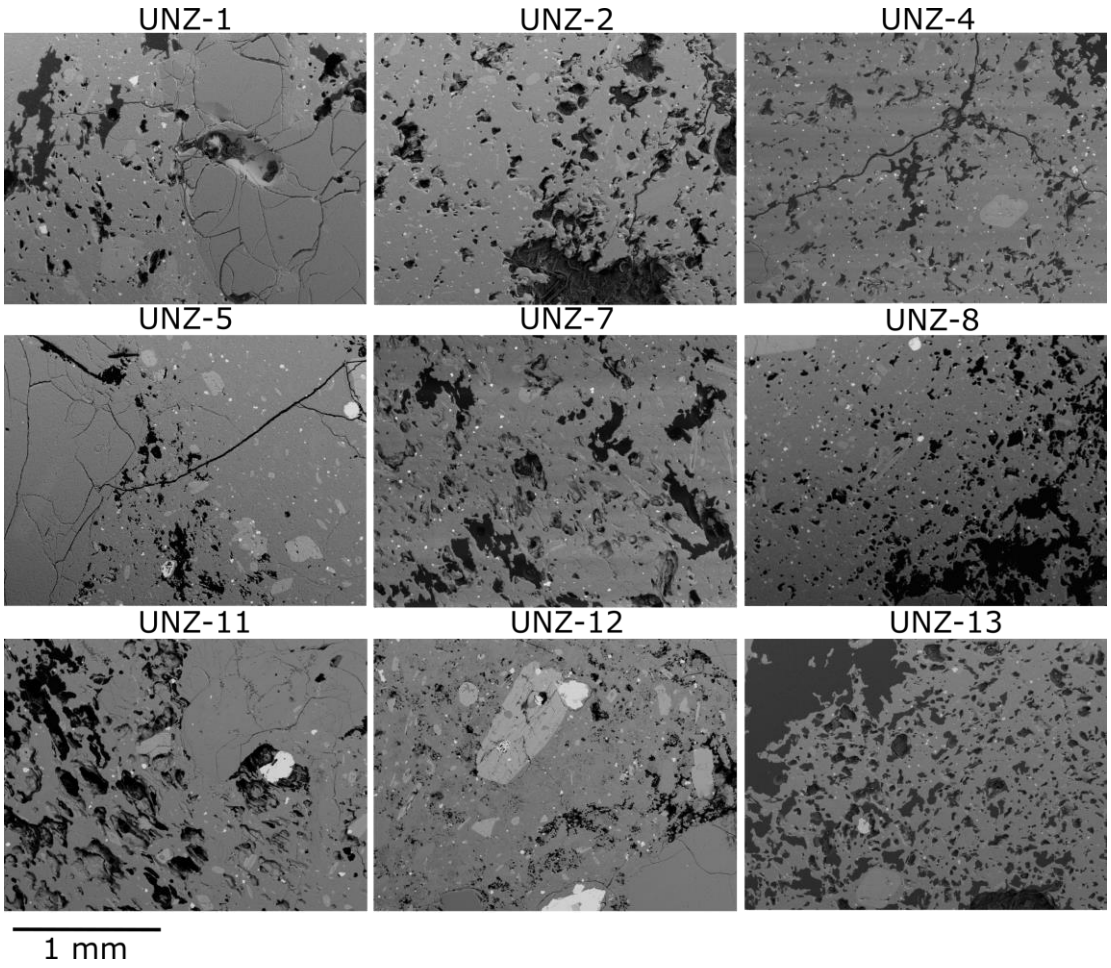

Figure 2.S.2. Backscattered electron images of all samples used in this study. These images were taken from polished stubs and are orientated so that the later applied principal stress, σ_1, was directed into the page.

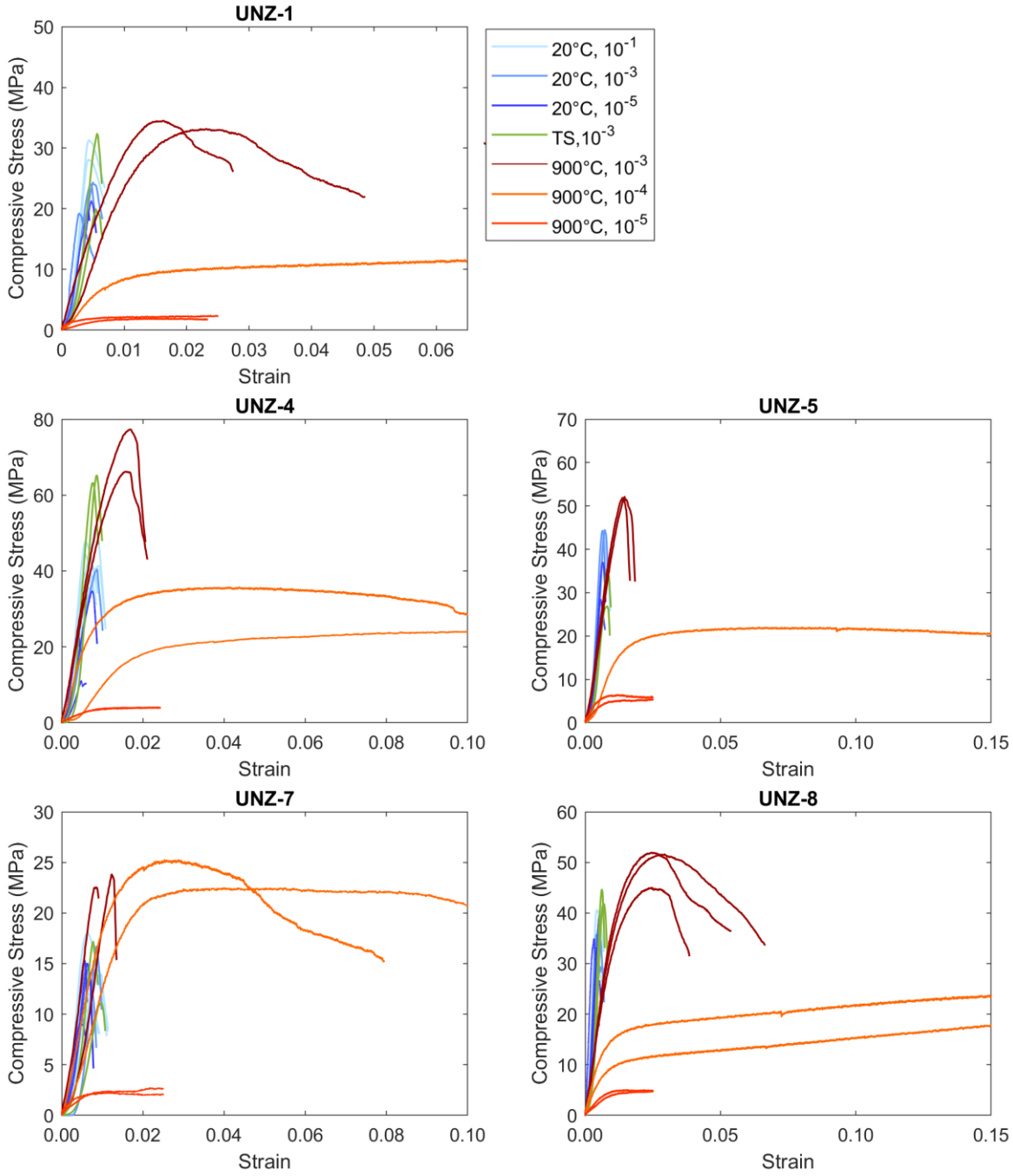

Figure 2.S.3. Stress-strain curves for uniaxial compressive strength tests conducted on thermally stressed and pristine samples at strain rates of 10^{-1}, 10^{-3} 10^{-5} s^{-1} at ambient temperatures, and on pristine samples at strain rates of 10^{-3}, 10^{-4}, 10^{-5} s^{-1} at temperatures of 900°C. The plots are separated into block number, and therefore porosity (see Table 3). These graphs show how strength is higher at both higher porosities and at higher temperatures. Thermally treated samples do not appear to vary in strength compared to their untreated equivalents, but do show a more concave-up initial portion of the curve. Experiments carried out at higher temperature and slower strain rates, 10^{-4} and 10^{-5} s^{-1}, deform viscously in response to applied stress.

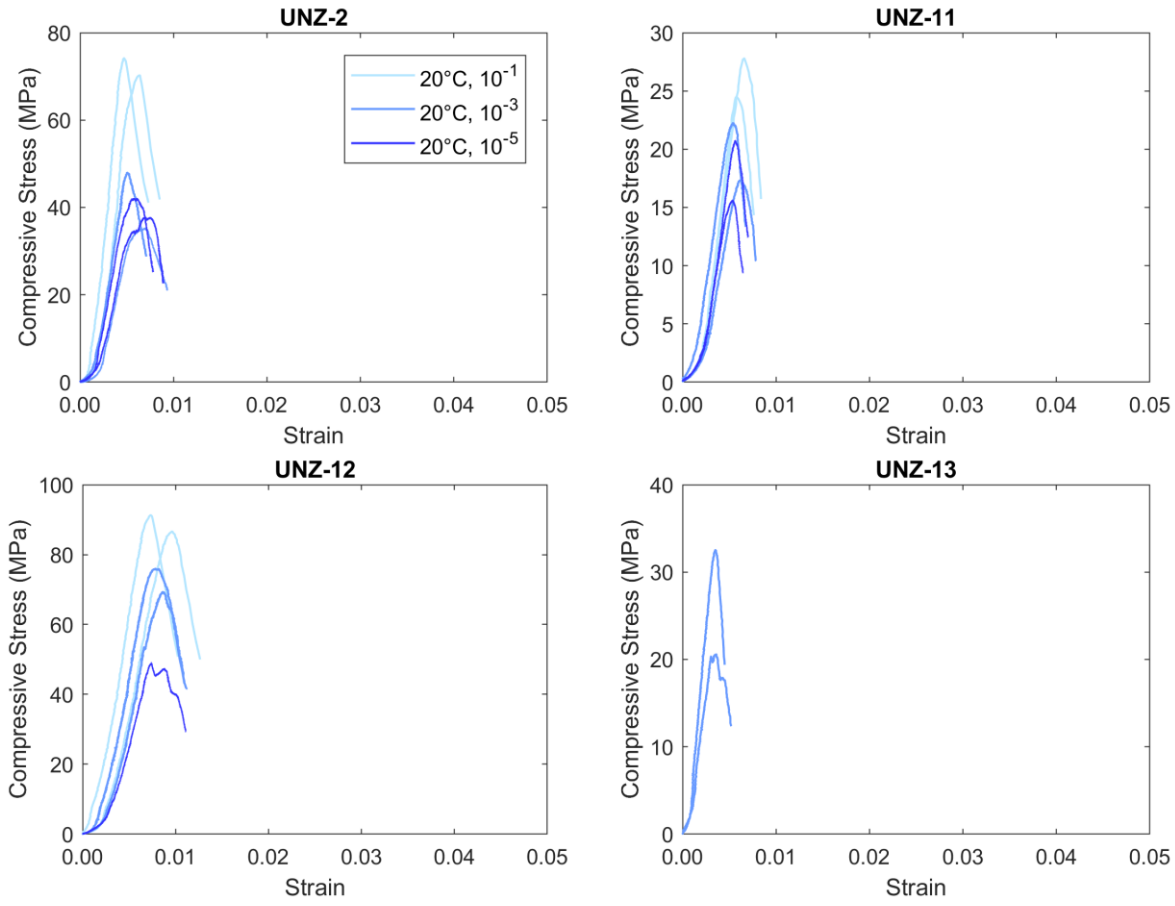

Figure 2.S.4. Stress-strain curves for rocks deformed at strain rates of 10^{-1},10^{-3} and 10^{-5} s^{-1} at ambient temperatures only. Here the curves demonstrate that samples deformed at higher strain rates achieve higher peak stresses across the range of porosities tested.

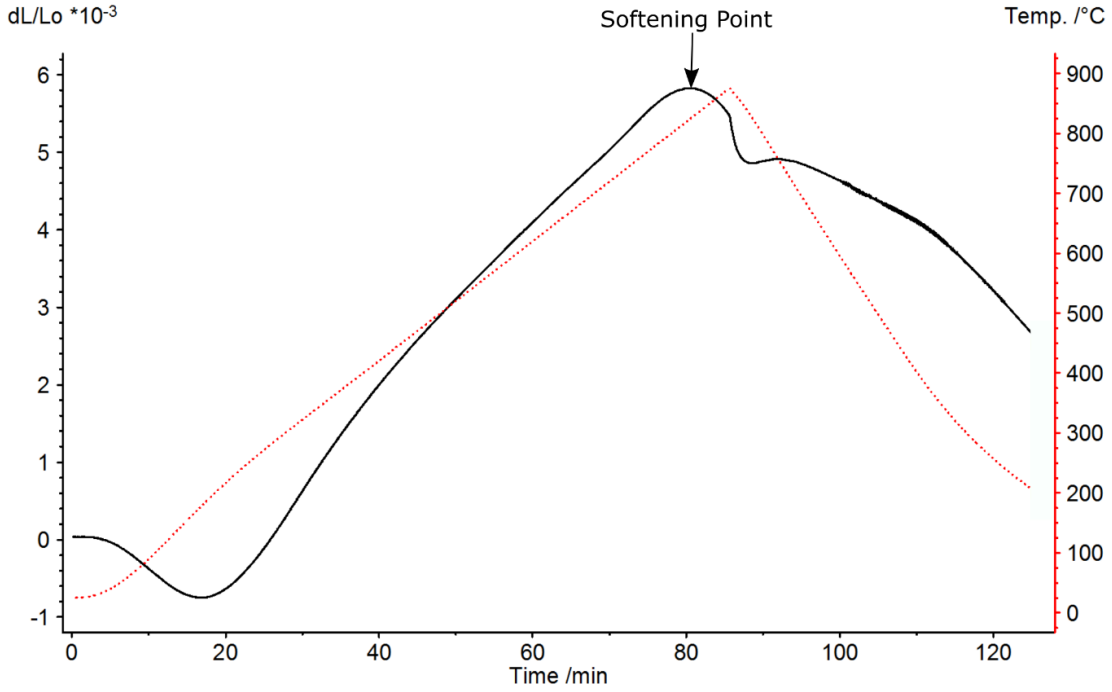

Figure 2.S.5. Thermal analysis result showing the softening point of sample UNZ-8. The sample was heated at 10°C/min to 1100 °C whilst applying a constant load of 2N. The softening point was detected as 824.6 °C, 80.6 minutes into the experiment, when the applied load counteracted the thermal expansion of the sample, causing an inflection point (i.e. switch to contraction).

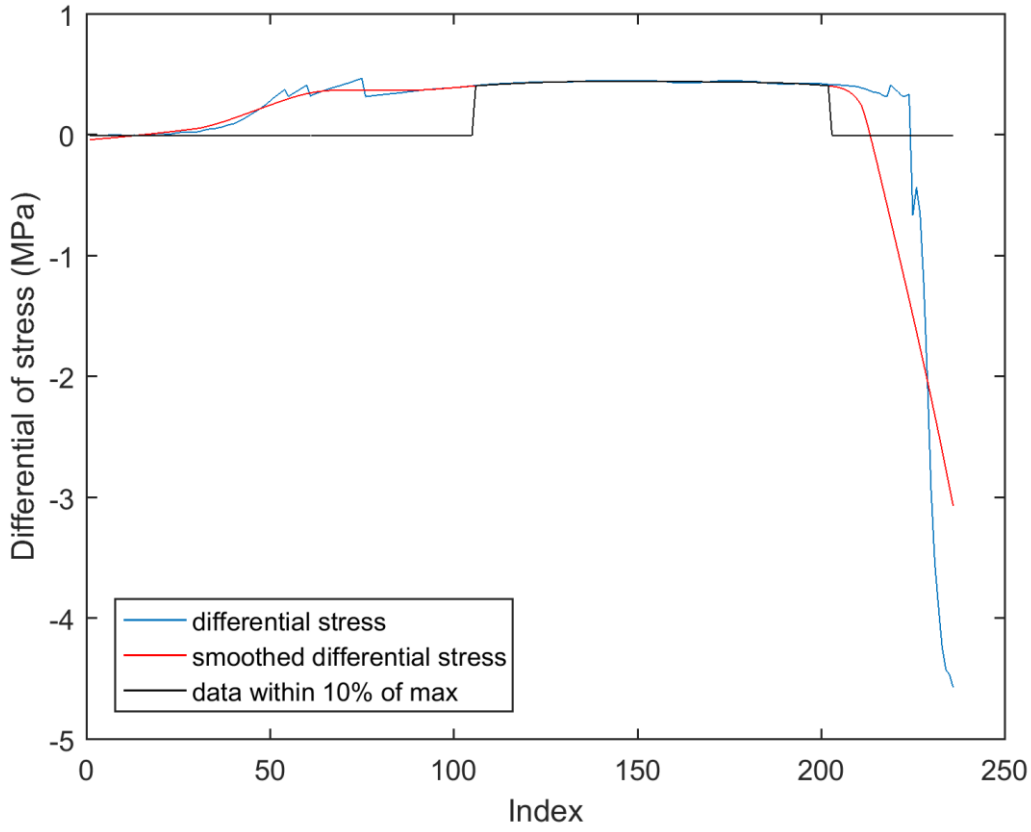

Figure 2.S.6. Example plot (from sample UNZ-2-2) produced by the script run to find the Young's Modulus of a sample. The code looks at the gradient of the stress-strain curve and finds at which strains (the index number of the vector, x-axis) the increase in stress (y-axis) is at a maximum. The blue line shows the calculated differential of the stress, the red line is the differential stress smoothed, and the black line shows the points at which the stress is within 10 % of its maximum. The Young's modulus is then calculated with the resulting values of stress and strain from the black selector line, the maximum slope of the stress-strain curve.

Over the careful few

engaged in their crow watching

over the council bricked and mortared lines,

-Untitled | Republic of Verse

Chapter 3: Developing a method to synthesise dense crystal-bearing magma: Sintering under load

3.1. Rationale

Chapters one and two have provided an insight into the physical, chemical and mechanical behaviour of complex natural volcanic materials. Magmas are polydisperse, multiphase systems that generally respond to deformation in a non-Newtonian manner (see Gonnermann, 2015, and references therein). Their heterogeneous nature has meant that current models of magma rheology are not yet advanced enough to fully describe their behaviour, particularly their transition from non-Newtonian viscous flow to brittle failure. To overcome the caveats of heterogeneity, efforts must be focused on understanding the fundamental responses of systems that can be controlled, before moving to more complex materials. The rheological properties of single phase silicate melts (both synthetic and natural) are generally well studied in both the liquid and glassy fields (Dingwell and Webb, 1990; Webb and Dingwell, 1990b). These melts respond as Newtonian fluids, where viscosity is constant with strain rate. However, it is well documented that volcanic materials have a non-Newtonian response to strain, where viscosity varies with strain rate. Therefore, by doping a synthetic silicate melt with variable quantities of complexities (e.g. particles or pores), departure from Newtonian behaviour can be experimentally investigated under controlled conditions to provide a complete non-Newtonian description of multi-phase systems. This framework has been adopted by many rheologists to date (e.g. Lejeune and Richet, 1995; Lejeune et al., 1999; Caricchi et al., 2007; Cordonnier et al., 2012a; Moitra and Gonnermann, 2015), and efforts have been used to improve modelling techniques (e.g. Costa, 2005; Caricchi et al., 2007; Costa et al., 2009; Moitra and Gonnermann, 2015). In this chapter we explore the processes and resulting challenges involved in synthesising two-phase (crystals and melt) magmas, by sintering viscous droplets under controlled load, to form the synthetic suspensions used for experimentation in Chapters 4 and 5.

3.2. Materials

3.2.1. Requirements

With the aim of creating two-phase samples that emulate dense, crystal-bearing magmas, component materials and synthesis conditions were selected judiciously, ensuring the final samples met specific criteria for pore volume and distribution, crystallinity, crystal size and distribution. Importantly for the subsequent studies investigating the effects of crystals on the rheology of dense suspensions, the initial two-phase suspension had to be sintered to a near-zero final gas volume fraction (i.e. pore volume). Additionally, for the synthetic suspension to respond to deformation as a crystal-bearing magma would, the crystalline phase chosen has similar shape and grain size distribution to that of crystals in natural magmas. Moreover, as uniaxial testing is only effective for investigating the rheology of suspensions with viscosities of ~ 10^8 to 10^{12} Pa.s (Hess et al., 2007), the synthetic suspension had to respond with such viscosities at achievable experimental temperatures.

Finally, the density contrast between the glass and crystalline phase must be distinct enough to enable the segmentation of the phases from X-ray computed tomography (XCT) scans of the synthetic suspensions; a requirement for *in-situ* testing at the synchrotron (see Chapter 5). To source materials that met these requirements, initial testing was conducted on plagioclase, rutile and olivine to find the particle size, polydispersity, density, aspect ratio and maximum packing fraction.

3.2.2. Analysis

Testing was carried out on each material (glass and crystals) to assess their characteristics and ensure they met the outlined requirements. Using a Beckman Coulter™ LS 13 320 laser diffraction particle size analyser with a measuring range of 0.375-2000 µm, particle statistics were reported via GRADISTAT (Blott and Pye, 2001). The distribution of particle size was measured for each material (Table 3.1) and polydispersity of the system calculated following the procedures outlined by Torquato (2002) and Wadsworth et al., (2017a), via:

$$\gamma = \frac{\langle R_i \rangle \langle R_i^2 \rangle}{\langle R_i^3 \rangle}, \tag{3.1}$$

where $\langle R_i^n \rangle$ is the nth moment of the distribution of the mean initial particle radius.

Further analysis found the density, ρ, of each material via $\rho = m/V$, where the volume, V, of a known mass, m, of each material was measured in an AccuPyc 1340 helium pycnometer from Micromeritics.

To assess the aspect ratio of the crystalline phase, a representative sample (~ 5-10 g) of each crystal type was set in epoxy, cut and polished to produce thin sections for textural analysis. Images were taken of each thin section using a DM2500P Lecia microscope in plane-polarised light (PPL). Image analysis was carried out in ImageJ, a software package developed by the National Institute for Health (https://imagej.nih.gov/ij/). Using the line selection tool, a straight line was drawn on each crystal's axis of rotation l_a (taken as the longest axis), and the crystal's maximum diameter, l_b, found perpendicular to l_a. The length of the line was then quantified via the measurement tool (in px) and the aspect ratio calculated as $r_p = \frac{l_a}{l_b}$. For the Spheriglass® beads r_p was defined as 1 i.e. a spherical particle.

Maximum packing values were then calculated according to Mueller at al. (2011b), via:

$$\varphi_m = \varphi_{m1} exp\left[-\frac{(log_{10} r_p)^2}{2b^2}\right], \tag{3.2}$$

where φ_{m1} is the maximum packing fraction for spherical particles and b is a fitting parameter. Klein et al., (2018) re-parameterised Eq. 3.9 and by testing additional samples, found more robust fitting parameters than those reported in Mader et al., (2013) of φ_{m1} = 0.637 and b = 1.171.

Table 3.1. Material properties of the components used to create synthetic samples. Image (a) is modified from Wadsworth et al. (2014) while image (b), (c) and (d) are plane polarised light (PPL) images. Mohs scale hardness values were taken from Samsonov (1968). Particle size, density, aspect ratio and polydispersity were measured for each material as detailed in section 3.3. The maximum packing of each material was calculated using the method developed by Mueller et al. (2011b) with fitting parameters taken from Klein et al. (2018).

Material	Spheriglass®	Plagioclase (albite)	Rutile	Olivine (Fayalite)
Image	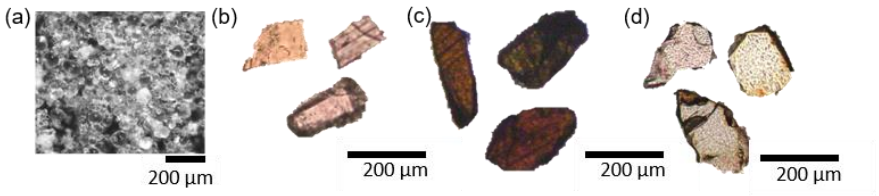			
Mohs scale hardness	5.5	6-6.5	6-6.5	7
Particle Size (µm)	150-250	53-180	53-180	53-180
Density (g cm^{-3})	2.50	2.66	4.29	3.29
Aspect Ratio	1.00	1.95	1.95	1.61
Polydispersity	0.91	0.83	0.89	0.59
Maximum Packing	0.64	0.66	0.66	0.63

3.2.3. Spheriglass®: the amorphous melt phase

Due to their rheological similarity to volcanic glasses, synthetic glasses are commonly used in studies which aim to understand the rheology of volcanic products (e.g. Lejeune et al., 1999; Hess et al., 2008; Cordonnier et al., 2012b, 2012a; Vasseur et al., 2013, 2015; Wadsworth et al., 2014, 2016, 2017a, 2018). The sintering dynamics of soda-lime silica glass beads (A-glass Spheriglass® microspheres from Potters Industries LLC) have been thoroughly investigated in recent years (Vasseur et al., 2013; Wadsworth et al., 2014, 2016, 2017a). For that reason, Spheriglass® spheres were selected as the amorphous melt phase for sample synthesis. After initial particle size analysis, the spheres were deemed monodisperse, $\gamma \sim 1$, (Table 1; Fig. 3.1a). Given the requirement for the resulting samples to be two-phase by having a negligible porosity, the sintering of the component materials had to be effective. As sintering is more rapid in polydisperse systems (Wadsworth et al., 2017a), the Spheriglass® microspheres used for the melt phase were crushed in an agate ball mill for 40 minutes, achieving a polydispersity of $\gamma = 0.54$ (Fig. 3.1b). For the final two-phase mixtures for synthesis of samples, ratios of crushed and uncrushed glass were then selected based on crystal volume fractions to move from a monodisperse system (Fig. 3.1c) to a polydisperse system (Fig. 3.1d).

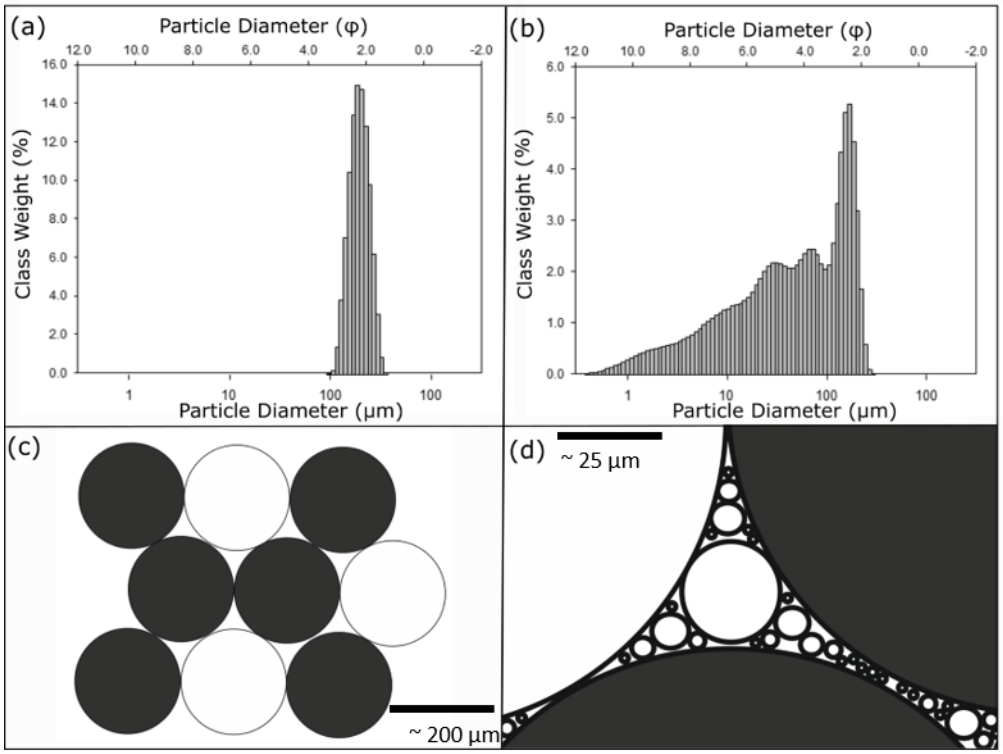

Figure 3.1. Particle size distributions for (a) whole and (b) crushed Spheriglass® beads. Example of (c) an idealised monodisperse crystal-glass system with whole glass beads in white and crystals in black and (d) a polydisperse crystal-glass system with whole and crushed glass beads in white with crystals in black.

3.2.4. The crystalline phase

For the crystalline phase, a particle size range of 53-180 μm was deemed appropriate for the test samples used in the experimental studies in Chapters 4 and 5. The lower bound was selected so that the smallest particles could still be resolved in X-ray images, and the upper bound was selected so that with cylindrical sample sizes of 3 mm by 6 mm, required for synchrotron-based X-ray computed micro-tomography (sXCT), the crystals did not exceed 10 % of the sample dimensions, a requirement for uniaxial compressive testing (Paterson and Wong, 2005). As mentioned above, the crystalline phase was required to have a contrasting density to the Spheriglass® beads for synthetic samples used for tomographic imaging, while also sharing geometrical properties with natural magmatic crystals.

As it is an abundant phenocryst in volcanic rocks, plagioclase (ρ = 2.6-2.76 g cm^{-3}; Hudson Institute of Minerology, 2018) was initially selected for sample synthesis. A natural albite crystal specimen (ρ = 2.66 g cm^{-3}, measured by pycnometry) was crushed in an agate ball mill on a 40-minute cycle before being sieved to the desired particle size range. The resulting crystals were then tested to see if they achieved the requirements. Although the plagioclase crystals are the most appropriate choice to produce a sample that would behave similarly to volcanic materials, an initial X-ray computed micro-tomography (XCT) scan performed at the University of Manchester X-ray Facility at Harwell proved the density contrast was not sufficient. Samples were fixed to a rotation stage and images were captured using a Nikon XCT 225ST operating at 120 kV and 90 mA. 3200 projections were collected for each scan over a 360 rotation. Data were reconstructed using the Nikon proprietary filtered back-

projection algorithms with a 7 μm voxel size. 3D visualisation and analysis of reconstructed images was performed in Avizo™ software (https://www.fei.com/software/amira-avizo/). Data revealed that the density contrast between crystals and the glass was insufficient to enable accurate phase segmentation in XCT images (Fig. 3.2a) and they were not selected as the crystal phase for samples used in Chapters 4 or 5.

Rutile (ρ = *4.29* g cm^{-3}, measured by pycnometry) was selected as a denser alternative to plagioclase. Although not abundant in volcanic rocks, it does harbour similar physical properties to primary minerals, e.g. it has a similar hardness to plagioclase (Table 1). Sourced rutile crystals were sieved to the desired range before being analysed. The rutile crystals that were used have a similar aspect ratio, polydispersity and therefore maximum packing to that of the plagioclase (Table 1). Given the similarity of these properties, rutile is anticipated to behave rheologically similarly to plagioclase in suspension (e.g. Klein et al., 2018). The strong density contrast between the glass and rutile grains led to highly contrasting greyscale values in tomographic reconstructions (Fig. 3.2b), making the crystal ideal for synchrotron X-ray computed tomography imaging. Therefore, these samples were used for synchrotron imaging (Chapter 5). However, the rutile crystals were problematic to source in bulk for the particle size range required for mass sample preparation, and so it was therefore essential to source a third crystal to produce synthetic two-phase samples for the extensive rheological testing in Chapter 4.

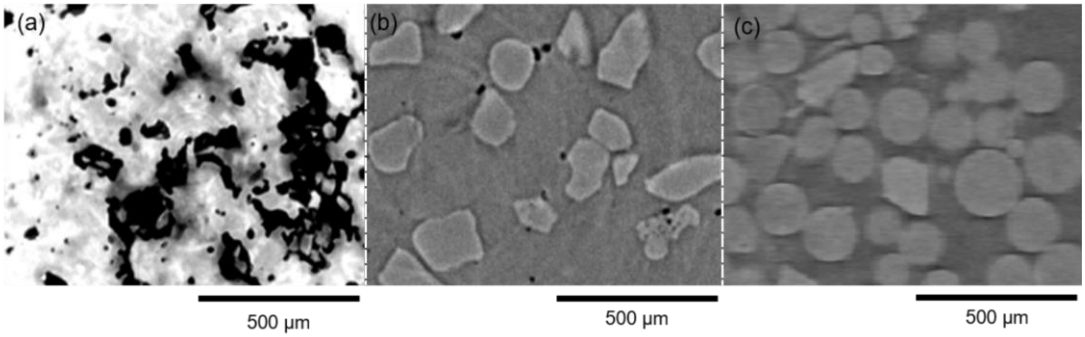

Figure 3.2. 2D slices from X-ray computed micro-tomography (XCT) data of crystals and Spheriglass® after sintering to form synthetic samples. Image (a) shows a sintered plagioclase-bearing sample, where black=pore space, very bright=plagioclase, bright=glass. Here glass and plagioclase crystals are almost indistinguishable. Image (b) shows a well sintered, rutile-bearing sample, where black=pore space, light grey=rutile, dark grey=glass. Here it is easy to distinguish between crystals and glass. Image (c) shows a poorly sintered (unconsolidated) olivine-bearing sample (image courtesy of Kate Dobson) where dark grey=pore space, grey circles=Spheriglass® beads and angular shapes=olivine, here glass and olivine are hard to distinguish between. These initial scans demonstrate that the higher the density contrast, the higher the greyscale contrast.

Olivine is a relatively dense (ρ = 3.21-4.39 g cm^{-3}) mineral which is abundant in mafic volcanic rocks (Hudson, 2018). Therefore, fayalite (the iron rich end member of olivine) crystals (ρ = *3.29* g cm^{-3}; measured by pycnometry) were sourced in bulk and were sieved to the particle size range required before being analysed (Table 3.1). The crystal size, polydispersity and thus maximum packing of the crystals were comparable to the plagioclase and rutile, leading to the assumption that the rheological

response of the suspensions created with them would be similar. However, when compared to rutile, the contrasting greyscale values between the Spheriglass® and olivine crystal was poor in tomographic reconstructions (Fig. 3.2c). As such, olivine was chosen for the synthesis of suspensions studied during *ex situ* testing (Chapter 4) as the samples could be made in bulk. Plagioclase was only used in the development of the sample synthesis methodology as it was initially unknown that the density contrast with the Spheriglass® would lead to poor grey-scale contrast during XCT, and yet the synthesis data remain relevant and robust.

3.3. Sintering

3.3.1. Background

Sintering, or volcanic welding, occurs by a combination of chemical diffusion and viscous flow on particles or melt droplets. The dimensionless ratio between the gravitational forces and surface tension forces acting upon a droplet is known as the Eötvös number,

$$Eo = \frac{\rho g R^2}{\Gamma}. \quad (3.3)$$

which can be used to describe the droplet's shape. Similarly, the Ohnesorge number is a force-balancing dimensionless number that describes the droplet's behaviour,

$$Oh = \frac{\mu}{\sqrt{\rho \Gamma R}}. \quad (3.4)$$

It is the ratio of the viscous forces over the inertial and surface tension forces and describes a droplet's tendency to stay in a droplet form, or separate. Here ρ is the density of the viscous droplet (kg m^{-3}), g is the gravitational acceleration (m s^{-2}), R is the radius of the droplet (m), Γ is the interfacial tension between droplets, acting at the free surface between air and melt (N m^{-1}), and μ is the viscosity of the droplet (Pa s). When a system can be described by a low Eötvös number and a large Ohnesorge number, gravitational and inertial effects are negligible and surface tension is the dominant driving force. In this regime, where $Eo \ll 1$ and $Oh \gg 1$, sintering occurs with the viscous relaxation of surface tension between droplets. Droplets are linked via necking to form a lattice of subspherical particles. This framework of necked droplets is unstable and, to minimise air-melt surface area, further collapse occurs under surface tension. Collapsing ultimately leaves behind only isolated pores, suspended in the viscous liquid, which define the final gas volume fraction. Densification can be described by the shrinkage of the porous network volume between the liquid droplets until the final porosity or gas volume fraction (Wadsworth et al., 2016). Recent modelling attempts based on both theoretical and experimental efforts (e.g. Prado et al., 2001, 2003a, 2003b; Quane and Russell, 2005; Vasseur et al., 2013; Wadsworth et al., 2014, 2016, 2017a) have been made to describe the sintering process, building upon the original theoretical works of the neck formation model (Frenkel, 1945) and the vented bubble model (Mackenzie and Shuttleworth, 1949). Wadsworth et al., (2014) show that the vented bubble model can be simplified to an analytical solution with time dependence,

$$\varphi_f = \varphi_i exp(-\frac{3}{2}\bar{t}_b), \quad (3.5)$$

where φ_f is the final porosity, φ_i is the initial porosity and $\bar{t}_b^*$ is the dimensionless bubble relaxation time. For cases where sintering occurs under isothermal conditions,

$$\bar{t}_b = \frac{\Gamma}{\mu}\int_0^t \frac{1}{a(t)}dt, \tag{3.6}$$

where $a(t)$ is the size of the pores in the lattice at time *t*. An implicit approximation can be made that the variation in *a* with *t* is negligible and for the monodispersed case $a(t) = a_i = R$, meaning

$$\varphi_f = \varphi_i \, exp\left(-\frac{3\Gamma t}{2\mu R}\right). \tag{3.7}$$

This exponential solution has been shown to be a good approximation to the full, time-dependent sintering model (Wadsworth et al., 2016), and has previously been used to successfully model experimental data due to its tractability (Gardner et al., 2018). A further complexity to the sintering system is in the case where sintering droplets are polydisperse. In the polydisperse case, $a_i < R$ and therefore Equation 3.6 cannot be simplified to Equation 3.7. As polydispersity causes a reduction in pore volume, it has an overall effect to decrease the sintering timescale (Wadsworth et al., 2017a).

The sintering process becomes more complex when crystals are introduced into the system. Crystals act as rigid bodies in the coalescing lattice, resulting in a retardation of the sintering process. Wadsworth (2016) suggested that there are two end member scenarios to consider when incorporating crystals into a melt phase. In the case where the radius of the crystals, R_x, is very much smaller than the radius of the sintering droplets, $R_x \ll R$, one can assume that the crystalline particles are suspended in the melt and the viscosity in the exponential solution can be replaced for that of a suspension (Klein et al., 2018). The effects of adding crystals would increase the viscosity term and lengthen the sintering timescale. In the other case, where $R_x \gg R$, the crystals act as barriers to coalescing droplets, restricting the sintering process and resulting in higher final gas volume fractions.

The models discussed thus far describe the evolution of sintering based on the assumption that the system is in a pressure equilibrium, where the isolated pore pressure of the interstitial fluid is equal to that of the pressure imposed by surface tension. However, pressure imposed via surface tension may not always be the dominant driving force, e.g. in a system with a high Eötvös number, or that under hydraulic pressure. The role of both internal and external forces is discussed theoretically by Wadsworth (2016) who suggests that where an external force is applied, the final porosity is reduced by a factor of the applied force over the Laplace force, La. The Laplace force acts to reduce the surface area of the droplet and is related to the Ohnesorge number via $La = \left(\frac{1}{Oh}\right)^2$. When this factor is much greater than unity, sintering is more rapid than in the case where surface tension is the dominant driving force.

The rheology and reduction in porosity during volcanic welding under load has been thoroughly investigated in synthetic and natural materials (e.g. Quane and Russell, 2005; Russell and Quane, 2005; Quane et al., 2009; Heap et al., 2014a, 2015b; Kolzenburg and Russell, 2014) though no systematic exploration of the effect of crystallinity on the timeframe of porosity evolution has been

made. By rearranging the rheological model of Russell and Quane (2005) we can achieve an estimation of the final porosity during sintering with the application of an applied stress, σ (Pa).

$$\varphi_f = \frac{ln\left[\frac{\alpha\sigma t}{\mu(1-\varphi_i)} + e^{\left(\frac{-\alpha\varphi_i}{1-\varphi_i}\right)}\right]}{ln\left[\frac{\alpha\sigma t}{\mu(1-\varphi_i)} + e^{\left(\frac{-\alpha\varphi_i}{1-\varphi_i}\right)}\right] + \alpha}. \quad (3.8)$$

Here α is a dimensionless, empirical constant that accounts for the dependence of the viscosity term on porosity, it is set as 2 from experiments by Heap et al., (2014a). Unlike the exponential solution in Equation 3.7, Equation 3.8 incorporates an applied stress, which, in most scenarios, cannot be neglected.

To obtain a controlled, synthetic product formed solely of two-phases (crystals and melt), Spheriglass® beads were to be sintered with a selected volume fraction of crystals. By modelling the process, we can gain an insight into the timescales required for achieving zero porosity.

3.3.2. Modelling the sintering process

Here, as the Spheriglass® beads used for sintering have a small radius, $R \leq 250$ μm, gravitational effects are negligible and surface tension is the dominant driving force. The system can thus be described by a low Eötvös number and a large Ohnesorge number and Eqn. 3.7 can be used to describe the sintering process. Wadsworth (2016) suggests that in the case where $R_x \ll R$ then the crystals can be considered as in suspension and the sintering process can modelled using Eq. 3.7 by adjusting the viscosity term, μ, to account for crystallinity. For the materials chosen, the glass particle size is greater than the size of the crystals used but cannot be said to be "much greater than" (Table 1). Nevertheless, an attempt was made to model the sintering process as a suspension via this approach.

Table 3.2. Composition of Spheriglass® 1922 A-glass beads (Potters Industries LLC)

Oxide	Spheriglass® 1922 A-glass
SiO_2	72.50
Na_2O	13.70
CaO	9.80
MgO	3.30
Al_2O_3	0.40
Fe_2O_3	0.20
K_2O	0.10
Total	100.00

The viscosity of the melt phase was calculated via the multicomponent model of Fluegel (2007). Inputting the chemistry of the Spheriglass® beads (Table 2), the model produced constants A = -2.4928, B = 4130.4, and T_0 = 262, and the viscosity was calculated as a function of temperature (T, in °C) via:

$$\mu = A + \frac{B}{(T-T_0)}. \quad (3.9)$$

Relative viscosities, η_r, of suspensions at near static conditions (i.e., neglecting strain rate effects) were then calculated for each crystal fraction, φ_x, using the method reported by Klein (2018). The method takes account the maximum packing, φ_m, and polydispersity, γ, of the selected crystal phase and uses an empirically derived constant, a = 0.173 (Fig. 3.3)

$$\eta_r = (1 - \varphi_x[1 - (1 - \varphi_m)\gamma^a]^{-1})^{-2}. \quad (3.10)$$

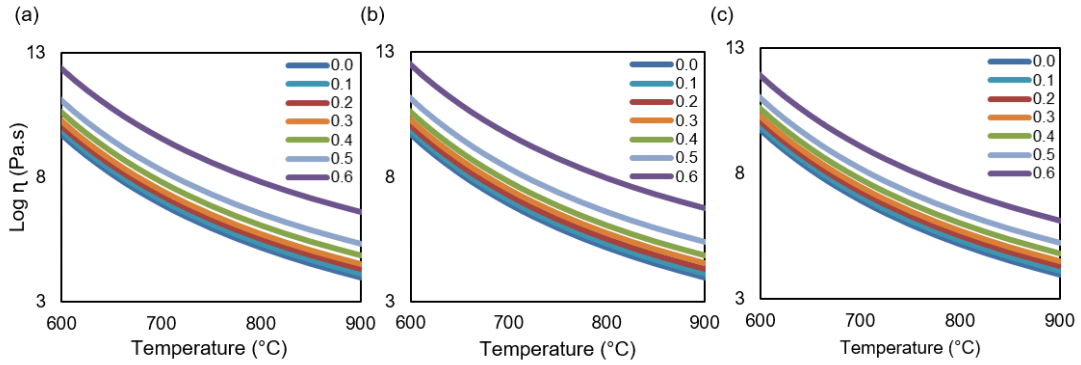

Figure 3.3. The logarithm of apparent viscosity with temperature for (a) plagioclase, (b) rutile and (c) olivine samples with properties as described in Table 3.1, and varying crystal fraction from 0 to 0.6 (legend). Apparent viscosities were found by combining the melt viscosity, calculated via the multicomponent model of Fluegel (2007), and the relative viscosity of crystal bearing suspensions, calculated for each crystal phase via Equation 3.9 and 3.10.

Sintering timescales for complete sample densification were estimated by using an apparent viscosity term (to consider the impacts of crystals on the suspension rheology), $\eta_a = \mu\eta_r$, in place of, μ, in Eq. 3.7. Results show that for sintering temperatures of 850 °C the sample should reach full densification in under 10 hours (Fig. 3.4 a-c). Decreasing the sintering temperature by 100 °C to 750 °C has an effect to increase sintering timescales to over 100 hours (Fig. 3.4 d-f).

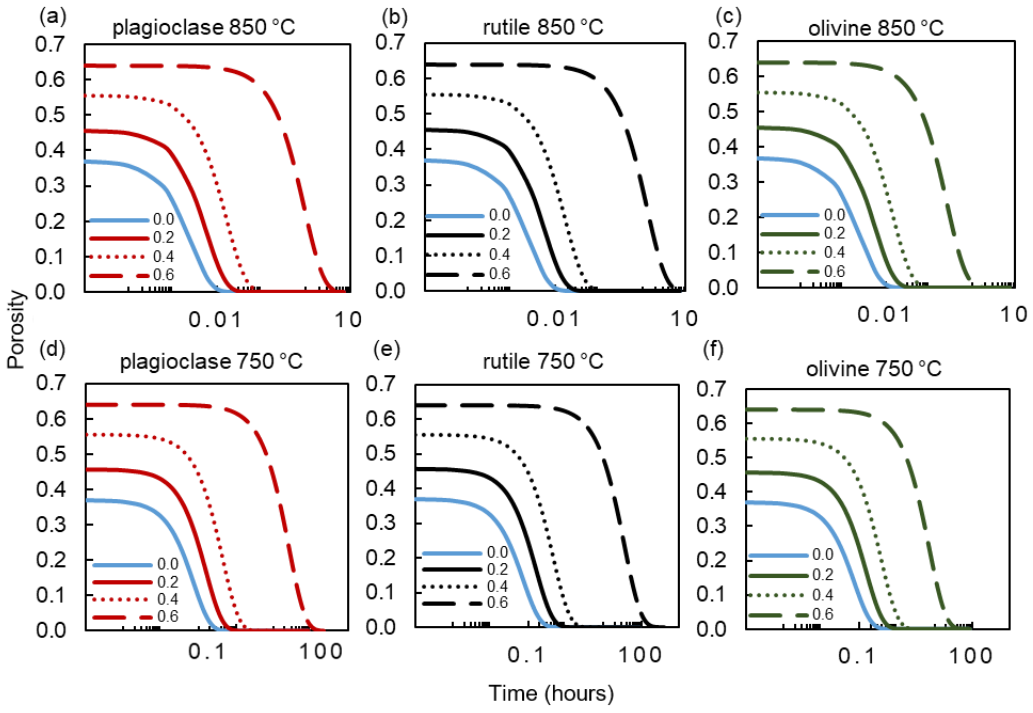

Figure 3.4. Estimated sintering time scales calculated from Eq. 3.5 for various crystal fractions (0, 0.2, 0.4 and 0.6) for the three crystal types at two different temperatures (a) plagioclase (b) rutile and (c) olivine at 850 °C, and (d) plagioclase, (e) rutile and (f) olivine at 750 °C.

For comparison, the model of Russell and Quane (2005) (Eqn. 3.8) was also used to predict the reduction in porosity under only gravitational stress. The load accelerates sintering, decreasing densification times. This model achieved a similar evolution in porosity reduction with time as Equation 3.7 (see section 3.4.1.2.), however Wadsworth et al. (2014) better captures the very end densification.

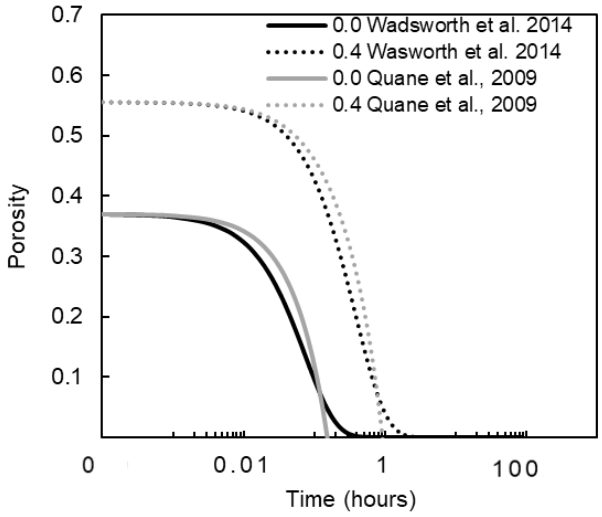

Figure 3.5. A comparison between the Russell and Quane (2005) and Wadsworth et al., (2014) models for the sintering time scales at 750 °C for a sample with 0.0 and 0.4 fractions of crystals with the characteristics of olivine as in Table 3.1.

3.4. Synthesising a two-phase magma

3.4.1. Sample preparation

3.4.1.1. Powder preparation

As the exact densities of each phase were known (Table 3.1), the required mass of each component could be calculated from the end target volume fraction. To maximise the full use of the crucible, and to minimise waste products, a desired final dense sample volume, V_f, was selected and component masses measured accordingly (Table 3a, b). With the aim of achieving the lowest possible initial pore fraction, the ratio of crushed to whole glass beads was selected as 50:50 for crystal volume fractions ≤ 0.2 and 75:25 for crystal fractions ≥ 0.3. Prepared powders were thoroughly mixed to ensure homogenisation. Small (~ 16x28 mm) and large (~ 26x38 mm) alumina crucibles, coated with high temperature concreate, were filled with the mixed powders. During filling the crucible was intermittently tapped carefully to ensure maximum dry packing of the powder (Vasseur et al., 2013) without causing particle segregation by density, which can produce bands. Initial porosities were calculated from the volume of the powder in the crucible, V_i, and its known dense equivalent via

$$\varphi_i = 1 - \frac{V_f}{V_i}. \quad (3.11)$$

The initial porosities of the loosely packed powders were incrementally higher with increasing crystals fraction, following $\varphi_i = 0.45\varphi_x + 0.37$ with an R^2 value of 0.92 (Fig. 3.6).

Table 3.3. Volumes and masses of constituents required for synthesis in small (a) and large (b) crucibles. Tables are split into measurements required for each crystal type (i) plagioclase (ii) rutile and (iii) olivine

(ai)

Final dense volume (cm^3)	2.80
Final dense height (cm)	0.70
plagioclase density ($g\ cm^{-3}$)	2.66
Spheriglass® density ($g\ cm^{-3}$)	2.50

plagioclase fraction	plagioclase (cm^3)	plagioclase (g)	Spheriglass® fraction	Spheriglass® (cm^3)	Spheriglass® whole (g)	Spheriglass® crushed (g)
0.10	0.28	0.74	0.90	2.52	3.15	3.15
0.20	0.56	1.49	0.80	2.24	2.80	2.80
0.30	0.84	2.23	0.70	1.96	1.23	3.68
0.40	1.12	2.98	0.60	1.68	1.05	3.15
0.50	1.40	3.72	0.50	1.40	0.88	2.63

(aii)

Final dense volume (cm^3)	2.80
Final dense height (cm)	0.70
rutile density ($g\ cm^{-3}$)	4.29
Spheriglass® density ($g\ cm^{-3}$)	2.50

rutile fraction	rutile (cm^3)	rutile (g)	Spheriglass® fraction	Spheriglass® (cm^3)	Spheriglass® whole (g)	Spheriglass® crushed (g)
0.10	0.28	1.20	0.90	2.52	3.15	3.15
0.20	0.56	2.40	0.80	2.24	2.80	2.80
0.30	0.84	3.60	0.70	1.96	1.23	3.68
0.40	1.12	4.80	0.60	1.68	1.05	3.15
0.50	1.40	6.01	0.50	1.40	0.88	2.63

(aiii)

Final dense volume (cm^3)	2.80
Final dense height (cm)	0.70
olivine density ($g\ cm^{-3}$)	3.29
Spheriglass® density ($g\ cm^{-3}$)	2.50

olivine fraction	olivine (cm^3)	olivine (g)	Spheriglass® fraction	Spheriglass® (cm^3)	Spheriglass® whole (g)	Spheriglass® crushed (g)
0.10	0.28	0.92	0.90	2.52	3.15	3.15
0.20	0.56	1.84	0.80	2.24	2.80	2.80
0.30	0.84	2.76	0.70	1.96	1.23	3.68
0.40	1.12	3.68	0.60	1.68	1.05	3.15
0.50	1.40	4.61	0.50	1.40	0.88	2.63

(bi)

Final dense volume (cm^3)	6.89
Final dense height (cm)	1.30
plagioclase density ($g\ cm^{-3}$)	2.66
Spheriglass® density ($g\ cm^{-3}$)	2.50

plagioclase fraction	plagioclase (cm^3)	plagioclase (g)	Spheriglass® fraction	Spheriglass® (cm^3)	Spheriglass® whole (g)	Spheriglass® crushed (g)
0.10	0.69	1.83	0.90	6.20	7.75	7.75
0.20	1.38	3.67	0.80	5.51	6.89	6.89
0.30	2.07	5.50	0.70	4.82	3.01	9.04
0.40	2.76	7.33	0.60	4.13	2.58	7.75
0.50	3.45	9.16	0.50	3.45	2.15	6.46

(bii)

Final dense volume (cm^3)	6.89
Final dense height (cm)	1.30
rutile density ($g\ cm^{-3}$)	4.29
Spheriglass® density ($g\ cm^{-3}$)	2.50

rutile fraction	rutile (cm^3)	rutile (g)	Spheriglass® fraction	Spheriglass® (cm^3)	Spheriglass® whole (g)	Spheriglass® crushed (g)
0.10	0.69	2.96	0.90	6.20	7.75	7.75
0.20	1.38	5.91	0.80	5.51	6.89	6.89
0.30	2.07	8.87	0.70	4.82	3.01	9.04
0.40	2.76	11.82	0.60	4.13	2.58	7.75
0.50	3.45	14.78	0.50	3.45	2.15	6.46

(biii)

Final dense volume (cm^3)	6.89
Final dense height (cm)	1.30
olivine density ($g\ cm^{-3}$)	3.29
Spheriglass® density ($g\ cm^{-3}$)	2.50

olivine fraction	olivine (cm^3)	olivine (g)	Spheriglass® fraction	Spheriglass® (cm^3)	Spheriglass® whole (g)	Spheriglass® crushed (g)
0.10	0.69	2.27	0.90	6.20	7.75	7.75
0.20	1.38	4.53	0.80	5.51	6.89	6.89
0.30	2.07	6.80	0.70	4.82	3.01	9.04
0.40	2.76	9.07	0.60	4.13	2.58	7.75
0.50	3.45	11.33	0.50	3.45	2.15	6.46

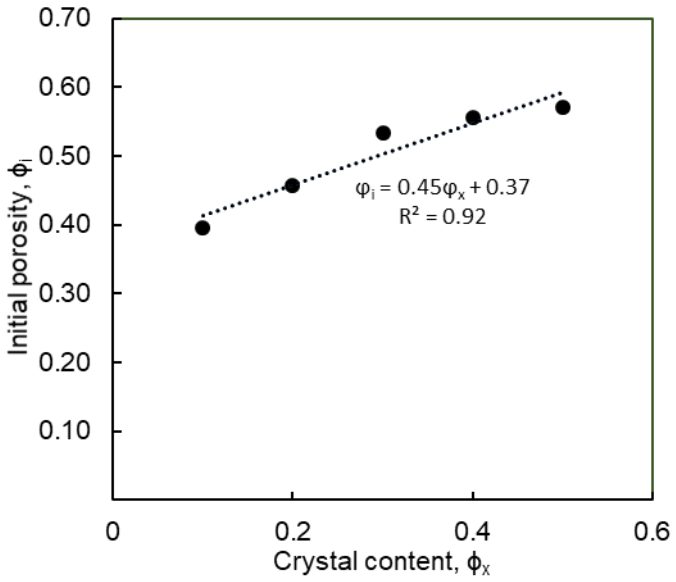

Figure 3.6. Initial porosities of prepared loose packed glass-crystal mixture powders increases with crystal fraction.

3.4.1.2. Sintering without load

A sintering temperature of 850 °C was selected based on the estimated viscosities of the mixtures (Fig. 3.3) to keep sintering timescales achievable (Fig. 3.4). Prepared powdered glass-crystal mixtures in crucibles were placed in a Carbolite CWF 13/23 box furnace and were heated at a rate of 5 °C min^{-1} to 850 °C ± 5 °C (sample temperature) while being monitored with a K-type thermocouple (Fig. 3.5a). Crystalline samples were compressed for between 5 and 120 hours, to constrain the evolution of gas volume fraction, and cooled to room temperature at 5 °C min^{-1}. Crystal-free samples were prepared by sintering glass powders over shorter dwelling periods of 25 minutes at 750 °C, as no crystals were present to increase suspension viscosity (e.g. Klein et al., 2018) and prohibit densification (Eqn. 3.7, 3.8). Under these conditions, the crystal-free samples reached the same final gas volume fractions as the crystal-bearing samples.

To limit temperature gradients in the sample which result in uneven densification, small crucibles were sintered one at a time at the same position within the furnace. The use of a small crucible also reduced the effects of external forcing from the weight of the sample upon itself which would act to increase the Eötvös number. The final samples were then cored and ground parallel to 6x12 mm (for samples for the *ex-situ* study, Chapter 4) and 3x6 mm (for samples for the *in-situ* study, Chapter 5) for further experimentation.

3.4.1.3. Sintering with load

Given the modelled densification timescale for the high crystal contents (~ 0.6) are > 10 hours at 850 °C, and that only one small crucible can be sintered at any one time in the Carbolite furnace, a more efficient process was sought for dense two-phase sample synthesis.

As discussed by Wadsworth (2016), sintering times can be significantly reduced by applying an external load. In this method the surface tension is no longer the dominant driving force, meaning the

Eötvös number is high and the system can no longer be modelled according to Eq. 3.7. Following this principle, large coated crucibles were filled with prepared powders and a cylindrical stainless-steel plug (24 mm diameter) was placed on top (Fig. 3.7b insert). The entire assembly was then placed between the pistons of a 100 kN Instron 8862 uniaxial press with a three-zone, split cylinder furnace in the Experimental Volcanology and Geothermal Research Laboratory at the University of Liverpool (Fig. 3.7b). Crystal bearing powders were heated at a rate of 5 °C min^{-1} to 850 °C ± 5 °C (sample temperature), dwelled for one hour to allow thermal equilibration, and then loaded to 2750 N at a rate of 250 N min^{-1} while the sample temperature was monitored with a K-type thermocouple. Glass-only powders were also sintered under such loads but at a lower temperature of 750 °C. This was to achieve glass only samples which were created under similar conditions to the crystal bearing samples, meaning final porosities, although of a negligible fraction, had similar morphologies.

As sintering cannot occur below the glass transition temperature, densification did not occur during heating, and only at experimental temperature, when the pistons were in contact with the sample and loading was occurring. Therefore, the sample volume, and thus porosity at any point in time, $\varphi_p(t)$, could be calculated from the monitored piston extension through time, $Ex(t)$, via

$$\varphi_p(t) = 1 - \left(\frac{h_f}{h_i - Ex(t)}\right) \tag{3.12}$$

Where h_i is the height of the prepared powder, and h_f is the expected height of a dense equivalent of the sample (i.e. an expected height for a fully dense sample given the mass of powder prepared and the density of its constituents is known). Piston displacement was stopped when the extension of the pistons equalled the expected extension, i.e. $ExpEx = (h_i - h_f)$. Samples were then cooled at a rate of 5 °C min^{-1} to room temperature. The samples were then cored to 6x12 mm (for samples for the *ex-situ* study, Chapter 4) and 3x6 mm (for samples for the *in-situ* study, Chapter 5) for further experimentation.

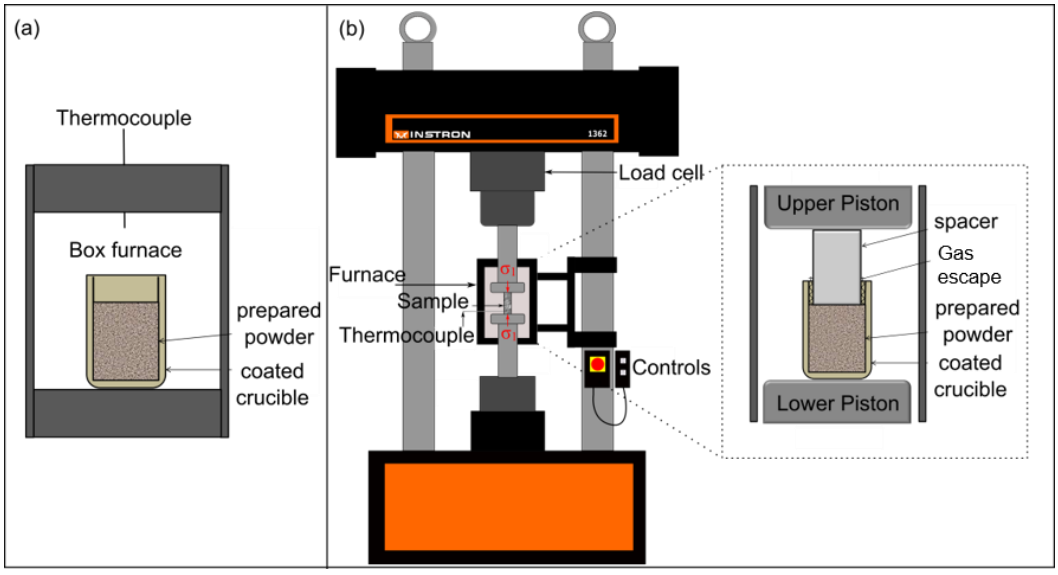

Figure 3.7. Experimental set up: (a) Prepared powders were sintered in large (~26x38 mm) alumina crucibles without load in a Carbolite box furnace at 850 °C; (b) Prepared powders were sintered in a

uniaxial press at 850 °C until the final sample height reached that of its fully dense equivalent. N.B. glass-only samples were sintered in both set-ups at the lower temperature of 750 °C.

3.4.2. Sample quality control

3.4.2.1. Porosity

For samples to be treated as two-phase (crystals and melt), it is key that they have a negligible porosity. Wadsworth et al. (2016) detail that the lowest possible final gas fraction achievable for monodisperse droplets while sintering (without load) is 0.03. Therefore, gas fractions of 0.03 were deemed negligible and samples with porosities of ≤ 0.03 were considered two-phase.

Each sample was quality tested to ensure it met the requirements before being used in further tests. The volume of connected and isolated pores was assessed at the University of Liverpool using a 1cc AccuPyc 1340 helium pycnometer from Micromeritics. The height, h, radius, r, and mass, m, each prepared sample was recorded, and its density, ρ_s, calculated as

$$\rho_s = \frac{m}{\pi r^2 h} \tag{3.13}$$

The total porosity of each sample could be estimated using the expected density, ρ_f, which is the dense rock equivalent density the sample would be expected to have given the known density of added crystals and glass,

$$\varphi_T = 1 - \left(\frac{\rho_s}{\rho_f}\right). \tag{3.14}$$

The helium pycnometer measures the skeletal volume, $V_{skeletal}$, of a specimen which can be used to calculate its connected porosity, φ_c, as:

$$\varphi_c = 1 - \left(\frac{V_{skeletal}}{\pi r^2 h}\right), \tag{3.15}$$

and isolated porosity, φ_i, as:

$$\varphi_i = \varphi_T - \varphi_c \tag{3.16}$$

3.4.2.2. Thermal properties

The synthesis process can alter the thermal properties of the glass phase through 1) chemical diffusion from the crystal phase, 2) crystallisation, or 3) stress concentration in the interstitial glass phase during cooling. To ensure rheological comparisons between our sample sets, it is essential that the rheological responses are only affected by the physical presence of the added crystal fraction and are not due to the alteration of the glass. Changes to the glass transition temperature, T_g, and softening point temperature (i.e. the temperature where viscous shortening overtakes thermal expansion), T_s, of the samples would indicate such a change in the glass from the presence of the crystalline phase.

To asses if the addition of the crystalline phase and the sintering process had any influence on the thermal properties of the glass, representative samples from each crystal fraction and crystal type were selected for testing in the Thermal Analysis Laboratory at the University of Liverpool. Differential scanning calorimetry (DSC) was carried out on 20 and 40 mg sample chips on a Netzsch

simultaneous thermal analyser (STA) Jupiter 449 F1. Samples were placed in a lidded, platinum crucible and heated at 10 °C min^{-1} to 675 ± 1°C in a 20 mL min^{-1} argon flow. To exclude the effect of a cooling history, samples were first taken to 675 °C (~ 125 °C above the published glass transition onset temperature of ~ 550 °C) and dwelled for 10 minutes before being cooled at a rate of 10 °C min^{-1} to 200 °C and held for a further 10 minutes. Samples were then reheated at a rate of 10 °C min^{-1} to 675 °C for one hour, to determine of the glass transition at a known cooling/heating rate; finally, the samples were cooled to room temperature at the same rate. A sapphire disk with the same mass as the synthesised samples was measured under the same temperature profile to allow for the determination of the specific heat capacity of the sample as a function of temperature for the second heating cycle of the DSC. The deflection and peak of the resulting exotherm was then used to find the onset and peak temperatures that define the glass transition temperature (T_g) interval.

Additionally, thermomechanical analysis (TMA) was performed on 6x5 mm cores using a Netzsch 402 F1 Hyperion under a 20 mL min^{-1} argon flow. The cores were subjected to the same heating profile as in the STA measurements and, on the second cycle, a constant 3 N load was applied. The softening temperature, T_s, of the sample was constrained as the temperature at which the sample extension (via thermal expansion) transitioned to shortening due to viscous relaxation of the applied load.

The glass transition and softening point temperatures were also used to inform the choice of temperatures to carry out deformation experiments in Chapters 4 and 5.

3.4.2.4. Homogeneity

To provide an additional constraint of sample homogeneity (including pore and crystal distribution), a selection of rutile-bearing samples were imaged using X-ray computed tomography (XCT) at the University of Manchester X-ray Facility at Harwell. Samples were fixed to a rotation stage and images were captured using a Nikon XCT 225ST operating at 120 kV and 90 mA. 3200 projections were collected for each scan over a 360 rotation. Data were reconstructed using the Nikon proprietary filtered back-projection algorithms with a 7 μm voxel size. 3D visualisation and analysis of reconstructed images was performed in Avizo™ software (https://www.fei.com/software/amira-avizo/). A cylindrical sub-volume, not much smaller than the sample (~ 0.1 mm from each edge), was extracted from each sample to reduce edge effects, and each phase was thresholded using global greyscale limits for each phase, 0 to 95 for pores, and 145 to 155 for rutile crystals. XCT The reconstructed image volumes were used to segment, visualise and assess crystal and pore volumes and distribution.

3.4.2.5. Mineralogical analysis

Analysis of the distribution of phases created by the sintering process was carried out using Quantitative Evaluation of Minerals by SCANning electron microscopy (QEMSCAN®). An automated scanning electron microscopy-energy dispersive X-ray spectrometry (SEM-EDS) technique developed by FEI. QEMSCAN® was carried out in field-scan mode, using a W-filament at the WellSite in the University of Liverpool. Uncovered, carbon-coated thin sections were subjected to a 15 kV accelerating voltage and ~5 nA beam current. Using a step size of 2 μm, two Brunker EDS

detectors recorded the discreate secondary x-rays emitted and the results were processed to resolve the elements present. Based on the elemental chemistries, spatially resolved species maps were created using a user-editable catalogue of minerals known as the Species Identification Protocol (SIP). Using iDiscover® software the resulting data were stitched to form a seamless map of each sample (3 mm diameter circles). Each phase present was allocated a colour and, where possible, assigned using the SIP. However, as the phases present were already known, these were defined accordingly as crystals, melt and pores. Quantification of each phase was then carried out by taking a normalised sum of pixels from the mapped image.

Back-scattered electron (BSE) images were taken of thin sections for further analysis. Images were acquired in a Hitachi TM3000 operating in BSE mode using a 15 kV beam voltage at a 10 mm working distance. Image analysis was then carried out to measure features using ImageJ. Lines were drawn using the line selection tool and their length quantified using the measurement tool before being converted to SI units via the scale on the image.

3.5. Results

3.5.1. Samples sintered at 850 °C

3.5.1.1. Samples sintered without load

For the samples prepared as described in section 3.4.1.2., the porosity of each quenched core was measured following the method outlined in section 3.4.2.1. (Fig. 3.8a). For crystal-free samples, total porosities were < 0.03 and so the samples met the required criteria and were considered dense. For samples with a 0.2 fraction of crystals, the measured porosities of samples gradually decreased in those held for longer time periods. This suggests that at lower crystal fractions (≤ 0.2) the crystallinity is not high enough to severely restrict the flow of the melt phase (i.e. suspension viscosity is low) and densification occurs in a realistically observable time frame. However, the time for near-complete densification (< 0.03) is five orders of magnitude greater than modelled (Figs. 3.4, 3.5), implying that the influence of the crystals on the viscosity term is much greater than predicted from current calculators (Fig. 3.3).

While the densification of the 0.2 crystal fraction sample during synthesis can be described as exponential, the 0.4 and 0.6 fractions cannot. At larger crystal fractions (≥ 0.4) it is likely that the crystal frameworks behave as barriers, leading to densification that is not exponential. In these suspensions with greater crystal fractions, although the samples were sintered sufficiently to prepare cores, no further densification appears to occur by increasing dwell time. Unintuitively, the porosity appears to increase slightly with time. This may be due to bubble rounding from surface tension, thus allowing porosity to be segmented more effectively.

For the crystal-bearing samples, the final gas volume fractions achieved while sintering without load were greater than the desired value of 0.03, making then unsuitable for the investigation of two-phase rheology. In addition, the remaining isolated pore fraction consists of large (≤ 500 μm), spherical ($r_p \sim 1$) bubbles (Fig. 3.8b) which have a high capillary number, the dimensionless ratio of viscous forces

and surface tension, (Ca > 1). These bubbles could potentially prohibit fluid flow (see e.g. Manga et al., 1998) and have an undesired effect on the rheological response to deformation, making the samples unsuitable for the study of two-phase behaviour. However, due to the synthesising process, the little remaining gas fraction is likely to consist of large spherical bubbles (Fig. 3.8b) that may affect the samples' rheology and so this too was discounted for use in Chapters 4 and 5.

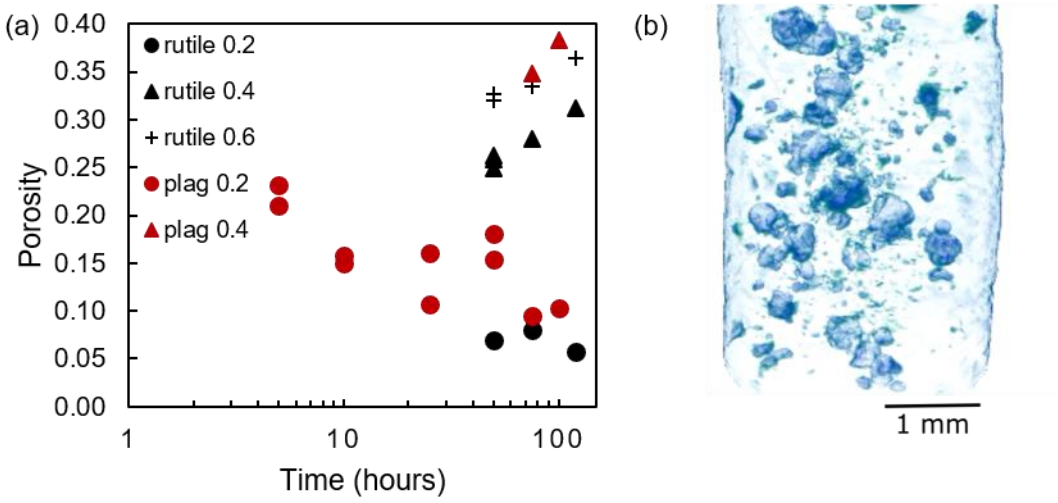

Figure 3.8. Sintering without load. (a) Final gas volume fractions measured via pycnometery for prepared crystalline powders of rutile and plagioclase with varied crystal fractions. The 0.2 crystal fraction samples decrease in porosity over time from an initial gas fraction of 0.32, while the 0.4 and 0.6 crystal fraction samples appear to increase in porosity over time. (b) A CT image of a 0.2 crystal fraction rutile sample sintered for 100 hours with an approximate final porosity of 0.05. Polydisperse, large (< 500 µm) spherical (r_p ~ 1) pores are seen as blue bubbles within the sample core (blue outline).

3.5.1.2. Samples sintered with load

Sintering with load (see section 3.4.1.3.) resulted in sample porosities of < 0.02. Porosity was also measured via the segmentation of XCT images for a select number of samples (Fig. 3.9a). The total porosities measured via this method are ≤ 0.03 for crystal fractions of ≤ 0.4 and ≤ 0.05 for crystal fractions ≤ 0.5, with a method uncertainty of 5 % of the measured value (Lin et al., 2015). Processing of XCT images (Fig. 3.9b) shows that pores are relatively small (< 50 µm) and are sub-spherical (r_p < 1) and thus should not have an effect on sample viscosity like those samples sintered without load as they have low capillary numbers and therefore do not have a dominant effect on the rheology (e.g. Manga et al., 1998). Crystallinity was also measured from XCT images, results gave expected crystal fractions within uncertainty. The samples prepared under load can therefore be considered two-phase (crystals and melt) and suitable for the rheological testing carried out in Chapters 4 and 5.

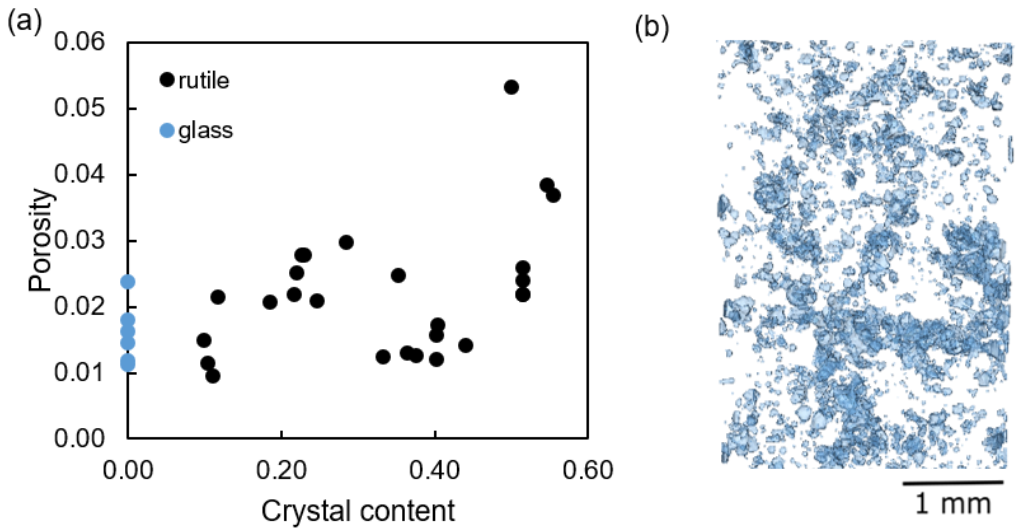

Figure 3.9. Sintering with load. (a) Total porosity against crystal content, measured by image thresholding in Avizo™ from XCT scans. Porosity ranges from 0.01 to 0.03 for crystal fractions up to ~0.4 and then increases to 0.03-0.05 for crystal fractions of ~0.5. (b) An XCT image of 0.2 crystal fraction sample of rutile (not visible) with porosity in blue. Pores are smaller (< 0.16 µm) and less spherical (r_p < 1) than those sintered under no load (Fig. 3.8b).

3.5.1.3. Thermal properties

For samples synthesised with and without load at 850 °C (sections 3.4.1.2. and 3.4.1.3.), the onset of the glass transition can be considered a constant temperature across the sample suite (with expected variation, Fig. 3.10a). The measured onset temperatures are representative of those measured by previous studies (Wadsworth et al., 2014) and thus can be said to be representative of the T_g of Spheriglass® with a standard 10 °C min^{-1} cooling/heating history. However, the peak of the T_g decreases by > 30 °C with the introduction of the crystalline phase, and then increases steadily with crystal content. As the peak of the T_g is decreasing suddenly with the introduction of the crystalline phase then it is likely that there is some chemical alteration of the glass. Although a minority may remain the same initial composition of Spheriglass® as implied by the constant onset temperature. The increase in peak T_g with crystal fraction suggests that alteration varies with increasing crystal fraction. However, as there is no difference between the plagioclase and rutile bearing samples, this is evidence that it is independent of crystal type, thus negating the occurrence of chemical exchange which could have contributed to altering the interstitial glass chemistry.

The softening point values increase with increasing crystal fraction by ~ 30 °C from the glass only sample to the 0.5 volume fraction demonstrating that the temperature where softening occurs (T_s; i.e. the temperature at which the relaxation of the imposed external load leads to deformation that exceeds that of the thermal expansion) increases with crystal fraction (Fig. 3.10b).

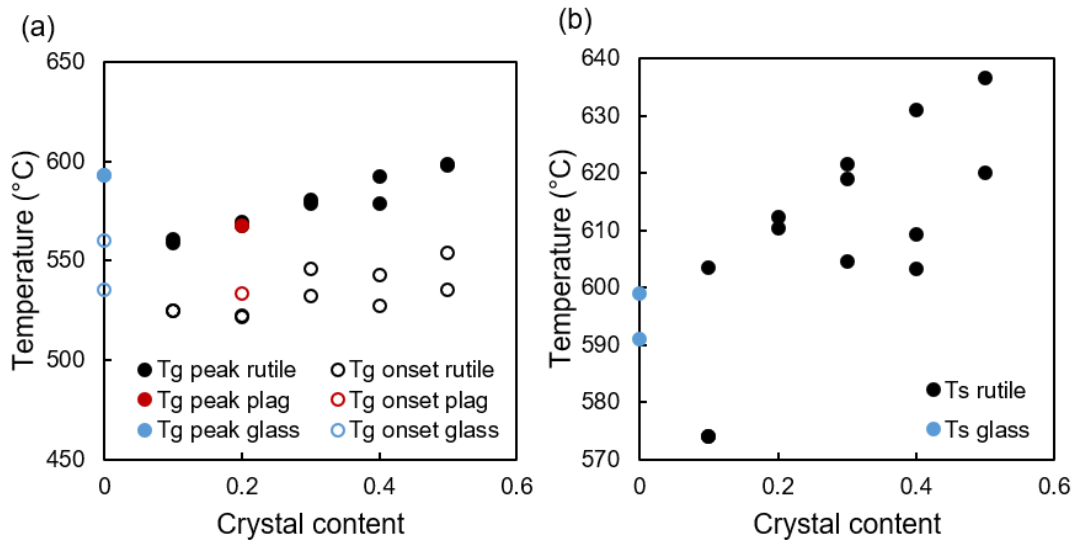

Figure 3.10. Thermal properties of samples synthesised under load. (a) The onset of the glass transition temperature, T_g, of the samples remains relatively constant with crystal content while the peak decreases with the introduction of crystals and then gradually increases as crystal content increases. (b) The softening point temperature, T_s, increases with crystal content from the 0.0 fraction at the same rate as T_g.

3.5.1.4. Sample Fabrics

For samples prepared with and without load at 850 °C, as described in sections 3.4.1.1. and 3.4.1.2., QEMSCAN® allowed for the visualisation of the pore and crystal distribution in the samples (Fig. 3.11). By inputting the chemistry of Spheriglass® (Table 2) into the SIP, glass with that composition could be labelled as such via the catalogue. Crystals could also be labelled via the SIP and were allocated a colour accordingly. In close proximity to the categorised Spheriglass®, was a group with similar composition but with lower sodium and higher calcium levels. This phase had a needle-like shape and appeared to form around the boundaries between sintered glass particles or along the outside of crystals (Fig. 3.11 a-f). It is likely that this phase is a crystallised version of Spheriglass® and was therefore labelled as such and inserted into the SIP. Quantification of the fraction of crystallised Spheriglass® (Fig. 3.11g) shows that the amount decreases with increasing phenocryst fraction until the 0.4 fraction, after which crystallisation increased slightly. BSE images of samples (Fig. 3.12a-e) show that Spheriglass® crystallises along the rims of rutile grains and that these rims become thicker with sintering time (Fig. 3.12f). It is therefore apparent that the Spheriglass® powders sintered at 850 °C crystallise around the margins of the phenocrysts (Fig. 3.12a-e) and glass bead boundaries (e.g. Fig. 11 a). The respective amount of crystallisation across the sample suite highlights a trade-off between the amount of Spheriglass® available to crystallise and the area available for heterogenous nucleation (Fig 11).

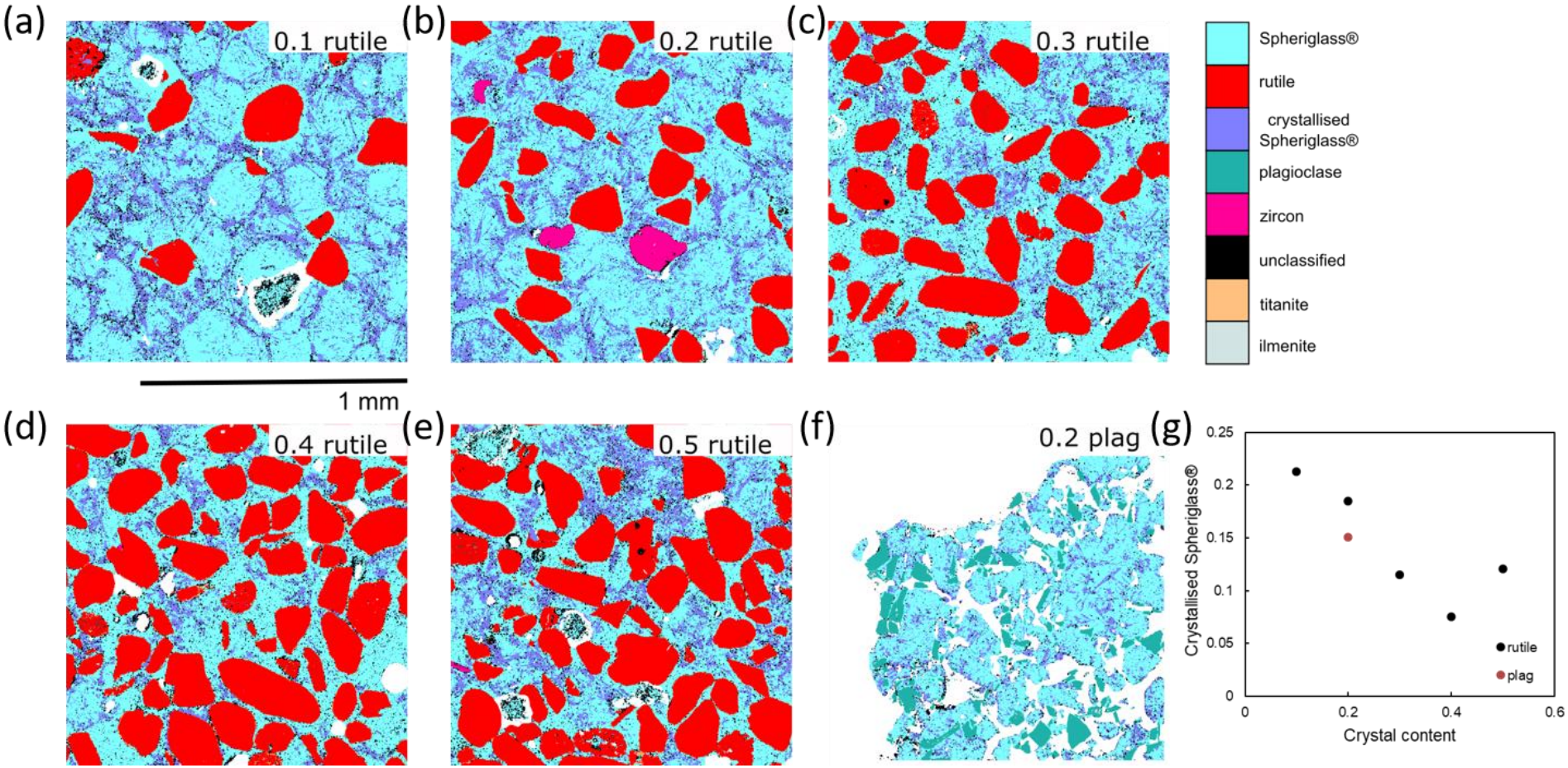

Figure 3.11. QEMSCAN® analysis of samples sintered under load at 850 °C. Mineral maps of thin sections (a-f) show the crystallised Spheriglass® phase in lilac, it is needle-like and forms around imperfections. The 0.2 plagioclase sample (f) is given as a comparison to show that crystallisation of the Spheriglass® phase occurs regardless of crystal type. Quantification of the crystallised spheriglass phase (g) shows that it decreases with increasing crystal fraction up until 0.4 where it then increases slightly at the 0.5 fraction.

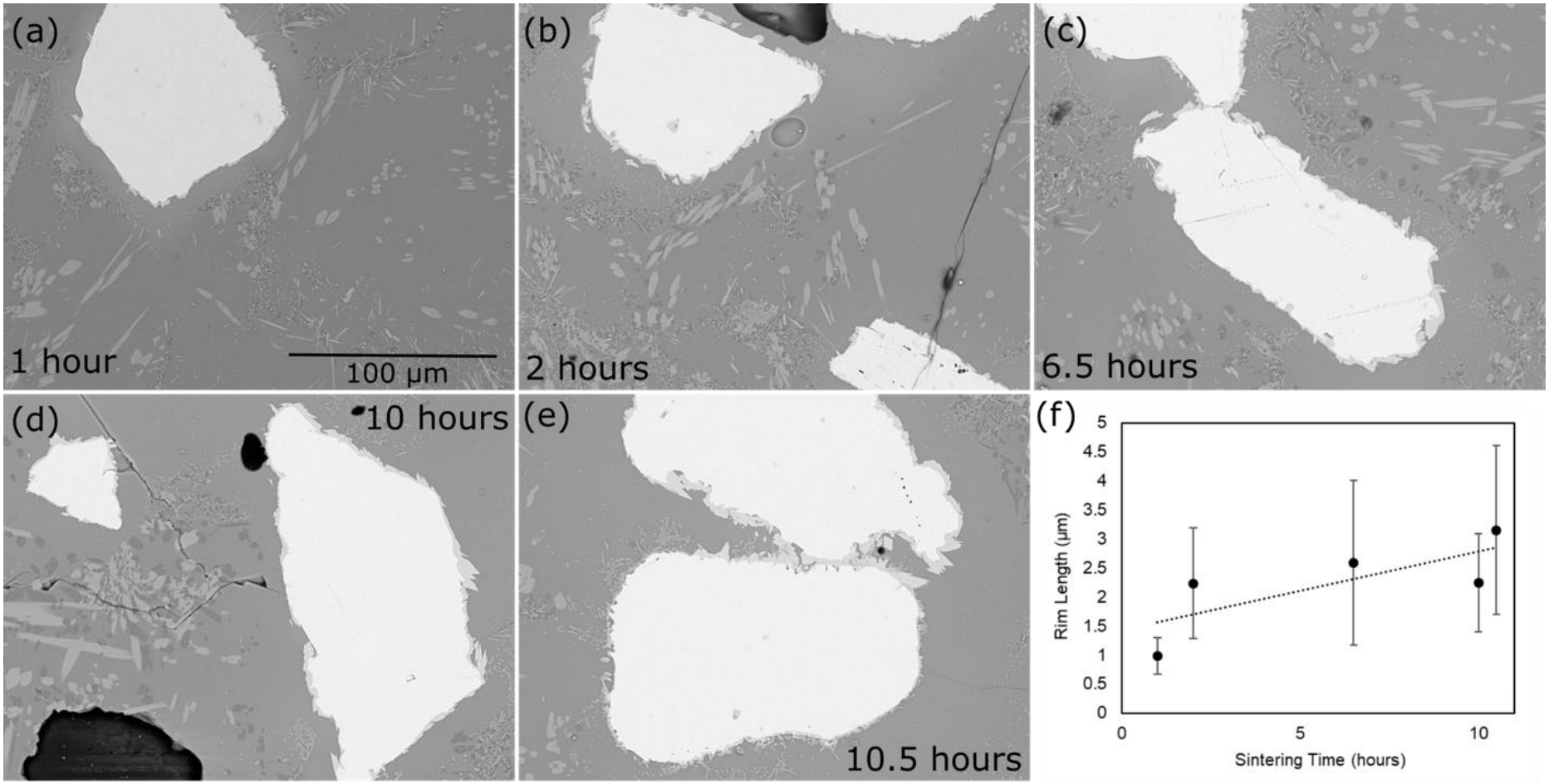

Figure 3.12. BSE images of synthesised samples bearing a 0.2 fraction of rutile. Samples were heated at a rate of 5 °C min^{-1} to 850 °C and, under no load, were dwelled for (a) 1 hour, (b) 2 hours, (c) 6.5 hours, (d) 10 hours and (e) 10.5 hours. The thickness of the rim that had crystallised around the rutile grains was measured and was plotted against sintering time (f). It is evident that rim thickness increases with sintering time.

3.5.1.5. Remarks

When sintering crystal-bearing powder mixtures at 850 °C the viscosity of the Spheriglass® was low enough for diffusion and thus crystallisation to occur (~$10^{4.5}$ Pas). Crystallisation of the Spheriglass® melt could be the reason for longer than expected sintering times (Fig. 3.8a).

Crystallisation of the Spheriglass® would alter the melt chemistry (Cashman and Blundy, 2000) which may account for the increase in the *peak* T_g (Fig. 3.10a). As the glass was only partially crystallised (around crystal margins and glass sphere edges) some of the uncrystallised melt, far from those areas, may still have the same chemistry as the original Spheriglass®. This would lead to the crystallised samples having the same *onset* T_g as the Spheriglass® (Fig. 3.10a).

The presence of newly formed microlites in the system may also be the reason for the exaggerated increase in the temperature at which softening occurs with crystal fraction (Fig. 3.10b). An increase in total crystallinity would increase the apparent viscosity and thus the temperature at which softening occurs.

Although the samples can be considered two-phase (crystals and melt), their chemistry and thus rheological behaviour are not comparable. This chemical alteration and addition of an incomparable microlite phase means that samples sintered at 850 °C are not suitable for rheological testing, therefore an alternate solution had to be found.

3.5.2. Samples sintered at 750 °C

Given insights from detailed investigations, crystal bearing samples were sintered at a new temperature, 100 °C lower than previously carried out. As modelled sintering timescales for an unloaded system at 750 °C reached almost 100 hours (Fig. 3.4) due to the lower viscosity of the Spheriglass, and as the sintering with load method successfully reached negligible final gas volume fractions, only the sintering under load method was carried out at the new lower temperature.

3.5.2.1. Samples sintered with load

Following the same procedure as detailed in section 3.4.1.3., samples were sintered at 750 °C. As detailed in section 3.4.1.3. and by applying Equation 3.11, porosity reduction could be monitored by the piston displacement through time and was stopped when a final porosity was achieved (e.g. Fig 3.13).

The model of Russell and Quane (2005) (Eqn. 3.8) was applied to the samples under these conditions by calculating suspension viscosities via Equation 3.10. The model predicted full densification times for samples with 0.1-0.5 crystals of 0.04-3.6 s, when load was applied (Fig. 3.13). However, expected extensions in the 0.5 crystal samples were not reached until almost an hour at peak load. This suggests that the viscosity term used in Eq. 3.8 is much higher than that calculated via Eq. 3.10.

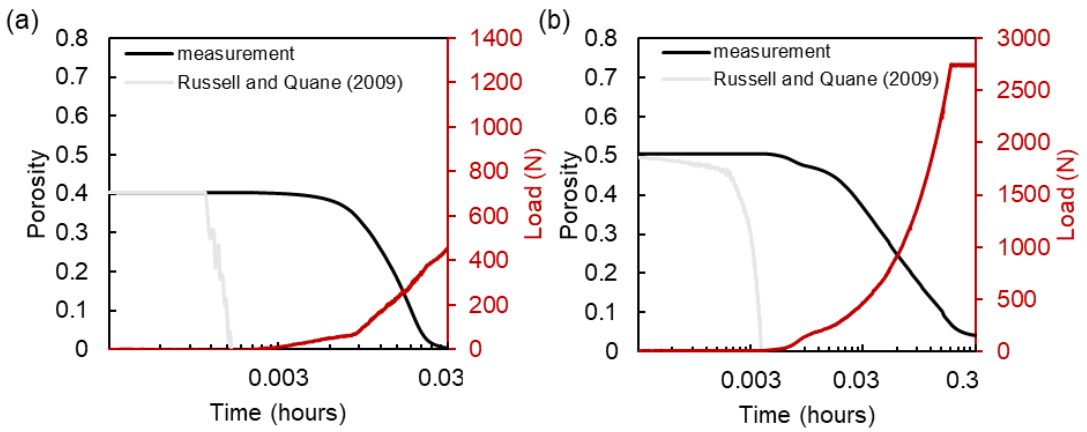

Figure 3.13. Porosity reduction with time at 750 °C as load on the sample is increased at 250 N min^{-1} for crystal fractions (a) 0.1 and (b) 0.5. Equation 3.8 (Russell and Quane, 2005) was applied to model densification of the powders when load was applied. The model overestimates the time required for densification by approximately 1-2 orders of magnitude.

3D reconstruction and analysis of the XCT images revealed that samples formed under loading conditions were homogenous (Fig. 3.14) with crystal content varying by ± 0.01-0.05 from the intended fraction, which is within error of the measurement method which is 5 % (Lin et al., 2015).

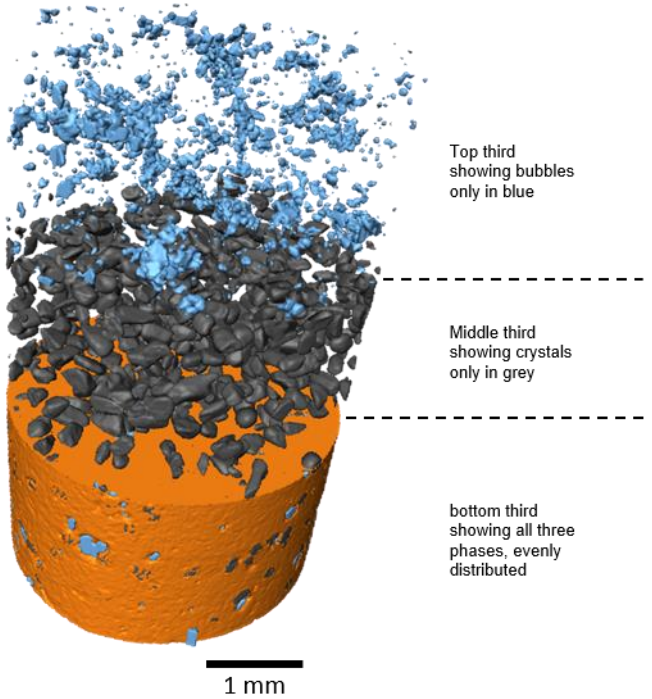

Figure 3.14. A 3-D reconstruction of a sample sintered under a load of 2750 N at 750 °C with 0.1 rutile particles (grey), and 0.01 pores (blue) homogeneously distributed throughout the sample. The Spheriglass® fraction (orange) remains uncrystallised. The image is split into three sections, with certain phases 'hidden' in each with the intention of demonstrating sample homogeneity. The top section shows only the pores, the middle only the crystals while the bottom section shows all three.

3.5.2.2. Thermal properties

STA measurements of resulting samples showed that, within error, both the onset and peak T_g remained constant with the addition of crystals (Fig. 3.15) for the samples sintered under load at 750 °C. This is another indication that no crystallisation or alteration of any kind occurred due to the sintering process.

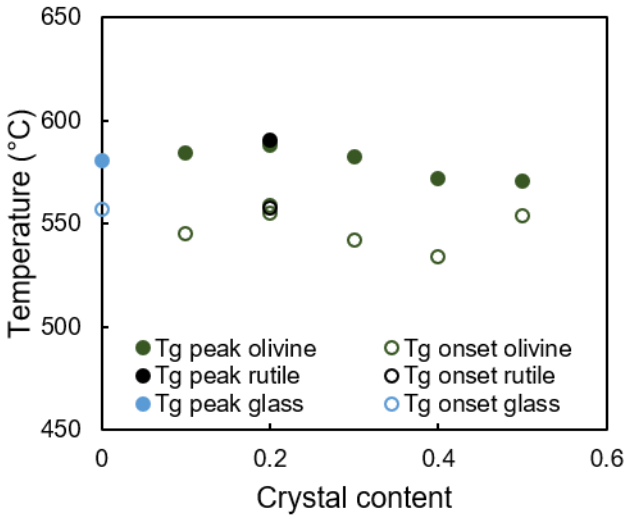

Figure 3.15. STA measurements of two-phase synthetic samples of glass with either olivine or rutile sintered under load at 750 °C. T_g onset and T_g peak remain approximately constant regardless of the volume of crystal particles.

3.5.2.3. Sample Fabrics

XCT data showed that samples contained the desired fraction of crystals within the 5 % expected error and porosities were approximately < 0.03. QEMSCAN® (Fig. 3.16) and SEM (Fig. 3.17) data show that samples synthesised at 750 °C under load for 0.03-0.3 hours were homogenous, with crystals and isolated pores well distributed throughout the samples. The analysis also found that, unlike samples created at 850 °C, only a small amount of glass alteration was present. This was considered negligible (< 0.03) as it would have little to no influence the samples rheology.

3.5.2.4. Remarks

Samples synthesised at 750 °C fit the criteria outlined in section 3.2.1. and so were selected for *ex situ* rheological testing (Chapter 4) and *in situ* synchrotron-based X-ray computed micro-tomography investigations of sample dilation (Chapter 5).

As sample densification with applied load can be tracked through time, three-phase suspensions with $\varphi_x \leq 0.5$ and $0.0 \leq \varphi_p \leq 0.5$ could be synthesised via the above method (e.g. Fig. 3.18).

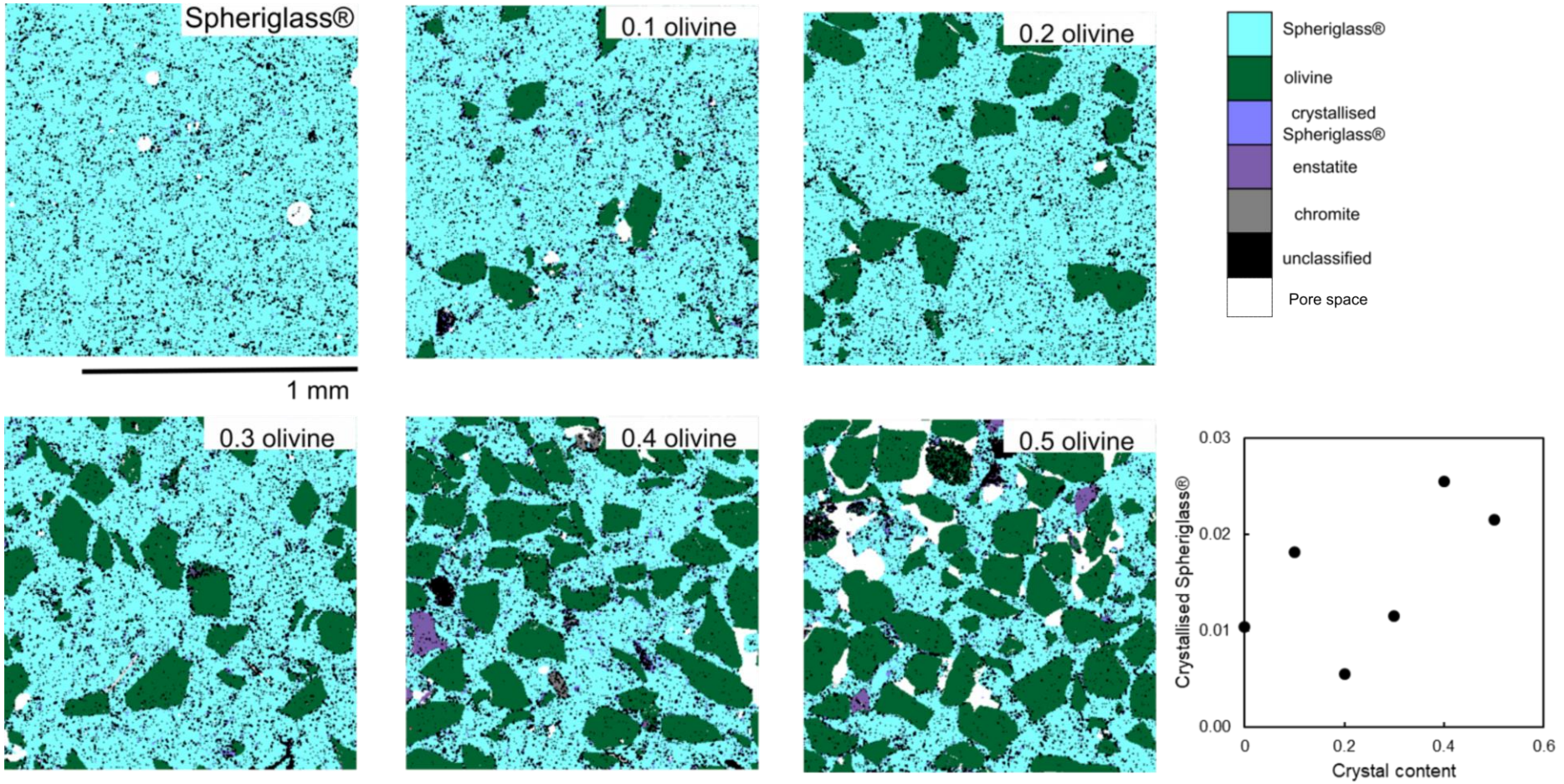

Figure 3.16. QEMSCAN® analysis of samples sintered under load at 750 °C for (a) Spheriglass® only, (b) 0.1 olivine, (c) 0.2 olivine, (d) 0.3 olivine, (e) 0.4 olivine, and (f) 0.5 olivine. (g) Total amounts of crystallised Spheriglass® are < 0.03 and do not vary systematically with phenocryst content. Crystallinity and porosity are well distributed throughout the sample.

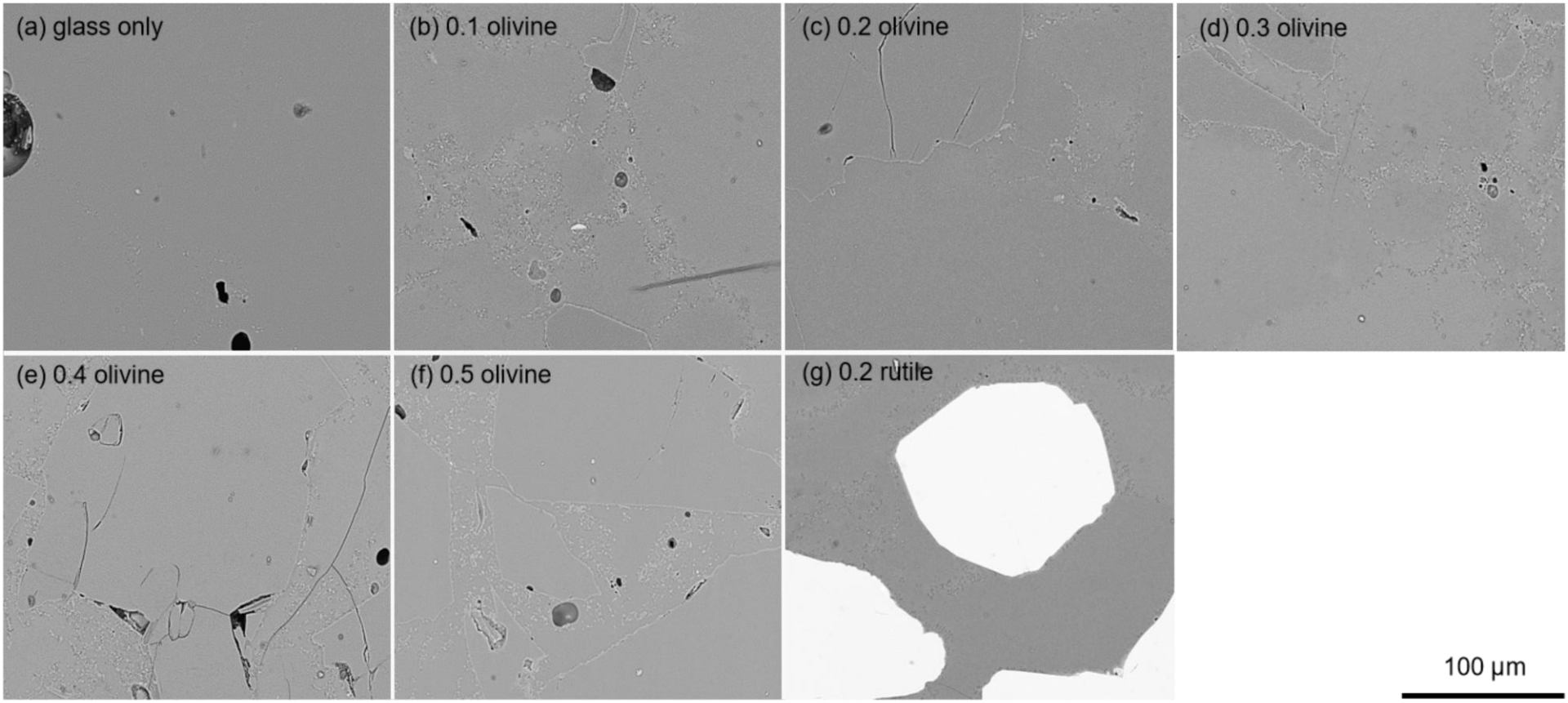

Figure 3.17. BSE images of samples synthesised under load at 750 °C. The glass only sample (a) has no microlite crystals. With the addition of the olivine (b-f) and rutile (g) phase there is a slight alteration of the glass, seen as small bright spots, but rheologically inconsequential compared to the amount in samples sintered at 850 °C, as demonstrated by constant. T_g measurements across the sample suite (Fig. 3.15).

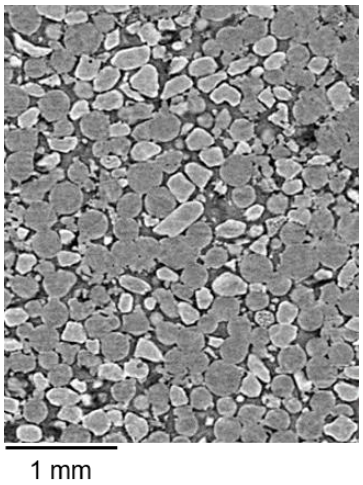

Figure 3.18. 2D grey scale image of 0.2 rutile crystals (lightest greyscale) sintered within Spheriglass® (medium greyscale) to a porosity (darkest greyscale) of 0.3. The sample was sintered under load at 750 °C until the piston extension through time, $Ex(t)$, reached the point where $\varphi_p(t)$ was equal to 0.3 (Eqn. 3.11). The image was taken on the i12 beamline at Diamond Light Source.

3.6. Summary

The method chosen to create two-phase synthetic samples for *ex situ* rheological testing (Chapter 4) and *in situ* synchrotron-based X-ray computed micro-tomography investigations (Chapter 5) has been presented in detail. Using a sintering process, synthetic Spheriglass® was combined with crystals of plagioclase, rutile and olivine under different temperature and load conditions. Samples with varying crystal contents were created and their suitability for the use in rheological studies (Chapters 4 and 5) was assessed using a stringent-criteria (section 3.2.1.). Using several techniques, samples were investigated for porosity, thermal properties, homogeneity and mineral composition. Conclusions drawn from analysis found that samples sintered with Spheriglass® and rutile were suited for the synchrotron study (Chapter 5) due to the strong density contrast between the two phases. While samples sintered with Spheriglass® and olivine were more suited for *ex-situ* studies (Chapter 4) as olivine crystals were more readily available, allowed for synthesis in bulk, and the study lacked the need for high phase contrast in XCT**.** Both crystal phases have comparable characteristics and physical properties to the plagioclase tested here, and which is a dominant phenocryst in natural volcanic systems. Further sample analysis found that sintering under a load of 2,750 N created the densest possible samples and allowed for the monitoring of densification by measuring the evolution of sample height within a cylindrical crucible with time. Due to the crystallisation of the Spheriglass® at the higher experimental temperatures (i.e., 850 ˚C), a sample synthesis temperature of 750 °C was preferred for subsequent rheological studies of two-phase suspensions. At this temperature, the Spheriglass® viscosity was low enough for prepared powders with high crystal fractions to sinter to close to zero porosities, but also low enough for crystallisation of the glass to be negligible.

Over the fighters

and no-mercy plain speakers

lined with esker ridges on each old cheek,

-Untitled | Republic of Verse

Chapter 4: The non-Newtonian rheology of crystal bearing melts

4.1. Introduction

4.1.1. The rheology of crystal-bearing silicate melts

The rheology of a magma describes the way in which this multi-phase suspension (of crystals and bubbles in a silicate melt) deform - including flow and rupture - as a response to local stresses inside a reservoir, a volcanic conduit or upon eruption (Dingwell, 1996). It is therefore a major input into magma transport and volcanic eruption models, and thus plays an imperative role in our ability to forecast volcanic hazards and improve risk mitigation strategies (Gonnermann and Manga, 2007; Mader et al., 2013). For non-turbulent flows of silicate melt suspensions, stress, σ, is expressed as a function of strain rate, $\dot{\varepsilon}$, via

$$\sigma = f(\dot{\varepsilon}). \tag{4.1}$$

For a Newtonian flow, stress increases linearly with strain rate via

$$\sigma = \mu\dot{\varepsilon}, \tag{4.2}$$

where the viscosity of the melt, μ, is a constant, independent of the applied strain rate. However, most magmatic bodies contain crystals and bubbles and exhibit non-Newtonian, shear-thinning behaviours (e.g. Caricchi et al., 2007; Lavallée et al., 2007; Cordonnier et al., 2009). Here, the apparent viscosity of the suspension, η_a, is not constant with strain rate but, in fact, decreases. Several fluid dynamic studies have attempted to explain the cause of shear-thinning behaviour (e.g. Cheng et al., 2011); however, in flowing magma, the exact mechanisms remain enigmatic (Deubelbeiss et al., 2011 and references therein). Thus far, it has been attributed to viscous heating in the interstitial melt (Cordonnier et al., 2012b); the non-Newtonian response of the melt phase (e.g. Webb and Dingwell, 1990b, 1990a); crystal shape (e.g. Mueller et al., 2010, 2011b; Mader et al., 2013); particle rearrangement due to finite strain (e.g. Caricchi et al., 2007; Costa et al., 2009), crystal plasticity (Kendrick et al., 2017) and fracture (Deubelbeiss et al., 2011; Pistone et al., 2012). However, the non-Newtonian behaviour of magmas cannot be attributed to any single mechanism, and the competing influence of various factors is, as yet, largely unexplained.

In silicate melts, Cordonnier et al., (2012b) relate the transition from Newtonian to non-Newtonian flow to when the ratio of the heat gained, $\emptyset_g$, to the heat lost, $\emptyset_l$, in a system (i.e. the Brinkman number, $Br = \frac{\emptyset_g}{\emptyset_l}$) is greater than unity. This occurs at a critical strain rate:

$$\dot{\varepsilon}_{VH} \approx \sqrt{\frac{\emptyset_l}{2\mu}}, \tag{4.3}$$

where, μ is the viscosity of the melt and for small laboratory specimens, under steady state conditions $\emptyset_l = 10^{4\pm0.5}$ Wm^{-2}. Their experiments showed that viscous heating above the critical strain rate contributed to the non-Newtonian behaviour of the melt.

The transition to non-Newtonian behaviour in a silicate melt is defined by its state of relaxation, also expressed as the dimensionless Deborah, De, number. [Note that this definition has been used interchangeably with the Weissenberg, *Wi*, number (e.g. Wadsworth et al., 2017b, 2018) which is defined as the frequency-independent equivalent to the Deborah number (Poole, 2012). Here, however, as we discuss the steady flow of a viscoelastic fluid, we note that the argument of nomenclature is trivial and henceforth refer only to the Deborah number as it is more widely used in volcanological literature (e.g. Cordonnier et al., 2012b, 2012a; Okumura et al., 2013; Gonnermann, 2015; Wadsworth et al., 2017b; Coats et al., 2018).] The Deborah number is defined as the ratio of the Maxwell relaxation timescale,

$$\tau = \mu/G_{\infty}, \tag{4.4}$$

and the timescale of observation,

$$\tau_{obs} = 1/\dot{\varepsilon}_{obs}, \tag{4.5}$$

where $\dot{\varepsilon}_{obs}$ is the strain rate of observation, giving

$$De = \frac{\dot{\varepsilon}_{obs}\,\mu}{G_{\infty}}, \tag{4.6}$$

where G_{∞} is the shear modulus and $\approx 10^{10\pm0.5}$ (Dingwell and Webb, 1989). To describe the behaviour of multiphase magmas, that is melt, plus crystals and bubbles, an alternative empirical relationship was also constrained for multiphase magmas in Chapter 2

$$De = \frac{\left(\sigma/_{k}\right)^{1/_{b}}\mu}{G_{\infty}} \tag{4.7}$$

where k and b are empirical constants obtained from the power law relationship of multiphase flow curves. The onset of non-Newtonian behaviour for single phase silicate melt has been constrained to occur at De = 10^{-3}, conditions in which deformation induces breakdown of the melt structure, and rupture has been constrained to occur at De =10^{-2} (Dingwell, 1996; Cordonnier et al., 2012a). Giving rise to a critical strain rate at the onset of non-Newtonian behaviour, $\dot{\varepsilon}_{n-N,0}$, which can be defined as

$$\dot{\varepsilon}_{n-N,0} = 10^{7\pm0.5}\mu^{-1} \tag{4.8}$$

and a critical strain rate at the onset of failure, $\dot{\varepsilon}_{fail,0}$, which can be defined as

$$\dot{\varepsilon}_{fail,0} = 10^{8\pm0.5}\mu^{-1} \tag{4.9}$$

Mader et al. (2013) suggest that when a fraction of crystals, φ_x, is present the critical strain rates should be reduced by a factor of $(1-\varphi_x)$ because the crystals behave as rigid bodies and thus strain must be accommodated in the smaller volume of remaining melt. Experimental results by Cordonnier et al. (2012a) found this reduction to be best described by $(1-\frac{\varphi_x}{\varphi_m})$ where φ_m is the maximum packing of particles, correcting for the localisation of stress due to particle geometries, giving the strain rate at the onset of non-Newtonian behaviour as

$$\dot{\varepsilon}_{n-N} = \dot{\varepsilon}_{n-N,0}\left(1-\frac{\varphi_x}{\varphi_m}\right), \tag{4.10}$$

and the strain rate at the onset of failure as

$$\dot{\varepsilon}_{fail} = \dot{\varepsilon}_{fail,0}\left(1 - \frac{\varphi_x}{\varphi_m}\right). \quad (4.11)$$

Mueller et al. (2010) show that the onset of non-Newtonian shear-thinning behaviour (i.e. when the flow index, n, is less than one) of particulate suspensions is dependent on the particle shape and volume via:

$$n = 1 - 0.2r_p\left(\frac{\varphi_x}{\varphi_m}\right)^4 \quad (4.12)$$

where $r_p$is the aspect ratio which is equal to the length of a particle's axis of rotation over the maximum diameter perpendicular to that axis. Mueller et al. (2011b) define the maximum packing of monodisperse particles, $\varphi_{m,0}$, in terms of their aspect ratio via

$$\varphi_{m,0} = \varphi_{m1} exp\left[-\frac{(log_{10}r_p)^2}{2b^2}\right], \quad (4.13)$$

where φ_{m1} is the maximum packing fraction of a particle with $r_p = 1$ and b is a fitting parameter. By extending the data set of Mader et al., (2013), which measured the maximum packing fraction of samples with $0.2 < r_p < 20$, Klein et al., (2018) were able to reparametrise the constants in Equation 4.13 for $0.02 < r_p < 20$ giving φ_{m1} and b as 0.637 and 1.171, respectively.

Klein et al. (2018) also reformulated the maximum packing fraction to account for the polydispersity of particles, γ, so

$$\varphi_m = 1 - (1 - \varphi_{m,0})\gamma^a \quad (4.14)$$

where a is a fitting parameter equal to 0.173.

In highly crystalline magmas ($0.5 \leq \varphi_x \leq 0.8$), crystals may physically interact with one another. In such cases, crystals may not necessarily act as rigid bodies. In these crystalline end-member magmas, additional factors have been proposed to underline shear-thinning behaviour. Deubelbeiss et al. (2011) conducted an experimental and numerical investigation into the causes of non-Newtonian behaviour in highly crystalline magmas. They found that although viscous heating had a localised microscopic effect, it had a negligible overall effect on the bulk rheology of the system. Their results also indicate that finite strain causes strain hardening and weakening due to particle rearrangement, but these effects were not sufficient to cause strain-rate related weakening. Deubelbeiss et al. (2011) postulate that strain localisation in the melt induces microscopic stresses that are significant enough to cause macroscopic non-Newtonian behaviour. They also note that the development of high stresses in the crystal phase which should modify them; indeed crystal plasticity (see Kendrick et al., 2017 for an overview) and crystal failure have been proposed to contribute to the non-Newtonian response of magmas (Lavallée et al., 2007; Pistone et al., 2012; Kendrick et al., 2017).

4.1.2. Rheological models

A full description of a fluid rheology is given by the Herschel and Bulkley (1926) model:

$$\sigma = \sigma_0 + K\dot{\varepsilon}^n \tag{4.15}$$

where σ_0 is the yield stress and K is the consistency of the flow. Although Lavallée et al. (2007, 2013) demonstrated that crystal-rich magmatic suspensions (even with ca. 0.80 crystals) do not have a yield strength, it has been suggested that they may exhibit yield strength when $\frac{\varphi_x}{\varphi_m} \geq 0.8$; in absence of yield strength, Equation 4.15 simplifies to

$$\sigma = K\dot{\varepsilon}^n. \tag{4.16}$$

When the flow is Newtonian (Eq. 2) $n = 1$ and the viscosity is equivalent to the consistency, $\mu \equiv K$. However, when a flow exhibits shear-thinning, $n < 1$, a power law model can be used to describe the relative viscosity (Mader et al., 2013),

$$\eta_r = K_r\dot{\varepsilon}^{n-1} \tag{4.17}$$

where, η_r is the relative viscosity, $\eta_r = \frac{\eta_a}{\mu} = \frac{\sigma}{\dot{\varepsilon}\mu}$ and K_r is the relative consistency, $K_r = \frac{K}{\mu}$.

When the abundance of crystals in a flow reaches concentrated levels, $\varphi \geq 0.25$, crystals interact, and their presence must be accounted for in viscosity calculations (Einstein, 1911). Originating from earlier works (Einstein, 1911; Roscoe, 1952; Maron and Pierce, 1956), Mader et al. (2013) reformulated the relative consistency as

$$K_r = \left(1 - \frac{\varphi_x}{\varphi_m}\right)^{-2} \tag{4.18}$$

Therefore, for Newtonian flows, $\eta_r = K_r$ and Equation 4.15 becomes the Maron Pierce (1956) equation, which has been used in recent literature to describe flow behaviour (e.g. Mueller et al., 2011b; Moitra and Gonnermann, 2015; Truby et al., 2015), and for non-Newtonian flows

$$\eta_r = K_r \cdot \dot{\varepsilon}^{n-1} = \left(1 - \frac{\varphi_x}{\varphi_m}\right)^{-2} \dot{\varepsilon}^{n-1}. \tag{4.19}$$

However, this estimation fails to capture the behaviour in highly concentrated regimes where $\varphi_x \geq \varphi_m$, implying that $\eta_r \to \infty$ and that dominantly crystalline materials are undeformable, which is not the case, as experimentally demonstrated (Lavallée et al., 2007, 2013; Kendrick et al., 2013b).

An empirical equation that attempts to describe the viscosity across the dilute to concentrated regimes $0 \leq \varphi_x \leq 1$ is that of Costa (2005), later improved in Costa et al. (2007a, 2007b, 2009)

$$\eta_r = \frac{1+\left(\frac{\varphi_x}{\varphi_*}\right)^{\delta}}{\left[1-F\left(\left(\frac{\varphi_x}{\varphi_*}\right),\xi,\omega\right)\right]^{B\varphi_*}}, \tag{4.20}$$

where B is the Einstein coefficient, ostensibly 2.5 (Einstein, 1911; Lejeune and Richet, 1995) and F is an error function 'erf' denoted as:

$$F = (1-\xi)\cdot erf\left[\frac{\sqrt{\pi}}{2\cdot(1-\xi)}\left(\frac{\varphi_x}{\varphi_*}\right)\cdot\left(1+\left(\frac{\varphi_x}{\varphi_*}\right)^{\omega}\right)\right], \tag{4.21}$$

where φ_* represents the critical solid fraction at which the viscosity begins to increase exponentially; ω controls the increase in viscosity as $\varphi_x \to \varphi_*$; ξ controls the value of viscosity at $\varphi_x = \varphi_*$, and δ

controls the increase in viscosity when $\varphi_x > \varphi_*$ (defined in equations 4.19 to 4.22). With further data analysis, Costa et al., (2009) built on the empirical fitting parameters of Caricchi et al. (2007) to redefine the variables as:

$$\varphi_* = \varphi_{n2} + \Delta\varphi \frac{(\dot{\varepsilon}/\dot{\varepsilon}_c)^{n3} - (\dot{\varepsilon}_c/\dot{\varepsilon})^{n3}}{(\dot{\varepsilon}/\dot{\varepsilon}_c)^{n3} + (\dot{\varepsilon}_c/\dot{\varepsilon})^{n3}}; \quad (4.22)$$

$$\omega = \omega_{n2} + \Delta\omega \frac{(\dot{\varepsilon}/\dot{\varepsilon}_d)^{n3} - (\dot{\varepsilon}_d/\dot{\varepsilon})^{n3}}{(\dot{\varepsilon}/\dot{\varepsilon}_d)^{n3} + (\dot{\varepsilon}_d/\dot{\varepsilon})^{n3}}; \quad (4.23)$$

$$\xi = \xi_{n2} + \Delta\xi \frac{(\dot{\varepsilon}/\dot{\varepsilon}_d)^{n3} - (\dot{\varepsilon}_d/\dot{\varepsilon})^{n3}}{(\dot{\varepsilon}/\dot{\varepsilon}_d)^{n3} + (\dot{\varepsilon}_d/\dot{\varepsilon})^{n3}}; \quad (4.24)$$

$$\delta = 13 - \omega; \quad (4.25)$$

where $\varphi_{n2} = (\varphi_\infty + \varphi_0)/2$, $\Delta\varphi = (\varphi_\infty - \varphi_0)/2$, $\omega_{n2} = (\omega_\infty + \omega_0)/2$, $\Delta\omega = (\omega_\infty - \omega_0)/2$, $\xi_{n2} = (\xi_\infty + \xi_0)/2$, and $\Delta\xi = (\xi_\infty - \xi_0)/2$; subscript ∞ indicates values at very high strain rates and subscript 0 indicates values at very low strain rates. In addition, $\dot{\varepsilon}_c$ and $\dot{\varepsilon}_d$ are characteristic strain rates that are functions of the material properties. Caricchi et al. (2007) empirically found that $\dot{\varepsilon}_c = 10^{-4.4}$ s^{-1} and $\dot{\varepsilon}_d = 10^{-3.37}$ s^{-1} so $\dot{\varepsilon}_d \cong 10\ \dot{\varepsilon}_c$. Likewise, n_3 is also an empirical parameter found by Caricchi et al. (2007) as ~ 0.33. Costa et al. (2009) find that Equation 4.20 fits data from Caricchi et al. (2007) well.

Here we study the rheology of two-phase (crystals and melt) synthetic samples which cross the dilute to concentrated regimes ($0 \leq \varphi_x \leq 0.5$). Using uniaxial compressive testing, the rheological response of samples to deformation at a range of strain rates is examined and the origin of the resulting behaviours is explored.

4.2. Methods

4.2.1. Sample preparation

To achieve dense glass samples with varying crystal fractions (0, 0.1, 0.2, 0.3, 0.4 and 0.5), 53-180 μm diameter olivine crystals were sintered with Spheriglass® beads (150-250 μm) under applied load. The crystals (density 3.29 g cm^{-3}) were mixed in varying volume fractions using their density and mass, with mixtures of crushed and whole spherical glass beads (density 2.5 g cm^{-3}) (see Table 4.1 for ratios). Cylindrical alumina crucibles (with internal height of 38.18 by 25.80 mm diameter) were then carefully filled with mixtures to ensure the closest packing possible without causing particle segregation and banding. A stainless-steel plug was slotted inside the crucible to rest on top of the powder. The crucible-plug assembly was then placed between the pistons of a 100 kN Instron 8862 uniaxial press in the Experimental Volcanology and Geothermal Research Laboratory at the University of Liverpool. The pistons and sample assembly were then enclosed in an integrated three-zone, split cylinder furnace from Severn Thermal Solutions. A K-type thermocouple was in contact with the assembly to monitor sample temperature using a Fluke t3000 FC reader, while the temperatures of the top, middle and bottom zones of the furnace were controlled and monitored throughout the experiment using three Eurotherm (3216) controllers. The sample assembly was then heated at 5 °C min^{-1} to a sample temperature of ~ 770 °C, which is 220 °C above the onset of the glass

transition of Spheriglass® at ~550 °C. To achieve a fully dense sintered suspension, the powder was subjected to a constantly increasing load at 250 N min^{-1} to 2500 N, where it was held until the piston reached the calculated extension (i.e., position) required to achieve a sample with dimensions of the dense equivalent of the powder. After cooling, cylindrical cores of 6 mm diameter and 12 mm length were then drilled from the resultant glassy suspensions. For a detailed description of sample preparation, see Chapter 3 section 3.4.

Table 4.1. Ratio of olivine and Spheriglass beads used in sample preparation

olivine fraction	olivine (cm^3)	olivine (g)	Spheriglass® fraction	Spheriglass® (cm^3)	Spheriglass® whole (g)	Spheriglass® crushed (g)
0.10	0.28	0.92	0.90	2.52	3.15	3.15
0.20	0.56	1.84	0.80	2.24	2.80	2.80
0.30	0.84	2.76	0.70	1.96	1.23	3.68
0.40	1.12	3.68	0.60	1.68	1.05	3.15
0.50	1.40	4.61	0.50	1.40	0.88	2.63

4.2.2. Sample characterisation

To ensure the synthesised samples were of sufficient quality for the study, several tests were carried out to characterise any physical or chemical change to the glass during synthesis. Differential scanning calorimetry (DSC) measurements were performed using a Netzsch STA 449 C simultaneous thermal analyser (STA) at the Volcanology and Geothermal Research Laboratory at the University of Liverpool to test if the onset of the glass transition temperature, T_g, had shifted with the addition of crystals. For this purpose, small 24-32 mg chips from each synthesised samples were heated in a lidded Pt crucible at 10 °C min^{-1} to 675 °C, and cooled at 10 °C min^{-1} to 200 °C while being flushed with argon at 20 mL min^{-1}, to produce a glass with a structure locked in at a known cooling rate; the sample was then reheated at 10 °C min^{-1} to 675 °C to assess the calorimetric response of the glass in the T_g interval and compare it with data obtained for glasses (with different crystallinity) at the same rate (for more detail see Chapter 3, section 3.4.2.2.). Additionally, uncovered, carbon-coated thin sections were prepared from samples of each crystallinity and were subject to Quantitative Evaluation of Minerals by SCANning electron microscopy (QEMSCAN®) WellSite in the Diagenesis Laboratory at the University of Liverpool (see Chapter 3, section 3.4.2.5 for a detailed description). As samples were required to have a negligible porosity, the volume of connected and isolated pores was assessed using a 1cc AccuPyc 1340 helium pycnometer from Micromeritics (Chapter 3, section 3.4.2.1.). Only dense, $\varphi_p < 0.05$, homogeneous samples, with a glass transition temperature akin to the Spheriglass® phase where used in the study.

4.2.3. Dry maximum packing fraction

For an estimation of the dry maximum packing of the crystals, a cylindrical alumina crucible (internal dimensions of 38.18 height by 25.80 mm diameter) was gradually filled with the olivine crystals, where the sides of the crucible were tapped to ensure a maximum packing. The resulting volume of the crystals was then calculated as $V_{crystals\_calc} = \pi r^2 \cdot h$, where r is the diameter of the crucible, and h is the height of the crystals in the crucible. The crucible was then placed in a 1cc AccuPyc 1340 helium pycnometer from Micromeritics and the exact volume of the crucible and crystals measured giving $V_{crystals+crucible}$. The crucible was then measured on its own giving $V_{crucible}$. The dry maximum packing was then calculated as:

$$\varphi_{dry} = \frac{V_{crystals+crucible} - V_{crucible}}{V_{crystals\_calc}} = \frac{V_{crystals}}{V_{crystals\_calc}} \quad (4.26)$$

4.2.4. Deformation experiments

The synthetic samples were used to investigate the effects of crystals ($0 \leq \varphi_x \leq 0.5$) on the rheology of suspensions (Table 4.2). The specimens were placed in the same uniaxial press and furnace apparatus described above and heated to 610 °C at a rate of 5 °C min^{-1}, monitored by a K-type thermocouple in contact with the sample. Here, four types of deformation experiment were performed. Initially a sample from each crystal content was deformed uniaxially at a constant strain rate of 10^{-4} s^{-1} until the applied stress plateaued for a significant length of time (Fig. 4.1a). These preliminary tests gave an initial insight into the rheological behaviour of the material and served as a repeat control to stepped strain rate tests performed later. Further initial testing was carried out on a 0.1 and a 0.3 crystal content sample, where stain rates were stepped from 10^{-6} s^{-1} to 10^{-5} s^{-1}, then back to 10^{-6} s^{-1}, before a final strain rate of 10^{-3} s^{-1} was applied (Fig. 4.1b). The 0.3 fraction sample was taken a step further to a strain rate of 10^{-2} s^{-1} (Fig. 4.1bi). These tests looked at the effects strain and strain rate had on the response of the samples and allowed for the design of a final experimental procedure. Samples from each crystal content were taken to total strains of 0.25, stepping from 10^{-6} s^{-1} to 10^{-5} s^{-1}, 10^{-4} s^{-1}, 10^{-3} s^{-1}, before finally being taken to 10^{-2} s^{-1} (Fig. 4.1c). A further constant strain rate test was carried out at 10^{-1} s^{-1} on the 0.0 and 0.1 fraction samples until brittle failure was reached (Fig. 4.1d). See Table 4.2 for a detailed experimental list.

4.2.5. Data processing and filtering

The 100 kN Instron 8862 uniaxial press used in the deformation experiments only allows accurate control between loads of 100 N and 100 kN, at applied strain rates between 10^{-6} and 10^{-1} s^{-1} (see Lamur, 2018, for a detailed description). Therefore, the experimental steps in which the load response to the imposed strain rate was < 100 N and the percentage variation in peak load was > 50% were discarded in later analysis (see Table 4.2).

Table 4.2. Samples tested with experimental conditions, resulting response and results from calculations carried out. Variations in recorded stress that were > 50% and measured loads < 100 N are highlighted in red. Samples with both load and variation marked were discounted from the study. N/A: Not applicable.

Sample Name	Sample temperature (°C)	Crystal fraction	Log (Strain rate) (s^{-1})	Peak load (N)	Peak stress (MPa)	Variation (%)	Total Strain (%)	Log (η_a) (Pa.s)	Log (η_r)	Critical packing fraction	K	n	R^2	De number (Coats et al., 2018)	De number (Eqn. 4.28)
Oliv_10_600_-4	628	0.1	-4.00	44.67	1.65	72	1.22	9.72	-0.09	0.82	12422	0.89	1.00	N/A	N/A
Oliv_20_600_-4	634.5	0.2	-4.00	192.48	7.08	42	1.65	10.27	0.46	0.82	16061	0.84	0.99	6.85E-05	4.86E-05
Oliv_30_600_-4	629.1	0.3	-4.00	329.87	12.07	29	0.81	10.54	0.73	0.82	6250	0.74	0.99	1.38E-04	4.07E-05
Oliv_40_600_-4	624	0.4	-4.00	568.71	20.81	20	0.51	10.80	0.99	0.82	3008	0.55	1.00	7.00E-05	3.30E-05
Oliv_50_600_-4	611.5	0.5	-4.00	881.23	31.95	13	0.66	11.01	1.20	0.82	3243	0.55	0.99	1.34E-04	2.52E-05
Oliv_10_600_stepped_1	not well constrained	0.1	-5.99	21.54	0.79	63	0.02	11.65	1.84	0.57	12422	0.89	1.00	N/A	N/A
	not well constrained	0.1	-5.00	25.96	0.95	75	0.19	10.57	0.77	0.66	12422	0.89	1.00	N/A	N/A
	not well constrained	0.1	-6.00	9.50	0.35	108	0.23	10.73	0.92	0.57	12422	0.89	1.00	N/A	N/A
	not well constrained	0.1	-3.05	319.05	11.71	38	0.25	9.61	0.20	0.66	12422	0.89	1.00	N/A	N/A
Oliv_30_600_stepped_1	611.4	0.3	-5.99	7.72	0.28	188	0.03	11.39	1.28	0.57	6250	0.74	0.99	N/A	N/A
	611.4	0.3	-5.00	38.42	1.41	79	0.20	10.85	1.35	0.66	6250	0.74	0.99	N/A	N/A

	611.4	0.3	-6.00	9.81	0.36	111	0.23	10.47	1.45	0.57	6250	0.74	0.99	N/A	N/A
	611.4	0.3	-3.00	1611.71	59.29	13	1.06	10.24	0.43	0.94	6250	0.74	0.99	N/A	N/A
	611.4	0.3	-2.02	6285.05	231.22	5	1.24	9.84	0.02	0.98	6250	0.74	0.99	N/A	N/A
SG_0_600_stepped_1	610	0	-5.99	-3.29	-0.12	-487	0.03	10.70	0.89	N/A	16728	0.91	1.00	N/A	N/A
	610	0	-5.00	-3.23	-0.12	-474	0.21	9.88	0.07	N/A	16728	0.91	1.00	N/A	N/A
	610	0	-4.00	69.05	2.53	94	0.65	9.89	0.08	N/A	16728	0.91	1.00	N/A	N/A
	610	0	-3.00	841.03	30.85	36	1.42	9.94	0.13	0.54	16728	0.91	1.00	6.41E-04	6.41E-04
	610	0	-2.01	6660.05	244.27	2	2.31	9.81	0.00	0.54	16728	0.91	1.00	6.22E-03	6.22E-03
Oliv_10_600_stepped_2	612.1	0.1	-6.00	-4.41	-0.16	-271	0.02	10.87	1.06	0.57	12422	0.89	1.00	N/A	N/A
	612.1	0.1	-5.00	-1.81	-0.07	-994	0.18	9.53	-0.28	0.66	12422	0.89	1.00	N/A	N/A
	612.1	0.1	-4.00	70.00	2.58	83	0.58	9.90	0.09	0.82	12422	0.89	1.00	N/A	N/A
	612.1	0.1	-3.00	726.03	26.74	24	1.32	9.88	0.07	0.94	12422	0.89	1.00	6.43E-04	5.74E-04
	612.1	0.1	-2.00	5613.87	206.74	3	2.22	9.72	0.09	0.98	12422	0.89	1.00	6.42E-03	5.76E-03
Oliv_20_600_stepped_1	612	0.2	-6.00	-0.32	-0.01	-4290	0.02	10.48	0.67	0.57	16061	0.84	0.99	N/A	N/A
	612	0.2	-5.00	10.71	0.39	210	0.17	10.15	0.35	0.66	16061	0.84	0.99	N/A	N/A
	612	0.2	-4.00	158.19	5.81	16	0.54	10.26	0.45	0.82	16061	0.84	0.99	5.42E-05	4.86E-05
	612	0.2	-3.00	1529.32	56.17	24	1.23	10.20	0.39	0.94	16061	0.84	0.99	7.95E-04	5.05E-04

	612	0.2	-2.03	7748.82	284.58	6	2.08	9.90	0.09	0.98	16061	0.84	0.99	5.43E-03	4.82E-03
Oliv_30_600_stepped_2	611.7	0.3	-6.00	16.38	0.60	76	0.03	11.39	1.58	0.57	6250	0.74	0.99	N/A	N/A
	611.7	0.3	-5.00	46.07	1.69	61	0.21	10.85	1.04	0.66	6250	0.74	0.99	N/A	N/A
	611.7	0.3	-4.00	263.86	9.68	37	0.68	10.47	0.66	0.82	6250	0.74	0.99	1.03E-04	4.07E-05
	611.7	0.3	-3.00	1712.99	62.87	12	1.59	10.24	0.43	0.94	6250	0.74	0.99	1.28E-03	4.37E-04
	611.7	0.3	-2.02	7083.37	259.97	6	2.62	9.84	0.03	0.98	6250	0.74	0.99	8.75E-03	4.26E-03
Oliv_40_600_stepped_1	613.3	0.4	-6.00	63.79	2.33	36	0.02	11.94	2.13	0.57	3008	0.55	1.00	1.26E-06	1.90E-07
	613.3	0.4	-5.00	154.11	5.63	27	0.16	11.30	1.49	0.66	3008	0.55	1.00	6.37E-06	2.54E-06
	613.3	0.4	-4.00	497.17	18.17	23	0.52	10.75	0.94	0.82	3008	0.55	1.00	5.46E-05	3.30E-05
	613.3	0.4	-3.00	2129.88	77.85	11	1.90	10.34	0.53	0.94	3008	0.55	1.00	7.88E-04	3.70E-04
	613.3	0.4	-2.03	6064.96	221.69	1	1.96	9.80	0.01	0.98	3008	0.55	1.00	5.38E-03	3.54E-03
Oliv_50_600_stepped_2	609.2	0.5	-6.02	132.71	4.81	35	0.02	12.26	2.45	0.57	3243	0.55	0.99	4.14E-06	7.58E-08
	609.2	0.5	-5.00	252.69	9.15	24	0.28	11.51	1.70	0.66	3243	0.55	0.99	1.35E-05	1.56E-06
	609.2	0.5	-4.00	734.55	26.60	18	0.55	10.92	1.11	0.82	3243	0.55	0.99	9.57E-05	2.51E-05
	609.2	0.5	-3.00	2654.69	96.12	13	1.31	10.43	0.62	0.94	3243	0.55	0.99	1.01E-03	3.02E-04
	609.2	0.5	-2.42	2560.16	92.70	6	2.08	9.85	0.04	0.98	3243	0.55	0.99	9.46E-04	1.20E-03
Oliv_10_600_-	614	0.1	-1.00	16898.00	620.64	N/A	3.82	N/A	N/A	0.99	12422	0.89	1.00	2.21E-02	5.78E-02

1_1															
SG_0_600_-1_1	614.4	0	-1.00	18481.76	678.99	N/A	0.84	N/A	N/A	N/A	16728	0.91	1.00	1.91E-02	6.43E-02

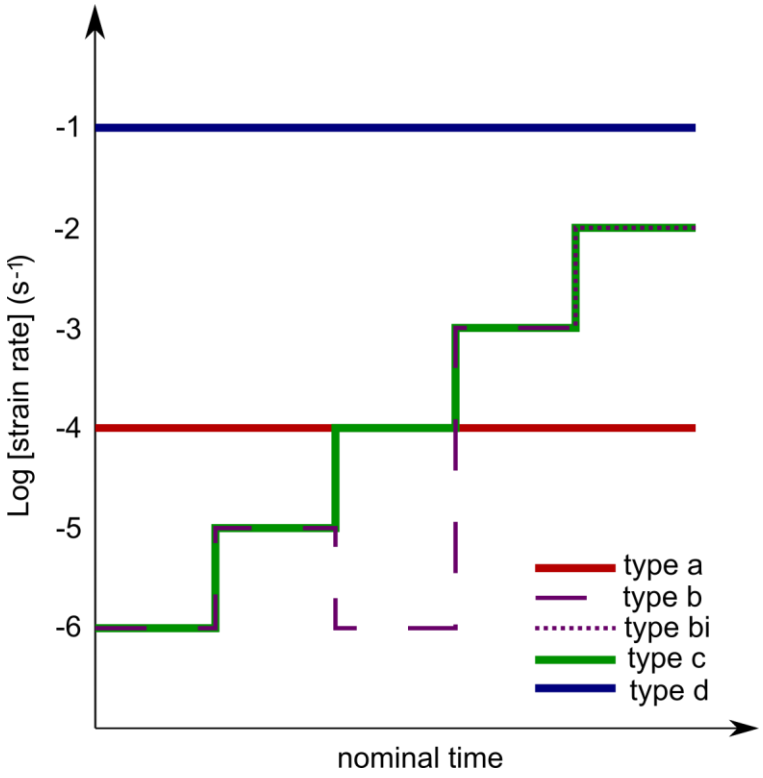

Figure 4.1. Types of deformation experiment carried out. Type a and d are constant strain rate experiments, while type b, bi and c are stepped strain experiments.

4.2.6. Data analysis

Raw displacement data were treated to account for the compliance of the pistons at each experimental temperature. For samples that had a viscous response, the apparent viscosities of each sample at each strain rate were then calculated via Gents' (1960) equation:

$$\eta_a = \frac{2\pi F h^4}{3V\dot{\varepsilon}(V+2\pi h^3)} \quad (4.27)$$

where F is the force applied on the sample; h is the initial height of the sample and V is the initial volume of the sample, which was assumed to be isovolumetric during the experiment (Hess et al., 2007). Mean apparent viscosities were then taken as the average value over the plateau in viscosity (defined by variation of approximately ± 10 %).

4.2.7. Viscosity modelling

In order to apply the Maron-Pierce equation (1956) (Eqn. 4.18) and the reformulated version of the Hershel-Buckley (1926) model (Eqn. 4.19) (after Mader et al., 2013), the maximum packing fraction of the olivine crystals (see Chapter 3) was calculated using Equation 4.14 and 4.15. Additionally, for the Hershel-Buckley (1926) model the flow index, n, (Eqn 4.13) was calculated. Both models were then applied to the data.

The empirical parameters of the Costa et al. (2005; 2009) models were adjusted to fit the characteristics of the system (Eqn. 4.20 and 4.21). Critically this involved adjusting the ω parameter

as this controls the increase in viscosity as $\varphi_x \rightarrow \varphi_*$, which is the regime of experimental interest ($0 \leq \varphi_x \leq 0.5$). Therefore, the ω_{n2}, $\Delta\omega$ and $\dot{\varepsilon}_d$ variables $n3$ (Eqn. 4.23) were required to be adjusted until an empirical fit was reached. Following Costa et al. (2009), variable $n3$ was kept as 0.33. The characteristic strain rate, $\dot{\varepsilon}_d$, was increased by an order of magnitude to 4.27×10^{-3}, which is within the range over which the melt phase is expected to become non-Newtonian (Eqn. 4.10). ω_{n2} and $\Delta\omega$ are both calculated from ω_0 and ω_∞, which are the change in viscosity with crystal content, $d\eta_r/d\varphi_x$, at very low and very high strain rates, respectively.

As the crystals' characteristics in this study are different to those used in the Caricchi et al., (2007) study, the critical packing fraction, φ_*, had to be calculated so as to reflect the crystal geometries used in this study (Eqn. 4.22). This required values of the critical packing fraction at very high, φ_∞, and very low strain rates, φ_0. At very low strain rates the crystals are likely to act as rigid bodies and φ_0 can be taken as the dry maximum packing fraction. Whereas at very high strain rates crystals can both deform plastically and/or fail, theoretically leading to a critical solid fraction that approaches unity at infinite strain rates as the crystal size approaches zero. Using these values, the φ_* term was calculated for the synthetic samples used here via Equation 4.22.

4.3. Results

4.3.1. Sample characteristics

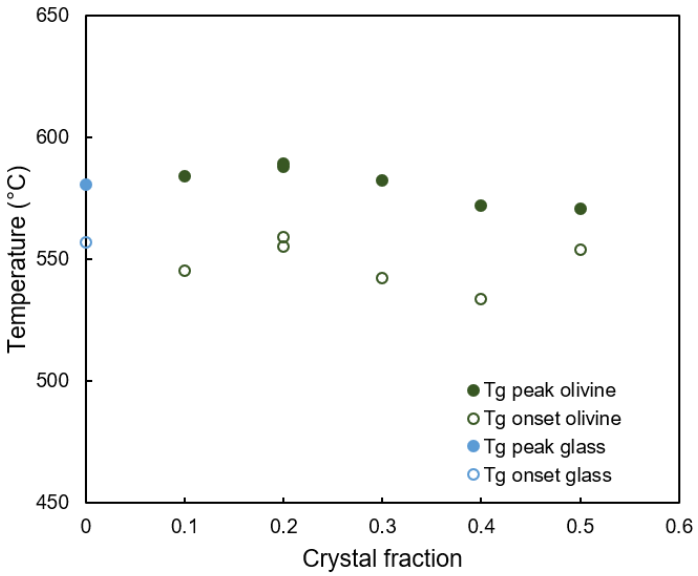

Figure 4.2. Glass transition temperature, T_g, peak and onset temperatures of samples measured by DSC for sintered Spheriglass® (blue) and sintered olivine samples (green). T_g onset and T_g peak remains comparatively constant with the addition of crystal particles.

The glass transition is a region in temperature-time space separates glassy unrelaxed behaviour from liquid relaxed behaviour in viscoelastic fluids. On short observation timescales, the glass transition can be described by the glass transition temperature, T_g (Dingwell and Webb, 1989). On heating a solid sample through its melting point, it will show an endothermic peak. The onset of this peak

signals the initiation of depolymerisation, while the peak signals maximum depolymerisation (Hale, 2002). The onset and peak of the glass transition temperature were measured for each crystal fraction, taken as the temperature at which the DSC signal deviated from the mean and peaked, respectively. The glass transition temperatures only mildly fluctuate with the addition of olivine crystals into the Spheriglass® phase (Fig. 4.2).

Through helium pycnometery, and applying Equation 4.26, the dry maximum packing fraction, φ_{dry}, of the olivine crystals was found to be approximately 0.54.

To verify the absolute content and distribution of phases within samples, QEMSCAN® data (Fig. 4.3) were analysed, showing that the synthetic sintered samples contain Spheriglass® and olivine crystals with minor traces of enstatite and chromite. Some Spheriglass® has crystallised during the sintering process at temperatures of 750 °C but this accounts for < 0.03 by area and so can be considered negligible. Additionally, porosity is also negligible: for crystallinities of $0 \leq \varphi_x \leq 0.4$, porosity is < 0.03, while for samples with $\varphi_x = 0.5$ porosity < 0.08. Pores are primarily located adjacent to crystals (Fig. 4.3).

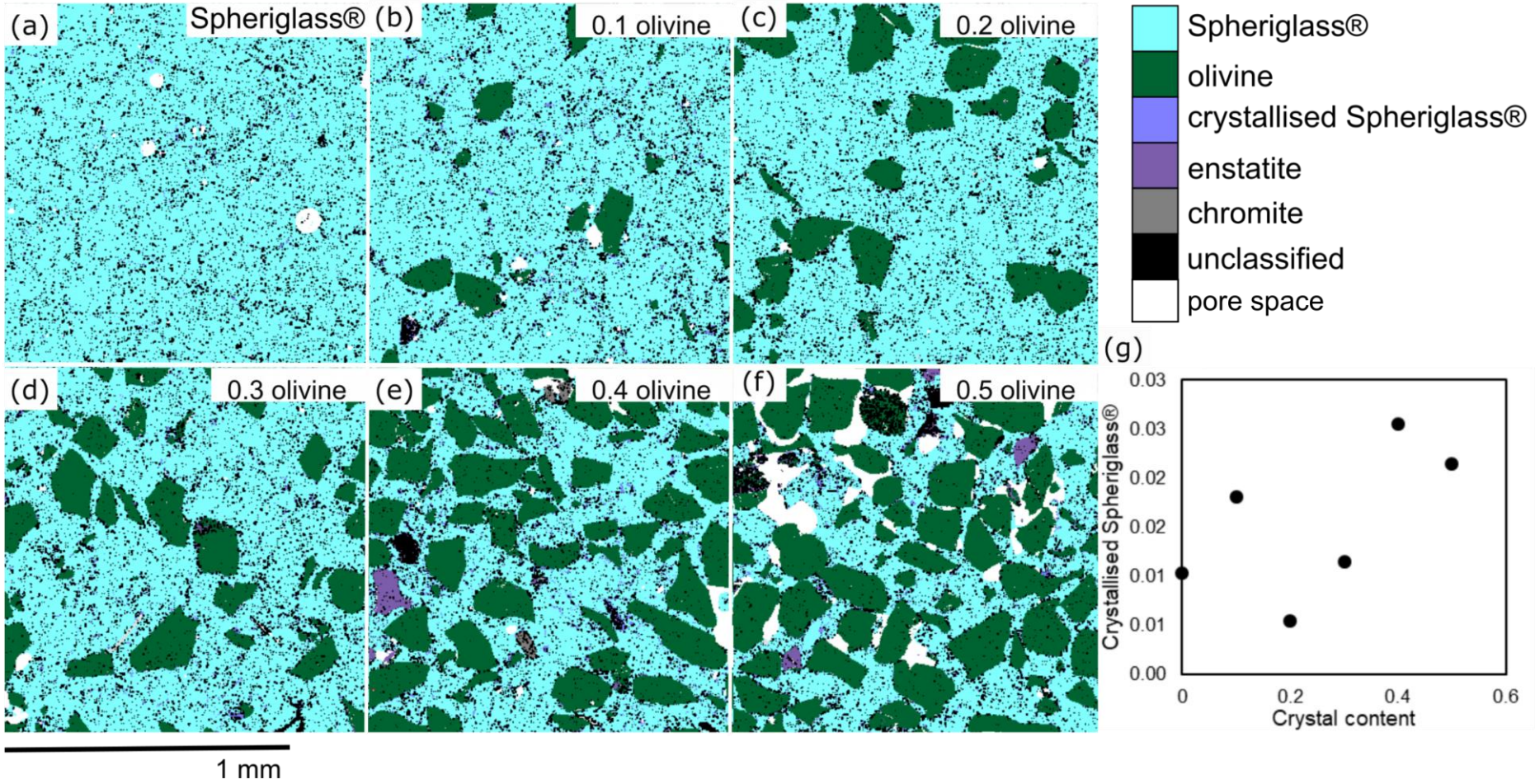

Figure 4.3. QEMSCAN® analysis of samples sintered under load at 750 °C for (a) Spheriglass® only, (b) 0.1 olivine, (c) 0.2 olivine, (d) 0.3 olivine, (e) 0.4 olivine, and (f) 0.5 olivine. QEMSCAN® maps show the distribution of phases within a material that can be used to assess the absolute contents of these components as well as their interrelation and distribution within the sample. Total amounts of crystallised Spheriglass® (g) are < 0.03 and do not vary systematically with phenocryst content.

4.3.2. Stress-strain data

The absolute stresses reached by the samples increased with crystal content and applied strain rate (Table 4.2). By plotting the normalised stress $\bar{\sigma} = \sigma/\sigma_{max}$, where σ_{max} is the maximum stress reached in any experiment, against strain, the stress-strain curves of each experiment can be compared. As detailed in section 4.2.5, certain data were omitted from analysis if they did not exceed 100 N and that had a variation greater than 50% around their peak load were not involved in data analysis (see red categories in Table 4.2). This mainly affected weaker, low crystallinity samples at lower strain rates (e.g. for crystal fractions ≤ 0.3 tested at $\dot{\varepsilon} < 10^{-4}s^{-1}$).

Figure 4.4 shows the stress-strain curves for the stepped strain experiments, where samples were taken to 0.25 strain (type c, Fig. 4.1c). Figure 4.5a-f segment the stress-strain curves from Figure 4.4 into the response from each applied strain rate. Figure 4.6 then shows the stress strain curves for the remaining experiment types (Fig. 4.1 a,b,bii,d).

At every applied strain rate, the stress response is initially elastic and recoverable. Here, when recordable by the machine, the stress-strain curve is linear (Fig. 4.4, Fig. 4.5). After this portion, each stress curve begins to plateau with strain signalling a viscous response (Fig. 4.4, Fig. 4.5). Stresses then either stay steady for a given strain rate (e.g. Fig. 4.5d iii); increase (i.e., strain hardening) if pore collapse (e.g. Fig. 4.5a iv), or decreases (strain weaken), if fractures propagate or crystals bend/align (e.g. Fig. 4.5e iv, Kendrick et al., 2013b). The evolution to strain weakening is also described as transitional behaviour which punctuates the viscous to brittle transition in deforming media, and after which a sample may rupture (Cordonnier et al., 2012a; Coats et al., 2018; Wadsworth et al., 2018). Beyond this rheological transition, a sample may also exhibit dominantly brittle behaviour, where stress increases elastically with strain before a sharp decrease occurs, signalling sample failure with little or no contribution of viscous flow (e.g. Coats et al., 2018).

For the type c stepped experiments (Fig. 4.1c, Fig. 4.4, Fig. 4.5), at strain rates of 10^{-6} and 10^{-5} s^{-1} the response is viscous, and the stress remains constant for each suspension examined across the range of crystal contents 0.0-0.5 (Fig. 4.5a-f, i&ii). At 10^{-4} s^{-1} the stress of the 0.0-0.3 crystal fractions remains constant (Fig. 4.5a-d iii), again signalling steady viscous flow. For samples with crystal fractions of 0.4 and 0.5, increasing the strain rate to 10^{-4} s^{-1} results in a slight strain weakening (Fig. 4.5e-f iii). As strain rate is increased further to 10^{-3} s^{-1}, samples with crystal fractions of 0.0-0.2 exhibit viscous flow with an element of strain hardening, evidenced by the slight increase in peak stress over strain (Fig. 4.5a-c iv). Meanwhile in the 0.3 fraction sample stress is constant with strain (Fig. 4.5d iv). At crystal fractions of 0.4-0.5 the curves show apparent strain weakening (Fig. 4.5e-f iv). When the strain rate is increased to the final value of 10^{-2} s^{-1}, the stress for fractions 0.0-0.4 plateaus with strain (Fig. 4.5a-e v). In the 0.2 and 0.3 samples (Fig. 4.5c-d v) there appears to also be small dips in stress, similar behaviour has previously been linked to evidence of microcracking (e.g. Tuffen et al., 2008; Cordonnier et al., 2012a). The 0.5 sample broke macroscopically, as rate was being increased, before reaching the final 10^{-2} s^{-1} strain rate (Fig. 4.5f v).

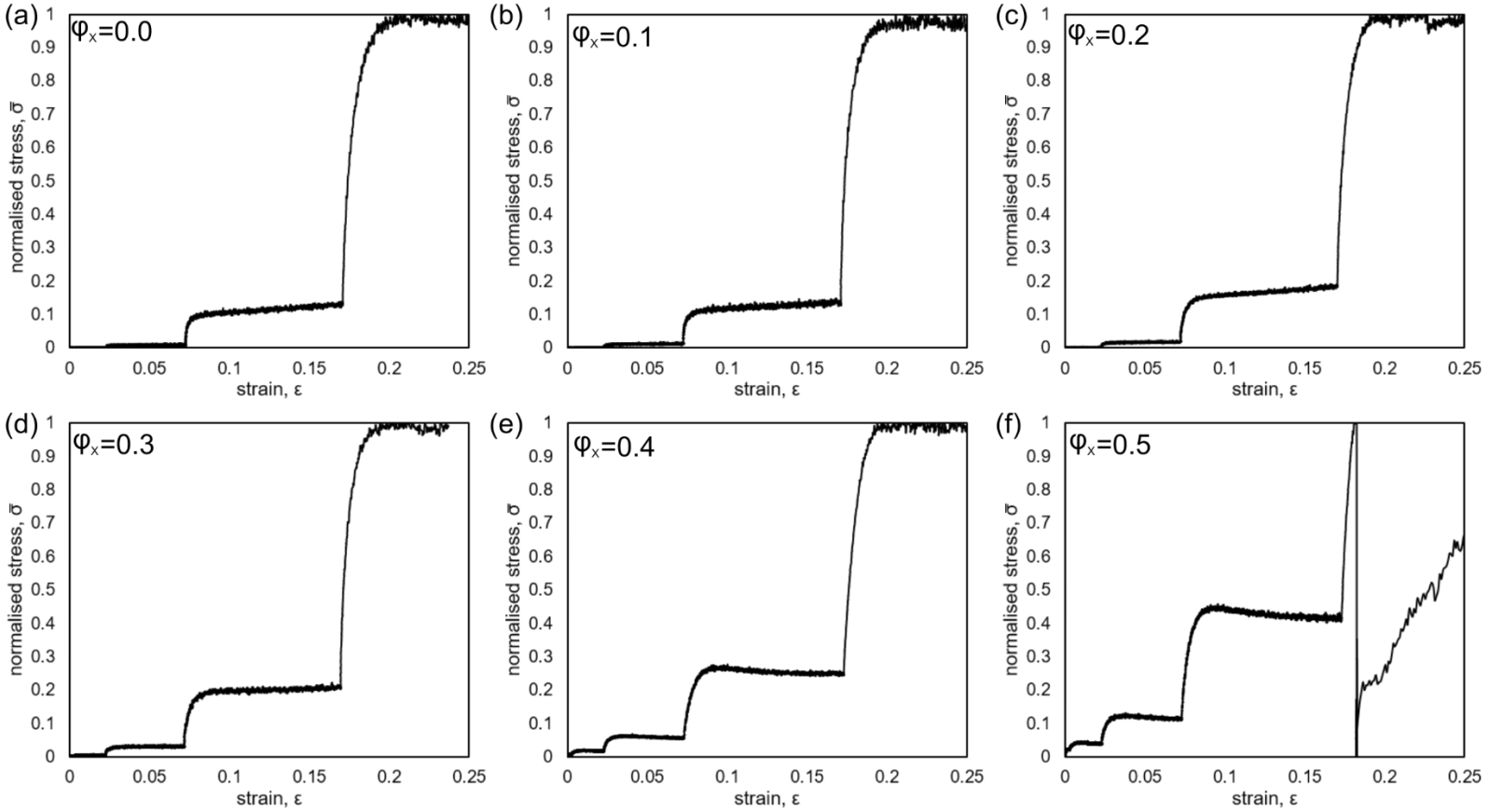

Figure 4.4. Normalised stress ($\bar{\sigma} = \sigma/\sigma_{max}$, where σ_{max} is the maximum stress reached in any experiment) against strain during stepped experiment type c (Fig. 4.1c) for (a) 0.0, (b) 0.1, (c) 0.2, (d) 0.3, (e) 0.4 and (f) 0.5 crystal fraction of olivine. At every applied strain rate, the initial stress response is linear, elastic and recoverable, then each stress curve begins to plateau with strain signalling a viscous response. Stresses then either remain constant, strain harden, strain weaken or completely drop off due to sample failure.

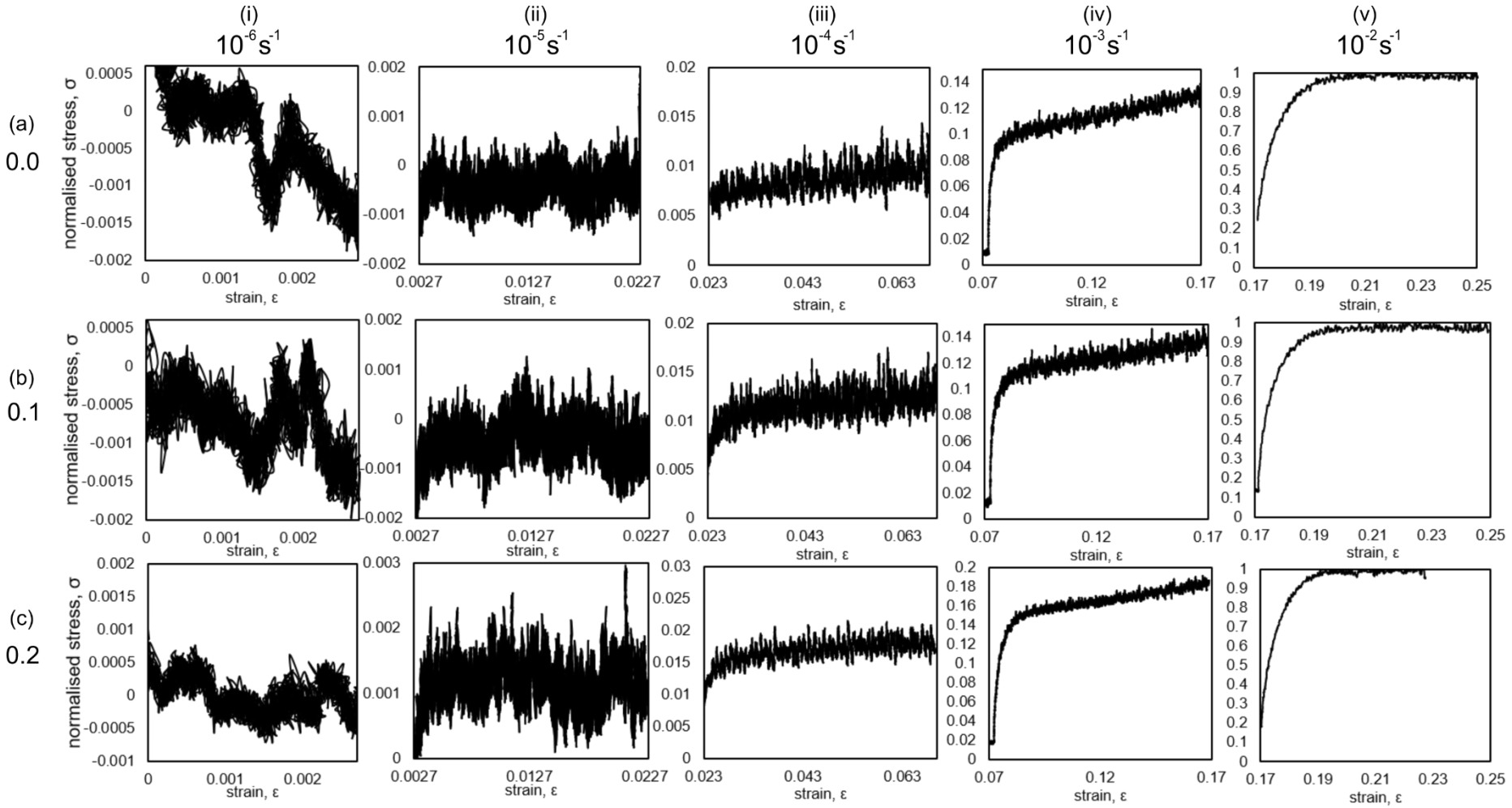
(i)
$10^{-6}s^{-1}$
(ii)
$10^{-5}s^{-1}$
(iii)
$10^{-4}s^{-1}$
(iv)
$10^{-3}s^{-1}$
(v)
$10^{-2}s^{-1}$
(a)
0.0
(b)
0.1
(c)
0.2
normalised stress, σ
strain, ε

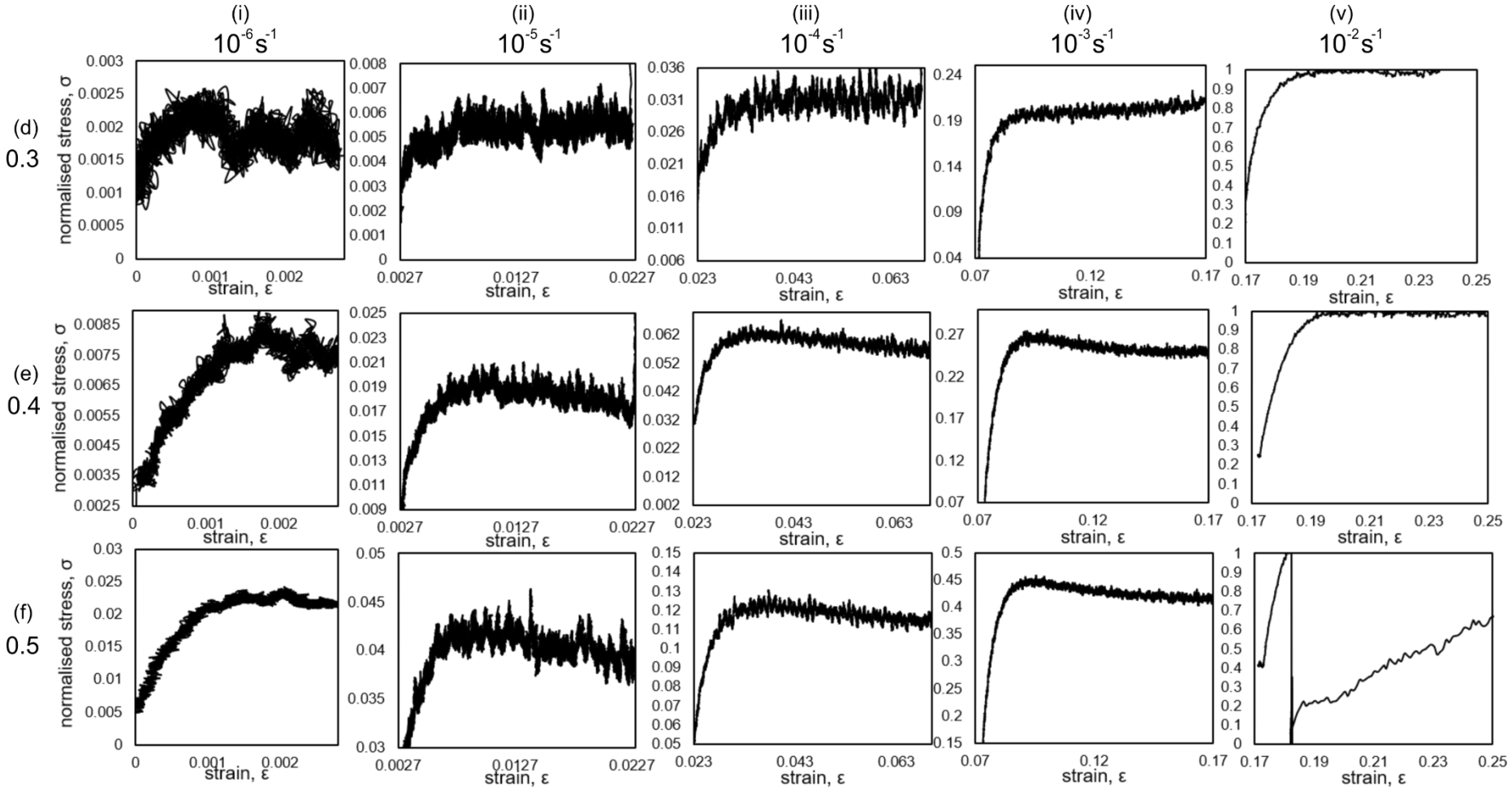

Figure 4.5. Normalised stress-strain curves for (a) 0.0, (b) 0.1, (c) 0.2, (d) 0.3, (e) 0.4 and (f) 0.5 olivine crystal fractions, segmented into applied strain rates (i) 10^{-6} s^{-1}, (ii) 10^{-5} s^{-1}, (iii) 10^{-4} s^{-1}, (iv) 10^{-3} s^{-1}, and (v) 10^{-2} s^{-1}.

For the constant strain rate experiments at 10^{-4} s^{-1} (Fig 4.1a), the 0.1 and 0.2 fraction samples responded with a strain hardening stress-strain curve (Fig 4.6a-b); the 0.3 fraction sample with a steady plateau (Fig 4.6c), and the 0.4 and 0.5 fraction samples with a steady plateau that has small dips in stress with increasing strain (Fig 4.6d-e). For the stepped experiments on 0.1 and 0.3, that returned to a previously applied strain rate step (Fig. 4.1. type bi and ii), their stress-strain curves plateau at each step (Fig. 4.6f- g). On returning to the previously applied strain rate step it appears that the 0.1 fraction sample appeared weaker and the 0.3 fraction appeared stronger (Table 4.2). However, the response of the two samples at this rate is below the response recordable of the machine. One of each of 0.0 and 0.1 fraction samples were taken to 10^{-1} s^{-1} in single-step experiments. Both samples failed macroscopically with preceding minor stress drops that can be associated with microscopic fracturing (Fig 4.6h-i).

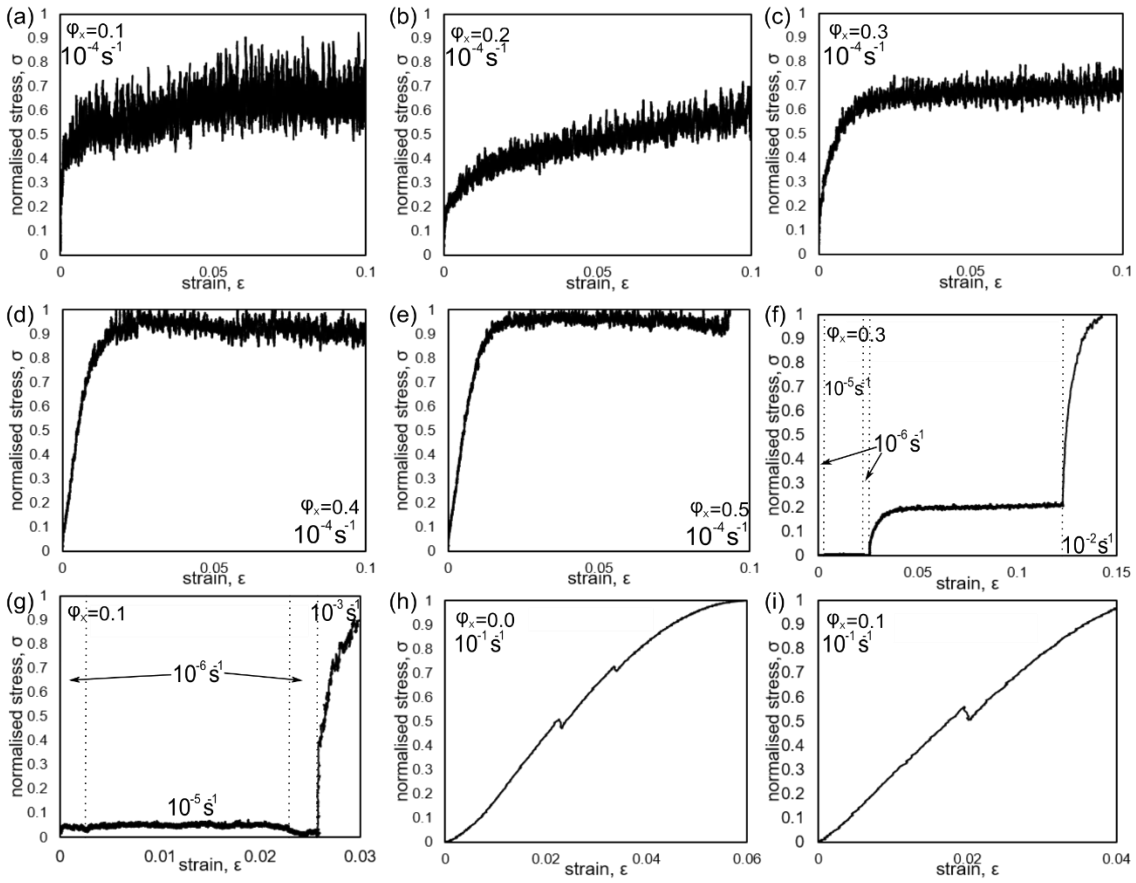

Figure 4.6. Normalised stress-strain curves for (a-e) constant strain rate experiments at 10^{-4} s^{-1}, alternative stepped experiments (f-g), and constant strain rate experiments at 10^{-1} s^{-1}. At 10^{-4} s^{-}1 the (a) 0.1 and (b) 0.2 fraction samples responded with a strain hardening; the (c) 0.3 fraction sample responded with a steady plateau, and the (d) 0.4 and (e) 0.5 fraction samples responded with a plateau with slight dips in stress. For the stepped experiments on (f) 0.3 and 0.1 (g), the stress-strain curves plateau at each step. At 10^{-1} s^{-1}, both the (h) 0.0 and (i) 0.1 olivine fraction samples failed macroscopically with preceding minor stress drops.

4.3.3. Microstructural deformation quantification via QEMSCAN®

QEMSCAN® images of samples after deformation show the microstructural damage that has taken place (Fig. 4.7). The small number of vesicles present in the samples (< 0.03) are flattened and elongate perpendicular to the applied stress direction during sintering (Fig 4.8a). From Figure 4.8 it is evident that most of the crystals have rotated to align their major axis perpendicular to the applied stress. Fractures appear in crystals in the 0.1 fraction sample and the number of fractured crystals, along with the number of fractures in each crystal, increases with crystal fraction. These fractures are parallel to the applied stress direction and are predominantly found in the regions of high stress (Fig. 4.9a). The fractured region appears to spread with crystal fraction. Microfractures in the 0.5 crystal fraction samples can be seen propagating from crystals into the melt region (Fig. 4.8f). These fractures are significant in the 0.5 fraction sample, where they have coalesced to result in macroscopic failure, observable from the characteristic hourglass shape of the sample which is often achieved during uniaxial compression of cylindrical brittle materials (Fig. 4.9a). Porosity is increased during deformation by the creation of fractures. This porosity increase creates a measurable dilatancy between the undeformed (Fig. 4.3) and deformed (Fig. 4.7) samples at a crystal fraction of 0.3 which increases with crystal fraction (Fig. 4.9b).

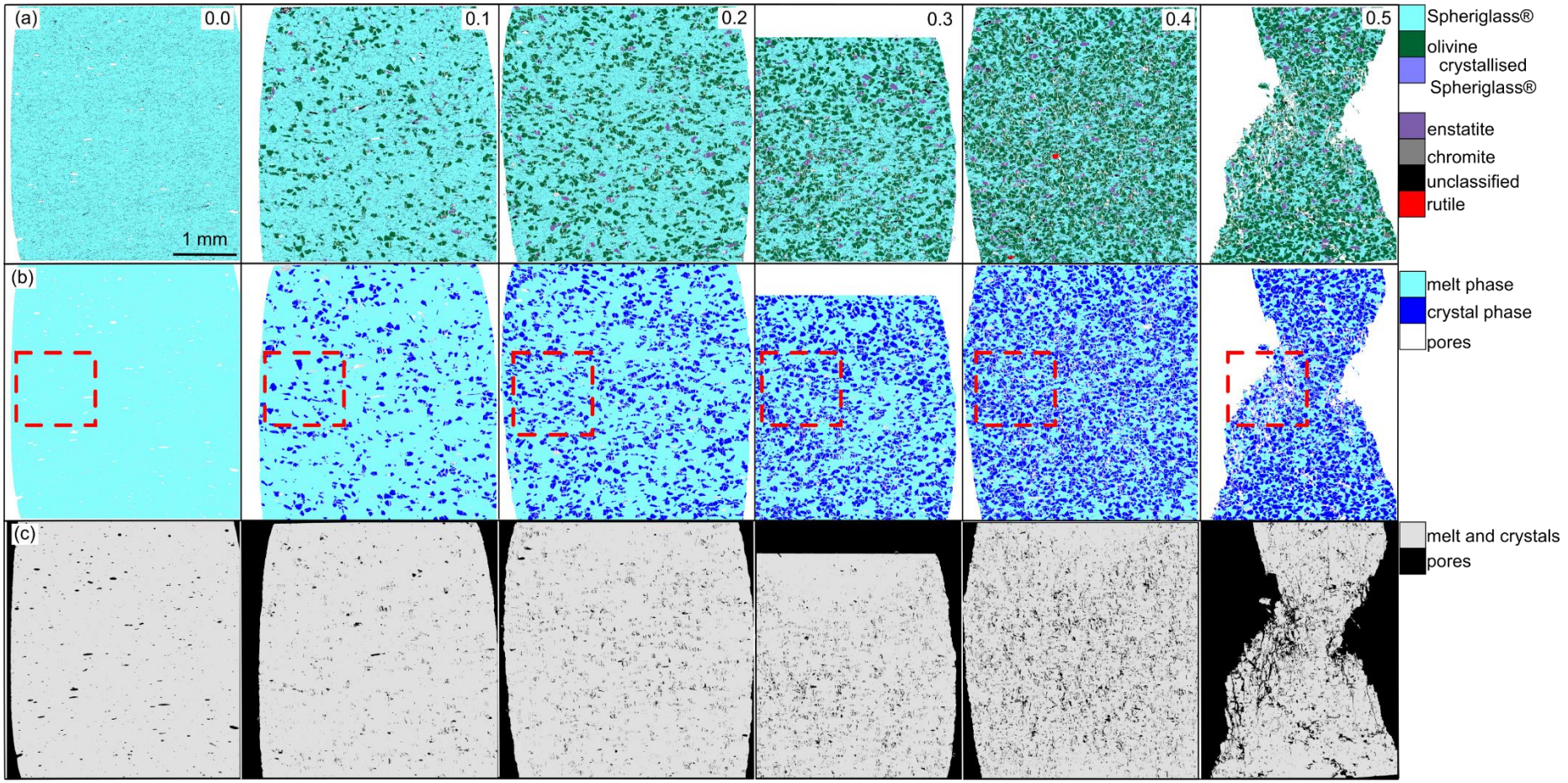

Figure 4.7. QEMSCAN® data for samples after stepped deformation to a final strain rate of 10^{-2} s^{-1} (Fig. 4.1c) for crystal fractions 0.0 to 0.5, samples are shown with their major principal stress axis aligned vertically. Note only the 0.5 fraction sample underwent complete macroscopic behaviour. (a) shows full mineral data for samples, (b) shows three phases, glass, crystals and bubbles, and (c) shows pores only in black. Red, dashed boxes show the areas zoomed into in Fig. 4.8.

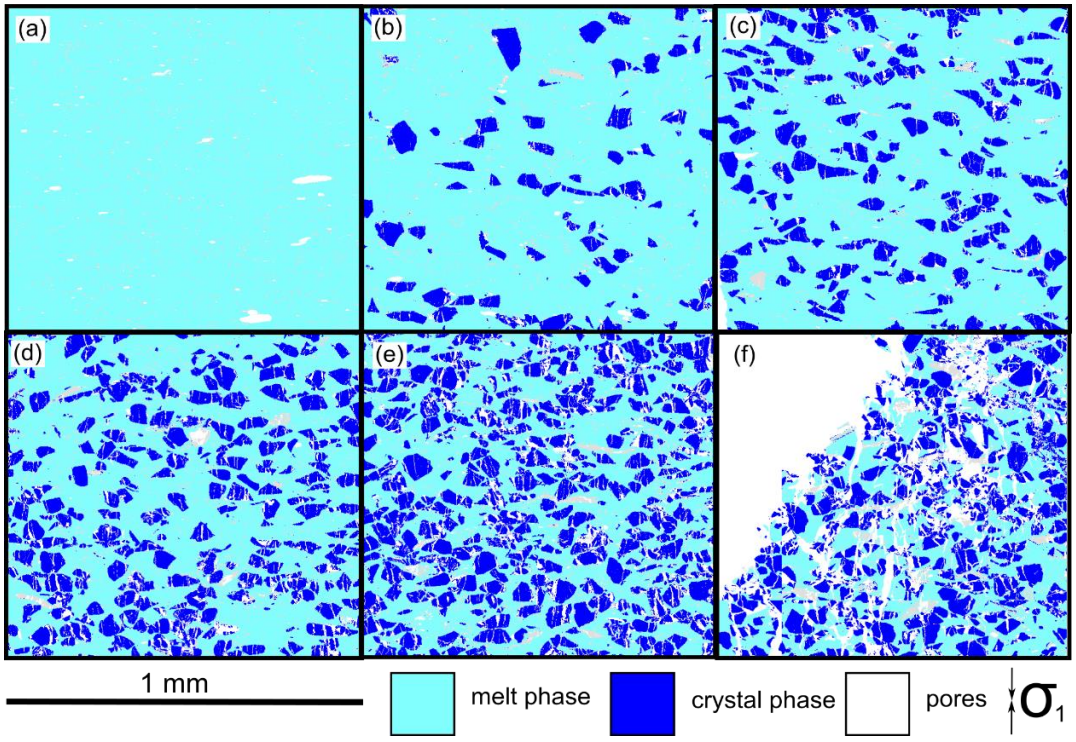

Figure 4.8. Zoomed in sections from QEMSCAN® data in Fig. 4.7. for (a) 0.0, (b) 0.1, (c) 0.2, (d) 0.3, (e) 0.4, (f) 0.5 fraction olivine. Pores are elongated so their major axis is parallel to σ_1, and crystals have rotated perpendicular to σ_1. The number of fractured crystals and number of fractures within crystals increases with crystal fraction. In the 0.5 fraction fractures have propagated into the melt and have coalesced to cause macroscopic deformation.

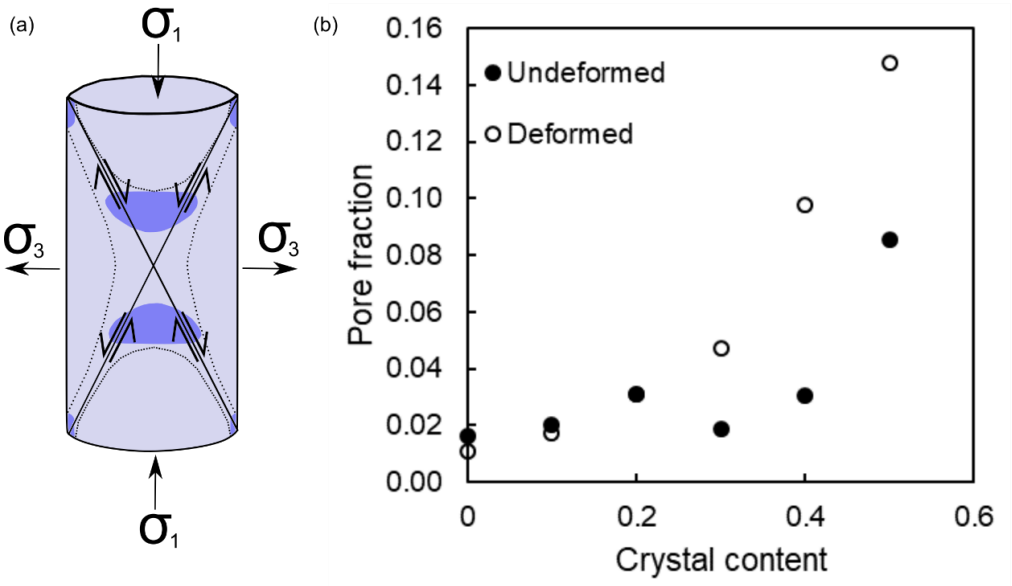

Figure 4.9. (a) Schematic of a core under uniaxial stress, where σ_1 is the major principal stress direction, $\sigma_3$is the minor principal stress direction. Internal arrows show direction of shear, shaded regions show the most critically stressed zones and dashed lines indicate the probable 'hourglass' pattern of collapse (modified from Hawkes and Mellor, 1970; Paterson and Wong, 2005). (b) Porosity with crystal content measured from QEMSCAN® data for undeformed and deformed samples. After the 0.3 crystal fraction, there is a significant difference between the porosity of the undeformed and deformed samples.

4.3.4. Viscosities

Apparent viscosities were calculated via Gent's equation (Eqn. 4.24) for each strain rate increment (Fig. 4.10). The apparent viscosity increases with crystal content and non-Newtonian behaviour is observed in suspensions with ≥ 0.2 crystal fraction. These non-Newtonian suspensions exhibit shear-thinning behaviour and the logarithm of the viscosities decreases linearly with increasing strain rate until they a strain rate of 10^{-2} s^{-1} where the viscosity for every sample is approximately that of the glass. There is a significant shift in the gradient of the slopes between the 0.3 and 0.4 crystal fractions.

Plotting the logarithm of the relative viscosity against crystal content (Fig. 4.11a), shows a linear relationship of the viscosity with crystal content for each strain rate. Plotting the gradients of these linear relationships against applied strain rate gives an indication of the effect crystals have on the relative viscosity (Fig. 4.11b). This reveals a linear relationship where $^{dlog(\eta_r)}/_{d\varphi_x} = -1.2\dot{\varepsilon} - 2.37$. In addition, the relative viscosities could also be plotted with strain rate for each crystal fraction and the gradients of the linear relationships found, giving a description of the non-Newtonian, shear-thinning characteristic of the suspension. These gradient values were plotted with crystal fraction (Fig. 4.11c) to find the linear relationship $^{dlog(\eta_r)}/_{dlog(\dot{\varepsilon})} = -1.22\varphi_x$. This relationship shows that the degree of non-Newtonian behaviour increases with crystal fraction. It also demonstrates that when adjusted for melt viscosity, the data reveal the onset of non-Newtonian behaviour to be between $0 < \varphi_x < 0.1$.

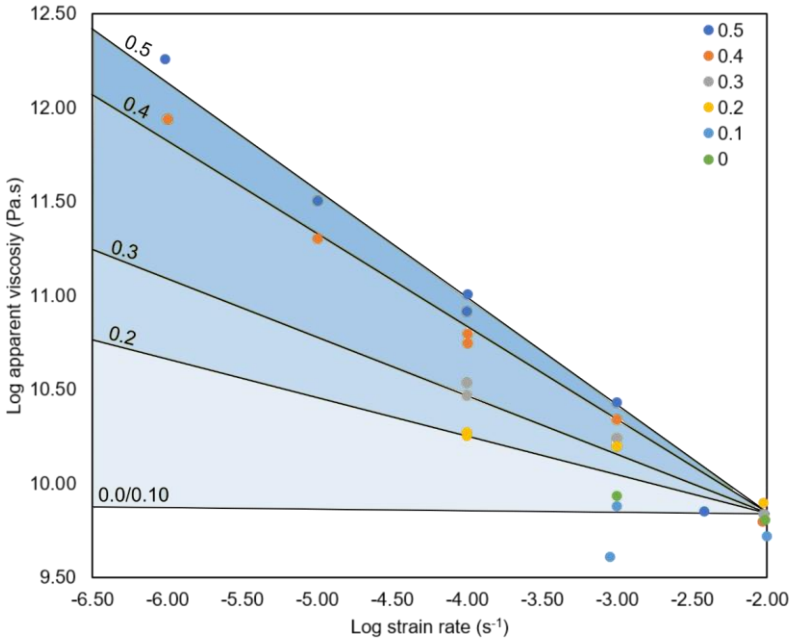

Figure 4.10. Logarithm of apparent viscosity vs the logarithm of applied strain rate for samples that displayed a viscous response within the limitations of the testing equipment. The onset of non-Newtonian behaviour occurs somewhere between the 0.1 and 0.2 crystal fraction, after which the logarithm of the apparent viscosity decreases linearly with increasing logarithm of strain rate, shear thinning. Areas of shaded blue represent intervals between tested crystal fractions, suggesting that within that interval would lie an intermediate crystal fraction.

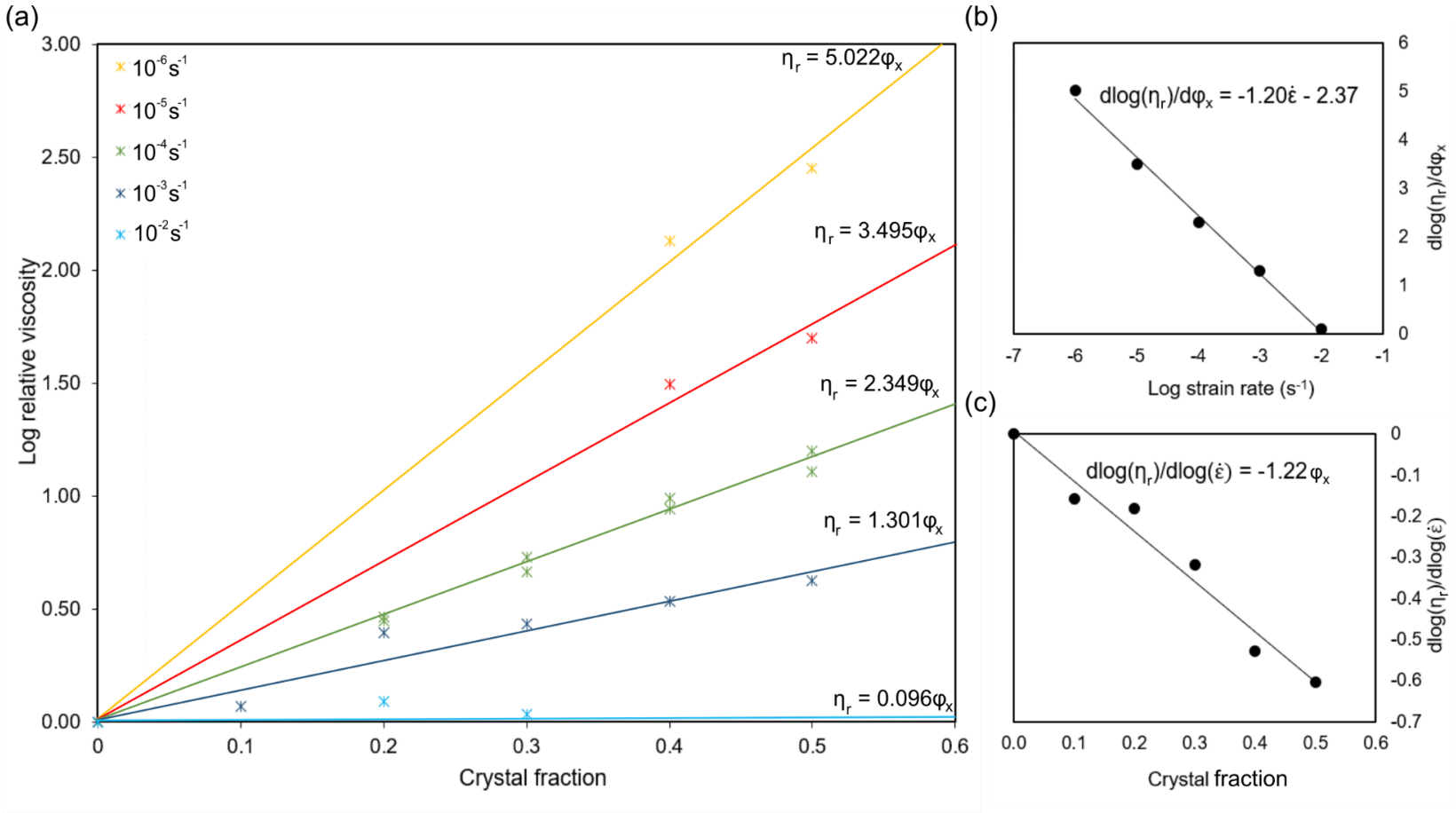

Figure 4.11. (a) The logarithm of the relative viscosity increases linearly with crystal content for each applied strain rate. The equation for each linear best line of fit is given above the line. (b) The gradient of each line of best fit decreases with applied strain rate. The points are fitted with a linear line and the equation given. This signifies the amount the viscosity changes with the addition of crystals with strain rate (c) The change in the logarithm of relative viscosity over the change in the logarithm of strain rate with crystal fraction. This signifies the degree in non-Newtonian behaviour that increases with crystal fraction.

4.3.5. Viscosity modelling

To model the viscosities obtained during uniaxial testing, several equations were applied to the data set. The Maron-Pierce (1956) equation, which describes Newtonian behaviour (Eqn. 4.18); the reformulated version of the Hershel-Buckley (1926) model for non-Newtonian flows with no yield stress (Eqn. 4.19), and the empirical model developed by Costa et al. (2005; 2009) (Eqns. 4.20 and 4.21), were all utilised for data-model comparison (Fig. 4.12).

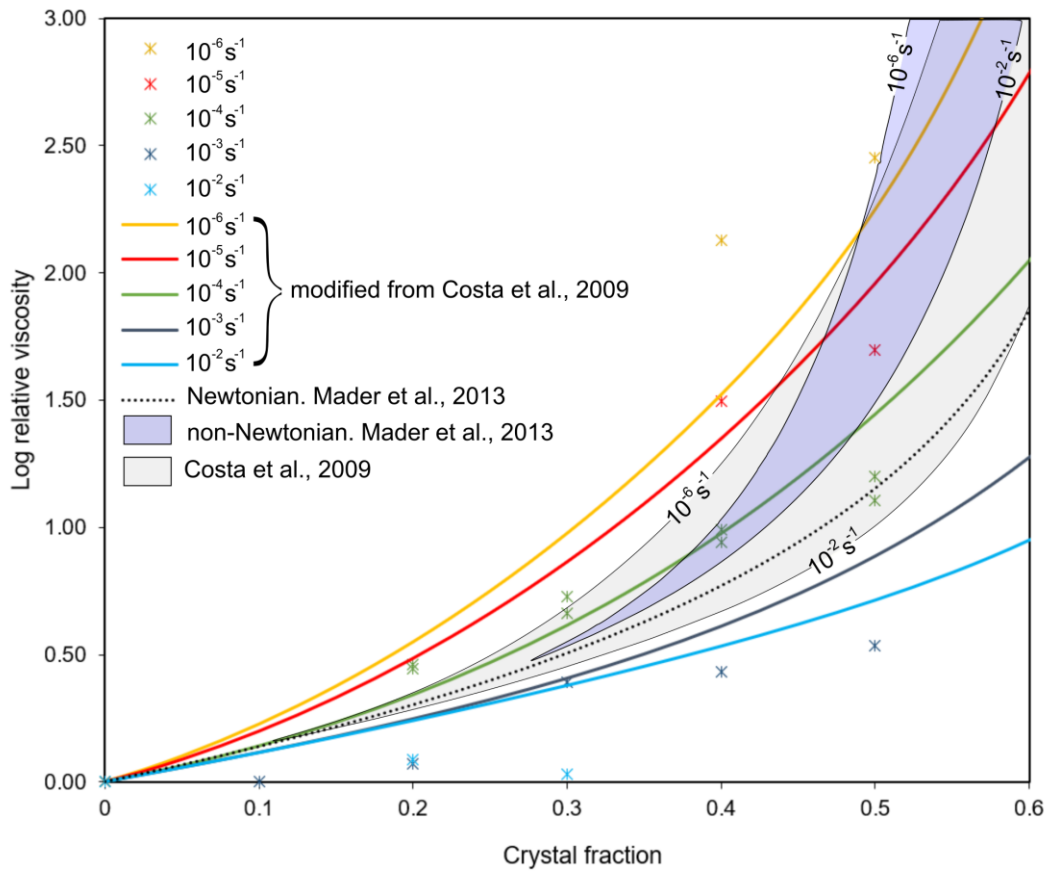

Figure 4.12. Logarithm of relative viscosity against crystal content for each strain rate tested. Results from uniaxial testing are plotted as data points. The Newtonian, Maron Pierce equation (Eqn. 4.18) is plotted as a dotted line. The range of viscosities for strain rates from 10^{-6} to 10^{-2} s^{-1}, calculated from the modified non-Newtonian Hershel Buckley equation (Eqn. 4.19) (Mader et al., 2013), is plotted in shaded blue. Similarly, the Costa et al. (2009) model, which uses the parameters from Carrichi et al. (2007), is plotted in shaded grey for strain rates range from 10^{-6} to 10^{-2} s^{-1} (Eqn. 4.20 and 4.21). Each of the coloured lines represents viscosities calculated for individual strain rates via the Costa 2009 model with modified parameters that fit the olivine data.

The Maron Pierce (1956) equation (shaded blue on Fig. 4.12) plots closely to the resulting viscosities from the 10^{-4} s^{-1} experiments. Although the model predicts the shape of the data trend well, the equation should estimate viscosities at far lower strain rates where behaviour would be expected to be essentially Newtonian (~ 10^{-9} s^{-1}).

Using Equation 4.13 and 4.14, the maximum packing fraction of the crystals, φ_m, was calculated as 0.63 [Note: this is a different value from the measured dry maximum packing fraction, φ_{dry} (see section 4.3.1)]. From Equation 4.12, the flow index of the sample was found to drop significantly below unity at a crystal fraction of ~ 0.3. Using these values, the reformulated Hershel-Buckley model (1926) could be calculated for the range of applied strain rates. Although model estimated relative viscosities within the bounds of the data points, the equation incorrectly predicted the crystal fraction onset of non-Newtonian behaviour as occurring at approximately 0.25-0.3 (in line with the n value). The experimentally determined onset is between the 0.0 and 0.1 crystal fraction (Fig. 4.11c). In addition, compared to experimental data, the range in estimated viscosity over the strain rate of interest is narrow, essentially underestimating the degree of non-Newtonian behaviour. Furthermore, from the 0.4 crystal fraction onwards, the results of the applied equation overestimate the increase in viscosity with increasing crystal content. This inaccuracy likely results from the need to keep the maximum packing constant in the equation, which assumes crystals are rigid, undeformable bodies, which do not fail or reorganise with strain.

The empirical model of Costa et al. (2009), with parameters obtained by Caricchi et al., (2007), was plotted against the experimental data (Fig. 4.12). The model predicts an onset of non-Newtonian behaviour at a crystal fraction of < 0.1, echoing that seen in the data set (Fig. 4.11c, 4.12). Although the spread in predicted viscosities with strain rate is broader than those calculated via the reformulated Hershel-Buckley (1926) model, the Costa et al. (2009) model still underestimates the spread in relative viscosity experimentally constrained for lower crystal content suspensions (< 0.3). This underestimation indicates that at these lower crystal contents some degree of non-Newtonian behaviour is still unaccounted for with such numerical approaches.

Using the equation given in Figure 4.11b, ω_0 could be calculated as 0.1 and ω_∞ as 8.46 (at a near static strain rate of 1x10^{-9} s^{-1}). This leads to the calculation of the ω parameter (Eqn. 4.23) and therefore, along with the adjustment of additional variables (see section 4.2.7), the Costa et al. (2005; 2009) model was modified for the olivine bearing samples (Table 4.3; Fig. 4.12). The adjusted model provided a much closer fit to the data than the parameters taken directly from Caricchi et al. (2007) (Fig. 4.12). The values of relative viscosity estimated with the modified parameters are close to those found from experimental testing, however, limitations are noticeable strain rates above 10^{-3} s^{-1} and below 10^{-5} s^{-1}. Additionally, the model slightly overestimates the increase in relative viscosity above a crystal fraction of 0.4.

Table 4.3. Modified (a) constant and (b) variable input parameters for the Costa et al. (2009) model

(a)

ε_c	ε_d	φ_{n2}	$\Delta\varphi$	ξ_{n2}	$\Delta\xi$	ω_{n2}	$\Delta\omega$	n_3
5.01E-05	4.27E-03	0.83	0.17	4.61E-04	4.39E-04	4.28	4.18	0.33

(b)

$\dot{\varepsilon}$	1.00E-09	1.00E-06	1.00E-05	1.00E-04	1.00E-03	1.00E-02
δ	8.82	12.87	12.75	12.25	10.58	7.58
ω	4.18	0.13	0.25	0.75	2.42	5.42
ϕ*	0.66	0.68	0.75	0.87	0.96	0.99
ξ	2.20E-05	2.55E-05	3.78E-05	9.00E-05	2.65E-04	5.81E-04

4.3.6. Rheological behaviour

The resulting rheological behaviour for every sample was determined at each applied strain rate by the shape of the stress-strain curve (Fig. 4.4-4.6). Each response was categorised as viscous flow, strain weakening (i.e. transitional between viscous and brittle) or brittle failure and was plotted as a function of the applied strain rate and the crystal content of the sample (Fig. 4.13). The strain rate at which viscous heating would be expected to accumulate in the melt, $\dot{\varepsilon}_{VH}$, was calculated as approximately 8.8x10^{-4} s^{-1} (Eqn. 4.3). This rate would be expected to slightly decrease as a function of crystal content present in a suspension. At such low rates ($\leq$ 1x10^{-4} s^{-1}), viscous heating would be minor and the data show there is no evidence of viscous heating having a significant effect on suspensions tested at low strain rates ($\leq$ 1x10^{-4} s^{-1}) in this study (Fig. 4.13). However, viscous heating may be partly responsible for the strain weakening witnessed in the transitional regime.

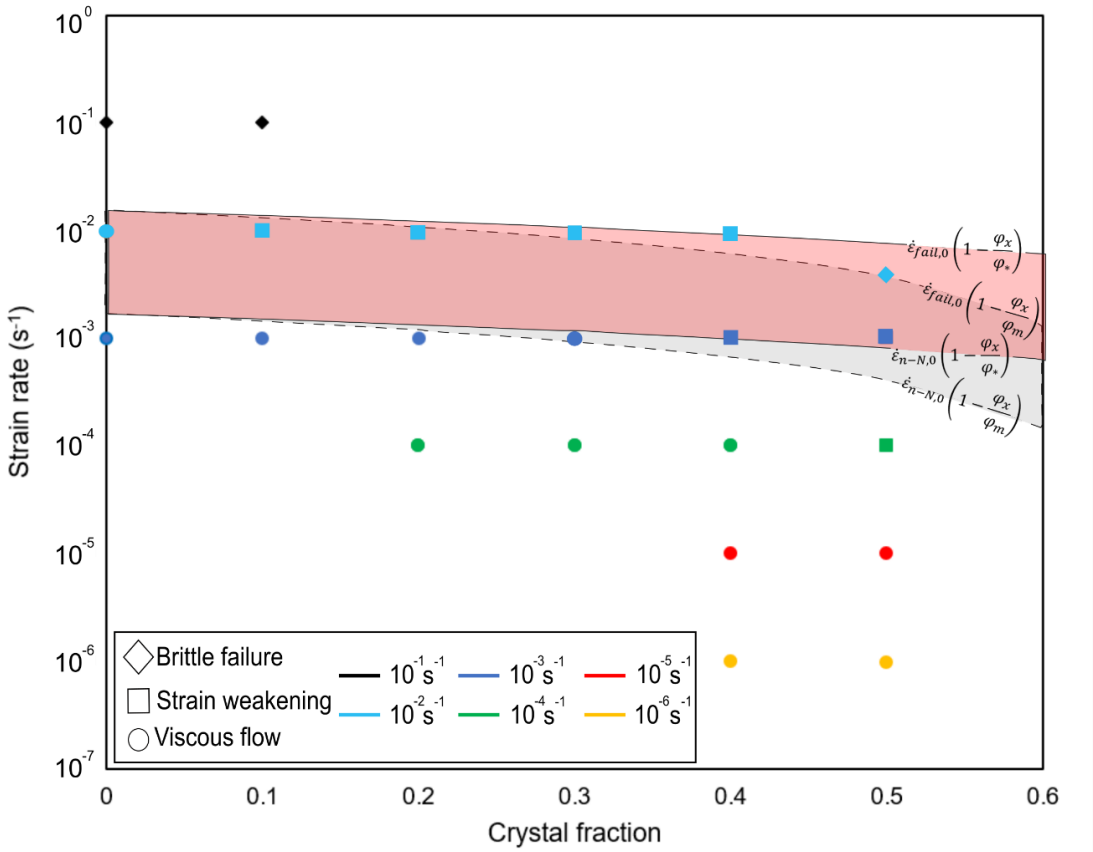

Figure 4.13. Resulting behaviours for each strain rate applied with crystal content. Behaviours were split into brittle failure, strain weakening or viscous flow as a result of their stress-strain curve. The shaded areas correspond to transitional zones. The grey transitional zone boundaries (dotted lines) were set by adjusting the strain rate at the onset of non-Newtonian behaviour, $\dot{\varepsilon}_{n-N}$, and the strain rate at failure, $\dot{\varepsilon}_{fail}$, by a factor which is proportional to $\left(1-\frac{\varphi_x}{\varphi_m}\right)$ via Equation 4.10 and 4.11 (Cordonnier et al., 2012a). The pink transitional zone boundaries (solid lines) were set by replacing φ_m with φ_* in Equations 4.10 and 4.11. Disregarding the data for the 0.5 crystal content, the pink transitional zone is a better fit to the data with viscous flow points sitting on or below the zone, all of the brittle failure points sitting above the zone, and all of the strain weakening points on or within the zone.

For the crystal-free melt, the strain rate at which the onset of Newtonian behaviour, $\dot{\varepsilon}_{n-N}$, (Eqn. 4.8) and the strain rate at which failure occurs, $\dot{\varepsilon}_{fail}$, (Eqn. 4.9) can be calculated as approximately $1.56\text{x}10^{-3}$ s^{-1} and $1.56\text{x}10^{-2}$ s^{-1}, respectively. With the addition of crystals, these critical strain rates are shifted by a factor which is proportional to $\left(1-\frac{\varphi_x}{\varphi_m}\right)$ as calculated via Equation 4.10 and 4.11 (Cordonnier et al., 2012a). The strain rates at which non-Newtonian behaviour and failure are expected to occur can be plotted for each crystal content (grey shaded area in Fig. 4.13). The area between the two bounding strain rates can be considered the transitional zone, in which samples would be expected to have a strain weakening response.

However, there are samples labelled transitional which are outliers to this calculated zone. By replacing the maximum packing fraction in Equations 4.10 and 4.11 with the empirically derived critical packing fraction (at the strain rates closest to the critical behaviour, see Table 4.3), the resulting transitional zone (pink zone in Fig. 4.13) gives a better fit to the data points. In the newly calculated strain rate boundaries, most samples are categorised in the correct zone. Nevertheless, the 0.5 fraction data far outlies any of the calculated transition zones and suggesting a different mechanism at play here.

4.3.7. Failure criterion for crystal bearing melts

As the non-Newtonian response exhibited by most viscoelastic materials can be modelled by the generalised Herschel-Bulkley relation (1926) (Eqn. 4.15), the peak stress reached at each applied strain rate could be plotted for all crystal fractions and a power law trend fit (Fig. 4.14a). As the olivine samples adhere to $\frac{\varphi_x}{\varphi_m} \leq 0.8$, there was no yield stress and the power law relations satisfied the reduced Herschel-Bulkley relation (1926) (Eqn. 4.16). The Ostwald (1925) constants, were found for each crystal fraction; these constants provide a description of the flow consistency, K, and the flow index, n, respectively. When $n = 1$ then viscosity is constant and the material is Newtonian, when $n < 1$ the material is non-Newtonian, shear-thinning. Here, the crystal-free melt sample exhibited a response that was close to Newtonian, with a flow index of 0.91. The flow index gradually decreases as crystals are added to a value of 0.51 at the 0.5 crystal fraction (Fig. 4.14c).

Comparing the flow consistency and the flow index to natural samples studied by Lavallée et al. (2007), we find a trend in both K (Fig. 4.14b) and n (Fig. 4.14c) values. Both values decrease exponentially with crystal content following $K = 18750e^{-3.6}\varphi_x$ and $n = 0.96e^{-1.04}\varphi_x$ for K and n, respectively.

Using the flow consistency and the flow index for each crystal fraction, the Deborah number formulation (Eqn. 4.5) from the empirical approach of Coats et al. (2018) could be applied to the data set via Equation 4.7. As with Figure 4.13, the samples were categorised according to their resulting behaviour (Fig. 4.15).

For each applied strain rate, the expected Deborah numbers could be modelled by replacing the strain rate of observation, $\dot{\varepsilon}_{\mathrm{obs}}$, term in Equation 4.6 with the applied strain rate multiplied by $\left(1-\frac{\varphi_x}{\varphi_*}\right)$, so

$$\mathrm{De} = \frac{\dot{\varepsilon}\left(1-\frac{\varphi_x}{\varphi_*}\right)\mu}{G_\infty}. \tag{4.28}$$

This gives the coloured dashed lines in Figure 4.15 which approximate where the Deborah number should lie.

To define the lower and upper bounds of the transition zone in Deborah number space, the strain rate of observation, $\dot{\varepsilon}_{\mathrm{obs}}$, term in Equation 4.6 could be replaced with the strain rate at the newly calculated onset of non-Newtonian behaviour, $\dot{\varepsilon}_{n-N}$, and the strain rate at failure, $\dot{\varepsilon}_{fail}$, respectfully (Fig. 4.15), such that

$$\mathrm{De}_{n-N} = \frac{\dot{\varepsilon}_{n-N,0}\left(1-\frac{\varphi_x}{\varphi_*}\right)\mu}{G_\infty}, \tag{4.29}$$

and

$$\mathrm{De}_{fail} = \frac{\dot{\varepsilon}_{\mathrm{fail},0}\left(1-\frac{\varphi_x}{\varphi_*}\right)\mu}{G_\infty}. \tag{4.30}$$

The empirically calculated Deborah numbers are generally a good fit to the limits, with the majority of strain weakening samples plotting in or close to the transition zone. Those that do not fit closely to the relation are those at very high strain rates ($\geq 10^{-1}$ s^{-1}) or at very low strain rates ($\leq 10^{-5}$ s^{-1}). The 0.5 crystal fraction sample is the main outlier of the dataset, with both strain weakening and failure occurring before the limit predicted by this equation.

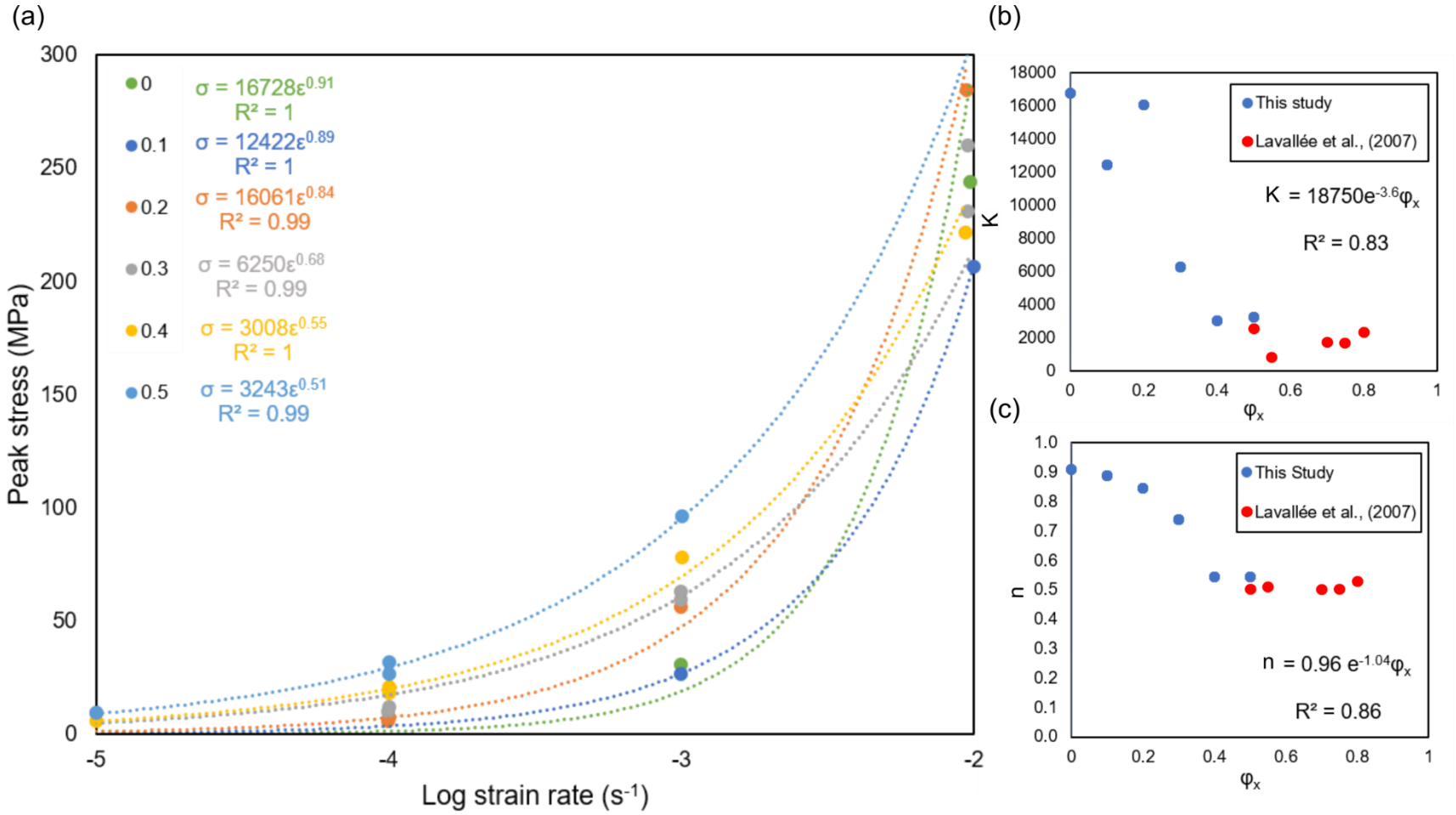

Figure 4.14. (a) Peak stress vs the logarithm of strain rate for each sample tested. Power laws are fitted for each crystallinity and equations and R^2 values given on the plot. Ostwald (1925) constants give (b) the flow consistency, *K* and (c) the flow index, *n*, as a function of crystal fraction for the synthetic samples used in this study and nature samples studied by Lavallée at al. (2007). Exponential relationships of the constants with crystal fraction are given on the plots along with their R^2 values.

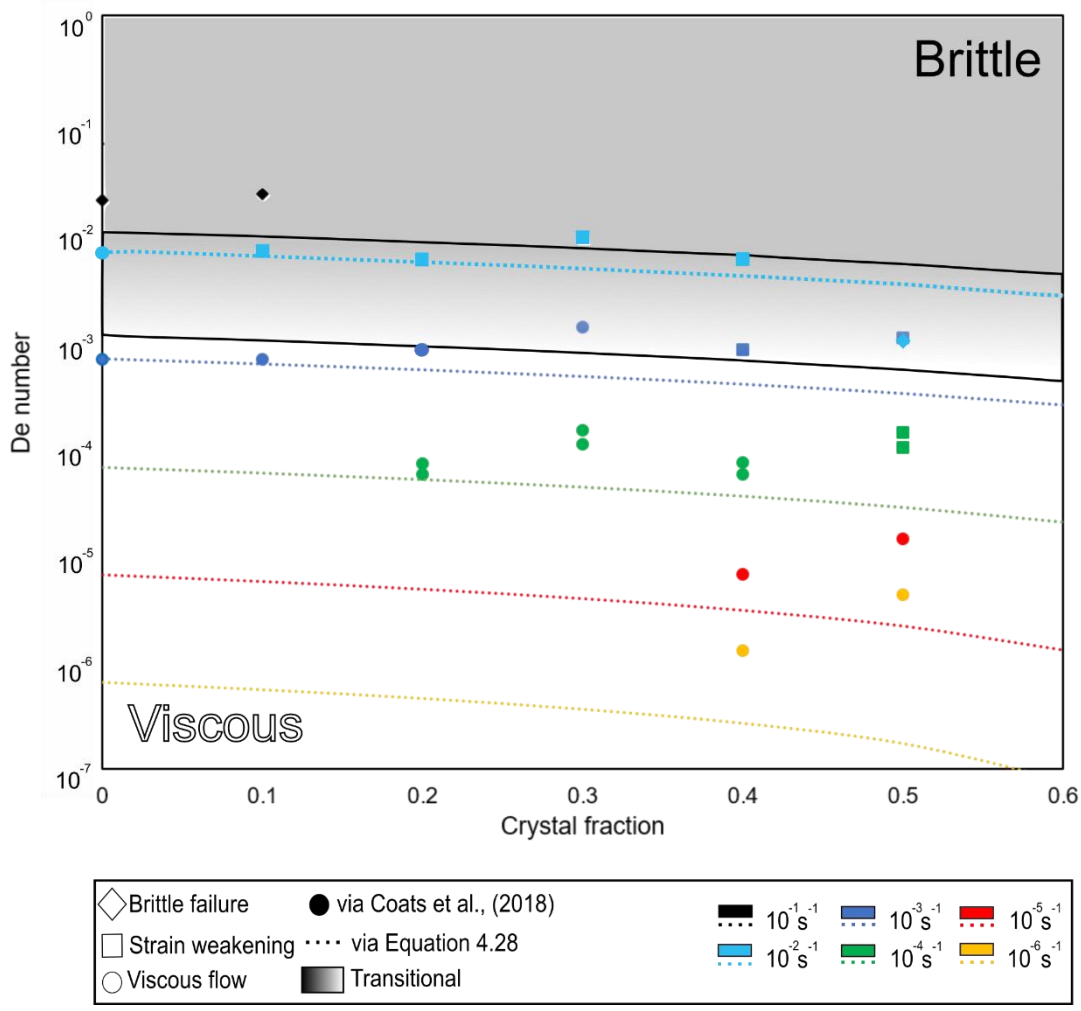

Figure 4.15. The Deborah number with crystal fraction for the olivine samples. Dotted lines represent the expected Deborah number calculated at various strain rates using Equation 4.28, where the colour of the line indicates the strain rate used in the calculation. Coloured shapes represent Deborah numbers calculated using the Equation generated by Coats et al. (2018) (Eqn. 4.5), where the colour of the shape represents the applied strain rate, and the morphology of the shape represents the resulting behaviour of the sample, brittle failure, strain weakening, or viscous flow. Generally, brittle behaviour occurs in the shaded grey zone, while viscous behaviour occurs in the white zone. Transitional, strain weakening behaviour occurs in the zone between the two which is bound by solid black lines and has a grey gradient.

4.4. Discussion

4.4.1. Sample characteristics

The samples used in this study were determined to be adequate for rheological testing of two-phase (crystals and melt) suspensions. There was no significant deviation in glass transition temperature with the addition of crystals (Fig 4.2) and the fraction of crystallised Spheriglass® was low (< 0.03) (Fig 4.3g), meaning the sample were of sufficient quality for the study on two-phase suspensions. The measured porosity was < 0.03 for samples with $0 \leq \varphi_x \leq 0.4$ (Fig 4.9d), which was taken as negligible and indeed, this seemed to have relatively no effect on the rheological response of the samples. However, in the $\varphi_x = 0.5$ samples the initial porosity was ~ 0.08. This increased pore

fraction may have been sufficient to affect the rheological response of the specimens; especially when comparing them to denser samples with lower crystallinities. The slightly higher porosity of the 0.5 crystal content samples may be the reason the modified model of Costa et al. (2009) overestimates the viscosity of the samples (Fig. 4.12), as elongate pores, with low capillary numbers, reduce the viscosity of a system (Manga et al., 1998). The addition of pores is also known to dramatically decrease the strength of a system, serving as a nucleation point for the propagation of fractures (Vasseur et al., 2015). Therefore, the 0.5 crystal fraction samples are more likely to accumulate damage at lower stresses than their lower crystalline samples which would account for the sample failing at a lower strain rates and Deborah number than expected (Fig. 4.13, 4.15). Therefore, it can be concluded that the transition zone boundaries coined by Equations 4.29 and 4.30 fit the data set at crystallinity < 0.4 well, but more work may be required to increase the power of our empirical solutions to predict the rheological regime of denser suspensions.

4.4.2. Viscosity modelling

Results from modelling the measured viscosities suggest that models based on mathematical relationships, such as the Newtonian Maron-Pierce equation (1956) (Eqn. 4.18) and the reformulated version of the non-Newtonian Hershel-Buckley (1926) model (Eqn. 4.19) (Mader et al., 2013), are a poor fit to the experimental data (Fig. 4.12). Although the calculated relative viscosities were within the range of the measured viscosities, both equations fail to accurately model the response of the samples. The Maron-Pierce equation (1956) estimated relative viscosities of 0-1 for $0 \leq \varphi_x \leq 0.5$, when the experimental data suggests relative viscosities of 0-2.5 for near-static Newtonian behaviour. Similarly, the non-Newtonian Hershel-Buckley (1926) model underestimates the window of non-Newtonian relative viscosities. For example, for $\varphi_x = 0.4$ the model estimated $\eta_r = \sim 0.8 - 1$ for strain rates of 10^{-6} to 10^{-2} s^{-1}, respectively, while the experimental data gave the range as $\eta_r = 0 - 2$ (Fig. 4.12).

There are several reasons why the model might underestimate the viscosity of the suspensions. Both the Newtonian Maron-Pierce equation (1956) (Eqn. 4.18) and the reformulated version of the non-Newtonian Hershel-Buckley (1926) model (Eqn. 4.19) feature the maximum packing fraction. The maximum packing fraction is also a variable in the equation for the flow index (Eqn. 4.12) which is then used in the calculation of the Hershel-Buckley (1926) model. The maximum packing fraction is a value which is calculated from particle characteristics, such as aspect ratio and polydispersity, and it is assumed that these physiognomies remain constant over the range of applied strain rates. However, it is apparent from stress-strain data and from QEMSCAN® images that during deformation crystals fracture, increasing porosity, and that this magnitude of porosity increase scales with crystal content. The amount of crystal fracture and generated porosity also increases with strain, and by extrapolation, strain rate. Crystal fracture would affect both the aspect ratio and polydispersity of the crystals and thus, the maximum packing fraction cannot be regarded as constant over the duration of deformation. Using a constant value for the maximum packing fraction in the flow index (Eqn. 4.12), the Maron-Pierce equation (1956) (Eqn. 4.18), and the reformulated version of the Hershel-Buckley (1926) (Eqn.

4.19), leads to a poor estimation for the onset of non-Newtonian behaviour, an overestimation of the viscosity with increasing crystal fraction, and an underestimation of the degree of shear-thinning.

The empirical based viscosity model of Costa et al. (2009) provided a much more robust fit to the data than the mathematical relationships. The onset of non-Newtonian behaviour was found to occur at a similar point to that seen in the dataset. Additionally, the spread in relative viscosities with strain rate was broader than those calculated via the reformulated Hershel-Buckley (1926) model, better capturing the degree of non-Newtonian behaviour across the spectrum of crystallinities tested. However, it was found that when using the parameters obtained by Caricchi et al. (2007) the model underestimated the degree of non-Newtonian behaviour that was experimentally constrained for lower crystal contents (< 0.3). The parameters detailed in Caricchi et al. (2007) were fitted using data across a range of crystal contents. While the high crystal fraction, $0.5 \leq \varphi_x \leq 0.8$, data was obtained from tests performed on two-phase suspensions at various strain rates, the lower fraction data, $\varphi_x \leq 0.3$, was taken from a previous study (Thomas, 1965) based on tests performed on suspensions of uniform spherical particles, where the only variation was particle diameter. While data $0.3 < \varphi_x < 0.5$ was extrapolated. It is therefore likely that the poor fit to the data is due to empirical parameters being based on a lack of data at the lower crystal fractions $\varphi_x \leq 0.5$.

When the parameters of the Costa et al. (2009) were adjusted to fit the characteristics of the olivine crystals, the fit to the dataset was more robust, particularly below the 0.3 crystal fraction. However, the model is unable to correctly estimate the experimentally derived viscosities obtained for strain rates above 10^{-3} s^{-1} and below 10^{-5} s^{-1}. At high strain rates this is likely from the non-Newtonian behaviour of the melt, the onset of which occurs at a strain rate of approximately 1.56 x10^{-3} s^{-1} (Eqn. 4.8). At very low strain rates this could be from an overestimation of the critical crystal fraction value when deformation is approaching static (Eq. 4.22). The model also overestimates the increase in relative viscosity above a crystal fraction of 0.4. This could originate from the higher initial pore content of the 0.5 fraction sample, which may have acted to reduce the viscosity of the experimental sample relative to the model. Therefore, the viscosity of the 0.5 fraction sample should be considered with caution when comparing modelling results to the experimental data. Given the better fit to the data of low crystallinity olivine samples, we suggest a modification of the ω parameter used in the Costa et al. (2005; 2009) model which controls the increase in viscosity as $\varphi_x \rightarrow \varphi_*$ (Table 4.3). For application to a complete set of rheological data, we suggest applying the methods carried out in section 4.2.7.

4.4.3. Non-Newtonian, shear-thinning behaviour

Non-Newtonian shear-thinning behaviour is a time independent behaviour in fluids that describes a reduction in the apparent viscosity with increasing strain rate. In studies of rigid, spherical particle bearing fluids it has be suggested that shear-thinning occurs from a combination of the alignment of particles and entropic forces (Brown and Jaeger, 2011; Cheng et al., 2011), where the response of the suspension becomes fully Newtonian when particles become fully aligned (e.g. Brown and Jaeger, 2011; Cheng et al., 2011; Liu et al., 2018; Fig. 1.2).

The concept of particle rearrangement being time independent is difficult to comprehend. However, it is advantageous to remind oneself that there is no such thing as true time independence, only actions occurring at such sort timescales they can be considered independent of time. One such example is the elasticity of water which occurs on extremely short time scales, meaning that the rheology of water is assumed Newtonian (Richardson, 2011).

The origin of shear thinning in magmas is highly debated. So far, it has been attributed to viscous heating (Cordonnier et al., 2012b); exceeding the relaxation time of the viscoelastic melt (Webb and Dingwell, 1990b, 1990a); the shape of natural crystals (e.g. Mueller et al., 2010, 2011b; Mader et al., 2013); crystal plasticity (Kendrick et al., 2017); crystal fracture (Deubelbeiss et al., 2011; Pistone et al., 2012), and particle rearrangement due to finite strain (e.g. Caricchi et al., 2007; Costa et al., 2009). No one study fully agrees on a single mechanism responsible for shear-thinning behaviour. However, it is widely accepted that the introduction of a critical fraction of particles into a melt is responsible for a shift in Newtonian to non-Newtonian, shear-thinning behaviour.

In the experimental dataset presented in this study, the exact mechanism behind the shear-thinning behaviour observed remains unclear. The magnitude of the reduction in viscosity with strain rate (e.g. Fig. 4.4) is likely to be a result of a combination of factors which will now be discussed.

The onset of non-Newtonian, shear-thinning behaviour of the suspension occurs at a crystal fraction of < 0.1 between $1x10^{-6}$ s^{-1} and $1x10^{-5}$ s^{-1} (Fig. 4.11a). After which the degree of shear thinning increases linearly with crystal fraction (Fig. 4.11c). The non-Newtonian response of the *melt phase* occurs at $1.56x10^{-3}$ s^{-1}, decreasing with the addition of crystals (Fig 4.13). Therefore, it is not possible to ascribe the shear-thinning behaviour seen at strain rates < $1.56x10^{-3}$ s^{-1} to the non-Newtonian response of the interstitial melt. For strain rates > $1.56x10^{-3}$ s^{-1}, it is unlikely that the non-Newtonian response of the melt is fully responsible for shear thinning behaviour observed in the suspensions, as the degree of shear-thinning is linear for the range of strain rates applied (Fig. 4.11b).

If crystal shape were a dominant control on shear-thinning in the olivine bearing samples, the onset of shear-thinning behaviour would occur when the flow index, or n-value (Eqn. 4.12), decreases to less than unity (Mueller et al., 2010). For the measured aspect ratio and polydispersity of the olivine crystals, the n-value decreases significantly below one at a crystal fraction of ~ 0.3. However, in the experiments shear-thinning behaviour occurs at a crystal fraction < 0.1 (Fig. 4.11a) and increases linearly with crystal fraction (Fig. 4.11c). Furthermore, the degree of shear-thinning with crystal fraction is more significant than modelled by equations featuring the n-value (Fig. 4.12). Therefore, it is likely that crystal shape is only a minor contributor, if any, to shear-thinning behaviour in the experimentally tested olivine samples.

QEMSCAN® data shows that particles have rotated perpendicular to the major principal stress (Fig. 4.7, 4.8). However, as samples were only thin sectioned and analysed after reaching 0.25 strain through a range of stepped strain rates (Fig. 4.1c), it is unclear whether an increase in strain rate has caused the particle rotation, or if this was a product of increased strain, or a hybrid of both mechanisms. For $0.0 < \varphi_x < 0.5$ suspensions, the viscosities at 10^{-2} s^{-1} appear Newtonian (e.g. Fig.

4.11a), as the impact of crystal content are fully counteracted by the extent of shear-thinning. It could be hypothesised that the mechanism behind this Newtonian response could be due to the linear arrangement of particles seen in the QEMSCAN® data.

Also evident from QEMSCAN® data is the presence fractured crystals (Fig. 4.7, 4.8). The number of fractured crystals, and the number of fractures within crystals, increases with crystal fraction from the 0.1 fraction sample to the 0.5 fraction sample. The dilation associated with crystal fracture increases the measurable porosity of the sample from the 0.3 crystal fraction onwards (Fig. 4.9b). Crystal fracture has been suggested as the dominant shear-thinning mechanism by Deubelbeiss et al. (2011). The generation of fractures and dilatancy in the sample would reduce the strength and therefore the viscosities of the samples. However, unlike particle rotation, this effect would be irreversible. Moreover, crystal fracture could be linked to critical crystal fraction, φ_*. The empirically derived critical crystal fraction is the solid fraction at which the viscosity exponentially increases towards infinity. It is found to increase with strain rate (Table 4.3) and is a variable in equations that are a good fit to the olivine data (Fig. 4.12, 4.13, 4.15). The increase in crystal fracture with strain rate would cause an irreversible increase in the maximum packing fraction of the crystals which would explain the increase in critical crystal fraction with increasing strain rate (Table 4.3).

From experiments carried out on the synthetic, olivine-bearing suspensions, conclusions can be drawn as to which mechanisms are responsible for inducing shear-thinning behaviour (Fig. 4.16). Results of experimentation and data processing indicate that crystal fracture, and resulting dilatancy, are sufficient to cause a substantial reduction in sample strength than is expected for an intact sample at that strain rate. For example, in Gent's equation (Eqn. 4.27), if strain rate increases by an order of magnitude, then the denominator increases by an order of magnitude; for constant viscosity (i.e. Newtonian behaviour), the numerator must also increase by the same factor, however, this is not the case, and so the apparent viscosity term reduces leading to the onset of non-Newtonian behaviour. This sample weakening causes a reduction in the viscosity with strain rate leading to a shear thinning response. Particle rotation is also a likely contributor to shear thinning, although conclusions cannot be fully drawn from the experiments carried out here alone. Minor contributions from crystal shape (in the present study) may also be responsible for the total reduction of stress with increasing strain rate.

4.4.4. Non-Newtonian, strain-weakening behaviour

Non-Newtonian, strain-weakening behaviour leads to a strain- (and therefore time-) dependent, reduction in viscosity. It is akin to an irreversible thixotropy, which is termed aging in other disciplines (Mewis and Wagner, 2009).

Strain-hardening behaviour occurs in a number strain rate steps in samples with crystal fractions ≤ 0.3 (Fig. 4.5 a,b,c iii, 4.5 a,b,c,d iv, 4.6 b). In these lower crystalline samples, pore closure or elongation is clearly seen in the QEMSCAN® data (Fig 4.8 a,b,c) and is likely to dominate over the effects of the crystals at these small fractions. Pore closure has previously been reported to result in strain hardening (Kendrick et al., 2013b), and is likely the cause of the behaviour in the olivine bearing samples.

Strain weakening occurs in at several strain rate steps in samples with crystal fractions ≥ 0.3 (Fig. 4.5e,f ii, 4.5e,f iii, 4.5d,e,f iv, 4.6d). Unlike strain hardening, the degree of strain weakening increases with crystal fraction and strain rate. For example, the gradient of the normalised stress decreases between the 0.4 and 0.5 samples at a strain rate of 10^{-3} s^{-1} (Fig 4.5e,f iv). Likewise, the gradient of the normalised stress for the 0.5 fraction sample reduces between applied strain rates 10^{-4} s^{-1} and 10^{-3} s^{-1} (Fig. 4.5f iii,iv). Samples with a strain weakening response were categorised as transitional and lie within the transitional regime (Fig. 4.13, 4.15). The onset of this transitional regime is linked with a combination of non-Newtonian behaviour in the interstitial melt phase (which occurs at lower strain rates than predicted from constraints on single-phase liquids; e.g. Webb and Dingwell, 1990b, 1990a) and rupture and realignment of the crystalline phase. We therefore suggest that in the olivine samples, strain weakening behaviour is principally influenced by the non-Newtonian response of the melt phase.

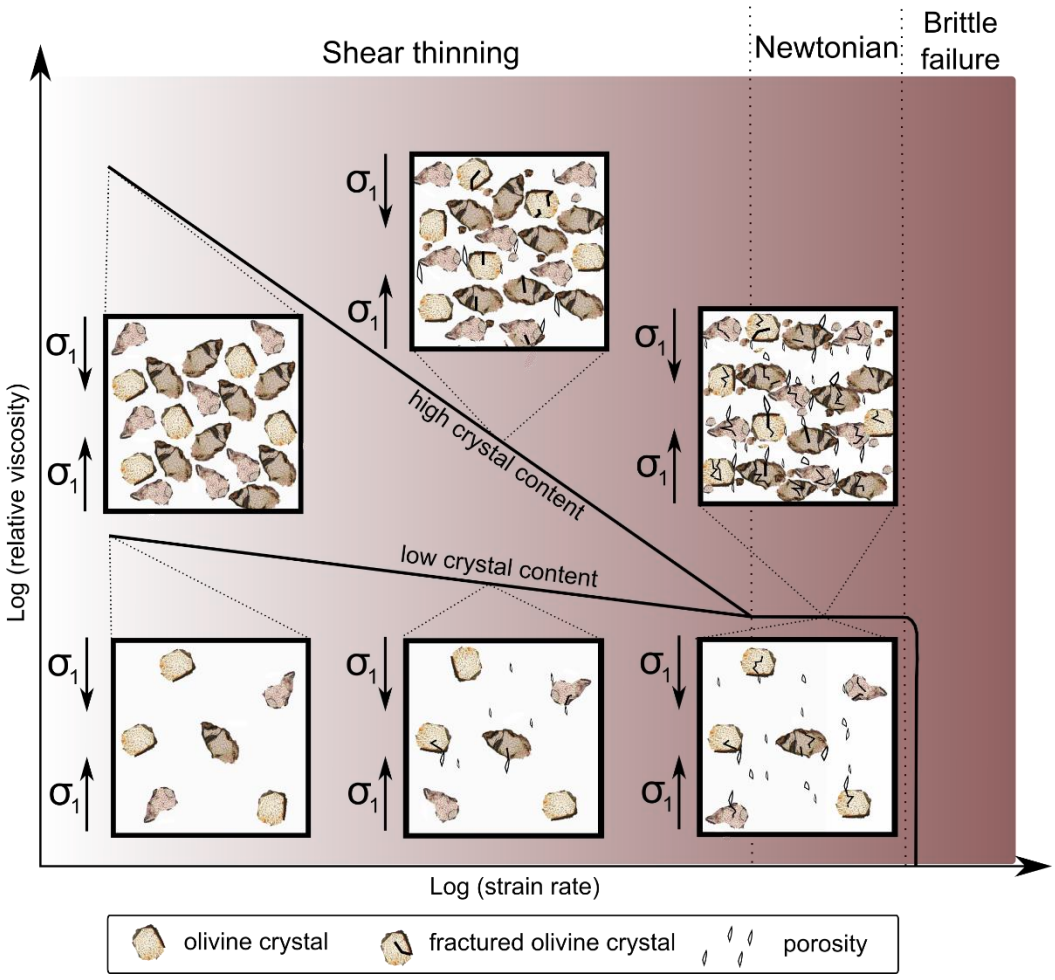

Figure 4.16. Sketch of how viscosity evolves with strain rate in a compression regime. In the shear thinning regime, samples with higher crystal contents decrease in viscosity far more rapidly than those with lower crystal contents. In this regime increasing strain rate causes crystals to fracture and porosity to form, decreasing the strength and thus viscosity of the sample. Crystals also rotate so their major axes are perpendicular to the applied stress, σ_1, and, when they are fully laminar, viscosities become Newtonian. A further increase in the strain rate causes brittle failure of the samples.

4.4.5. A failure criterion for crystal and pore bearing melts

In the synthetic, olivine-bearing suspensions, macroscopic failure of the specimens occurs at strain rates of 10^{-1} s^{-1} (Fig. 4.6h,i) and the 0.5 fraction sample at a strain rate < 10^{-2} s^{-1} (Fig. 4.5f v). For the samples tested at strain rates of 10^{-1} s^{-1}, this occurred above the onset of non-Newtonian behaviour of the melt (Fig. 4.13, 4.15). However, for the 0.5 fraction sample, this occurred at strain rates for which we anticipate the interstitial melt to display a non-Newtonian response.

If the 0.5 fraction sample were to be discarded on the grounds that the slightly higher initial porosity influenced its rheological response, the behaviours of the remaining samples would fit approximately within the defined transition zone (Fig. 4.13, 4.15) between fully viscous and fully brittle deformation. This implies the $(1-\frac{\varphi_x}{\varphi_*})$ factor applied to the equations of the Deborah number (Eqn. 4.28,4.29,4.30) provides a good estimation for the behaviour of the experimental data. Therefore, the response to an applied strain rate for a two-phase (crystal and melt) sample can be approximated if its crystal fraction is known and if its critical crystal fraction, φ_*, can be calculated.

With an exception of the 0.5 fraction sample, the Deborah numbers calculated for each strain rate and crystal fraction via Equation 4.28 align well with those calculated from the empirical equation of Coats et al. (2018) (Fig. 4.15). For certainty of behaviour, or if the critical crystal fraction could not be calculated, the Deborah number could be computed via the empirical relation if the strength of the sample was known. Where the flow consistency and flow index of each sample could be estimated from the Ostwald (1925) parameters, taken from the exponential relations found for natural and synthetic samples (Fig. 4.14b,c).

Coats et al. (2018) (see Chapter 2) found that the fraction of pores, φ_p, decreases the Deborah number at the onset of non-Newtonian behaviour following

$$De_{n-N} = -1.7 \times 10^{-4}\varphi_p + 9.40 \times 10^{-5}, \quad (4.31)$$

for samples with a crystal fraction of 0.75. Above a pore fraction of approximately 0.27 the onset of non-Newtonian behaviour is equivalent to the onset of failure and so $De_{n-N} = De_{fail}$. Combining this equation with the result from the olivine samples studied here, $De_{n-N} = 10^{-3}(1-\frac{\varphi_x}{\varphi_*})$, we can formulate a linear equation for three-phase melts that follows

$$De_{n-N} = -1.7 \times 10^{-4}\varphi_p + 10^{-3}(1-\frac{\varphi_x}{\varphi_*}) \quad (4.32)$$

that converges at $\varphi_p \geq 0.27$ to $De_{n-N} = De_{fail}$. Therefore, if the porosity, crystal fraction and critical crystal fraction are known of a material, the strain rate at which non-Newtonian behaviour, and perhaps failure, occurs can be estimated within a precision of ~ 0.2 log units.

4.5. Conclusion

Uniaxial testing on a suite of dense, variably crystalline ($0 \leq \varphi_x \leq 0.5$) suspensions has given a unique insight into their rheological behaviour. The results of experiments and modelling has yielded three major conclusions:

1. The use of the mathematically derived maximum packing fraction in viscosity models does not provide a good estimation of the rheological behaviour of the samples. It leads to an underestimation of the onset of non-Newtonian behaviour, overestimates the exponential increase in viscosity with crystal fraction, and underestimates the degree of shear-thinning. The empirical based viscosity model of Costa et al. (2009), which can be adjusted to the specific characteristics of each dataset, provided a much more robust fit to the data than the combination of theoretical, mathematical relationships.
2. Crystal fracture and resultant dilatancy are major causes of shear thinning behaviour. Considering the character of the crystalline phase in the suspensions tested, the contributions from particle rotation cannot be determined.
3. The onset of non-Newtonian behaviour in the melt phase has been linked to transitional strain weakening behaviour that occurs just before failure. It can be linked to the Deborah number which, at the onset of non-Newtonian behaviour, follows the relationship $De_{n-N} = 10^{-3}(1 - \frac{\varphi_x}{\varphi_*})$. By combining the results of this study to that in Chapter 2, it was found that for three-phase systems, this follows the relationship $De_{n-N} = -1.7 \times 10^{-4}\varphi_p + 10^{-3}(1 - \frac{\varphi_x}{\varphi_*})$, where at or above a porosity of 0.27, $De_{n-N} = De_{fail}$. This empirical equation for the onset of non-Newtonian behaviour for three-phase melts could be used to predict the strain rate at which failure is expected to occur in multiphase magma undergoing shear in volcanic systems.

These results and constraints may improve the way suspension rheologies are modelled. The observations made here suggest that crystal rupture and resultant dilation may be responsible for the occurrence of shear thinning in crystal-bearing suspensions. While further action may be required to test this hypothesis, such as taking internal images at each stage of the stepped experiment or by recording the acoustic emissions from fracturing crystals, it is clear that the decrease in viscosity with strain rate could have at least partially resulted from crystal fracture and dilation. This will be further explored in Chapter 5.

Over the Europeans

and northfolk of the cirque and valley

in their ancient song tongues, and their dreams

-Untitled | Republic of Verse

Chapter 5: Illuminating dilation of magmatic suspensions during shear using 4D synchrotron imaging

Abstract

Magmas are complex mixtures of crystals and bubbles suspended in a viscoelastic melt and during transport, these suspensions exhibit non-Newtonian, shear-thinning rheology. The non-Newtonian behaviour of magmatic suspensions is generally attributed to crystal-crystal interaction, crystal and bubble alignment, crystal and bubble deformation, rupture of crystals and melt, and combination thereof. Although the degree of shear-thinning is known to increase with crystal and bubble fractions, its origin remains poorly understood. We performed high-temperature (700 ˚C) uniaxial compressive tests (at strain rates of $1.67x10^{-5}$, $1x10^{-4}$ and $1.67x10^{-4}$ s^{-1}) on synthetic two-phase (crystals and silicate melt) suspensions (with 0.0-0.5 fraction crystals) whilst imaging the internal sample structure using synchrotron-based X-ray computed micro-tomography to quantify the response of phases to deformation. During experimentation, we witnessed dilation resulting from small tears that nucleate around broken crystals and propagate in the melt and crystalline phases with strain. The data indicate that dilation of suspensions scales with crystallinity, applied strain rate and the magnitude of strain. We advance that this dilation may contribute to the shear thinning nature of such materials. We also postulate that dilation may prompt important magmatic and volcanic processes, including interstitial melt extraction (i.e., filter pressing) and volatile exsolution, which would accelerate magma differentiation, for instance, during deformation of a mush or during eruption of a crystal-rich lava dome. Dilation (and ultimately rupture) also impacts pore connectivity and permeable outgassing, which are important to regulate the volcanic dilemma, flow or blow. We conclude that dilation, systematically quantified here for the first time in magmatic suspensions, may significantly impact magma transport and evolution.

5.1. Introduction

The rheology of magma plays an important role in magma storage (Marsh, 2015), convection (Marsh, 2015), crystallisation (Cashman and Blundy, 2000), degassing (Melnik and Sparks, 1999), outgassing (e.g. Wadsworth et al., 2017a), transport (Sparks, 1997, 2003), and eruption style (see Cashman and Sparks, 2013 and references therein), as well as slip processes in melt-bearing faults (e.g. pseudotachylytes; Kendrick et al., 2012) and emplacement of impact melts (Dence, 1971; Schultz and Mustard, 2004). These processes are impacted by the viscosity of magmatic suspensions, their ability to accumulate or release stress and the mechanisms by which they flow.

Magmas consists of a melt phase (generally silicic) with variable fractions of crystals and gas bubbles. Whereas single-phase silicate melts are Newtonian viscoelastic bodies (Dingwell and Webb, 1990), which deform whilst conserving volume (isovolumetric), magmatic suspensions tend to exhibit non-Newtonian, shear-thinning rheologies (e.g. Caricchi et al., 2007; Lavallée et al., 2007; Cordonnier et al., 2009; Coats et al., 2018), enhanced by the fraction of crystals (Caricchi et al., 2007) and bubbles

(Truby et al., 2015). Shear-thinning magma rheology generally is defined by a power law relationship between stress and strain rate, where the power is less than unity (Barnes et al., 1989); this results in a time-independent flow behaviour reflected as an apparent viscosity reduction with strain rate (e.g., Lavallée et al., 2007).

Several studies have attempted to resolve the origin of shear-thinning behaviour in magmas. Webb and Dingwell (1990a, 1990b) observed shear thinning during deformation of single-phase melts at strain rate approaching the viscoelastic limit of the material and ascribed it to structural breakdown (i.e., rupture) at the molecular level. In magmatic suspensions however, multiple factors can promote a shear thinning rheology. The interactions of crystals can induce lubrication and drag forces (Marzougui et al., 2015). These forces are exaggerated by particle aspect ratio and orientation that cause non-uniformity of forces around crystal boundaries (Bergantz et al., 2017), which can act to fluidise the system (e.g. Mueller et al., 2010, 2011b). Furthermore, the rearrangement of crystals during strain increases the laminarity of the flow (Caricchi et al., 2007; Lavallée et al., 2007); the configuration of this rearrangement towards fully laminar flow, and thus the extent of this fluidisation, has been described to be strain rate dependent (e.g. Liu et al., 2018 and references therein). Deubelbeiss et al. (2011) numerically demonstrated that the development of shear thinning with strain rate is commensurate with stress accumulation in the crystal phase; complementary laboratory experiments corroborated such constraints they evidenced crystal plasticity and failure, induced by increasing strain and strain rates in shear thinning magmas (Kendrick et al., 2013b, 2017). It is likely that, similar to other materials (Brown and Jaeger, 2011; Cheng et al., 2011), shear-thinning is a result of a combination of mechanisms with variable impacts. A complete understanding of magma rheology of magma requires a description of these mechanisms. Here, making use of recent advances in x-ray tomographic imaging during laboratory testing (e.g. Madonna et al., 2013; Arzilli et al., 2016; Singh et al., 2018), we conduct *in-situ* deformation experiments on a suite of two-phase magmas to isolate the effects of crystals on volumetric changes during flow.

5.2. Materials and methods

Synchrotron X-ray computed micro-tomography (sXCT) was utilised to examine the *in-situ* microstructural response of two-phase (melt and crystal) samples to uniaxial compression at high temperature and various strain rates. This non-destructive imaging technique has been used to quantify the microstructures of a variety of rock samples (e.g. Madonna et al., 2013; Arzilli et al., 2016; Singh et al., 2018). Here, samples consisted of borosilicate Spheriglass® beads sintered with various fractions (0.1, 0.2, 0.3 and 0.4) of rutile crystals (50-180 μm) under compression of 2750 N at a temperature of 750 °C (see Chapter 3). The initial porosity of the samples was quantified via helium pycnometry and estimated using QEMSCAN® image processing; the samples so prepared were dense with a porosity lower than 0.05.

Samples were heated at 5 °C.min^{-1} to 700 °C ±10 °C (furnace temperature) using a custom-built PID-controlled resistance furnace, with an X-ray transparent window, known as 'Etna' (Xu et al., 2016). The window allowed for imaging of the internal sample as it was rotating along its vertical long axis. Thermal equilibration was achieved in 10 minutes, then the samples were compressed axially,

perpendicular to the rotation axis, using a bespoke deformation rig, P2R, designed for *in-situ* testing (e.g. Cai et al., 2014). Compression was applied at a rate of 0.6 μm s^{-1} (~ $1x10^{-4}$ s^{-1}) on all crystal fractions, at 0.1 μm s^{-1} (~ $1.67x10^{-5}$ s^{-1}) on the 0.4 fraction and at 1 μm s^{-1} (~ $1.67x10^{-4}$ s^{-1}) on the 0.2 fraction, until axial strains (shortening) of ~ 0.22 were reached.

sXCT was carried out using a monochromatic beam (53 keV) at the I12-JEEP beamline at Diamond Light Source using the pco.edge camera with a voxel size of 3.24 μm (Drakopoulos et al., 2015). Samples were imaged cold, upon reaching dwell temperature, during and after experimentation. 2150 projections were acquired over 180 rotation (10 ms projection exposure time), resulting in a single 3D frame acquisition time of approximately 10 seconds. Phase contrast retrieval was not performed. For each compression experiment a number of 3D frames were acquired (342 3D frames were collected at 0.1 μms^{-1}, 114 frames at 0.6 $\mu ms^{-1,}$ and 68 frames at 1 μms^{-1}). The data were reconstructed using a filtered back projection algorithm with a ring artefact removal (Titarenko et al., 2010; after Karagadde et al., 2015).

Visualisation and analysis of the reconstructed images was carried out using the standard algorithms Avizo™ software (https://www.fei.com/software/amira-avizo/) on frames representing strains of approximately 0, 0.03, 0.09, 0.12, 0.16 and 0.2. Due to the technological challenge of these experiments, occasional lapses in data acquisition exist, however, data was extrapolated when necessary. Images were down-sampled to 8 bit greyscale images with a voxel size of 6.48 μm and the sample volume labelled (watershed segmentation tool) at each frame of interest. Segmentation of the pores was achieved using a global threshold of 95 to select all the pore edges, followed by a 2D fill applied in the xy, xz and yz orientations. The volume fraction of porosity was measured at each strain interval.

5.3. Results

Uniaxial deformation of the suspensions at high temperature (700 °C) results in lateral expansion, producing a barrel-shape silhouette (Fig 5.1). Observation of the samples' silhouette show that barrelling does not centrally develop in the sample, but preferentially near the base, indicating that this region is slightly warmer due to the mild temperature gradient (ca. 10 °C) in the furnace.

5.3.1. Dilation during shear of magmatic suspensions

Reconstruction of the magmatic suspensions' internal structure developed during shear illuminates the evolution of the porous network. The data show that strain causes an increase in pore (blue) fraction in each suspension, even though the initial porosity of the samples differs slightly (Fig. 5.1). The data also indicate that pores are preferentially created in crystal-rich suspensions.

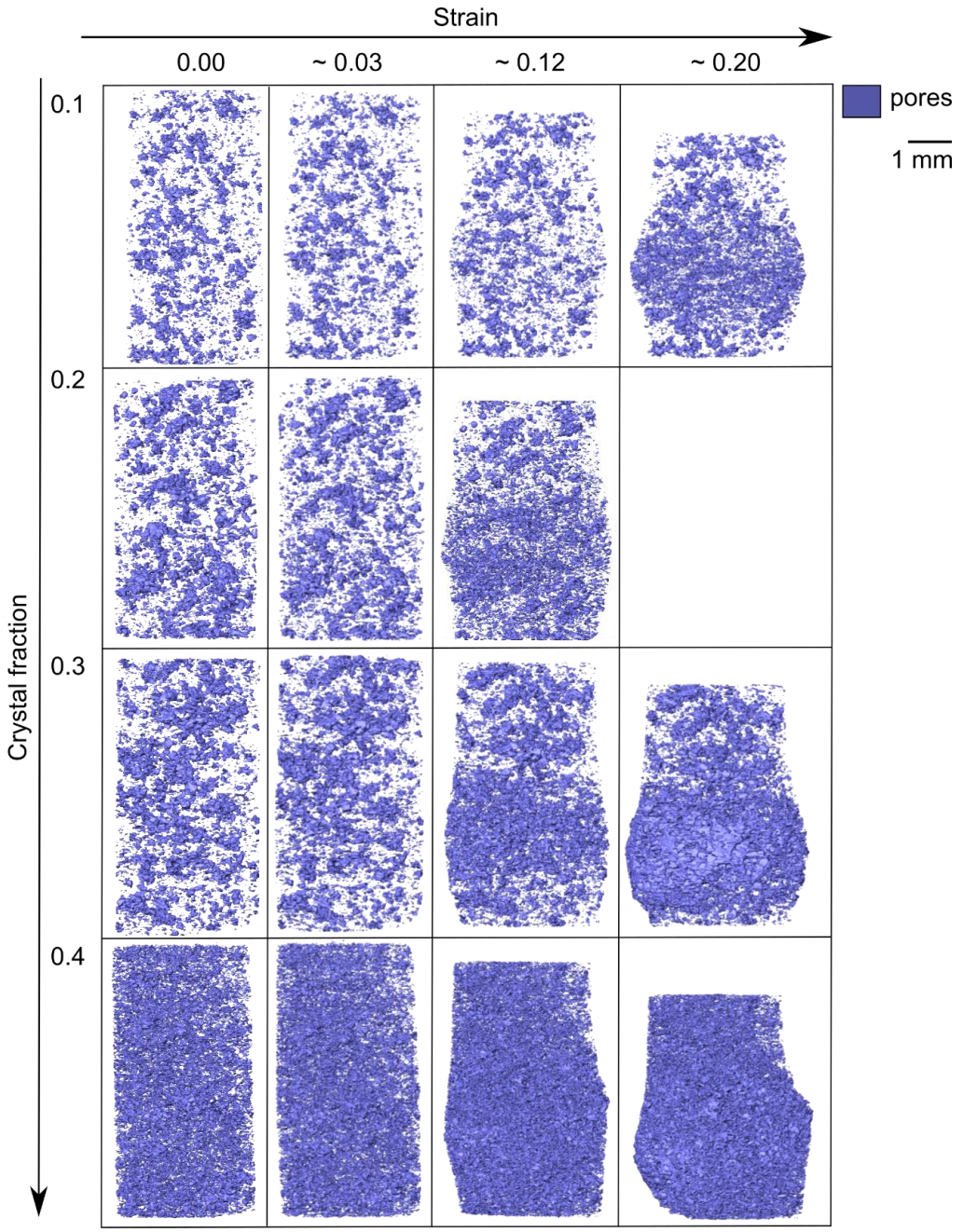

Figure 5.1. 3D pore evolution with strain and crystal content for samples deformed at 0.6 µms^{-1} at 700 °C. Porosity increase with strain is greater for higher crystal fractions. Generated porosity is in the form of fractured crystals and tears in the melt fraction due to dilation in areas of strain localisation, here highest in the area of the bulges at higher total strains.

3D visualisation of the samples in Avizo™ software allows us to quantify the porosity of the suspension at each strain increment (Fig 5.2a). The data shows linear increase in porosity of suspension with strain, following:

$$\varphi_p = \frac{d\varphi_p}{d\varepsilon}\,\varepsilon + \varphi_{pi}, \qquad (5.1)$$

where φ_p is the porosity, φ_{pi} is the initial porosity, ε is the strain and $\frac{d\varphi_p}{d\varepsilon}$ is the change in porosity with strain (Fig. 5.2a). The regressions fitting the datasets indicates an increased change in porosity with strain as a function of crystallinity in the sample.

To quantify the effect crystallinity has on this change in porosity with strain we plot the variation in porosity with strain, $\frac{d\varphi_p}{d\varepsilon}$, with crystal content (Fig. 5.2b). In doing so, we assume that the deformation of a single phase viscoelastic liquid (i.e., crystal- and vesicle-free) is isovolumetric (see Dingwell, 1995; Eichhubl, 2004; Lamur et al., 2019, data repository) and thus the relationship obtain passes through the origin of the graph. Doing so for the most complete dataset at a strain rate of 10^{-4} s^{-1} (i.e., deformation rate of 0.6 μm s^{-1}), we obtain the following linear relationship:

$$\frac{d\varphi_p}{d\varepsilon} = 1.25\varphi_x \quad (5.2).$$

As the linear fit agrees well with the data, we extend this method to the dataset at other strain rate and find that

$$\frac{d\varphi_p}{d\varepsilon} = 1.66\varphi_x \quad (5.3)$$

for $\dot{\varepsilon}$ = 1.67x10^{-5} s^{-1} (0.1 μm s^{-1}), and

$$\frac{d\varphi_p}{d\varepsilon} = 1.55\varphi_x \quad (5.4)$$

for a strain rate $\dot{\varepsilon}$ = 1.67x10^{-4} s^{-1} (i.e., deformation rate of 1 μm s^{-1}).

These regressions imply that as deformation of a given suspension proceeds, the porosity increases with strain at a rate commensurate with the crystallinity. By plotting the variation in the change in porosity with strain, with crystal content for each strain rate, we find that

$$\frac{d\left(d\varphi_p/d\varepsilon\right)}{d\varphi_x} = 0.36log(\dot{\varepsilon}) + 2.99, \quad (5.5)$$

with an R^2 value of 0.79 (Fig. 5.2c). Therefore, as

$$\frac{d\varphi_p}{d\varepsilon} = \frac{d\left(d\varphi_p/d\varepsilon\right)}{d\varphi_x}\varphi_x, \quad (5.6)$$

we can rewrite Eq. 5.5 to

$$\frac{d\varphi_p}{d\varepsilon} = 0.36log(\dot{\varepsilon}) + 2.99\varphi_x, \quad (5.7)$$

which gives the relation of porosity increase to strain rate (Eqn.5.1) as

$$\varphi_p = \left\{\left[0.36log(\dot{\varepsilon}) + 2.99\right]\varphi_x\right\}\varepsilon + \varphi_{pi} \quad (5.8)$$

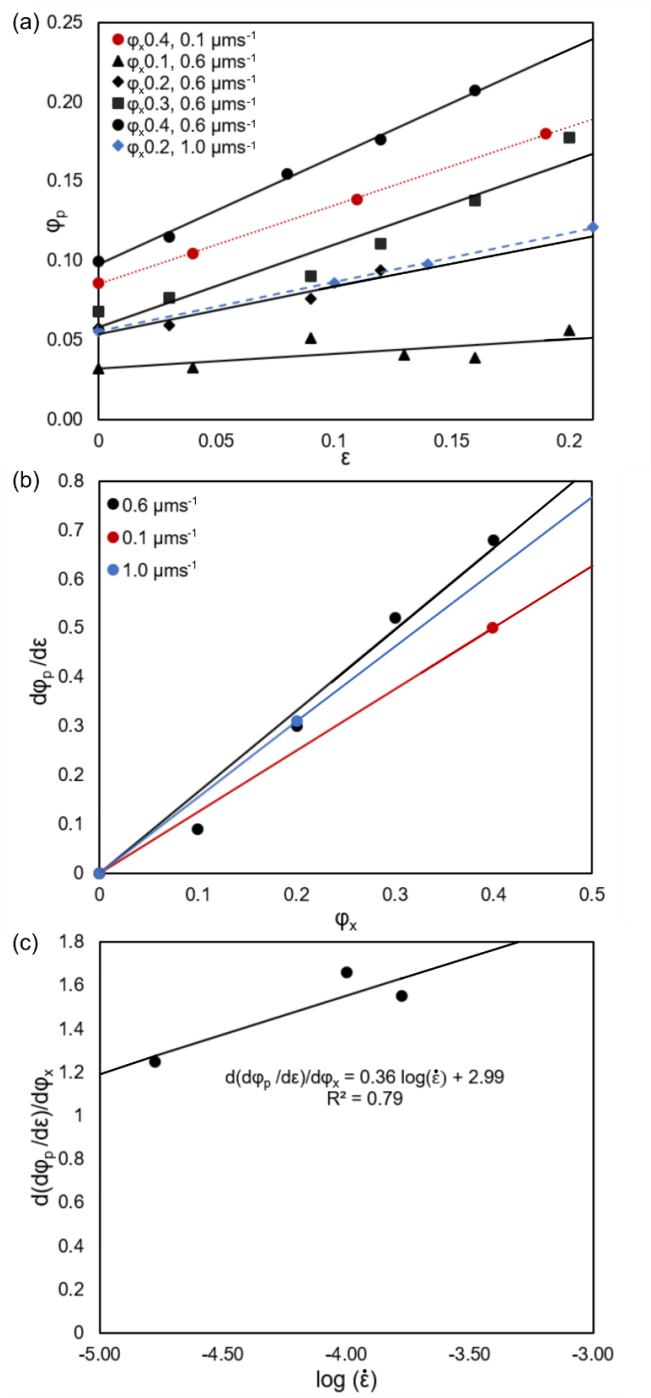

Figure 5.2. Quantification of suspensions dilation induced by shear. (a) Porosity evolution of suspensions with strain upon shear at deformation rates of 0.1 μms^{-1} ($\dot{\varepsilon} = 1.67\text{x}10^{-5}$ s^{-1}), 0.6 μms^{-1} ($\dot{\varepsilon} = 1\text{x}10^{-4}$ s^{-1}), and 1 μms^{-1} ($\dot{\varepsilon} = 1.67\text{x}10^{-4}$ s^{-1}). A linear regression is plotted through the points giving $\varphi_p = \frac{d\varphi_p}{d\varepsilon}\,\varepsilon + \varphi_{pi}$ for each crystallinity and deformation rate. (b) Slopes of the linear regressions obtained in (a) , $\frac{d\varphi_p}{d\varepsilon}$, plotted against crystal fraction for each deformation rate applied. The data is fitted with linear regressions intercepting the origin. (c) Slopes of the regressions obtained in (b), $\frac{d\left(d\varphi_p/d\varepsilon\right)}{d\varphi_x}$, plotted against the logarithm of applied strain rate. The linear regression obtained follows $\frac{d\left(d\varphi_p/d\varepsilon\right)}{d\varphi_x} = 0.36log(\dot{\varepsilon}) + 2.99$, and an R^2 value of 0.79

5.3.2. Textural description of dilatant microstructures

The tomographic reconstructions produced in this study illuminate the evolution of microstructures produced by shear of suspensions with different crystallinity. Compressing samples induced dilation which increased with strain (Fig. 5.3a, 5.S.1-6). Dilation manifests as small tears in areas of strain localisation along melt-crystal boundaries. These tears increase in width and length with strain, propagating parallel to the major principal stress, eventually coalescing (Fig. 5.3a).

In order to understand the potential role of dilation in the rheological evolution of suspensions (for which the apparent viscosity decreases as a function of strain rate, with a decreasing rate commensurate with crystallinity; e.g. Caricchi et al., 2007) we compared the resultant microstructures obtained after 0.1 strain for the suspensions with 0.2 (low) and 0.4 (high) crystallinity deformed at different strain rates (Fig. 5.3b). Data from the suspensions with 0.4 crystals have shown that deformation under the lowest applied strain rate (~1.67×10^{-5} s^{-1}) results in crystals being well distributed, without preferential alignment against the applied stress field (Fig. 5.3a). Here, pores are a mixture of vesicles (initial porosity remnant from sample formation) and small tears developed by shear. The tears are ~ 0.1 mm in length and ~ 0.01 mm in width and are orientated sub-parallel to the principal stress. As strain rate is increased to ~ 1×10^{-4} s^{-1}, crystals appear to rotate slightly so their minor axis is more commonly aligned preferentially with the principle applied stress, σ_1 (Fig. 5.3b). Tears appear to have increased in size, with some as large as ~ 0.15 mm in length and ~ 0.02 mm in diameter.

In comparison, the data obtained from shearing of suspensions with a lower crystallinity of 0.2 show contrasting evolution, at low applied strain rate of 10^{-4} s^{-1}, crystals do not appear to have rotated (Fig. 5.3c) following 0.11 strain. Tears develop along crystal-melt boundaries, but they do not propagate into the crystals. The extent of tears is lower than in higher crystallinity suspensions; they reach < 0.01 mm in length and < 0.001 mm in width (Fig. 5.3b). At a higher strain rate of ~ 1.67×10^{-4} s^{-1} (Fig. 5.3d). we observe that the tears have multiplied in number and have increased in length to ~ 0.08 mm and in width to ~ 0.03 mm. Crystals also appear to have rotated slightly so their minor axes are close to parallel with principal stress.

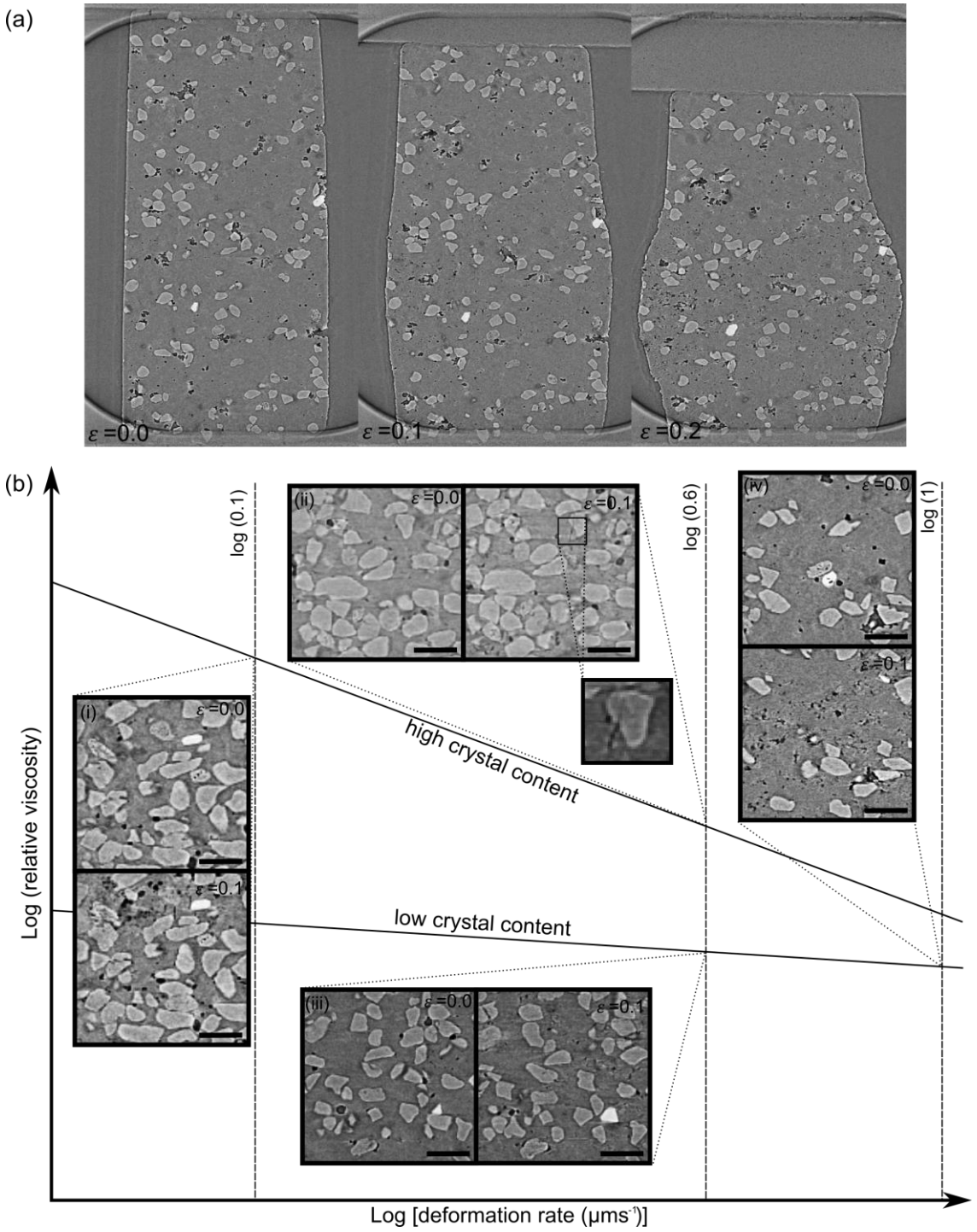

Figure 5.3. Microstructural evoution of shearing magmatic suspensions at 700 °C. a) 2D slices of the 6 mm high 0.1 fraction sample tested at 0.6 μm s^{-1}, through strain. Crystals are seen as the brighter greyscale, pores as the darker greyscale, and the melt as the medium grey scale. b) Rheological framework to interpret the dilation of shearing suspensions; this includes a schematic of relative viscosity decrease with deformation rate for low and high crystallinity based on Caricchi et al., (2007). Shear-thinning (resulting in viscosity decrease with strain rate) is more prominent in crystal-rich suspensions. Dashed lines indicate the strain rate of the experiments. Boxes show a 2D slice at 0.0 and 0.1 strain for the suspensions with 0.4 crystals tested at (i) ~ $1.67x10^{-5}$ s^{-1} and (ii) ~ $1x10^{-4}$ s^{-1} (the inset magnifies a tear), and for the suspensions with 0.2 crystals tested at (iii) ~ $1x10^{-4}$ s^{-1} and (iv) ~ $1.67x10^{-4}$ s^{-1}. For each image displayed, axial deformation was applied vertically, and the scale bar equates to 0.3 mm.

The tomographic reconstructions obtained in this study highlight that during shear, magmatic suspensions undergo dilation due to progressive tearing as cracks nucleate along melt-crystal boundaries and propagate in the melt, then in the crystalline phase. We find that crystallinity and strain rate increase the development of dilation, tearing and crystal rotation during shear of magmatic suspensions.

5.4. Discussion and implications

5.4.1. Impact of dilation on magmatic suspension rheology

The occurrence of shear thinning of suspensions has been ascribed to multiple variables. As experimentally shown by Caricchi et al. (2007) crystal alignment impacts the rheological evolution of magmatic suspensions and contribute to shear-thinning behaviour. However, numerical simulations by Deubelbeiss et al. (2011) have shown that alignment is not the sole cause of shear-thinning and that stress partitioning maybe significant, as high stresses preferentially accumulate in the crystalline phase. Such stress accumulation may force crystal plastic deformation, which may result in rupture at high strain rates (Kendrick et al., 2017). Here, we find vestige of crystal rupturing following progressive tearing of the suspensions. Yet, the systematic dilation of the suspensions as a function of crystallinity, strain (Fig. 5.2a) and strain rate (Fig. 5.2c), may prove an important contributor to the development shear thinning in suspensions. The presence of pores, like crystals, promote stress partitioning in a suspension and thus the systematic evolution of porosity in dilatant suspensions may provide a compelling mechanism to explain shear thinning. Volumetric expansion has been previously invoked to explain strain weakening of shearing crystal-rich lavas (Kendrick et al., 2013b) and it is widely accepted that the strength of rocks and magmas decrease with porosity (see Coats et al., 2018, and references therein). It can therefore be concluded that along with crystal alignment and plasticity, dilation may be a contributing factor in shear-thinning and a major cause of strain weakening. If that is the case, its impact on magmatic processes should not be overlooked.

5.4.2. Implications of shear-induced dilation on magmatic and volcanic processes

The presence of crystals has long been recognised to play an important role in the rheology of magmas (Shaw, 1965; Marsh and Maxey, 1985; Kerr and Lister, 1991; Bagdassarov and Dingwell, 1992). The constraint on dilation made here may prove to have important implications for magmatic as well as volcanic processes. Dilation formed by tearing results in the creation of an area with lower pressure, which we suggest may trigger physical, as well as chemical, magma differentiation. Firstly, the local pressure reduction resulting from dilation may promote the preferential infiltration of melt, thus triggering filter pressing, which has been ascribed to be an important mechanism of differentiation in magma mush (Fig. 5.4a; Sisson and Bacon, 1999; Pistone et al., 2015). Dilation-induced melt extraction would promote the differentiation of evolved melts, which has been observed in large intrusive batholiths (McBirney, 1995). Secondly, the resultant low-pressure from dilation may locally promote vesiculation as volatile saturation is proportional to pressure (e.g. Fig. 5.4a; Zhang, 1999). This would modify the resultant viscosity of the interstitial melt (Hess and Dingwell, 1996) as

well as the buoyancy of magma (Parmigiani et al., 2016), thus impacting the force driving magma ascent and eruption.

The physical properties of magma - especially viscosity, porosity (via buoyancy) and permeability - are important controls on magma ascent and eruption processes (Mueller et al., 2008). The observations made here that shearing magmatic suspensions, which have long been described to be shear thinning (e.g. Lejeune and Richet, 1995), undergo systematic dilation as a function of crystallinity, applied strain rate and magnitude of strain suggest that the architecture of the porous network will be modified where strain localises. In volcanic conduits, strain has been described to localise near the conduit margins, based on observations of the porous network architecture (e.g. Schauroth et al., 2016), crystal plasticity and reactions (e.g. Wallace et al., 2019), magnetic properties (Kendrick et al., 2012; Wallace et al., 2019), and brittle processes in shear zones (e.g. Smith, 2000; Cashman et al., 2008). Strain localisation near conduit margins would thus not only lead to a zone of lower apparent viscosity but also to a zone in which dilatant process may prevail (Fig. 5.4b). The occurrence of dilation vs compaction has not been systematically mapped for magmatic suspensions, but we have a good understanding for rocks. In general, dilation is favoured in the densest of materials (for which strain cannot compact pores) deformed at high strain rates and in areas of low effective pressure (which is the difference between confining pressure and pore pressure) (Rutter, 1986; Heap et al., 2015a). Thus, for dense magmatic suspensions, we expect that magma would be prone to dilate during flow in the upper conduit, especially where the strain rate is high near conduit margins. In such scenarios, dilation would promote the localised construction of a permeable porous network that controls outgassing along curvilinear features (Lavallée et al., 2013; Gaunt et al., 2014), which may regulate the level of explosivity of an eruption (e.g. Edmonds, 2008; Calder et al., 2015) (Fig. 5.4c). Macroscopic rupture may further ensue from the development of tears associated with dilation which may result in fault-controlled processes such as comminution, faulting and frictional melting (Kendrick et al., 2012), which impact magma ascent dynamics and generate concomitant seismicity, commonly used to track the state of ascending magmas (e.g. Iverson et al., 2006; Lamb et al., 2015). Finally, during flow of erupted lava, strain localises at the base of the flow, where it commonly undergoes brecciation (Fig. 5.4d). Here we advance that the dilation observed in shearing suspensions may be an important contributor to the generation of such clinker textures in, for instance, a'a flows (Macdonald, 1953). Thus, the impact of shear-induced dilation in dense, crystal-bearing magmas may resound across a range of magmatic and volcanic processes.

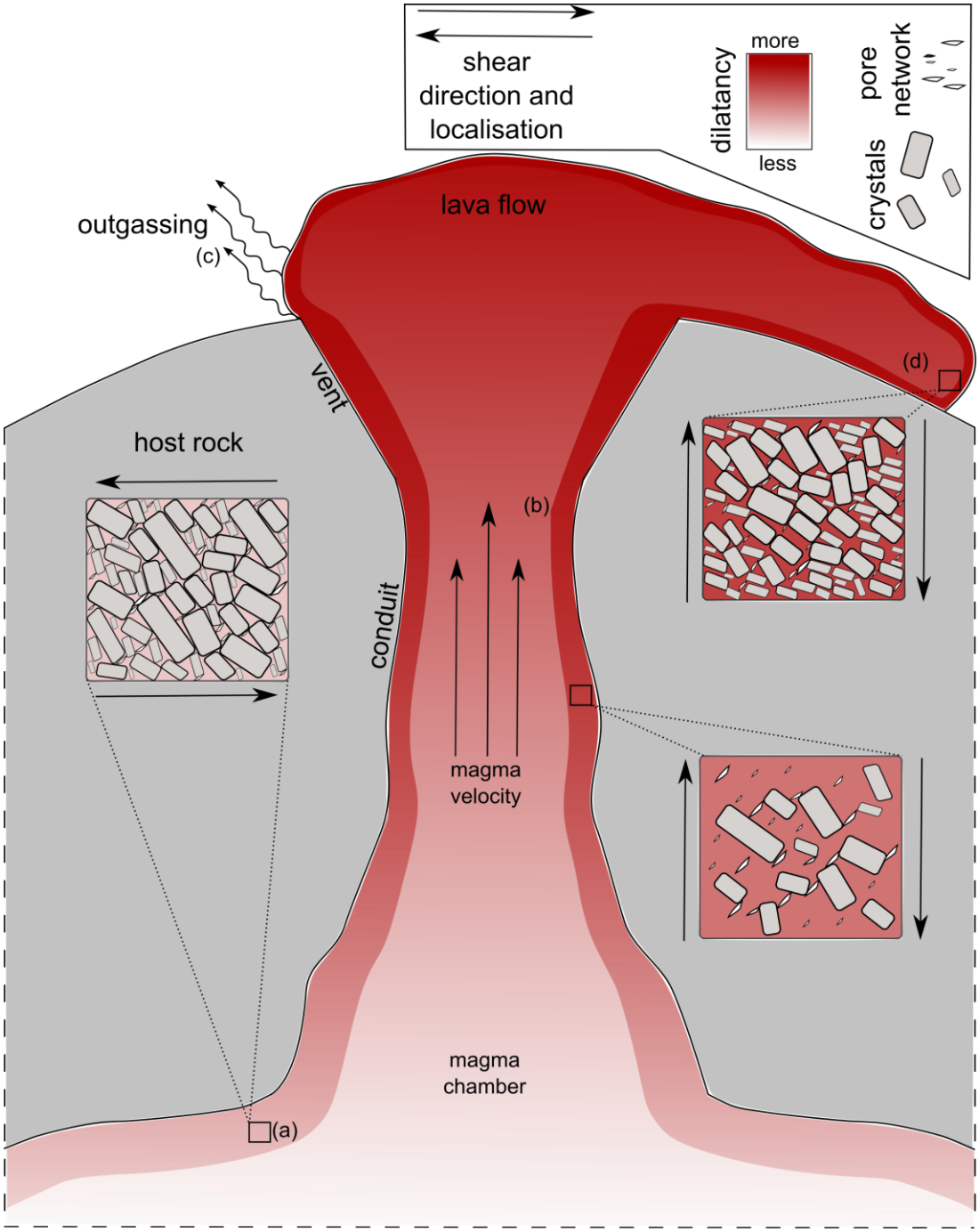

Figure 5.4. Occurrence and impact of dilation in magmatic and volcanic systems. (a) Dilation may preferentially impact magmatic mush, where it may trigger vesiculation as well as filter pressing. (b) Dilation may also take place in ascending magma where it shears near conduit margins, potentially causing vesiculation as well as modifying the permeable porous network; progressive shear-induced dilation may lead seismogenic rupture, which may impact magma ascent. (c) dilation would promote the localised construction of a permeable porous network that controls outgassing. (d) Dilation at the base of lava flow may result in the generation of clinker bottom textures.

5.5. Conclusion

Synchrotron-X-ray computed micro-tomography during magma suspension deformation has provided a first systematic constraint on the development of dilation, favoured by the presence of crystals, applied strain rate and magnitude of strain. The experiments have shown that this dilation is manifested as small tears along the melt-crystal boundaries in areas of strain localisation which develop preferentially at higher crystallinities and increase in size and number density with applied strain and strain rates. We conclude that dilation is likely an important control on the shear-thinning rheology of magmas, which may provoke physical and chemical changes that impact magmatic and volcanic processes during shear.

5.6. Supplementary files

5.6.1. Sample preparation

The volume of synthesised suspension prepared was determined from the properties of its constituent phases (i.e., glass and crystals) and to ensure that cylindrical core with a height of > 6 mm could be prepared. The required mass of each was calculated from the end target volume as the exact densities of the glass and rutile phase were known (Table 5.S.1). The end target volume was selected to equate to a fully dense suspension with a height that would allow samples of the required height (6 mm) to be cored for laboratory testing (Table 5.S.2).

Table 5.S.1. Material properties of phases used in sample synthesis

Material	Spheriglass®	Rutile
Image	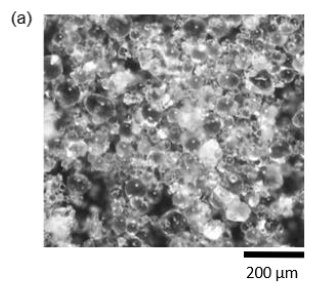	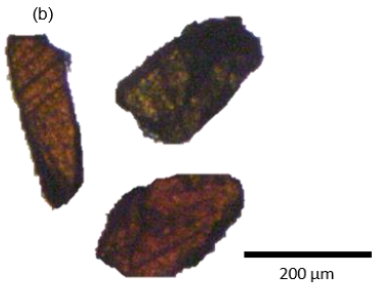
Mohs scale hardness	5.5	6-6.5
Particle Size (µm)	150-250	53-180
Polydispersity	0.93	0.89
Density (g.cm^{-3})	2.50	4.29
Aspect Ratio	1.00	1.95
Maximum Packing	0.64	0.66

To ensure the synthesis of dense suspensions, powders were prepared with a mixture of whole and crushed Spheriglass® beads, increasing the prepared powders polydispersity which enhances sintering (Wadsworth et al., 2017a). For crystal volume fractions ≤ 0.2 the ratio of crushed to whole glass beads was selected as 50:50, while for crystal fractions ≥ 0.3 it was set as 75:25. The crystal and glass powders were thoroughly mixed to ensure homogenisation. Large alumina crucibles (~ 26x38 mm) were first finely coated with high temperature cement before filling with the mixed powders to prevent the sample from sticking against the wall of the crucibles. During filling the crucible was intermittently tapped carefully to ensure maximum dry packing of the powder (following Vasseur et al., 2013) without causing particle segregation due to settling by density contrast which can produce bands.

Table 5.S.2. Volumes and masses of Spheriglass® and rutile required for sample synthesis

Target volume (cm^3)	33.30
Rutile density (g/cm^3)	4.29
Spheriglass® density (g/cm^3)	2.50

Rutile fraction	Rutile (cm^3)	Rutile (g)	Spheriglass® fraction	Spheriglass® (cm^3)	Spheriglass® (g)
0.10	3.33	14.29	0.90	29.97	74.93
0.20	6.66	28.57	0.80	26.64	66.61
0.30	9.99	42.86	0.70	23.31	58.28
0.40	13.32	57.15	0.60	19.98	49.96

A cylindrical stainless-steel plug (24 mm diameter) was placed on top of the powder-filled crucible and the entire assembly was then placed between the pistons of a 100 kN Instron 8862 uniaxial press with a three-zone, split furnace in the Experimental Volcanology and Geothermal Research Laboratory at the University of Liverpool. The assembly was heated at a rate of 5 °C min^{-1} to a sample temperature of 750 °C ± 5 °C, then dwelled for one hour to allow thermal equilibration. The mixture was then loaded to 2750 N at a rate of 250 N min^{-1} while temperature was monitored with a K-type thermocouple.

As sintering cannot occur below the glass transition temperature, densification did not occur during heating, and only at experimental temperature, when the pistons were in contact with the powder mixtures and loading was occurring. Therefore, the suspension porosity at any point in time, $\varphi_p(t)$, could be calculated from the monitored piston extension through time, $Ex(t)$, via

$$\varphi_p(t) = 1 - \left(\frac{h_f}{h_i - Ex(t)}\right), \quad (5.S.1)$$

where h_i is the height of the prepared powder, and h_f is the expected height of a dense equivalent of the suspension. Piston displacement was stopped when the extension of the pistons equalled the difference between $h_i$and h_f. Suspensions so sintered were then cooled at a rate of 5 °C min^{-1} to room temperature. The suspensions were then cored to prepare 3x6 mm cylindrical samples for experimentation.

5.6.2. Experimental time series

Two-dimensional (2D) images at incremental steps in strain are shown for each sample.

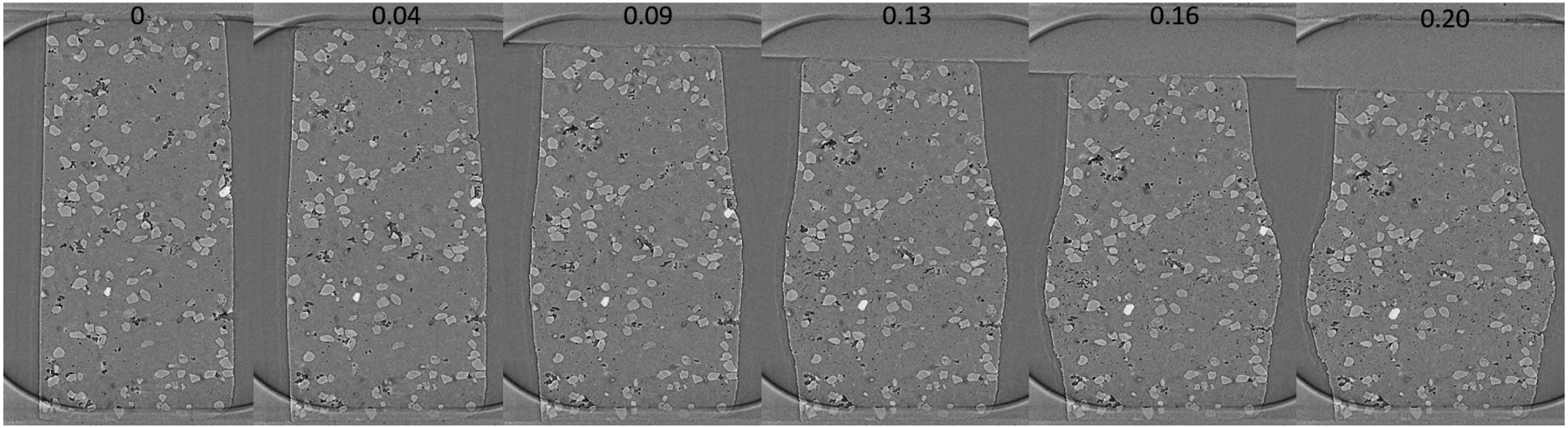

Figure 5.S.1. 2D slices of the 6 mm high 0.1 fraction sample tested at 0.6 µm s^{-1}, through strain (noted at the top of the sample) at 700 °C. Crystals are seen as white and light grey in these greyscale images, pores as the darker greyscale, and the melt as the medium grey scale.

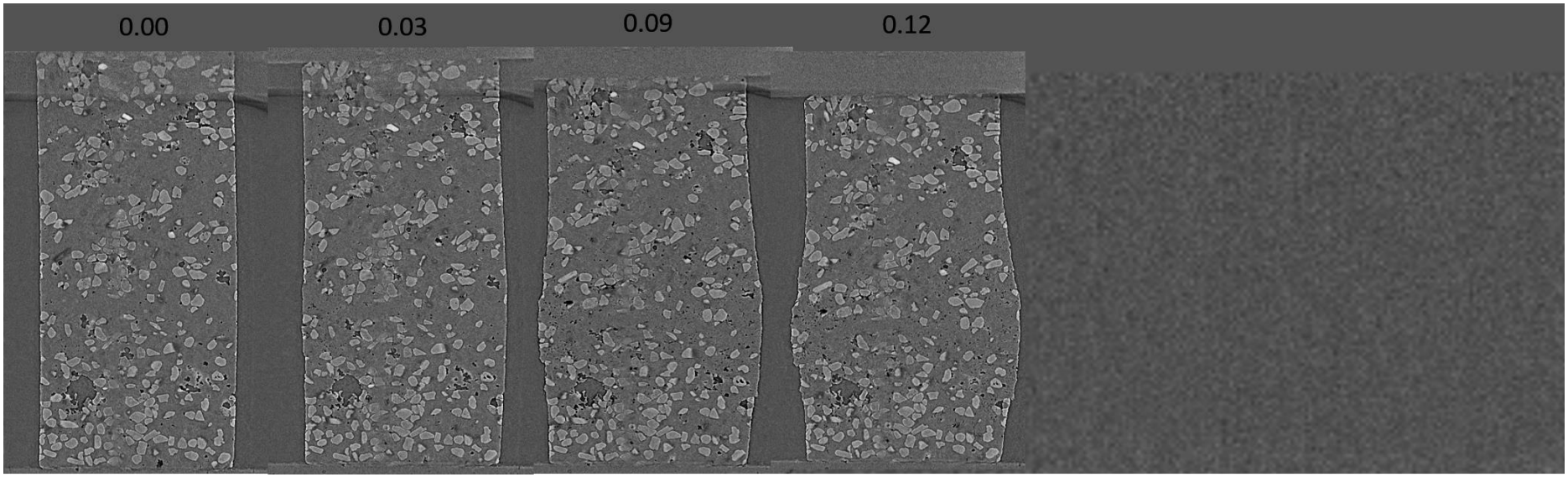

Figure 5.S.2. 2D slices of the 6 mm high 0.2 fraction sample tested at 0.6 µm s^{-1}, through strain (noted at the top of the sample) at 700 °C. Crystals are seen as white and light grey in these greyscale images, pores as the darker greyscale, and the melt as the medium grey scale.

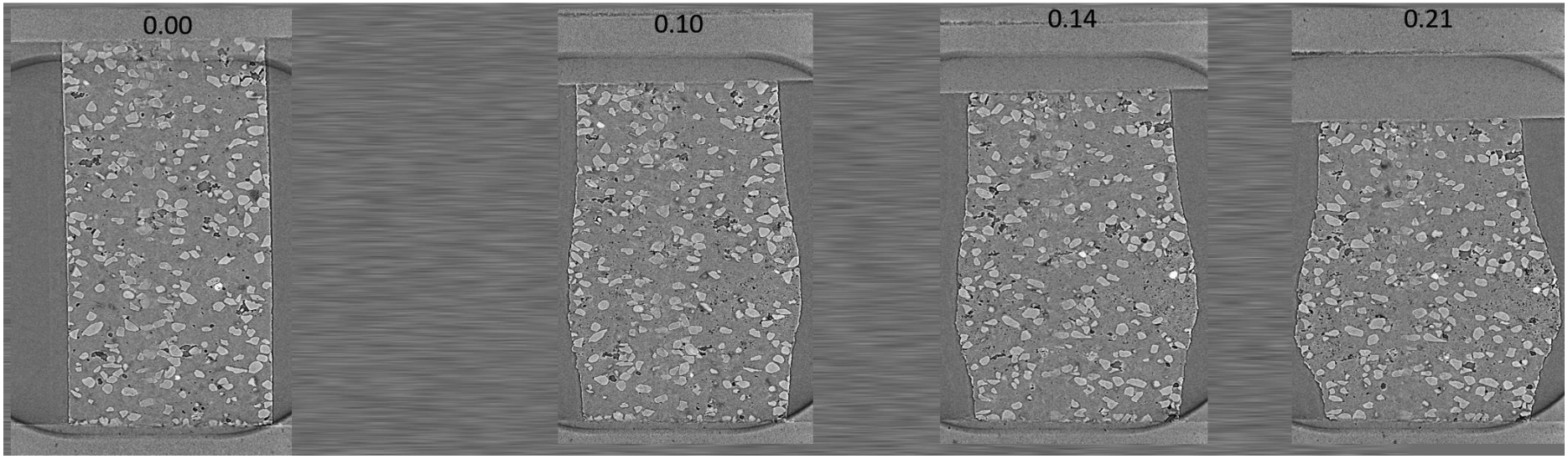

Figure 5.S.3. 2D slices of the 6 mm high 0.2 fraction sample tested at 1 µm s^{-1}, through strain (noted at the top of the sample) at 700 °C. Crystals are seen as white and light grey in these greyscale images, pores as the darker greyscale, and the melt as the medium grey scale.

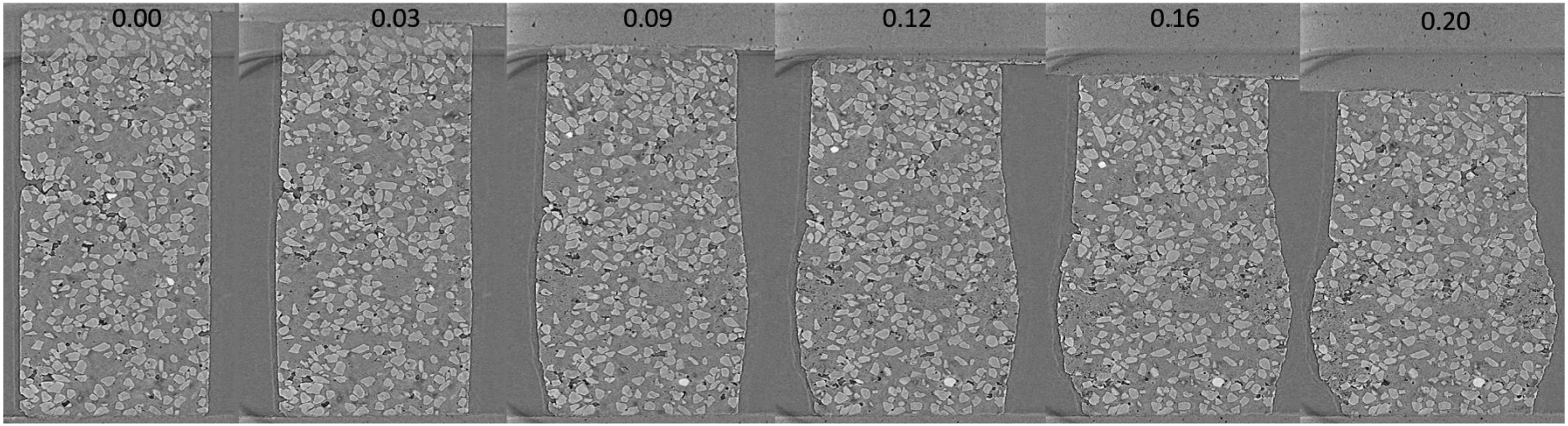

Figure 5.S.4. 2D slices of the 6 mm high 0.3 fraction sample tested at 0.6 µm s^{-1}, through strain (noted at the top of the sample) at 700 °C. Crystals are seen as white and light grey in these greyscale images, pores as the darker greyscale, and the melt as the medium grey scale.

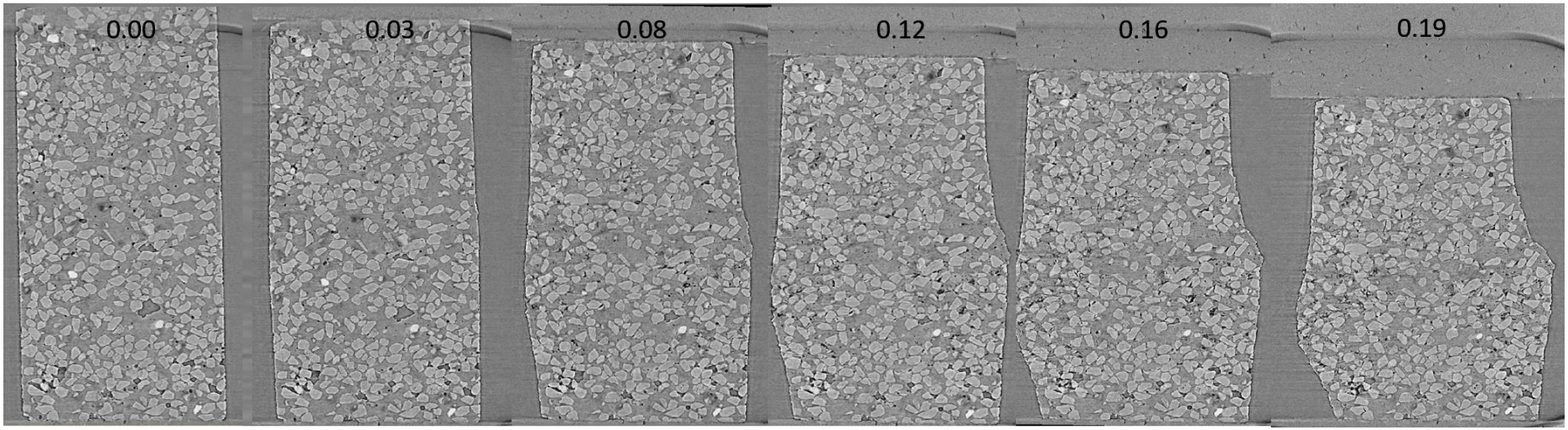

Figure 5.S.5. 2D slices of the 6 mm high 0.4 fraction sample tested at 0.6 µm s^{-1}, through strain (noted at the top of the sample) at 700 °C. Crystals are seen as white and light grey in these greyscale images, pores as the darker greyscale, and the melt as the medium grey scale.

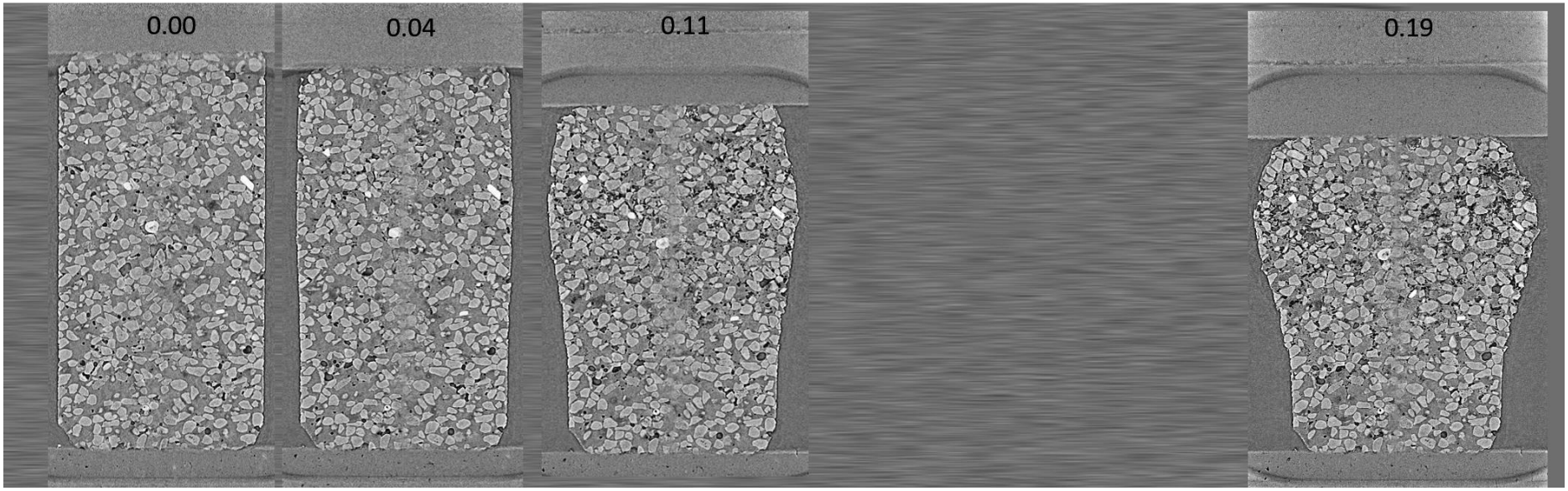

Figure 5.S.3. 2D slices of the 6 mm high 0.4 fraction sample tested at 0.1 µm s^{-1}, through strain (noted at the top of the sample) at 700 °C. Crystals are seen as white and light grey in these greyscale images, pores as the darker greyscale, and the melt as the medium grey scale.

Walk on through the wind,

Walk on through the rain,

Though your dreams may be tossed and blown.

Walk on, walk on with hope in your heart

And you'll never walk alone.

You'll never walk alone.

- You'll never walk alone | Oscar Hammerstein II

Chapter 6: Implications and outlook

6.1. Summary of key findings

This doctoral dissertation addresses the rheology of magmas and investigates the role crystals and pores play on their response to volcanic forces. Through laboratory testing, materials could be deformed under controlled volcanic conditions where variables could be isolated, and the response of the material monitored and assessed accordingly. With the aim of examining the effect porosity has on the microstructural response to deformation, natural samples, from Mt. Unzen lava dome in Japan, were selected due to their consistent crystallinity and variable porosity. However, to isolate the effects of crystallinity samples had to be synthesised using analogue materials. The rheological response of these variably crystalline samples was then examined under controlled conditions. Synchrotron based computed X-ray micro-tomography was then employed to image the response of the material to deformation. Relating findings of these investigations to previous work allowed scaling of results through dimensional analysis and the employment of numerical modelling in an effort to describe the processes observed in the laboratory.

Chapter 2 details the role porosity and alteration played on the flow and failure of natural lava samples from Mt. Unzen volcano in Japan. The volcano hosts the Heisei-Shinzan dome complex which erupted between 1990 and 1995, generating partial collapses which lead to several pyroclastic density currents. By performing uniaxial compressive tests at room temperature on *rocks* and at high temperature on *lavas*, the conditions which lead to failure could be examined.

At room temperature, the strength of the rocks decreased with porosity, a correlation which has been well documented in volcanology literature (Al-Harthi et al., 1999; Heap et al., 2014c, 2014b, 2016b; Schaefer et al., 2015). Following results obtained by Schaefer et al. (2015), the Mt. Unzen rocks also show a slight strength increase with strain rate. In altered rocks, the deposition of a secondary mineral phase within pores appeared to strengthen the material by shifting it from a regime dominated by connected porosity to one dominated by isolated pores. Alteration has also been shown to weaken volcanic rocks (e.g. Pola et al., 2012), therefore care and consideration should be employed when modelling the strength of such materials.

At high temperatures (900 °C) lavas appeared stronger than their rock counterparts when tested at similar strain rates. In this magmatic state, the strength of the Mt. Unzen material also decreased with porosity, however here we noted a strong positive correlation between strength and strain rate. Both the strengthening of material at elevated testing temperature, and the strain rate strengthening effect have previously been witnessed during tests on basalts (Schaefer et al., 2015), but not previously in a melt-bearing lava. The presence of melt meant that at high temperature conditions, the flow response of the material could also be observed. For samples with a viscous response, apparent viscosities were independent of porosity across the range tested. It is likely that pore pressurisation was insufficient to maintain pore structure, and therefore during deformation pore collapse resulted in a similar pore structure across the sample spectrum. As with other tests on highly crystalline dome materials, samples had a non-Newtonian, shear-thinning response to deformation (Lavallée et al., 2007). At low

strain rates ($\leq 10^{-4}$ s^{-1}) samples responded viscously while at higher strain rates ($\geq 10^{-4}$ s^{-1}) the lavas displayed an increasingly brittle response. Samples which displayed hybrid viscous-brittle behaviour, i.e. non-wholesale fracturing, were termed transitional (see also Wadsworth et al., 2018).

To constrain the conditions which initiate the failure of multiphase viscoelastic materials, the dimensionless Deborah numbers of the samples at failure, i.e. the critical Deborah numbers (De_c), were constrained. Comparing these to the recognised critical Deborah number of a melt phase (10^{-3}, for the onset of non-Newtonian behaviour, and 10^{-2} for failure; Webb and Dingwell, 1990), it was shown that the presence of the crystalline phase decreased the critical Deborah number from 10^{-3}-10^{-2} to 6.6×10^{-4}-1×10^{-4}. The porosity of the material, φ_p, further decreased the critical Deborah number following the linear trend $De_c = -1.7 \times 10^{-4}\varphi_p + 9.40 \times 10^{-5}$, such that the failure of more porous materials could be achieved at slightly lower deformation rate than less porous materials.

The work presented in Chapter 2 reveals that for advanced mitigation of hazards posed by the collapse of lava domes (active or inactive) or volcanic edifices, stability models should take the complex nature, and importantly variability, of the materials into account. This includes, but is not limited to, the porosity and alteration of the lava, the temperature of the dome and strain rate of extrusion or post-emplacement loading. The work at magmatic temperatures also suggested that current three phase models (e.g. Costa et al., 2009; Truby et al., 2015) may not be fully applicable to dome lavas and other crystal-rich lavas. Experimentation and analysis suggested that the dimensionless Deborah number at failure is affected by the presence of crystal and pore phases. Thus, to investigate this further, the concept was conceived to generate synthetic materials in which variables could be controlled independently.

Chapter 3 presents the process taken to synthesise analogue two-phase (crystals and melt) magma samples. Creating these well-constrained samples was key to understanding the effects crystals have on magma rheology, facilitating the controlled manipulation of the crystallinity variable. Samples were synthesised by sintering synthetic Spheriglass® glass beads with known natural crystal fractions of either plagioclase, rutile or olivine. The selected crystals were of a nominated size range with consideration of the final sample geometries for experimental testing, and their aspect ratio and density were measured before sintering. Synthesised samples were tested for final porosity, thermal properties, homogeneity and mineral composition using various techniques available, and compared against a set of criteria (i.e. porosity < 0.05) to define their use in subsequent experimental testing. Investigations found samples sintered with rutile crystals were more suited for synchrotron study (Chapter 5) due to the strong density contrast between the crystal and glass phase. However, samples sintered with olivine crystals were selected for ex-situ studies (Chapter 4) as olivine crystals were more readily available and allowed bulk synthesis. The sintering method explored in Chapter 3 allowed for the observation of densification through time by measuring the evolution of sample height. This meant that sintering could be ceased when a desired sample porosity was reached. For the samples in this study, synthesis was terminated when the final sample porosity was as close to zero as possible. However, the technique could be utilised to create samples of any desired crystal fraction and porosity. The density contrast of the plagioclase crystals to the Spheriglass® was not strong

enough for good contrast in CT imaging, therefore only olivine and rutile crystals were used in sample synthesis. Without loading the prepared material powders, the samples did not sinter to low enough porosities. However, by applying a controlled load, close to negligible (< 0.05) porosities could be achieved and sample densification could be monitored, allowing for a repeatable synthesising process. The sintering process was refined over various temperatures and load conditions before the optimal conditions were selected of 750 °C with an increasing load of 250 $Nmin^{-1}$ to 2750 N. This allowed for the creation of the densest possible samples as at these conditions, the viscosity of the Spheriglass® was high enough to allow the mobilisation of the glass around the crystals, but low enough to ensure it did not crystallise.

Numerical models used to emulate the sintering process both without (Wadsworth et al., 2014) and with (Russell and Quane, 2005) load show that the models underestimate sintering times. The viscosity term used in both models was calculated for each crystal fraction using estimations of the maximum packing fraction (Klein et al., 2018). Outcomes show that combining numerical models that poorly estimate values can lead to run away effects resulting in the inadequate modelling of processes, such as gross underestimations of sintering times. Our current understanding of densification under load is lacking information on microstructural controls. Testing carried out on controlled synthetic samples could help rectify this.

Chapter 4 details testing carried out on the synthetic, olivine bearing suspensions created in Chapter 3. Uniaxial testing was carried out on the dense ($0.08 \leq \varphi_p$) crystalline ($0 \leq \varphi_x \leq 0.5$) samples at high temperature (610 °C, where melt viscosities are ~10^9 Pas). Testing on the analogue material to examine the effect of crystal content on magma rheology gave a unique insight into the behaviour of magmas undergoing deformation. Samples were tested at a range of strain rates ($1 \times 10 \leq \dot{\varepsilon} \leq 1 \times 10^{-1}$) which resulted in a viscous through to brittle response of the material. The onset of non-Newtonian shear thinning behaviour occurred at crystal fractions < 0.1 at strain rates < 1×10^{-6}, where the degree of the behaviour was enhanced by the addition of crystals. Analysis of results suggested that the non-Newtonian, shear-thinning viscosity of the samples could not be effectively modelled with conventional mathematical models (e.g. Mueller et al., 2010, 2011b; Mader et al., 2013; Klein et al., 2018). These models involve the mathematically derived maximum packing fraction, which is assumed constant throughout changes in strain and strain rate. The equations involved in the models underestimated the onset of non-Newtonian behaviour, overestimated the exponential increase in viscosity with crystal fraction, and underestimated the degree of shear-thinning. Instead tests found that the empirically-based viscosity model of Costa et al. (2009) provided a much more robust fit to the data as it could be adjusted for characteristic strain rates and dynamic crystal packing of the samples.

The critical crystal fraction, φ_*, found from fitting the model of Costa et al. (2009) to the data, describes the evolutionary maximum packing of the sample as strain rate is increased. The evolutionary nature of the critical crystal fraction can be explained by the plastic deformation and failure of crystals (Kendrick et al., 2017) as strain rate is increased. QEMSCAN® images from samples shows that after deformation at increasing strain rate, crystals are aligned perpendicular to the

major principal stress direction. Images also show that crystals are fractured, and sample porosity is increased, with effects more pronounced at higher crystal fraction. It was shown previously (Caricchi et al., 2007) and in this study that the degree of shear thinning increases with crystal fraction. It can therefore be concluded that the plastic failure of crystals, and resulting dilatancy, contributes to shear-thinning behaviour, while the contributions from particle rotation or potential other influences cannot be determined from this study.

Experiments also showed that the Deborah number of samples at the onset of non-Newtonian behaviour, signalled by a transitional response to stain, follows the relationship $De_{n-N} = 10^{-3}(1 - \frac{\varphi_x}{\varphi_*})$. This supersedes the previous relationship which used the apparent viscosity of the suspension in place of the interstitial glass viscosity and the maximum packing fraction of the samples in place of the critical crystal fraction (Cordonnier et al., 2012a). By using the critical crystal fraction, we can integrate the non-Newtonian, shear-thinning nature of viscoelastic materials into models of their behaviour. Combining the results found in this Chapter with those found in Chapter 2, I found that that for three-phase viscoelastic materials the Deborah number at the onset of non-Newtonian behaviour follows the relationship $De_{n-N} = -1.7 \times 10^{-4}\varphi_p + 10^{-3}(1 - \frac{\varphi_x}{\varphi_*})$. Where at, or above a porosity of 0.27, $De_{n-N} = De_{fail}$. The results of Chapter 4 further our understanding of non-Newtonian, shear-thinning behaviour could, attributing it in-part to crystal fracture and dilatancy. Moreover, the formulations allow us to predict the rheological response of a given material (with known characteristics) to deformation across a broad spectrum of material properties, $0.0 \leq \varphi_x \leq 0.5$, $0.09 \leq \varphi_p \leq 0.27$.

Chapter 5 explores the ideas suggested in Chapter 4 further. Here, the synthetic rutile-bearing samples described in Chapter 3 were deformed under uniaxial compression at temperatures of 700 °C, whilst imaging the internal sample structure using synchrotron-based, X-ray computed micro-tomography. Experiments were carried out over the range of crystallinities ($0.0 \leq \varphi_x \leq 0.5$). Through the 3D quantification of snapshots of samples during deformation it was found that dilation increases with strain and strain rate, and that these effects are increasingly pronounced at higher crystal fraction. Images also show that dilation is manifested as small tears in areas of strain localisation along the melt-crystal boundaries. As both strain and strain rate are increased tears increase in size and number. If samples were taken to higher strains, and/or strain rates, it is likely that tearing would continue until macroscopic failure ensued. Tomographic reconstructions of the experiments also display evidence of increased particle rotation and alignment with strain rate and indicate that this mechanism is enhanced with increasing crystal fraction. Observations and analysis of results gathered in Chapter 5 construct the conclusion that dilation likely has a key control on the shear-thinning rheology of magmas, and that it may incite physicochemical changes that could influence magmatic and volcanic processes during the eruptive process.

The combination of works presented in this doctoral dissertation demonstrate the value of conducting laboratory testing on both natural and synthetic materials. By isolating the variables observed in natural volcanic settings and distilling them into experiments with constrained physical properties and

controlled environments, we were able to investigate the rheology of a magma through flow to failure. This work has provided a more complete picture of the role of pores, and of crystals, in the rheological response of materials to stress and strain and has helped define a criterion for the onset of brittle behaviour which is so vital to the understanding of effusive to explosive transitions during volcanic eruptions.

6.2. Implications for magma modelling

Experiments on both natural and synthetic crystal bearing suspensions demonstrate the dynamic nature of these viscoelastic materials through strain and strain rate. Current mathematical models of magma rheology (e.g. see Mader et al., 2013 and references therein; Moitra et al., 2013; Truby et al., 2015; Klein et al., 2018), are governed by equations which are based on general assumptions, such as the rigidity of particles. In Chapter 4 these models have provided a poor fit to the data; the models fail to sufficiently capture the onset of non-Newtonian behaviour, underestimate the degree of shear-thinning and overestimate the exponential increase in viscosity with crystal fraction. We also find that when these viscosity models are combined with porosity reduction mathematical models (e.g. Russell and Quane, 2005; Wadsworth et al., 2014) the error is propagated and the results of these models unrealistic.

Due to their theoretical nature, these models fail to incorporate complementary processes such as crystal plasticity and failure (Kendrick et al., 2017), particle rotation and dilation. The models make a major assumption that the maximum packing fraction, φ_m, of a material is constant throughout strain and strain rate. However, it is clear that the evolving nature of these crystalline materials leads to a maximum packing faction that is a variable of both strain and strain rate. Therefore, it cannot be assumed to be a constant derived from the material's original state.

Empirical models on magma rheology have managed to capture this evolution through the empirically derived critical crystal fraction, φ_* (Costa, 2005; Caricchi et al., 2007; Costa et al., 2009). The variable is a function of the minimum and infinite maximum packing fractions and the applied strain rate. Adjusting the empirical based viscosity model of Costa et al. (2009) to the specific characteristics of the olivine bearing samples (Chapter 4) achieved a much more robust fit. Exchanging the maximum packing fraction for the critical packing fraction in equations for the Deborah number at the onset of non-Newtonian behaviour and at failure, allowed the generation of a failure criterion for multiphase melts.

Additionally, an empirical equation for the Deborah number for variably porous, highly crystalline samples was generated from tests on the Mt. Unzen dome material. The equation is based on the strength, flow consistency and flow index of the sample. Tests on crystal bearing synthetic samples have shown that this empirical equation can be extended to lower crystalline specimens and that the flow consistency and flow index of a sample rely on crystal content. Therefore, if the strength and crystallinity of a dome rock is known, its Deborah number can be calculated and compared to the critical Deborah numbers that mark the onset and failure of the material.

This doctoral dissertation provides strong evidence that empirical modelling, based on experiments of natural and synthetic materials, is an essential tool in modelling the response of volcanic materials to deformation. The conclusions drawn in this dissertation are likely to play a vital role in the failure forecasting of volcanic eruptions.

6.3. Implications to volcanic settings

As magmas rise through the narrowing conduit, depressurisation causes volatile exsolution (e.g. Dingwell et al., 1996) which, in turn, drives crystallisation (e.g. Cashman, 1992). The rheology of the magma therefore evolves as it rises to the surface, degassing and becoming more crystalline. Strain localisation becomes more prevalent as conduit width reduces and ascent rate increases (e.g. Costa et al., 2007a); friction at the conduit walls further intensifies strain localisation (Lavallée et al., 2015b). Vesiculation and crystallisation of magma during ascent has complex consequences for the resulting rheology of the viscoelastic material. The growth of crystals in a melt increases the apparent viscosity, while bubble nucleation can either increase or decrease the viscosity depending on the bubbles capillary number (see Mader et al., 2013 and refeences therein). Currently, little is known about the temperature and viscosity of magmas during this period of ascent. Further complexities arise due to variations in strain localisation and eruption rate and this chaotic evolution of ascending magma has profound consequences on the style of volcanic eruptions. These non-linear processes produce a range of geophysical signals (e.g. Melnik and Sparks, 1999), such as low frequency events associated with magma movement and failure, high frequency events from fault slipping, e.g. country rock failure and hybrid events that signal processes such as gas flushing (Mcnutt and Roman, 2015). There is a very close link between volcanic seismicity and volcanic activity, however the complexities related with volcanic processes make interpreting signals equivocal, meaning forecasting eruptive style still remains an enigma and one of the greatest challenges in volcanology to date (Cassidy et al., 2018).

Throughout the magma storage and transport process dilation plays a significant role. In deep magmatic settings, highly crystalline suspensions known as magma mushes dilate in response to deformation. Local pressure drops from the generation of pore space allow the infiltration of melt, known as filter-pressing, a process which promotes melt differentiation (Sisson and Bacon, 1999; Pistone et al., 2015). These pressure differentials also promote vesiculation as the decrease in pressure causes volatiles to exsolve (e.g. Zhang, 1999). Dilation of crystal mushes therefore affects magma rheology, increases buoyancy and thus drives magma to ascend (Parmigiani et al., 2016).

Moving further up in the volcanic system, strain localisation in the conduit would further induce dilation, inciting shear thinning and thus localised reductions in viscosity. Strain localisation would also cause dilation processes to dominate, leading to the coalescence of tears (e.g. Smith, 2000). Wholesale failure then occurs when the failure criteria are met under certain crystallinities and porosities.

At conduit margins, dilation is likely the dominant cause of permeable pathways in viscous magmas. These pathways act as both a degassing mechanism, and outgassing pathway, reducing volcanic

pressure and the potential of an explosive eruption (e.g. Kendrick et al., 2013b; Farquharson et al., 2015; Lamur et al., 2017).

Upon extrusion, lava may form a lava dome or lava flows which serve to construct the volcanic edifice. This lava cools and contracts (Lamur et al., 2018), forming fractures that weaken the structure. Such constructions are thus prone to collapse, particularly from continued volcanic activity, which may incite inflation or deflation of the dome, or from external forcing such as heavy rainfall, earthquakes, or collapse events (e.g. Voight and Elsworth, 2000). Testing on samples collected from Mt. Unzen lava dome indicate that the temperature, porosity and alteration, as well as the rate of deformation imposed on the material, all need to be taken into consideration when modelling the stability of extruding or cooling domes and inactive relics.

To improve our ability to predict eruptions, we need to further our understanding of volcanic processes and their related signals. By carrying out laboratory experiments in controlled environments, linking these with field observations and successfully modelling our results, we step closer to achieving this outcome. In section 6.4 I will address the future directions of the work outlined in this doctoral dissertation which aim to facilitate this goal.

6.4. Future Directions

In this doctoral dissertation I present rheological constrains on pore and crystal bearing magmas through the use of natural and synthetic materials and novel experimental techniques. Whilst the experimental data have been examined to target the specific objectives set out in this study, some potential future directions were identified during these investigations. In Chapter 5 I deformed rutile bearing synthetic glass samples uniaxially at high temperature whilst imaging the internal sample structure using synchrotron-based X-ray computed micro-tomography. With 2150 images per frame, this imaging technique gathers several tens of terabytes of data per experiment. The investigation documented in Chapter 5 covers a quantification of the dilation of a series of controlled tests, however, given the dataset collected several objectives could potentially be achieved given further analysis. For example, digital volume correlation (DVC) of X-ray tomography images (Bay et al., 1999) could be performed to track relative motions of particles in the synthetic suspensions. This could be used to highlight areas of strain localisation using Avizo^{TM} software (Fig. 6.1; Madi et al., 2013). This quantification of strain across the sample volume could then be described as a function of crystal content, strain and strain rate. This would provide insights into how strain conditions at conduit edges evolve and contribute towards eruptive processes. I also postulate that with advances in particle tracking, particle translation and rotation could be traced during strain and as a function of changing strain rate (e.g. Druckrey and Alshibli, 2014). This would allow the quantification of the role particle alignment plays in the shear thinning and strain weakening processes observed in the experiments.

The samples that remained in tact from Chapters 4 and 5 were collected after cooling and were stored. In Chapter 4, a number of these samples were placed in epoxy, sliced in half vertically and polished before being analysed using QEMSCAN®. The samples remining from testing in Chapter 5 could

also be prepared in the same way as those in Chapter 4, allowing scanning-electron microscope based microstructural-crystallographic characterisation techniques to be applied. Following Kendrick et al. (2017), deformation of crystals could be identified using electron backscatter diffraction (EBSD), and as such strain accommodated in the crystal fraction with changing applied deformation rate for the suite of different crystal fraction samples could be quantified. This would give a valuable insight into the plastic behaviour of crystals in the samples and, in combination with the DVC method detailed above could elucidate their role in shear thinning behaviour.

A final avenue for exploration to examine the combined effect of pores (Chapter 2) and crystals (Chapters 3-5) would be to produce a further suite of synthetic suspensions. In addition to the dense, crystal-bearing synthetic samples used here, controlled pore-bearing crystalline samples could also be created using the techniques outlined in Chapter 3. *Ex-situ* and *in-situ* experimentation could be implemented on these samples to carefully quantify microstructural and microtextural changes, as well as quantifications of stress and strain achieved as a result of varying strain rate. As in Wadsworth et al. (2018), acoustic emission data could be obtained from these samples during deformation. This would indicate the onset of microfracturing, adding a further categorisation technique to help identify samples as transitional. With the addition of pore-bearing and multi-phase samples to the crystal-bearing synthetic sample suite, the failure criterion based on the dimensionless Deborah number could be further refined for the co-variance of both porosity and crystallinity. This could then be tested by applying the criterion to natural samples with known microstructures during laboratory deformation tests, and eventually to examine effusive-explosive transitions of various volcanoes with magmas with constrained parameters.

The work presented throughout this doctoral dissertation has shown that experimentation in controlled laboratory environments is essential to improve our ability to predict volcanic eruptions. By isolating variables through the use of laboratory equipment and analogue materials, magmatic processes and their associated signals can be identified. The studies involved in this doctoral dissertation have shown that empirical modelling is a reliable approach and demonstrates that current numerical methods could benefit from experimental inputs. If volcanologists want to achieve the elusive goal of forecasting the time and style of volcanic eruptions, then experimentation must be involved.

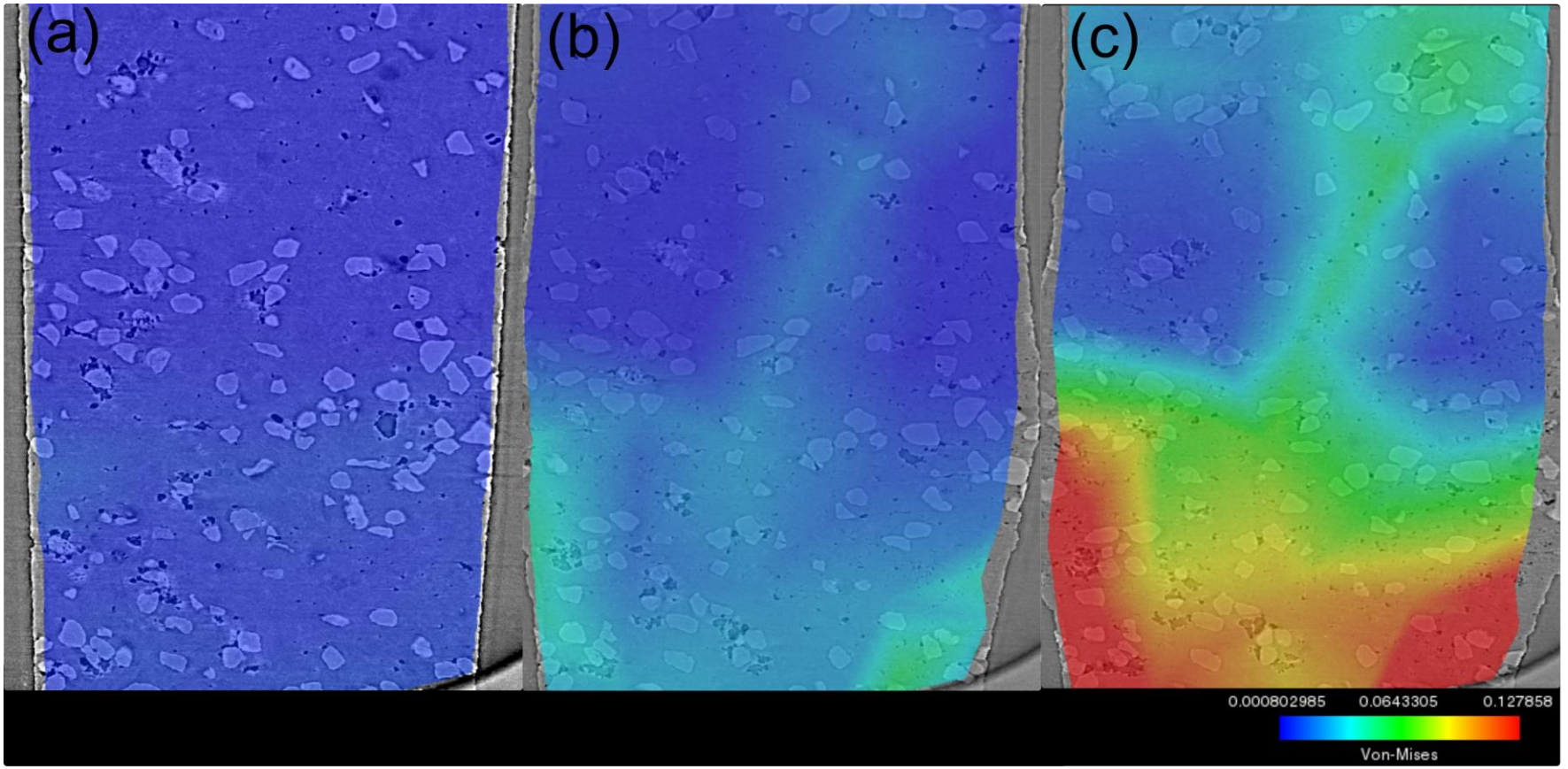

Figure 6.1. Proof-of-concept: A digital volume correlation was performed in Avizo™ software on synchrotron based computed X-ray micro-tomography data of a rutile-bearing sample with 0.1 fraction of crystals (This sample is seen in Fig. 5.S.1.). Von-mises strain was calculated at (a) 0, (b) 0 to 0.11 and (c) 0 to 0.22 strain and is displayed as a colour map washed over a 2D slice of the sample. Strain localised at the sample edges and through the (almost) centre of the sample. Areas of low strain occur at the bulge in the middle of the sample, where dilation is most prominent (see Chapter 5).

Bibliography

Al-Harthi, A. A., Al-Amri, R. M. and Shehata, W. M.: The porosity and engineering properties of vesicular basalt in Saudi Arabia, Eng. Geol., 54(3–4), 313–320, doi:10.1016/S0013-7952(99)00050-2, 1999.

Almberg, L. D., Larsen, J. F., Eichelberger, J. C., Vogel, T. a. and Patino, L. C.: Comparison of eruptive and intrusive samples from Unzen Volcano, Japan: Effects of contrasting pressure-temperature-time paths, J. Volcanol. Geotherm. Res., 175(1–2), 60–70, doi:10.1016/j.jvolgeores.2008.03.020, 2008.

Angelo Heilprin: Mont Pelée and the Tragedy of Martinique: A Study of the Great Catastrophes of 1902, with Observations and Experiences in the Field, J. B. Lippincott Company., 1903.

Arzilli, F., Cilona, A., Mancini, L. and Tondi, E.: Using synchrotron X-ray microtomography to characterize the pore network of reservoir rocks : A case study on carbonates, Adv. Water Resour., 95, 254–263, doi:10.1016/j.advwatres.2015.07.016, 2016.

Ashby, M. F. and Sammis, C. G.: The damage mechanics of brittle solids in compression, Pure Appl. Geophys., 133(3), 489–521, doi:10.1007/BF00878002, 1990.

Ashwell, P. A., Kendrick, J. E., Lavallée, Y., Kennedy, B. M., Hess, K.-U., Von Aulock, F. W., Wadsworth, F. B., Vasseur, J. and Dingwell, D. B.: Permeability of compacting porous lavas, J. Geophys. Res. - Solid Earth, (120), 1605–1622, doi:10.1002/2014JB011519.Received, 2015.

Avard, G. and Whittington, A. G.: Rheology of arc dacite lavas: experimental determination at low strain rates, Bull. Volcanol., 74(5), 1039–1056, doi:10.1007/s00445-012-0584-2, 2012.

Bagdassarov, N. S. and Dingwell, D. B.: A rheological investigation of vesicular rhyolite, J. Volcanol. Geotherm. Res., 50(3), 307–322, doi:10.1016/0377-0273(92)90099-Y, 1992.

Ball, J. L., Stauffer, P. H., Calder, E. S. and Valentine, G. A.: The hydrothermal alteration of cooling lava domes, Bull. Volcanol., 77(12), 1–16, doi:10.1007/s00445-015-0986-z, 2015.

Barmin, A., Melnik, O. and Sparks, R. S. J.: Periodic behavior in lava dome eruptions, Earth Planet. Sci. Lett., 199(1–2), 173–184, doi:10.1016/S0012-821X(02)00557-5, 2002.

Barnes, H. A., Hutton, J. F. and Walters, K.: An Introduction to Rheology, third., Elsevier, Amsterdam., 1989.

Baud, P., Wong, T.-F. and Zhu, W.: Effects of porosity and crack density on the compressive strength of rocks, Int. J. Rock Mech. Min. Sci., 67, 202–211, doi:10.1016/j.ijrmms.2013.08.031, 2014.

Bay, B. K., Smith, T. S., Fyhrie, D. P. and Saad, M.: Digital Volume Correlation : Three-dimensional Strain Mapping Using X-ray Tomography, Exp. Mech., 39(3), 217–226, doi:10.1007/BF02323555, 1999.

Bergantz, G. W., Schleicher, J., M. and Burgisser, A.: On the kinematics and dynamics of crystal-rich systems, J. Geophys. Res. Solid Earth, 122, 6131–6159, doi:10.1002/2017JB014218, 2017.

Blott, S. J. and Pye, K.: GRADISTAT: a grain size distribution and statistics package for the analysis of unconsolidated sediments, Earth Surf. Process. Landforms, 26(11), 1237–1248, doi:10.1002/esp.261, 2001.

Blundy, J. and Cashman, K. V.: Ascent-driven crystallisation of dacite magmas at Mount St Helens , 1980 ± 1986, Contrib. to Mineral. Petrol., 140(6), 631–650, doi:10.1007/s004100000219, 2001.

Blundy, J., Cashman, K. V. and Humphreys, M.: Magma heating by decompression-driven crystallization beneath andesite volcanoes, Nature, 443, 76–80, doi:10.1038/nature05100, 2006.

Brace, W. F., Paulding, B. W. and Scholz, C.: Dilatancy in the fracture of crystalline rocks, J. Geophys. Res., 71(16), 3939–3953, doi:10.1029/JZ071i016p03939, 1966.

Brantut, N., Heap, M. J., Meredith, P. G. and Baud, P.: Time-dependent cracking and brittle creep in crustal rocks: A review, J. Struct. Geol., 52(1), 17–43, doi:10.1016/j.jsg.2013.03.007, 2013.

Brown, E. and Jaeger, H. M.: Through Thick and Thin, Science (80-.)., 333(September), 1230–1232, doi:10.1126/science.1211155, 2011.

Bubeck, A., Walker, R. J., Healy, D., Dobbs, M. and Holwell, D. A.: Pore geometry as a control on rock strength, Earth Planet. Sci. Lett., 457, 38–48, doi:10.1016/j.epsl.2016.09.050, 2017.

Cai, B., Karagadde, S., Yuan, L., Marrow, T. J., Connolley, T. and Lee, P. D.: In situ synchrotron tomographic quantification of granular and intragranular deformation during semi-solid compression of an equiaxed dendritic Al–Cu alloy, Acta Mater., 76, 371–380, doi:10.1016/j.actamat.2014.05.035, 2014.

Calder, E. S., Luckett, R., Sparks, R. S. J. and Voight, B.: Mechanisms of lava dome instability and generation of rockfalls and pyroclastic flows at Soufrière Hills Volcano, Montserrat, in Geological Society, London, Memoirs, vol. 21, pp. 173–190., 2002.

Calder, E. S., Lavallée, Y., Kendrick, J. E. and Bernstein, M.: Lava Dome Eruptions, in The Encyclopedia of Volcanoes, edited by H. Sigurdsson, B. Houghton, H. Rymer, J. Stix, and S. McNutt, pp. 343–362, Elsevier., 2015.

Caricchi, L., Burlini, L., Ulmer, P., Gerya, T., Vassalli, M. and Papale, P.: Non-Newtonian rheology of crystal-bearing magmas and implications for magma ascent dynamics, Earth Planet. Sci. Lett., 264(3–4), 402–419, doi:10.1016/j.epsl.2007.09.032, 2007.

Carpio, P., Salvador, M. D., Borrell, A., Navarro, L. and Sánchez, E.: Molten salt attack on multilayer and functionally-graded YSZ coatings, Ceram. Int., 44(11), 12634–12641, doi:10.1016/j.ceramint.2018.04.062, 2018.

Cashman, K. V.: Groundmass crystallization of Mount St. Helens dacite, 1980-1986: a tool for interpreting shallow magmatic processes, Contrib. to Mineral. Petrol., 109(4), 431–449, doi:10.1007/BF00306547, 1992.

Cashman, K. V. and Blundy, J.: Degassing and crystallization of ascending andesite and dacite, Phil Trans. Roy. Soc. Lond., 358(1770), 1487–1513, doi:https://doi.org/10.1098/rsta.2000.0600, 2000.

Cashman, K. V. and Sparks, R. S. J.: How volcanoes work: A 25 year perspective, Bull. Geol. Soc. Am., 125(5–6), 664–690, doi:10.1130/B30720.1, 2013.

Cashman, K. V., Thornber, C. and Pallister, J. S.: From Dome to Dust : Shallow Crystallization and Fragmentation of Conduit Magma During the 2004 – 2006 Dome Extrusion of Mount St . Helens , Washington,

in Analysis, edited by D. R. Sherrod, W. E. Scott, and P. H. Stauffer, pp. 387–413. [online] Available from: http://cat.inist.fr/?aModele=afficheN&cpsidt=22527815, 2008.

Cassidy, M., Manga, M., Cashman, K. V. and Bachmann, O.: Controls on explosive-effusive volcanic eruption styles, Nat. Commun., 1(9), 2839, doi:10.1038/s41467-018-05293-3, 2018.

Castro, J. M. and Dingwell, D. B.: Rapid ascent of rhyolitic magma at Chaitén volcano, Chile, Nature, 461(7265), 780–783, doi:10.1038/nature08458, 2009.

Castro, J. M., Manga, M. and Martin, M. C.: Vesiculation rates of obsidian domes inferred from H2O concentration profiles, Geophys. Res. Lett., 32(21), 1–5, doi:10.1029/2005GL024029, 2005.

Cheng, X., Mccoy, J. H., Israelachvili, J. N. and Cohen, I.: Imaging the Microscopic Structure of Shear Thinning and Thickening Colloidal Suspensions, Science (80-.)., 333(September), 1276–1280, doi:10.1126/science.1207032, 2011.

Coats, R., Kendrick, J. E., Wallace, P. A., Miwa, T., Hornby, A. J., Ashworth, J. D., Matsushima, T. and Lavallée, Y.: Failure criteria for porous dome rocks and lavas: a study of Mt. Unzen, Japan, Solid Earth, 9, 1299–1328, 2018.

Cole, P. D., Calder, E. S., Druitt, T. H., Hoblitt, R., Robertson, R., Sparks, R. S. J. and Young, S. R.: Pyroclastic flows generated by gravitational instability of the 1996-97 lava dome of Soufriere Hills Volcano, Montserrat, Geophys. Res. Lett., 25(18), 3425–3428, 1998.

Colombier, M., Wadsworth, F. B., Gurioli, L., Scheu, B., Kueppers, U., Di Muro, A. and Dingwell, D. B.: The evolution of pore connectivity in volcanic rocks, Earth Planet. Sci. Lett., 462, 99–109, doi:10.1016/j.epsl.2017.01.011, 2017.

Cordonnier, B., Hess, K.-U., Lavallée, Y. and Dingwell, D. B.: Rheological properties of dome lavas: Case study of Unzen volcano, Earth Planet. Sci. Lett., 279(3–4), 263–272, doi:10.1016/j.epsl.2009.01.014, 2009.

Cordonnier, B., Caricchi, L., Pistone, M., Castro, J. M., Hess, K.-U., Gottschaller, S., Manga, M., Dingwell, D. B. and Burlini, L.: The viscous-brittle transition of crystal-bearing silicic melt: Direct observation of magma rupture and healing, Geology, 40(7), 611–614, doi:10.1130/G3914.1, 2012a.

Cordonnier, B., Schmalholz, S. M., Hess, K.-U. and Dingwell, D. B.: Viscous heating in silicate melts: An experimental and numerical comparison, J. Geophys. Res. Solid Earth, 117(2), 1–13, doi:10.1029/2010JB007982, 2012b.

Costa, A.: Viscosity of high crystal content melts: Dependence on solid fraction, Geophys. Res. Lett., 32(22), 1–5, doi:10.1029/2005GL024303, 2005.

Costa, A., Melnik, O., Sparks, R. S. J. and Voight, B.: Control of magma flow in dykes on cyclic lava dome extrusion, Geophys. Res. Lett., 34(November), 1–5, doi:10.1029/2006GL027466, 2007a.

Costa, A., Melnik, O. and Sparks, R. S. J.: Controls of conduit geometry and wallrock elasticity on lava dome eruptions, Earth Planet. Sci. Lett., 260, 137–151, doi:10.1016/j.epsl.2007.05.024, 2007b.

Costa, A., Caricchi, L. and Bagdassarov, N.: A model for the rheology of particle-bearing suspensions and

partially molten rocks, Geochemistry, Geophys. Geosystems, 10(3), 1–13, doi:10.1029/2008GC002138, 2009.

Dence, M.: Impact Melts, J. Geophys. Res., 76(23), 5552–5565, doi:10.1029/JB076i023p05552, 1971.

Deubelbeiss, Y., Kaus, B. J. P., Connolly, J. and Caricchi, L.: Potential causes for the non-Newtonian rheology of crystal-bearing magmas, Geochemistry, Geophys. Geosystems, 12(5), 1–22, doi:10.1029/2010GC003485, 2011.

Dickie, A. M. and Kokini, J. L.: An Improved Model for Food Thickness from non-Newtonian Mechanics in the Mouth, J. Food Sci., 48(1), 57–61, doi:https://doi.org/10.1111/j.1365-2621.1983.tb14787.x, 1983.

Dingwell, D. B.: Viscosity and Anelasticity of Melts, in Mineral Physics and Crystallography A Handbook of Physical Constants, edited by T. J. Ahrens, pp. 209–217, American Geophysical Union., 1995.

Dingwell, D. B.: Volcanic Dilemma: Flow or Blow?, Science (80-.)., 273, 1054–1055, doi:10.1126/science.273.5278.1054, 1996.

Dingwell, D. B.: Transport properties of magmas: diffuison and rheology, Elements, 2, 282–286, doi:10.2113/gselements.2.5.281, 2006.

Dingwell, D. B. and Webb, S. L.: Structural relaxation in silicate melts and non-Newtonian melt rheology in geologic processes, Phys. Chem. Miner., 16(5), 508–516, doi:10.1007/BF00197020, 1989.

Dingwell, D. B. and Webb, S. L.: Relaxation in silicate melts, Eur. J. Mineral., 2(4), 427–449, doi:10.1127/ejm/2/4/0427, 1990.

Dingwell, D. B., Romano, C. and Hess, K.-U.: The effect of water on the viscosity of a haplogranitic melt under P-T-X conditions relevant to silicic volcanism, Contrib. to Mineral. Petrol., 124(1), 19–28, doi:https://doi.org/10.1007/s004100050170, 1996.

Drakopoulos, M., Connolley, T., Reinhard, C., Atwood, R. C., Magdysyuk, O., Vo, N., Hart, M., Connor, L., Humphreys, B., Howell, G., Davies, S., Hill, T., Wilkin, G., Pedersen, U., Foster, A., Maio, N. De, Basham, M., Yuan, F. and Wanelik, K.: I12 : the Joint Engineering , Environment and Processing (JEEP) beamline at Diamond Light Source beamlines, J. Synchrotron Radiat., 22, 828–838, doi:10.1107/S1600577515003513, 2015.

Druckrey, A. M. and Alshibli, K. A.: 3D Behavior of Sand Particles Using X-ray Synchrotron Micro-Tomography, in Geo-Congress 2014 Technical Papers, pp. 2814–2822, Atlanta, Georgia., 2014.

Edmonds, M.: New geochemical insights into volcanic degassing, Philos. Trans. R. Soc. A Math. Phys. Eng. Sci., 366(1885), 4559–4579, doi:10.1098/rsta.2008.0185, 2008.

Eggertsson, G. H., Lavallée, Y., Kendrick, J. E. and Markússon, S.: Improving fluid flow in geothermal reservoirs by thermal and mechanical stimulation: The case of Krafla volcano, Iceland, J. Volcanol. Geotherm. Res., doi:https://doi.org/10.1016/j.jvolgeores.2018.04.008, 2018.

Eichhubl, P.: Growth of ductile opening-mode fractures in geomaterials, in The Initiation, Propagation, and Arrest of Joints and Other Fractures, edited by J. W. Cosgrove and T. Engelder, pp. 11–24, The Geological Society, London., 2004.

Einstein, A.: A new determination of the molecular dimensions, Ann. Phys., 34, 591-592 (Translation of the 1906 German version, 1911.

Elsworth, D. and Voight, B.: Evaluation of volcano flank instability triggered by dyke intrusion, Geol. Soc. London, Spec. Publ., 110, 45–53, doi:10.1144/GSL.SP.1996.110.01.03, 1996.

Farquharson, J. I., Heap, M. J., Varley, N. R., Baud, P. and Reuschlé, T.: Permeability and porosity relationships of edifice-forming andesites: A combined field and laboratory study, J. Volcanol. Geotherm. Res., 297, 52–68, doi:10.1016/j.jvolgeores.2015.03.016, 2015.

Farquharson, J. I., Heap, M. J., Baud, P., Reuschlé, T. and Varley, N. R.: Pore pressure embrittlement in a volcanic edifice, Bull. Volcanol., 78(1), 6, doi:10.1007/s00445-015-0997-9, 2016.

Fink, J. H. and Anderson, S. W.: Lava domes and coulees, in The Encyclopedia of Volcanoes, edited by H. Sigurdsson, B. Houghton, H. Rymer, J. Stix, and S. McNutt, pp. 307–318, Academic Press., 2000.

Fink, J. H. and Griffiths, R. W.: Morphology , Eruption Rates , and Rheology of Lava Domes : Insights from Laboratory Models, J. Geophys. Res., 103(January), 527–545, 1998.

Fluegel, A.: Glass viscosity calculation based on a global statistical modelling approach, Glas. Technol. J. Glas. …, 48(1), 13–30 [online] Available from: http://www.ingentaconnect.com/content/sgt/gt/2007/00000048/00000001/art00003, 2007.

Frenkel, J.: Viscous flow ofcrystalline bodies under the action of surface tension, J. Phys., 9(385), 385–391, 1945.

Gardner, J., Wadsworth, F. B., Llewellin, E. W., Watkins, J. M. and Coumans, J. P.: Experimental sintering of ash at conduit conditions and implications for the longevity of tuffisites, Bull. Volcanol., 1–14, 2018.

Gaunt, E. H., Sammonds, P. R., Meredith, P. G., Smith, R. and Pallister, J. S.: Pathways for degassing during the lava dome eruption of Mount St. Helens 2004-2008, Geology, 42(11), 947–950, doi:10.1130/G35940.1, 2014.

Gent, A. N.: Theory of the parallel plate viscometer, Br. J. Appl. Phys., 11(February), 85–87, doi:10.1088/0508-3443/11/2/310, 1960.

Ghiorso, M. S. and Sack, R.: Chemical mass transfer in magmatic processes IV. A revised and internally consistent thermodynamic model for the interpolation and extrapolation of liquid-solid equilibria in magmatic systems at elevated temperatures and pressures, Contrib. to Mineral. Petrol., 119(November 2015), 197–212, doi:10.1007/BF00307281, 1995.

Giordano, D. and Dingwell, D. B.: The kinetic fragility of natural silicate melts The kinetic fragility of natural silicate melts, J. Phys. Condens. Matter, 15(11), S945–S954, doi:https://doi.org/10.1088/0953-8984/15/11/318, 2003.

Giordano, D., Romano, C. R., Dingwell, D. B., Poe, B. P. and Behrens, H. B.: The combined effects of water and fluorine on the viscosity of silicic magmas, Geochim. Cosmochim. Acta, 68(24), 5159–5168, doi:10.1016/j.gca.2004.08.012, 2004a.

Giordano, D., Romano, C., Papale, P. and Dingwell, D. B.: The viscosity of trachytes , and comparison with basalts , phonolites , and rhyolites, Chem. Geol., 213, 49–61, doi:10.1016/j.chemgeo.2004.08.032, 2004b.

Giordano, D., Russell, J. K. and Dingwell, D. B.: Viscosity of magmatic liquids: A model, Earth Planet. Sci. Lett., 271(1–4), 123–134, doi:10.1016/j.epsl.2008.03.038, 2008.

Gonnermann, H. M.: Magma Fragmentation, Annu. Rev. Earth Planet. Sci. Vol 43, 43, doi:10.1146/annurev-earth-060614-105206, 2015.

Gonnermann, H. M. and Manga, M.: The Fluid Mechanics Inside a Volcano, Annu. Rev. Fluid Mech., (39), 321–356, doi:10.1146/annurev.fluid.39.050905.110207, 2007.

Goto, A.: A new model for volcanic earthquake at Unzen Volcano: Melt rupture model, Geophys. Res. Lett., 26(16), 2541–2544, 1999.

Gottsmann, J., Lavallée, Y., Martí, J. and Aguirre-Díaz, G.: Magma-tectonic interaction and the eruption of silicic batholiths, Earth Planet. Sci. Lett., 284(3–4), 426–434, doi:10.1016/j.epsl.2009.05.008, 2009.

Griffiths, L., Heap, M. J., Xu, T., Chen, C. and Baud, P.: The influence of pore geometry and orientation on the strength and stiffness of porous rock, J. Struct. Geol., 96(February), 149–160, doi:10.1016/j.jsg.2017.02.006, 2017.

Hale, A.: Thermosets, in Handbook of Thermal Analysis and Calorimetry, vol. 3: Applica, edited by S. Z. D. Cheng, pp. 295–354., 2002.

Hale, A. J. and Wadge, G.: The transition from endogenous to exogenous growth of lava domes with the development of shear bands, J. Volcanol. Geotherm. Res., 171, 237–257, doi:10.1016/j.jvolgeores.2007.12.016, 2008.

Harris, A. J. L., Flynn, L. P., Matías, O. and Rose, W. I.: The thermal stealth flows of Santiaguito dome , Guatemala : Implications for the cooling and emplacement of dacitic block-lava flows, GSA Bull., (5), 533–546, 2002.

Hawkes, I. and Mellor, M.: Uniaxial testing in rock mechanics laboratories, Eng. Geol., 4(3), 179–285, doi:https://doi.org/10.1016/0013-7952(70)90034-7, 1970.

Heap, M. J. and Faulkner, D. R.: Quantifying the evolution of static elastic properties as crystalline rock approaches failure, Int. J. Rock Mech. Min. Sci., 45(4), 564–573, doi:10.1016/j.ijrmms.2007.07.018, 2008.

Heap, M. J., Vinciguerra, S. and Meredith, P. G.: The evolution of elastic moduli with increasing crack damage during cyclic stressing of a basalt from Mt. Etna volcano, Tectonophysics, 471(1–2), 153–160, doi:10.1016/j.tecto.2008.10.004, 2009.

Heap, M. J., Faulkner, D. R., Meredith, P. G. and Vinciguerra, S.: Elastic moduli evolution and accompanying stress changes with increasing crack damage: Implications for stress changes around fault zones and volcanoes during deformation, Geophys. J. Int., 183(1), 225–236, doi:10.1111/j.1365-246X.2010.04726.x, 2010.

Heap, M. J., Lavallée, Y., Laumann, A., Hess, K.-U., Meredith, P. G. and Dingwell, D. B.: How tough is tuff in the event of fire?, Geology, 40(4), 311–314, doi:10.1130/G32940.1, 2012.

Heap, M. J., Lavallée, Y., Laumann, A., Hess, K.-U., Meredith, P. G., Dingwell, D. B., Huismann, S. and Weise, F.: The influence of thermal-stressing (up to 1000 °C) on the physical , mechanical , and chemical properties of siliceous-aggregate , high-strength concrete, Constr. Build. Mater., 42, 248–265, doi:10.1016/j.conbuildmat.2013.01.020, 2013a.

Heap, M. J., Mollo, S., Vinciguerra, S., Lavallée, Y., Hess, K.-U., Dingwell, D. B., Baud, P. and Iezzi, G.: Thermal weakening of the carbonate basement under Mt . Etna volcano (Italy): Implications for volcano instability, J. Volcanol. Geotherm. Res., 250, 42–60, doi:10.1016/j.jvolgeores.2012.10.004, 2013b.

Heap, M. J., Kolzenburg, S., Russell, J. K., Campbell, M. E., Welles, J., Farquharson, J. I. and Ryan, A.: Conditions and timescales for welding block-and-ash flow deposits, J. Volcanol. Geotherm. Res., 289, 202–209, doi:10.1016/j.jvolgeores.2014.11.010, 2014a.

Heap, M. J., Lavallée, Y., Petrakova, L., Baud, P., Reuschlé, T., Varley, N. R. and Dingwell, D. B.: Microstructural controls on the physical and mechanical properties of edifice-forming andesites at Volcán de Colima, Mexico, J. Geophys. Res. Solid Earth, 119(4), 2925–2963, doi:10.1002/2013JB010521, 2014b.

Heap, M. J., Xu, T. and Chen, C.: The influence of porosity and vesicle size on the brittle strength of volcanic rocks and magma, Bull. Volcanol., 76(9), 856, doi:10.1007/s00445-014-0856-0, 2014c.

Heap, M. J., Farquharson, J. I., Baud, P., Lavallée, Y. and Reuschlé, T.: Fracture and compaction of andesite in a volcanic edifice, Bull. Volcanol., 77(6), 55, doi:10.1007/s00445-015-0938-7, 2015a.

Heap, M. J., Farquharson, J. I. and Kolzenburg, S.: Timescales for permeability reduction and strength recovery in densifying magma, Earth Planet. Sci. Lett., 429, 223–233, doi:http://dx.doi.org/10.1016/j.epsl.2015.07.053, 2015b.

Heap, M. J., Russell, J. K. and Kennedy, L. A.: Mechanical behaviour of dacite from Mount St . Helens (USA): A link between porosity and lava dome extrusion mechanism (dome or spine)?, J. Volcanol. Geotherm. Res., 328, 159–177, doi:10.1016/j.jvolgeores.2016.10.015, 2016a.

Heap, M. J., Wadsworth, F. B., Xu, T., Chen, C. and Tang, C.: The strength of heterogeneous volcanic rocks: A 2D approximation, J. Volcanol. Geotherm. Res., 319(April), 1–11, doi:10.1016/j.jvolgeores.2016.03.013, 2016b.

Herschel, W. H. and Bulkley, R.: Konsistenzmessungen von Gummi-Benzollösungen, KolloidZeitschrift, 39, 291–230, doi:http://dx.doi.org/10.1007/BF01432034, 1926.

Hess, K.-U. and Dingwell, D. B.: Viscosities of hydrous leucogranitic melts: A non-Arrhenian model, Am. Mineral., 81(9–10), 1297–1300, doi:10.2138/am-1996-9-1031, 1996.

Hess, K.-U., Cordonnier, B., Lavallée, Y. and Dingwell, D. B.: High-load, high-temperature deformation apparatus for synthetic and natural silicate melts, Rev. Sci. Instrum., 78(7), doi:10.1063/1.2751398, 2007.

Hess, K.-U., Cordonnier, B., Lavallée, Y. and Dingwell, D. B.: Viscous heating in rhyolite: An in situ experimental determination, Earth Planet. Sci. Lett., 275(1–2), 121–126, doi:10.1016/j.epsl.2008.08.014, 2008.

Heymann, L., Peukert, S. and Aksel, N.: On the solid-liquid transition of concentrated suspensions in transient shear flow, Rheol. Acta, 41(4), 307–315, doi:10.1007/s00397-002-0227-1, 2002.

Hoek, E. and Bieniawski, Z. T.: Brittle Rock Fracture Propagation In Rock Under Compression Brittle Rock Fracture Propagation in Rock Under Compression, Int. J. Fract. Mech., 1(3), 137–155, doi:10.1007/BF00186851, 1965.

Hornby, A. J., Kendrick, J. E., Lamb, O. D., Hirose, T., De Angelis, S. H., Von Aulock, F. W., Umakoshi, K., Miwa, T., Henton De Angelis, S., Wadsworth, F. B., Hess, K.-U., Dingwell, D. B. and Lavallée, Y.: Spine growth and seismogenic faulting at Mt. Unzen, Japan, J. Geophys. Res. Solid Earth, 120, doi:10.1002/2014JB011660, 2015.

Hudson, I. of M.: Fayalite-Forsterite Series, Mindat.org [online] Available from: https://www.mindat.org/min-8658.html (Accessed 11 December 2018), 2018.

Hudson Institute of Minerology: Albite-Anorthite Series, Mindat.org [online] Available from: https://www.mindat.org/min-3231.html (Accessed 11 December 2018), 2018.

Iverson, R. M., Dzurisin, D., Gardner, C. A., Gerlach, T. M., Lahusen, R. G., Lisowski, M., Major, J. J., Malone, S. D., Messerich, J. A., Moran, S. C., Pallister, J. S., Qamar, A. I., Schilling, S. P. and Vallance, J. W.: Dynamics of seismogenic volcanic extrusion at Mount St Helens in 2004 – 05, Nature, 444(1), 439–443, doi:10.1038/nature05322, 2006.

Jahangiri, P., Streblow, R. and Müller, D.: Simulation of Non-Newtonian Fluids using Modelica, Proc. 9th Int. Model. Conf., 57–62, doi:10.3384/ecp1207657, 2012.

Karagadde, S., Lee, P. D., Cai, B., Fife, J. L., Azeem, M. A., Kareh, K. M., Puncreobutr, C., Tsivoulas, D., Connolley, T. and Atwood, R. C.: Transgranular liquation cracking of grains in the semi-solid state, Nat. Commun., 6, 8300, doi:10.1038/ncomms9300, 2015.

Kavanagh, J. L., Engwell, S. L. and Martin, S. A.: A review of laboratory and numerical modelling in volcanology, Solid Earth, 9, 531–571, doi:10.5194/se-9-531-2018, 2018.

Kendrick, J. E., Lavallée, Y., Ferk, A., Perugini, D., Leonhardt, R. and Dingwell, D. B.: Extreme frictional processes in the volcanic conduit of Mount St . Helens (USA) during the 2004-2008 eruption, J. Struct. Geol., 38, 61–76, doi:10.1016/j.jsg.2011.10.003, 2012.

Kendrick, J. E., Smith, R., Sammonds, P., Meredith, P. G., Dainty, M. and Pallister, J. S.: The influence of thermal and cyclic stressing on the strength of rocks from Mount St. Helens, Washington, Bull. Volcanol., 75(7), 1–12, doi:10.1007/s00445-013-0728-z, 2013a.

Kendrick, J. E., Lavallée, Y., Hess, K.-U., Heap, M. J., Gaunt, E. H., Meredith, P. G. and Dingwell, D. B.: Tracking the permeable porous network during strain-dependent magmatic flow, J. Volcanol. Geotherm. Res., 260, 117–126, doi:10.1016/j.jvolgeores.2013.05.012, 2013b.

Kendrick, J. E., Lavallée, Y., Mariani, E., Dingwell, D. B., Wheeler, J. and Varley, N. R.: Crystal plasticity as an indicator of the viscous-brittle transition in magmas, Nat. Commun., 8(1), 1926, doi:10.1038/s41467-017-01931-4, 2017.

Kerr, R. C. and Lister, J. R.: The Effects of Shape on Crystal Settling and on the Rheology of Magmas, J. Geol., 99(3), 457–467, doi:http://www.jstor.org/stable/30062628, 1991.

Klein, J., Mueller, S. P., Helo, C., Schweitzer, S., Gurioli, L. and Castro, J. M.: An expanded model and application of the combined effect of crystal-size distribution and crystal shape on the relative viscosity of magmas, J. Volcanol. Geotherm. Res., 357, 128–133, doi:10.1016/j.jvolgeores.2018.04.018, 2018.

Kohashi, S., Shimokawa, S., Shimizu, K., Satohira, Y., Yamada, T. and Kimura, T.: Document for the committee of survey and countermeasure on lava dome collapse in Unzen Volcano (in Japanese)., 2012.

Kolzenburg, S. and Russell, J. K.: Welding of pyroclastic conduit infill: A mechanism for cyclical explosive eruptions, J. Geophys. Res. Solid Earth, 119(November 2015), 5305–5323, doi:10.1002/2013JB010931.Received, 2014.

Kolzenburg, S., Heap, M. J., Lavallée, Y., Russell, J. K., Meredith, P. G. and Dingwell, D. B.: Strength and permeability recovery of tuffisite-bearing andesite, Solid Earth, 3(1), 191–198, doi:10.5194/se-3-191-2012, 2012.

Krieger, I. M. and Dougherty, T. J.: A Mechanism for Non-Newtonian Flow in Suspensions of Rigid Spheres, Trans. Soc. Rheol., 3(1), 137–152, doi:10.1122/1.548848, 1959.

Kueppers, U., Scheu, B., Spieler, O. and Dingwell, D. B.: Field-based density measurements as tool to identify preeruption dome structure: set-up and first results from Unzen volcano, Japan, J. Volcanol. Geotherm. Res., 141(1–2), 65–75, doi:10.1016/j.jvolgeores.2004.09.005, 2005.

Kushnir, A. R. L., Martel, C., Bourdier, J.-L., Heap, M. J., Reuschlé, T., Erdmann, S., Komorowski, J.-C. and Cholik, N.: Probing permeability and microstructure: Unravelling the role of a low-permeability dome on the explosivity of Merapi (Indonesia), J. Volcanol. Geotherm. Res., 316, 56–71, doi:10.1016/j.jvolgeores.2016.02.012, 2016.

Kushnir, A. R. L., Martel, C., Champallier, R. and Arbaret, L.: In situ confirmation of permeability development in shearing bubble-bearing melts and implications for volcanic outgassing, Earth Planet. Sci. Lett., 458, 315–326, doi:10.1016/j.epsl.2016.10.053, 2017.

Kutílek, M.: Non-darcian flow of water in soils - laminar region. A review, Dev. Soil Sci., 2, 327–340, doi:10.1016/S0166-2481(08)70550-6, 1972.

Lamb, O. D., De Angelis, S. H., Umakoshi, K., Hornby, A. J., Kendrick, J. E. and Lavallée, Y.: Repetitive fracturing during spine extrusion at Unzen volcano, Japan, Solid Earth, 6(4), 1277–1293, doi:10.5194/se-6-1277-2015, 2015.

Lamb, O. D., De Angelis, S. H., Wall, R. J., Lamur, A., Varley, N. R., Reyes-Dávila, G., Arámbula-Mendoza, R., Hornby, A. J., Kendrick, J. E. and Lavallée, Y.: Seismic and experimental insights into eruption precursors at Volcán de Colima, Geophys. Res. Lett., 44(12), 6092–6100, doi:10.1002/2017GL073350, 2017.

Lamur, A.: Development , impact and longevity of fractures in magmatic , volcanic and geothermal systems, The Uniersity of Liverool. [online] Available from: https://livrepository.liverpool.ac.uk/3019206/, 2018.

Lamur, A., Kendrick, J. E., Eggertsson, G. H., Wall, R. J., Ashworth, J. D. and Lavallée, Y.: The permeability of fractured rocks in pressurised volcanic and geothermal systems, Sci. Rep., (May), 1–9, doi:10.1038/s41598-017-05460-4, 2017.

Lamur, A., Lavallée, Y., Iddon, F. E., Hornby, A. J., Kendrick, J. E., Von Aulock, F. W. and Wadsworth, F. B.: Disclosing the temperature of columnar jointing in lavas, Nat. Commun., 9(1), doi:10.1038/s41467-018-03842-4, 2018.

Lamur, A., Kendrick, J. E., Wadsworth, F. B. and Lavallée, Y.: Fracture healing and strength recovery in magmatic liquids, Geology, 47(2), 1–4, doi:10.1130/G45512.1/4617342/g45512.pdf, 2019.

Laumonier, M., Arbaret, L., Burgisser, A. and Champallier, R.: Porosity redistribution enhanced by strain localization in crystal-rich magmas, Geology, 39(8), 715–718, doi:10.1130/G31803.1, 2011.

Lavallée, Y., Hess, K.-U., Cordonnier, B. and Dingwell, D. B.: Non-Newtonian rheological law for highly crystalline dome lavas, Geology, 35(9), 843–846, doi:10.1130/G23594A.1, 2007.

Lavallée, Y., Meredith, P. G., Dingwell, D. B., Hess, K.-U., Wassermann, J., Cordonnier, B., Gerik, A. and Kruhl, J. H.: Seismogenic lavas and explosive eruption forecasting., Nature, 453(7194), 507–510, doi:10.1038/nature06980, 2008.

Lavallée, Y., Varley, N. R., Alatorre-Ibargüengoitia, M. a., Hess, K.-U., Kueppers, U., Mueller, S. P., Richard, D., Scheu, B., Spieler, O. and Dingwell, D. B.: Magmatic architecture of dome-building eruptions at Volcán de Colima, Mexico, Bull. Volcanol., 74(1), 249–260, doi:10.1007/s00445-011-0518-4, 2012.

Lavallée, Y., Benson, P. M., Heap, M. J., Hess, K.-U., Flaws, A., Schillinger, B., Meredith, P. G. and Dingwell, D. B.: Reconstructing magma failure and the degassing network of domebuilding eruptions, Geology, 41(4), 515–518, doi:10.1130/G33948.1, 2013.

Lavallée, Y., Hirose, T., Kendrick, J. E., Hess, K.-U. and Dingwell, D. B.: Fault rheology beyond frictional melting, Proc. Natl. Acad. Sci., 201413608, doi:10.1073/pnas.1413608112, 2015a.

Lavallée, Y., Dingwell, D. B., Johnson, J. B., Cimarelli, C., Hornby, A. J., Kendrick, J. E., Von Aulock, F. W., Kennedy, B. M., Andrews, B. J., Wadsworth, F. B., Rhodes, E. and Chigna, G.: Thermal vesiculation during volcanic eruptions, Nature, 528(7583), 544–547, doi:10.1038/nature16153, 2015b.

Lavallée, Y., Heap, M. J., Kueppers, U., Kendrick, J. E. and Dingwell, D. B.: The fragility of Volcán de Colima – a material constraint, in Volcán de Colima – Managing the Threat, edited by N. R. Varley and J. C. Komorowski, Springer., 2018.

Lejeune, A. M. and Richet, P.: Rheology of crystal-bearing silicate melts : An experimental study at high viscosities, J. Geophys. Res., 100(B3), 4215–4229, 1995.

Lejeune, A. M., Bottinga, Y., Trull, T. W. and Richet, P.: Rheology of bubble-bearing magmas, Earth Planet. Sci. Lett., 166(1–2), 71–84, doi:http://dx.doi.org/10.1016/S0012-821X(98)00278-7, 1999.

Lin, Q., Neethling, S. J., Dobson, K. J., Courtois, L. and Lee, P. D.: Quantifying and minimising systematic and random errors in X-ray micro-tomography based volume measurements, Comput. Geosci., 77, 1–7, doi:10.1016/j.cageo.2014.12.008, 2015.

Liu, Z., Pandelaers, L. and Blanpain, B.: Viscosity of Heterogeneous Silicate Melts : A Review, Metall. Mater. Trans. B, 49(5), 2469–2486, doi:10.1007/s11663-018-1374-9, 2018.

Llewellin, E. W. and Manga, M.: Bubble suspension rheology and implications for conduit flow, J. Volcanol. Geotherm. Res., 143(1–3), 205–217, doi:10.1016/j.jvolgeores.2004.09.018, 2005.

Lopez, D. L. and Williams, S. N.: Catastrophic Volcanic Collapse: Relation to Hydrothermal Processes, Science (80-.)., 260(5115), 1794–1796, doi:10.1126/science.260.5115.1794, 1993.

Macdonald, G. A.: Pahohoe, aa, and block lava, Am. J. Sci., 251(3), 169–191, doi:10.2475/ajs.251.3.169, 1953.

Mackenzie, J. and Shuttleworth, R.: A phenomenological theory of sintering, Proceeding R. Soc. B, 62(12), 833–852, doi:doi:10.1088/0370-1301/62/12/310, 1949.

Mader, H. M., Llewellin, E. W. and Mueller, S. P.: The rheology of two-phase magmas: A review and analysis, J. Volcanol. Geotherm. Res., 257, 135–158, doi:10.1016/j.jvolgeores.2013.02.014, 2013.

Madi, K., Tozzi, G., Zhang, Q. H., Tong, J., Cossey, A., Au, A., Hollis, D. and Hild, F.: Medical Engineering & Physics Computation of full-field displacements in a scaffold implant using digital volume correlation and finite element analysis, Med. Eng. Phys., 35, 1298–1312, doi:10.1016/j.medengphy.2013.02.001, 2013.

Madonna, C., Quintal, B., Frehner, M., Almqvist, B. S. G., Tisato, N., Pistone, M., Marone, F. and Saenger, E. H.: Synchrotron-based X-ray tomographic microscopy for rock physics investigations, Geophysics, 78(1), D53–D64, doi:10.1190/GEO2012-0113.1, 2013.

Mandal, P. K., Chakravarty, S., Mandal, A. and Amin, N.: Effect of body acceleration on unsteady pulsatile flow of non-newtonian fluid through a stenosed artery, Appl. Math. Comput., 189, 766–779, doi:10.1016/j.amc.2006.11.139, 2007.

Manga, M., Castro, J. M., Cashman, K. V. and Lowewenberg, M.: Rheology of bubble-bearing magmas, J. Volcanol. Geotherm. Res., 87, 15–28, 1998.

Maron, S. H. and Pierce, P. E.: Application of ree-eyring generalized flow theory to suspensions of spherical particles, J. Colloid Sci., 11, 80–95, doi:10.1016/0095-8522(56)90023-X, 1956.

Marsh, B. D.: Magma chambers, in The Encyclopedia of Volcanoes, edited by H. Sigurdsson, B. Houghton, H. Rymer, J. Stix, and S. McNutt, pp. 343–362, Academic Press., 2015.

Marsh, B. D. and Maxey, M. R.: On the distribution and separation of crystals in convecting magma, J. Volcanol. Geotherm. Res., 24(1–2), 95–150, doi:10.1016/0377-0273(85)90030-7, 1985.

Martel, C. and Schmidt, B. C.: Decompression experiments as an insight into ascent rates of silicic magmas, Contrib. to Mineral. Petrol., 397–415, doi:10.1007/s00410-002-0404-3, 2003.

Marzougui, D., Chareyre, B. and Chauchat, J.: Microscopic origins of shear stress in dense fluid – grain mixtures, Granul. Matter, 17(3), 297–309, doi:10.1007/s10035-015-0560-6, 2015.

Matsushima, T. and Takagi, A.: GPS and EDM monitoring of Unzen Volcano ground deformation, Earth, Planets Sp., 52(11), 1015–1018 [online] Available from: http://svr4.terrapub.co.jp/journals/EPS/pdf/5211/52111015.pdf (Accessed 5 November 2013), 2000.

Maxwell, J. C.: On the dynamical theory of gases, Phil Trans. Roy. Soc. Lond., 157, 49–88, doi:10.1098/rstl.1867.0004, 1867.

McBirney, A. R.: Mechanisms of differentiation in the Skaergaard Intrusion, J. Geol. Soc. London., 152(1989), 421–435, doi:10.1144/gsjgs.152.3.0421, 1995.

McBirney, A. R. and Murase, T.: Rheological properties of magmas, Annu. Rev. Earth Planet. Sci., 12, 337–57, 1984.

McKenzie, D. and Holness, M.: Local deformation in compacting flows: Development of pressure shadows, Earth Planet. Sci. Lett., 180(1–2), 169–184, doi:10.1016/S0012-821X(00)00152-7, 2000.

Mcnutt, S. R. and Roman, D. C.: Volcanic Seismicity, in The Encyclopedia of Volcanoes, edited by H. Sigurdsson, B. Houghton, H. Rymer, J. Stix, and S. McNutt, pp. 1011–1034, Elsevier Inc., 2015.

Melnik, O. and Sparks, R. S. J.: Nonlinear dynamics of lava dome extrusion, Nature, 402, 37–41, 1999.

Melnik, O. and Sparks, R. S. J.: Controls on conduit magma flow dynamics during lava dome building eruptions, J. Geophys. Res. B Solid Earth, 110(2), 1–21, doi:10.1029/2004JB003183, 2005.

Merle, O.: The scaling of experiments on volcanic systems, Front. Earth Sci., 3(June), 1–15, doi:10.3389/feart.2015.00026, 2015.

Mewis, J. and Wagner, N. J.: Thixotropy, Adv. Colloid Interface Sci., 148, 214–227, doi:10.1016/j.cis.2008.09.005, 2009.

Moitra, P. and Gonnermann, H. M.: Effects of crystal shape and size modality on magma rheology, Geochemistry, Geophys. Geosystems, (16), 1–26, doi:10.1002/2014GC005554, 2015.

Moitra, P., Gonnermann, H. M., Houghton, B. F. and Giachetti, T.: Relating vesicle shapes in pyroclasts to eruption styles, Bull. Volcanol., 75(2), 1–14, doi:10.1007/s00445-013-0691-8, 2013.

Mueller, S., Melnik, O., Spieler, O., Scheu, B. and Dingwell, D. B.: Permeability and degassing of dome lavas undergoing rapid decompression: An experimental determination, Bull. Volcanol., 67(6), 526–538, doi:10.1007/s00445-004-0392-4, 2005.

Mueller, S., Scheu, B., Spieler, O. and Dingwell, D. B.: Permeability control on magma fragmentation, Geology, 36(5), 399–402, doi:10.1130/G24605A.1, 2008.

Mueller, S., Scheu, B., Kueppers, U., Spieler, O., Richard, D. and Dingwell, D. B.: The porosity of pyroclasts as an indicator of volcanic explosivity, J. Volcanol. Geotherm. Res., 203(3–4), 168–174, doi:10.1016/j.jvolgeores.2011.04.006, 2011a.

Mueller, S. P., Llewellin, E. W. and Mader, H. M.: The rheology of suspensions of solid particles, Proceeding R. Soc., 466, 1201–1228, doi:10.1098/rspa.2009.0445, 2010.

Mueller, S. P., Llewellin, E. W. and Mader, H. M.: The effect of particle shape on suspension viscosity and implications for magmatic flows, Geophys. Res. Lett., 38(13), 1–5, doi:10.1029/2011GL047167, 2011b.

Nakada, S. and Fujii, T.: Preliminary report on the activity at Unzen Volcano (Japan), November 1990-November 1991: Dacite lava domes and pyroclastic flows, J. Volcanol. Geotherm. Res., 54(3–4), 319–333, doi:10.1016/0377-0273(93)90070-8, 1993.

Nakada, S. and Motomura, Y.: Petrology of the 1991-1995 eruption at Unzen: Effusion pulsation and

groundmass crystallization, J. Volcanol. Geotherm. Res., 89(1–4), 173–196, doi:10.1016/S0377-0273(98)00131-0, 1999.

Nakada, S., Miyake, Y., Sato, H., Oshima, O. and Fujinawa, A.: Endogenous growth of dacite dome at Unzen volcano (Japan), 1993-1994, Geology, 23(2), 157, doi:10.1130/0091-7613(1995)023<0157:EGODDA>2.3.CO;2, 1995a.

Nakada, S., Miyake, Y., Sato, H., Oshima, O. and Fujinawa, A.: Endogenous growth of dacite dome at Unzen volcano (Japan), 1993–1994, Geology, 23(2), 157, doi:10.1130/0091-7613(1995)023<0157:EGODDA>2.3.CO;2, 1995b.

Nakada, S., Shimizu, H. and Ohta, K.: Overview of the 1990 – 1995 eruption at Unzen Volcano, J. Volcanol. Geotherm. Res., (89), 1–22, doi:10.1016/S0377-0273(98)00118-8, 1999a.

Nakada, S., Shimizu, H. and Ohta, K.: Overview of the 1990 – 1995 eruption at Unzen Volcano, J. Volcanol. Geotherm. Res., 89(89), 1–22, doi:10.1016/S0377-0273(98)00118-8, 1999b.

NASA/METI/AIST/Japan Spacesystems, and U. S. /Japa. A. S. T.: NASA EOSDIS Land Processes DAAC ASTER, DEM Prod. N032E130, doi:10.5067/ASTER/AST14DEM.003, 2001.

Okumura, S., Nakamura, M., Uesugi, K., Nakano, T. and Fujioka, T.: Coupled effect of magma degassing and rheology on silicic volcanism, Earth Planet. Sci. Lett., 362, 163–170, doi:10.1016/j.epsl.2012.11.056, 2013.

Ostwald, W.: Concerning the function rate of the viscosity of dispersion systems, , 36(4), 248–250, 1925.

Pallister, B. J. S., Thornber, C. R., Cashman, K. V., Clynne, M. a, Lowers, H. a, Mandeville, C. W., Brownfield, I. K. and Meeker, G. P.: Petrology of the 2004 – 2006 Mount St . Helens Lava Dome — Implications for Magmatic Plumbing and Eruption Triggering, in A Volcano Rekindled: The Renewed Eruption of Mount St. Helens 2004-2006, U.S. Geological Survey Professional Paper 1750, edited by D. R. Sherrod, W. E. Scott, and P. H. Stauffer, pp. 647–702., 2008.

Parmigiani, A., Faroughi, S., Huber, C., Bachmann, O. and Su, Y.: Bubble accumulation and its role in the evolution of magma reservoirs in the upper crust, Nature, 532, 492–495, doi:10.1038/nature17401, 2016.

Passmore, E., Maclennan, J., Fitton, G. and Thordarson, T.: Mush Disaggregation in Basaltic Magma Chambers : Evidence from the AD 1783 Laki Eruption, J. Petrol., 53(12), 2593–2623, doi:10.1093/petrology/egs061, 2012.

Paterson, M. S. and Wong, T.-F.: Experimental Rock Deformation: The Brittle Field, 2nd Edition, Second Edi., Springer, Berlin Heidelberg., 2005.

Phan-Thien, N. and Mai-Duy, N.: Understanding Viscoelasticity: An Introduction to Rheology, Third., edited by K. H. Becker, J.-M. Di Meglio, S. Hassani, B. Munro, R. Needs, W. T. Rhodes, H. E. Stanley, S. Scott, M. Stutzmann, and A. Wipf, Springer International Publishing, Cham, Switzerland., 2017.

Pierson, T. C., Janda, R. J., Thouret, J.-C. and Borrero, C. A.: Perturbation and melting of snow and ice by the 13 November 1985 eruption of Nevado del Ruiz , Colombia , and consequent mobilization , flow and deposition of lahars, J. Volcanol. Geotherm. Res., 41, 17–66, 1990.

Pistone, M., Caricchi, L., Ulmer, P., Burlini, L., Ardia, P., Reusser, E., Marone, F. and Arbaret, L.: Deformation experiments of bubble- and crystal-bearing magmas: Rheological and microstructural analysis, J. Geophys. Res., 117(B5), B05208, doi:10.1029/2011JB008986, 2012.

Pistone, M., Arzilli, F., Dobson, K. J., Cordonnier, B., Reusser, E., Ulmer, P., Marone, F., Whittington, A. G., Mancini, L., Fife, J. L. and Blundy, J. D.: Gas-driven filter pressing in magmas : Insights into in-situ melt segregation from crystal mushes, Geology, 43(8), 699–702, doi:10.1130/G36766.1, 2015.

Pistone, M., Cordonnier, B., Ulmer, P. and Caricchi, L.: Rheological flow laws for multiphase magmas: An empirical approach, J. Volcanol. Geotherm. Res., 321, 158–170, doi:10.1016/j.jvolgeores.2016.04.029, 2016.

Pola, A., Crosta, G., Fusi, N., Barberini, V. and Norini, G.: Influence of alteration on physical properties of volcanic rocks, Tectonophysics, 566–567, 67–86, doi:10.1016/j.tecto.2012.07.017, 2012.

Polacci, M., Arzilli, F., La Spina, G., Le Gall, N., Cai, B., Hartley, M. E., Di Genova, D., Vo, N. T., Nonni, S., Atwood, R. C., Llewellin, E. W., Lee, P. D. and Burton, M. R.: Crystallisation in basaltic magmas revealed via in situ 4D synchrotron X-ray microtomography, Sci. Rep., 8(1), 1–13, doi:10.1038/s41598-018-26644-6, 2018.

Poole, R.: The Deborah and Weissenberg numbers, Br. Soc. Rheol. Rheol. Bull., 53, 32–39, 2012.

Prado, M. O., Zanotto, E. D. and Müller, R.: Model for sintering polydispersed glass particles, J. Non. Cryst. Solids, 279(2–3), 169–178, doi:10.1016/S0022-3093(00)00399-9, 2001.

Prado, M. O., Fredericci, C. and Zanotto, E. D.: Isothermal sintering with concurrent crystallization of polydispersed soda-lime-silica glass beads, J. Non. Cryst. Solids, 331(1–3), 145–156, doi:10.1016/j.jnoncrysol.2003.08.076, 2003a.

Prado, M. O., Zanotto, E. D. and Fredericci, C.: Sintering polydispersed spherical glass particles, J. Mater. Res., 18(6), 1347–1354, doi:10.1557/JMR.2003.0185, 2003b.

Quane, S. L. and Russell, J. K.: Welding: insights from high-temperature analogue experiments, J. Volcanol. Geotherm. Res., 142(1–2), 67–87, doi:10.1016/j.jvolgeores.2004.10.014, 2005.

Quane, S. L., Russell, J. K. and Friedlander, E. a.: Time scales of compaction in volcanic systems, Geology, 37(5), 471–474, doi:10.1130/G25625A.1, 2009.

Reid, M. E., Keith, T. E. C., Kayen, R. E., Iverson, N. R., Iverson, R. M. and Brien, D. L.: Volcano collapse promoted by progressive strength reduction: New data from Mount St. Helens, Bull. Volcanol., 72(6), 761–766, doi:10.1007/s00445-010-0377-4, 2010.

Reiner, M.: The Deborah Number, Phys. Today, 17(1), 62, doi:10.1063/1.3051374, 1964.

Richardson, S. M.: Non-Newtonian fluids, Thermopedia, doi:10.1615/AtoZ.n.non-newtonian_fluids, 2011.

Roscoe, R.: The viscosity of suspensions of rigid spheres, Br. J. Appl. Phys., 3(8), 267–269, doi:10.1088/0508-3443/3/8/306, 1952.

Russell, J. K. and Quane, S. L.: Rheology of welding: Inversion of field constraints, J. Volcanol. Geotherm. Res., 142(1-2 SPEC. ISS.), 173–191, doi:10.1016/j.jvolgeores.2004.10.017, 2005.

Rust, A. C. and Manga, M.: Effects of bubble deformation on the viscosity of dilute suspensions, J. Non-

Newtonain Fluid Mechanaics, 104, 53–63, 2002.

Rutter, E. H.: On the nomenclature of mode of failure transitions in rocks, Tectonophysics, 122(3–4), 381–387, doi:10.1016/0040-1951(86)90153-8, 1986.

Sakuma, S., Kajiwara, T., Nakada, S., Uto, K. and Shimizu, H.: Drilling and logging results of USDP-4 - Penetration into the volcanic conduit of Unzen Volcano, Japan, J. Volcanol. Geotherm. Res., 175(1–2), 1–12, doi:10.1016/j.jvolgeores.2008.03.039, 2008.

Sammis, C. G. and Ashby, M. F.: The failure of brittle porous solids under compressive stress states, Acta Metall., 34(3), 511–526, 1986.

Samsonov, G. V., Ed.: Mechanical Properties of the Elements, in Handbook of the Physicochemical Properties of the Elements, p. 432, Plenum Publishing Corporation, New York., 1968.

Schaefer, L. N., Kendrick, J. E., Oommen, T., Lavallée, Y. and Chigna, G.: Geomechanical rock properties of a basaltic volcano, Front. Earth Sci., 3(June), 1–15, doi:10.3389/feart.2015.00029, 2015.

Schauroth, J., Wadsworth, F. B., Kennedy, B., Aulock, F. W. Von, Lavallée, Y., Damby, D. E., Vasseur, J., Scheu, B. and Dingwell, D. B.: Conduit margin heating and deformation during the AD 1886 basaltic Plinian eruption at Tarawera volcano , New Zealand, Bull. Volcanol., 78(12), doi:10.1007/s00445-016-1006-7, 2016.

Scholz, C. H.: Microfracturing and the inelastic deformation of rock in compression, J. Geophys. Res., 73(4), 1417, doi:10.1029/JB073i004p01417, 1968.

Schultz, P. H. and Mustard, J. F.: Impact melts and glasses on Mars, J. Geophys. Res., 109(E01001), 1–23, doi:10.1029/2002JE002025, 2004.

Scott, W. E., Sherrod, D. R. and Gardner, C. A.: Overview of the 2004 to 2006, and continuing, eruption of Mount St. Helens, Washington, in A Volcano Rekindled: The Renewed Eruption of Mount St. Helens, 2004-2006, U.S. Geological Survey Professional Paper 1750, vol. 1750, edited by D. R. Sherrod, W. E. Scott, and P. H. Stauffer, pp. 3–22. [online] Available from: http://pubs.usgs.gov/pp/1750/chapters/pp2008-1750_chapter01.pdf, 2008.

Shaw, H.: Comments on viscosity crystal settling and convection in granitic magmas, Am. J. Sci., 263(2), 120–152, doi:10.2475/ajs.263.2.120, 1965.

Shaw, H. R.: Obsidian-H20 Viscosities at 1000 and 2000 Bars in the Temperature Range 7000 ° to 900 °C, J. Geophys. Res., 68(23), 6337–6343, doi:10.1029/JZ068i023p06337, 1963.

Siebert, L., Glicken, H. and Ui, T.: Volcanic hazards from Bezymianny- and Bandai-type eruptions, Bull. Volcanol., 49(1), 435–459, doi:10.1007/BF01046635, 1987.

Siebert, L., Cottrell, E., Venzke, E. and Andrews, B.: Earth's Volcanoes and Their Eruptions: An Overview, in The Encyclopedia of Volcanoes, edited by H. Sigurdsson, B. F. Houghton, S. McNutt, H. Rymer, and J. Stix, pp. 239–256, Elsevier., 2015.

de Silva, S. and Lindsay, J. M.: Primary Volcanic Landforms, in The Encyclopedia of Volcanoes, edited by H. Sigurdsson, B. Houghton, S. McNutt, H. Rymer, and J. Stix, pp. 273–298, Elsevier., 2015.

Singh, K., Menke, H., Andrew, M., Rau, C., Bijeljic, B. and Blunt, M. J.: Time-resolved tomography datasets of drainage and imbibition in carbonate rocks, Nat. Sci. Data, 5, 1–8, doi:10.1038/sdata.2018.265, 2018.

Sisson, T. W. and Bacon, C. R.: Gas-driven filter pressing in magmas, Geology, 27(7), 613–616, doi:10.1130/0091-7613(1999)027<0613:GDFPIM>2.3.CO;2, 1999.

Smith, J. V.: Textural evidence for dilatant (shear thickening) rheology of magma at high crystal concentrations, J. Volcanol. Geotherm. Res., 99(1–4), 1–7, doi:10.1016/S0377-0273(99)00191-2, 2000.

Smith, R., Kilburn, C. R. J. and Sammonds, P. R.: Rock fracture as a precursor to lava dome eruptions at Mount St Helens from June 1980 to October 1986, Bull. Volcanol., 69(6), 681–693, doi:10.1007/s00445-006-0102-5, 2007.

Smith, R., Sammonds, P. R., Tuffen, H. and Meredith, P. G.: Evolution of the mechanics of the 2004-2008 Mt. St. Helens lava dome with time and temperature, Earth Planet. Sci. Lett., 307(1–2), 191–200, doi:10.1016/j.epsl.2011.04.044, 2011.

Sparks, R. S. J.: Causes and consequences of pressurisation in lava dome eruptions, Earth Planet. Sci. Lett., 150(3–4), 177–189, doi:10.1016/S0012-821X(97)00109-X, 1997.

Sparks, R. S. J.: Forecasting volcanic eruptions, Earth Planet. Sci. Lett., 210, 1–15, doi:10.1016/S0012-821X(03)00124-9, 2003.

Sparks, R. S. J. and Young, S. R.: The eruption of Soufrière Hills Volcano , Montserrat (1995-1999): overview of scientific results, in The Eruption of Soufri~re Hills Volcano, Montserrat, from 1995 to 1999., edited by T. H. Druitt and B. P. Kokelaar, pp. 45–69, Geological Society, London, Memoirs., 2002.

Stasiuk, M. V. and Jaupart, C.: Lava flow shapes and dimensions as reflections of magma system conditions, J. Volcanol. Geotherm. Res., 78(1–2), 31–50, doi:10.1016/S0377-0273(97)00002-4, 1997.

Stickel, J. J. and Powell, R. L.: Fluid mechanics and rheology of dense suspensions, Annu. Rev. Fluid Mech., 37, 129–49, doi:10.1146/annurev.fluid.36.050802.122132, 2005.

Surono, Jousset, P., Pallister, J., Boichu, M., Buongiorno, M. F., Budisantoso, A., Costa, F., Andreastuti, S., Prata, F., Schneider, D., Clarisse, L., Humaida, H., Sumarti, S., Bignami, C., Griswold, J., Carn, S., Oppenheimer, C. and Lavigne, F.: The 2010 explosive eruption of Java's Merapi volcano-A "100-year" event, J. Volcanol. Geotherm. Res., 241–242, 121–135, doi:10.1016/j.jvolgeores.2012.06.018, 2012.

Takarada, S., Miyabuchi, Y., Hoshizumi, H., Matsushima, T. and Nagai, D.: A02: Unzen and Aso volcanoes, central Kyushu, Japan: Unzen's new lava dome climb and 1991-95 poyroclastic flows and Aso's active crater and one of the largest calderas in Japan, 2013.

Tanguy, J. C.: Rapid dome growth at Montagne Pelée during the early stages of the 1902-1905 eruption: A reconstruction from Lacroix's data, Bull. Volcanol., 66(7), 615–621, doi:10.1007/s00445-004-0344-z, 2004.

Thomas, D. G.: Transport characteristics of suspension: VIII. A note on the viscosity of Newtonian suspensions of uniform spherical particles, J. Colloid Sci., 20(3), 267–277, doi:10.1016/0095-8522(65)90016-4, 1965.

Titarenko, V., Bradley, R., Martin, C., Withers, P. J. and Titarenko, S.: Regularization methods for inverse

problems in X-ray tomography, Proc. SPIE, 7804(78040Z), 1–10, doi:10.1117/12.860260, 2010.

Torquato, S.: Random Heterogeneous Materials: Microstructure and Macroscopic Properties, edited by S. S. Antman, J. E. Marsden, L. Sirovich, and S. Wiggins, Springer Science and Business Media, New York., 2002.

Truby, J. M., Mueller, S. P., Llewellin, E. W. and Mader, H. M.: The rheology of three-phase suspensions at low bubble capillary number., Proc. Math. Phys. Eng. Sci., 471(2173), 20140557, doi:10.1098/rspa.2014.0557, 2015.

Tuffen, H., Dingwell, D. B. and Pinkerton, H.: Repeated fracture and healing of silicic magma generate flow banding and earthquakes?, Geology, 31(12), 1089–1092, doi:10.1130/G19777.1, 2003.

Tuffen, H., Smith, R. and Sammonds, P. R.: Evidence for seismogenic fracture of silicic magma, Nature, 453(May), 511–514, doi:10.1038/nature06989, 2008.

Ujiie, K., Tsutsumi, A., Fialko, Y. and Yamaguchi, H.: Experimental investigation of frictional melting of argillite at high slip rates : Implications for seismic slip in subduction-accretion complexes, J. Geophys. Res., 114(B04308), 1–12, doi:10.1029/2008JB006165, 2009.

Umakoshi, K., Takamura, N., Shinzato, N., Uchida, K., Matsuwo, N. and Shimizu, H.: Seismicity associated with the 1991–1995 dome growth at Unzen Volcano, Japan, J. Volcanol. Geotherm. Res., 175(1–2), 91–99, doi:10.1016/j.jvolgeores.2008.03.030, 2008.

Vallance, J. W., Schneider, D. J. and Schilling, S. P.: Growth of the 2004-2006 Lava-Dome Complex at Mount St. Helens, Washington, in A Volcano Rekindled: The Renewed Eruption of Mount St. Helens 2004-2006, edited by D. R. Sherrod, W. E. Scott, and P. H. Stauffer, pp. 169–208, U.S. Geological Survey Professional Paper 1750., 2008.

Vasseur, J., Wadsworth, F. B., Lavallée, Y., Hess, K.-U. and Dingwell, D. B.: Volcanic sintering: Timescales of viscous densification and strength recovery, Geophys. Res. Lett., 40(21), 5658–5664, doi:10.1002/2013GL058105, 2013.

Vasseur, J., Wadsworth, F. B., Lavallée, Y., Bell, A. F., Main, I. G. and Dingwell, D. B.: Heterogeneity: The key to failure forecasting, Sci. Rep., 5, 1–7, doi:10.1038/srep13259, 2015.

Venezky, D. Y. and Rutherford, M. J.: Petrology and Fe–Ti oxide reequilibration of the 1991 Mount Unzen mixed magma, J. Volcanol. Geotherm. Res., 89(1–4), 213–230, doi:10.1016/S0377-0273(98)00133-4, 1999.

Voight, B.: Structural stability of andesite volcanoes and lava domes, Philos. Trans. R. Soc. London, 358, 1663–1703, doi:10.1098/rsta.2000.0609, 2000.

Voight, B. and Elsworth, D.: Failure of volcano slopes, Geotechnique, 47(1), 1–31, 1997.

Voight, B. and Elsworth, D.: Instability and collapse of hazardous gas-pressurized lava domes, Geophys. Res. Lett., 27(1), 1–4, 2000.

Voight, B., Glicken, H., Janda, J. and Douglass, P. M.: Catastrophic rockslide avalanche of May 18, in The 1980 eruptions of Mount St Helens, Washington, vol. 1250, edited by P. W. Lipman and D. R. Mullineaux, pp. 347–378, Geological Survey Professional Paper., 1981.

Voight, B., Sparks, R. S. J., Miller, A. D., Stewart, R. C., Hoblitt, R. P., Clarke, A., Ewart, J., Aspinall, W. P., Baptie, B., Calder, E. S., Cole, P. D., Druitt, T. H., Hartford, C., Herd, R. A., Jackson, P., Lejeune, A. M., Lockhart, A. B., Loughlin, S. C., Luckett, R., Lynch, L., Norton, G. E., Robertson, R., Watson, I. M., Watts, R. and Young, S. R.: Magma Flow Instability and Cyclic Activity at Soufriere Hills Volcano , Montserrat , British West Indies, , 643(May), 2009.

Vona, A., Romano, C., Dingwell, D. B. and Giordano, D.: The rheology of crystal-bearing basaltic magmas from Stromboli and Etna, Geochim. Cosmochim. Acta, 75(11), 3214–3236, doi:10.1016/j.gca.2011.03.031, 2011.

Vona, A., Romano, C., Giordano, D. and Russell, J. K.: The multiphase rheology of magmas from Monte Nuovo (Campi Flegrei, Italy), Chem. Geol., 346, 213–227, doi:10.1016/j.chemgeo.2012.10.005, 2013.

Wadsworth, F. B.: Densification of permeable liquids and magmas, LMU München., 2016.

Wadsworth, F. B., Vasseur, J., Von Aulock, F. W., Hess, K.-U., Scheu, B., Lavallée, Y. and Dingwell, D. B.: Nonisothermal viscous sintering of volcanic ash, J. Geophys. Res. Solid Earth, 119, 8792–8804, doi:10.1002/2014JB011453.Received, 2014.

Wadsworth, F. B., Vasseur, J., Llewellin, E. W., Schauroth, J., Dobson, K. J., Scheu, B. and Dingwell, D. B.: Sintering of viscous droplets under surface tension, Proceeding R. Soc., 472(20150780), doi:10.1098/rspa.2015.0780, 2016.

Wadsworth, F. B., Vasseur, J., Llewellin, E. W. and Dingwell, D. B.: Sintering of polydisperse viscous droplets, Phys. Rev. E, 95(3), 033114, doi:10.1103/PhysRevE.95.033114, 2017a.

Wadsworth, F. B., Witcher, T., Vasseur, J., Dingwell, D. B. and Scheu, B.: When Does Magma Break?, in Advances in Volcanology, Springer, Berlin, Heidelberg., 2017b.

Wadsworth, F. B., Witcher, T., Vossen, C. E. J., Hess, K.-U., Unwin, H. E., Scheu, B., Castro, J. M. and Dingwell, D. B.: Combined effusive-explosive silicic volcanism straddles the multiphase viscous-to-brittle transition, Nat. Commun., 9(1), 4696, doi:10.1038/s41467-018-07187-w, 2018.

Wallace, P. A., Kendrick, J. E., Miwa, T., James, D., Coats, R., Utley, J. E. P., Angelis, S. H. De, Mariani, E., Biggin, A., Kendrick, R., Nakada, S., Matsushima, T. and Lavallée, Y.: Petrological architecture of a magmatic shear zone : A multidisciplinary investigation of strain localisation during magma ascent at Unzen volcano , Japan, J. Petrol., 60(4), 791–826, doi:10.1093/petrology/egz016, 2019.

Wallace, P. A., Kendrick, J. E., Ashworth, J. D., Miwa, T., Coats, R., De Angelis, S. H., Mariani, E., Utley, J., Biggan, A. and Lavallée, Y.: Petrological architecture of a magmatic shear zone: A multidisciplinary investigation of strain localisation during magma ascent at Unzen volcano, Japan, n.d.

Walter, T. R., Troll, V. R., Cailleau, B., Belousov, A., Schmincke, H. U., Amelung, F. and Bogaard, P.: Rift zone reorganization through flank instability in ocean island volcanoes: An example from Tenerife, Canary Islands, Bull. Volcanol., 67(4), 281–291, doi:10.1007/s00445-004-0352-z, 2005.

Webb, S. L. and Dingwell, D. B.: Non-Newtonian Rheology of Igneous Melts at High Stresses and Strain Rates: Experimental Results for Rhyolite, Andesite, Basalt, and Nephelinite, J. Geophys. Res., 95(B10), 15,695-

15,701, 1990a.

Webb, S. L. and Dingwell, D. B.: The onset of non-Newtonian rheology of silicate melts - A fiber elongation study, Phys. Chem. Miner., 17(2), 125–132, doi:10.1007/BF00199663, 1990b.

Webb, S. L. and Knoche, R.: The glass-transition, structural relaxation and shear viscosity of silicate melts, Chem. Geol., 128(1–4), 165–183, doi:10.1016/0009-2541(95)00171-9, 1996.

Webb, S. L., Knoche, R. and Dingwell, D. B.: Determination of Silicate Liquid Thermal Expansivity Using Dilatometry and Calorimetry, Eur. J. Mineral., 4(1), 95–104, 1992.

Xu, W. W., Tzanakis, I., Srirangam, P. and Mirihanage, W. U.: Synchrotron Quantification of Ultrasound Cavitation and Bubble Dynamics in Al-10Cu Melts, Ultrason. Sonochem., 31(July), 355–361, doi:10.1016/j.ultsonch.2016.01.017, 2016.

Yamamoto, T., Takarada, S. and Suto, S.: Pyroclastic flows from the 1991 eruption of Unzen volcano, Japan, Bull. Volcanol., 55(3), 166–175, doi:10.1007/BF00301514, 1993.

Yilmaz, T. I., Gilg, H. ., Wallace, P. A., Hess, K.-U., Wadsworth, F. B., Utley, J., Kendrick, J. E., Lavallée, Y., Nakada, S. and Dingwell, D. B.: Rapid three-stage clay alteration of conduit dykes from the Mt Unzen USDP-4 drill core, Geology, n.d.

Young, S. R., Sparks, R. S. J., Aspinall, W. P., Lynch, L. L., Miller, A. D., Robertson, R. E. A. and Shepherd, J. B.: Overview of the eruption of Soufriere Hills Volcano, Montserrat, 18 July 1995 to December 1997, Geophys. Res. Lett., 25(18), 3389–3392, doi:10.1029/98GL01405, 1998.

Zhang, Y.: H2O in rhyolitic glasses and melts: measurement, speciation, solubility, and diffusion, Rev. Geophys., 34(4), 493–516, doi:10.1029/1999RG900012, 1999.

Zhu, W., Baud, P. and Wong, T.-F.: Micromechanics of cataclastic pore collapse in limestone, J. Geophys. Res. Solid Earth, 115(4), doi:10.1029/2009JB006610, 2010.